Multiwavelength and Multimessenger emission from Active Galactic Nuclei

Contents

1 Topics **5**
- 1.1 ICRANet participants . . . 5
- 1.2 Students . . . 5
- 1.3 Ongoing collaborations . . . 5

2 Brief description **7**

3 Publications-2022 **11**
- 3.1 Publications-2012-2021 . . . 12

4 A thirteen-year-long broadband view of BL Lac **21**
- 4.1 Introduction . . . 21
- 4.2 Fermi-LAT Observations and Data Analysis . . . 24
  - 4.2.1 *Swift* XRT . . . 27
  - 4.2.2 *Swift* UVOT . . . 29
  - 4.2.3 Archival data . . . 30
- 4.3 Modeling the SEDs . . . 31
  - 4.3.1 SEDs modeling results . . . 33
- 4.4 Discussion . . . 37
- 4.5 Conclusion . . . 42

5 Modeling the time variable spectral energy distribution of the blazar CTA 102 from 2008 to 2022 **45**
- 5.1 Introduction . . . 45
- 5.2 Multiwavelength observations of CTA 102 . . . 48
  - 5.2.1 Fermi-LAT observations of CTA 102 . . . 48
  - 5.2.2 Swift observations of CTA 102 . . . 49
  - 5.2.3 NuSTAR observations of CTA 102 . . . 51
  - 5.2.4 Archival optical data . . . 51
- 5.3 Multiwavelength variability . . . 52
- 5.4 Broadband SED modeling . . . 54
- 5.5 Results and Discussion . . . 56
  - 5.5.1 Long-term broadband SED modeling . . . 57
  - 5.5.2 Energy distribution of the emitting electrons . . . 59
  - 5.5.3 Formation of electron spectrum . . . 62

5.5.4 Jet power 65
5.6 Conclusion 66

6 Time-dependent lepto-hadronic modeling of the emission from blazar jets with SOPRANO: the case of TXS 0506+056, 3HSP J095507.9+355101 and 3C 279 67
6.1 Introduction 67
6.2 *SOPRANO*: Simulator Of Processes in Relativistic AstroNomical Objects 70
6.3 Model Setup: Analytical estimation of model parameters . . . 72
6.4 Modeling of Blazar SEDs 78
6.4.1 Modeling of TXS 0506+056 SED 78
6.4.2 Modeling of 3HSP J095507.9+355101 SED 82
6.4.3 Modeling of 3C 279 SED during the 2015 flare 85
6.5 Discussion 87
6.6 Conclusion 90
.1 Physical processes in *Soprano* and their kinetic equations . . . 92
.1.1 Kinetic equations for all particles 92
.1.2 Synchrotron emission and cooling 94
.1.3 Inverse Compton scattering. 95
.1.4 Pair production 96
.1.5 Bethe-Heitler pair production 97
.1.6 Photo-hadronic interaction : pion production 99
.1.7 Particle decay 101
.1.8 Photon and particle escape 102
.2 Numerical discretization and prescription in *SOPRANO* . . . 103
.3 Code tests and examples 107
.3.1 Synchrotron and inverse Compton cooling for electrons 107
.3.2 Proton cooling on black-body photons by photo-pair and photo-pion interaction 108
.3.3 Decay time 109

1 Topics

- High energy gamma-rays from active galactic nuclei
- High energy neutrinos from blazars
- High energy emission from gamma-ray bursts

1.1 ICRANet participants

- Sahakyan Narek
- Gasparyan Sargis
- Israyelyan Davit

1.2 Students

- Harutyunyan Gevorg
- Khachatryan Mher
- Vazgen Vardanyan
- Manvel Manvelyan

1.3 Ongoing collaborations

- Razmik Mirzoyan (Max Planck Institute for Physics, Munich, Germany)
- Paolo Giommi (ASI Science Data Center)
- Damien Begue (Bar Ilan University, Israel)
- Ulisses Barres de Almeida (Centro Brasileiro de Pesquisas Fisicas - CBPF/MCT)
- Bernardo Fraga (Centro Brasileiro de Pesquisas Fisicas - CBPF)
- Karlica Mile (Nova Gorica)

2 Brief description

The main scientific activities of our group are in the field of X- and gamma-ray Astrophysics and Astroparticle physics. The results from the data analysis of Swift UVOT/XRT, NuStar, Chandra and Fermi LAT telescopes are used to investigate the particle acceleration and emission processes in the different classes of active galactic nuclei. The analysis of available data allows to investigate the emission processes and relativistic outflows in the most extreme regimes (keV-TeV).
Below we present several abstracts from the papers published in 2022, also with MAGIC collaboration.

- Modelling the time variable spectral energy distribution of the blazar CTA 102 from 2008 to 2022

We present long-term multiwavelength observations of blazar CTA 102 ($z = 1.037$). Detailed temporal and spectral analyses of γ-ray, X-ray and UV/optical data observed by Fermi-LAT, Swift XRT, NuSTAR and Swift-UVOT over a period of 14 years, between August 2008 and March 2022, was performed. We found strong variability of source emission in all the considered bands, especially in the γ-ray band it exhibited extreme outbursts when the flux crossed the level of $10^{-5}\ photon\ cm^{-2}\ s^{-1}$. Using the Bayesian Blocks algorithm, we split the adaptively binned γ-ray light curve into 347 intervals of quiescent and flaring episodes and for each period built corresponding multiwavelength spectral energy distributions (SEDs), using the available data. Among the considered SEDs, 117 high-quality (quasi) contemporaneous SEDs which have sufficient multiwavelength data, were modeled using JetSeT framework within a one-zone leptonic synchrotron and inverse Compton emission scenario assuming the emitting region is within the broad-line-region and considering internal and external seed photons for the inverse Compton upscattering. As a result of modeling, the characteristics of the relativistic electron distribution in the jet as well as jet properties are retrieved and their variation in time is investigated. The applied model can adequately explain the assembled SEDs and the modelling shows that the data in the bright flaring periods can be reproduced for high Doppler boosting and magnetic field. The obtained results are discussed in the context of particle cooling in the emitting region.

- A thirteen-year-long broadband view of BL Lac

We present the results of an extensive analysis of the optical, ultraviolet, X-ray and γ-ray data collected from the observations of the BL Lac objects prototype BL Lacertae carried out over a period of nearly 13 years, between August 2008 and March 2021. The source is characterized by strongly variable emission at all frequencies, often accompanied by spectral changes. In the γ-ray band several prominent flares have been detected, the largest one reaching the flux of $F_\gamma(> 196.7\,MeV) = (4.39 \pm 1.01) \times 10^{-6}\,photon\,cm^{-2}\,s^{-1}$. The X-ray spectral variability of the source during the brightest flare on MJD 59128.18 (06 October 2020) was characterized by a softer-when-brighter trend due to a shift of the synchrotron peak to $\sim 10^{16}$ Hz, well into the HBL domain. The widely changing multiwavelength emission of BL Lacertae was systematically investigated by fitting leptonic models that include synchrotron self-Compton and external Compton components to 511 high-quality and quasi-simultaneous broad-band spectral energy distributions (SEDs). The majority of selected SEDs can be adequately fitted within a one-zone model with reasonable parameters. Only 46 SEDs with soft and bright X-ray spectra and when the source was observed in very high energy γ-ray bands can be explained in a two-zone leptonic scenario. The HBL behaviour observed during the brightest X-ray flare is interpreted as due to the emergence of synchrotron emission from freshly accelerated particles in a second emission zone located beyond the broad line region.

- Time-dependent lepto-hadronic modeling of the emission from blazar jets with SOPRANO: the case of TXS 0506+056, 3HSP J095507.9+355101 and 3C 279

The observation of a very-high-energy neutrino by IceCube (IceCube-170922A) and its association with the flaring blazar TXS 0506+056 provided the first multimessenger observations of blazar jets, demonstrating the important role of protons in their dynamics and emission. In this paper, we present SOPRANO (`https://www.amsdc.am/soprano`), a new conservative implicit kinetic code which follows the time evolution of the isotropic distribution functions of protons, neutrons and the secondaries produced in photo-pion and photo-pair interactions, alongside with the evolution of photon and electron/positron distribution functions. SOPRANO is designed to study leptonic and hadronic processes in relativistic sources such as blazars and gamma-ray bursts. Here, we use SOPRANO to model the broadband spectrum of TXS 0506+056 and 3HSP J095507.9+355101, which are associated with neutrino events, and of the extreme flaring blazar 3C 279. The SEDs are interpreted within the guise of both a hadronic and a hybrid model. We discuss the implications of our assumptions in terms of jet power and neutrino flux.

- The first hard X-ray spectral catalogue of Blazars observed by NuSTAR

Blazars are a peculiar class of active galactic nuclei that enlighten the sky at all wavelengths. The electromagnetic emission of these sources is jet-dominated, resulting in a spectral energy distribution (SED) that has a typical double-humped shape. X-ray photons provide a wealth of information on the physics of each source as in the X-ray band, we can observe the tail of SED first peak, the rise of the second one or the transition between the two. NuSTAR, thanks to its capability of focusing X-rays up to 79 keV provides broad-band data particularly suitable to compute SEDs in a still poorly explored part of the spectrum. In the context of the Open Universe initiative, we developed a dedicated pipeline, NuSTAR_Spectra, a shell-script that automatically downloads data from the archive, generates scientific products and carries out a complete spectral analysis. The script homogeneously extracts high level scientific products for both NuSTAR's telescopes and the spectral characterization is performed testing two phenomenological models. The corresponding X-ray properties are derived from the data best fit, and the SEDs are also computed. The systematic processing of all blazar observations of the NuSTAR public archive allowed us to release the first hard X-ray spectroscopic catalogue of blazars (NuBlazar). The catalogue, updated to 2021 September 30, includes 253 observations of 126 distinct blazars, 30 of which have been multiply observed.

- Multiwavelength study of the gravitationally lensed blazar QSO B0218+357 between 2016 and 2020

We report multiwavelength observations of the gravitationally lensed blazar QSO B0218+357 in 2016-2020. Optical, X-ray and GeV flares were detected. The contemporaneous MAGIC observations do not show significant very-high-energy (VHE, $\gtrsim 100\,\mathrm{GeV}$) gamma-ray emission. The lack of enhancement in radio emission measured by OVRO indicates the multi-zone nature of the emission from this object. We constrain the VHE duty cycle of the source to be < 16 2014-like flares per year (95% confidence). For the first time for this source, a broadband low-state SED is constructed with a deep exposure up to the VHE range. A flux upper limit on the low-state VHE gamma-ray emission of an order of magnitude below that of the 2014 flare is determined. The X-ray data are used to fit the column density of $(8.10 \pm 0.93_{stat}) \times 10^{21}\mathrm{cm}^{-2}$ of the dust in the lensing galaxy. VLBI observations show a clear radio core and jet components in both lensed images, yet no significant movement of the components is seen. The radio measurements are used to model the source-lens-observer geometry and determine the magnifications and time delays for both components. The quiescent emission is modeled with the high-energy bump explained as a combination of

synchrotron-self-Compton and external Compton emission from a region located outside of the broad line region. The bulk of the low-energy emission is explained as originating from a tens-of-parsecs scale jet.

- Proton acceleration in thermonuclear nova explosions revealed by gamma rays

Classical novae are cataclysmic binary star systems in which the matter of a companion star is accreted on a white dwarf (WD). Accumulation of hydrogen in a layer eventually causes a thermonuclear explosion on the surface of the WD, brightening the WD to $\sim 10^5$ solar luminosities and triggering ejection of the accumulated matter.They provide extreme conditions required to accelerate particles, electrons or protons, to high energies. Here we present the detection of gamma rays by the MAGIC telescopes from the 2021 outburst of RS Ophiuchi (RS Oph), a recurrent nova with a red giant (RG) companion, that allowed us, for the first time, to accurately characterize the emission from a nova in the 60 GeV to 250 GeV energy range. The theoretical interpretation of the combined Fermi-LAT and MAGIC data suggests that protons are accelerated to hundreds of GeV in the nova shock. Such protons should create bubbles of enhanced Cosmic Ray density, on the order of 10 pc, from the recurrent novae.

3 Publications-2022

- Sahakyan, N., Israyelyan, D., Harutyunyan, G., Gasparyan, S., Vardanyan, V., Khachatryan, M. 2022. Modelling the time variable spectral energy distribution of the blazar CTA 102 from 2008 to 2022. Monthly Notices of the Royal Astronomical Society 517, 27572768. doi:10.1093/mnras/stac2875
- Sahakyan, N., Giommi, P. 2022, A 13-yr-long broad-band view of BL Lac, Monthly Notices of the Royal Astronomical Society 513, 46454656. doi:10.1093/mnras/stac1011
- Gasparyan, S., Bégué, D., Sahakyan, N. 2022. Time-dependent lepto-hadronic modelling of the emission from blazar jets with SOPRANO: the case of TXS 0506 + 056, 3HSP J095507.9 + 355101, and 3C 279. Monthly Notices of the Royal Astronomical Society 509, 21022121. doi:10.1093/mnras/stab2688
- Middei R., Giommi P., Perri M., Turriziani S., Sahakyan N., Chang Y., Leto C., Verrecchia F., 2022 The first hard X-ray spectral catalogue of Blazars observed by NuSTAR. Monthly Notices of the Royal Astronomical Society 514, 31793190. doi:10.1093/mnras/stac1185
- Rueda, J. A., Li, L., Moradi, R., Ruffini, R., Sahakyan, N., Wang, Y. 2022. On the X-Ray, Optical, and Radio Afterglows of the BdHN I GRB 180720B Generated by Synchrotron Emission. The Astrophysical Journal 939. doi:10.3847/1538-4357/ac94c9
- Wang, Yu, Rueda J., Ruffini R., Moradi R., Liang L., Aimuratov Y., Rastegarnia F., Eslamzadeh S., Sahakyan N., Zheng Y., 2022 GRB 190829A-A Showcase of Binary Late Evolution, The Astrophysical Journal 936. doi:10.3847/1538-4357/ac7da3
- MAGIC Collaboration, Acciari V., Ansoldi S.,.... Gasparyan, S.,...Sahakyan N.,.... 2022, Investigating the Blazar TXS 0506+056 through Sharp Multiwavelength Eyes During 2017-2019. The Astrophysical Journal 927. doi:10.3847/1538-4357/ac531d
- MAGIC Collaboration, Abe H., Abe S.,.... Gasparyan, S.,...Sahakyan N.,.... 2022, Gamma-ray observations of MAXI J1820+070 during the 2018 outburst. Monthly Notices of the Royal Astronomical Society 517, 47364751. doi:10.1093/mnras/stac2686

- MAGIC Collaboration, Adams C., Batista P.,.... Gasparyan, S.,...Sahakyan N.,.... 2022, Multiwavelength Observations of the Blazar VER J0521+211 during an Elevated TeV Gamma-Ray State, The Astrophysical Journal 932. doi:10.3847/1538-4357/ac6dd9

- MAGIC Collaboration, Acciari V., Ansoldi S.,.... Gasparyan, S.,...Sahakyan N.,.... 2022, Proton acceleration in thermonuclear nova explosions revealed by gamma rays. Nature Astronomy 6, 689697. doi:10.1038/s41550-022-01640-z

- MAGIC Collaboration, Acciari V., Ansoldi S.,.... Gasparyan, S.,...Sahakyan N.,.... 2022, Multi-epoch monitoring of TXS 0506+056 with MAGIC and MWL partners. 37th International Cosmic Ray Conference. doi:10.22323/1.395.0875

- MAGIC Collaboration, Acciari V., Ansoldi S.,.... Gasparyan, S.,...Sahakyan N.,.... 2022, Multiwavelength variability and correlation studies of Mrk421 during historically low X-ray and γ-ray activity in 2015–2016. 37th International Cosmic Ray Conference. doi:10.22323/1.395.0866

- MAGIC Collaboration, Acciari V., Ansoldi S.,.... Gasparyan, S.,...Sahakyan N.,.... 2022. Combined searches for dark matter in dwarf spheroidal galaxies observed with the MAGIC telescopes, including new data from Coma Berenices and Draco. Physics of the Dark Universe 35. doi:10.1016/j.dark.2021.100912

- MAGIC Collaboration, Acciari V., Ansoldi S.,.... Gasparyan, S.,...Sahakyan N.,.... 2022, Multiwavelength study of the gravitationally lensed blazar QSO B0218+357 between 2016 and 2020. Monthly Notices of the Royal Astronomical Society 510, 23442362. doi:10.1093/mnras/stab3454

- Rueda J., Ruffini R., Li L., Moradi R., Sahakyan, N., Wang Y., 2022. The white dwarf binary merger model of GRB 170817A, International Journal of Modern Physics D 31. doi:10.1142/S0218271822300130

3.1 Publications-2012-2021

- Sahakyan, N., Modelling the broad-band emission of 3C 454.3, Monthly Notices of the Royal Astronomical Society, Volume 504, Issue 4, 2021, pp.5074-5086.

- Sahakyan, N. and Giommi, P., The strange case of the transient HBL blazar 4FGL J1544.3-0649, Monthly Notices of the Royal Astronomical Society, Volume 502, Issue 1, 2021, pp.836-844.

- Giommi, P.....sahakyan, N....., X-ray spectra, light curves and SEDs of blazars frequently observed by Swift, Monthly Notices of the Royal Astronomical Society, Volume 507, Issue 4, 2021, pp.5690-5702.

- Ruffini, R..... Sahakyan, N....., The morphology of the X-ray afterglows and of the jetted GeV emission in long GRBs, Monthly Notices of the Royal Astronomical Society, Volume 504, Issue 4, 2021, pp.5301-5326.

- MAGIC Collaboration, Adams, C.....Sahakyan, N....., Observation of the Gamma-Ray Binary HESS J0632+057 with the H.E.S.S., MAGIC, and VERITAS Telescopes, The Astrophysical Journal, Volume 923, Issue 2, id.241, 2021, 30 pp.

- MAGIC Collaboration, Acciari V., Ansoldi S.,.... Gasparyan, S.,...Sahakyan N.,.... Search for Very High-energy Emission from the Millisecond Pulsar PSR J0218+4232, The Astrophysical Journal, Volume 922, Issue 2, id.251, 2021, 14 pp.

- MAGIC Collaboration, Acciari V., Ansoldi S.,.... Gasparyan, S.,...Sahakyan N.,.... Investigation of the correlation patterns and the Compton dominance variability of Mrk 421 in 2017, Astronomy & Astrophysics, Volume 655, id.A89, 2021, 36 pp.

- MAGIC Collaboration, Acciari V., Ansoldi S.,.... Gasparyan, S.,...Sahakyan N.,.... First detection of VHE gamma-ray emission from TXS 1515-273, study of its X-ray variability and spectral energy distribution, Monthly Notices of the Royal Astronomical Society, Volume 507, Issue 1, 2021, pp.1528-1545.

- MAGIC Collaboration, Acciari V., Ansoldi S.,.... Gasparyan, S.,...Sahakyan N.,.... Multiwavelength variability and correlation studies of Mrk 421 during historically low X-ray and -ray activity in 2015-2016, Monthly Notices of the Royal Astronomical Society, Volume 504, Issue 1, 2021, pp.1427-1451.

- MAGIC Collaboration, Algaba J., Anczarski J.,.... Gasparyan, S.,...Sahakyan N.,.... Broadband Multi-wavelength Properties of M87 during the 2017 Event Horizon Telescope Campaign, The Astrophysical Journal Letters, Volume 911, Issue 1, id.L11, 2021, 43 pp.

- Abdalla H., Adam R.,.... Gasparyan, S.,...Sahakyan N.,.... H.E.S.S. and MAGIC observations of a sudden cessation of a very-high-energy γ-ray flare in PKS 1510-089 in May 2016, Astronomy & Astrophysics, Volume 648, id.A23, 2021, 22 pp.

- MAGIC Collaboration, Acciari V., Ansoldi S.,.... Gasparyan, S.,...Sahakyan N.,...., VHE gamma-ray detection of FSRQ QSO B1420+326 and modeling of its enhanced broadband state in 2020, Astronomy & Astrophysics, Volume 647, id.A163, 2021, 19 pp.
- MAGIC Collaboration, Acciari V., Ansoldi S.,.... Gasparyan, S.,...Sahakyan N.,...., MAGIC Observations of the Nearby Short Gamma-Ray Burst GRB 160821B, The Astrophysical Journal, Volume 908, Issue 1, id.90, 2021, 11 pp.
- Sahakyan N., Israyelyan D., Harutyunyan G., Khachatryan M., Gasparyan S., Multiwavelength study of high-redshift blazars, Monthly Notices of the Royal Astronomical Society, olume 498, Issue 2, 2020, p.2594-2613.
- Sahakyan N., Broad-band study of high-synchrotron-peaked BL Lac object 1ES 1218+304, Monthly Notices of the Royal Astronomical Society, Volume 496, Issue 4, 2020, pp.5518-5527
- Sahakyan, N., Investigation of the -ray spectrum of CTA 102 during the exceptional flaring state in 2016-2017, Astronomy and Astrophysics, Volume 635, id.A25, 2020, 10 pp.
- Sahakyan N., Israyelyan D., Harutyunyan G., A Multiwavelength Study of Distant Blazar PKS 0537-286, Astrophysics, volume 63, 2020, p. 459469
- Sahakyan N., Harutyunyan G., Israelyan D., Khachatryan M., Exploring the Origin of Multiwavelength Emission from High-Redshift Blazar B3 1343 + 451, Astrophysics, Volume 63, Issue 3, 2020, p.334-348
- Giommi P., Chang Y., Turriziani S., Glauch T., Leto C., Verrecchia F., Padovani P., Penacchioni A., Arneodo F., Barres de Almeida U., Brandt C., Capalbi M., Civitarese O., D; Elia V., Di Giovanni A., De Angelis M., Del Rio Vera J., Di Pippo S., Middei R., Perri M., Pollock A., Puccetti S., Ricard N., Ruffini R., Sahakyan N., Open Universe survey of Swift-XRT GRB fields: Flux-limited sample of HBL blazars, Astronomy and Astrophysics, Volume 642, id.A141, 2020, 9 pp.
- Sahakyan N., High Energy -ray variability of NGC 1275 and 3C 120, Proceedings of the International Astronomical Union, Volume 342, 2020, pp. 172-175
- MAGIC Collaboration, VERITAS Collaboration, Abeysekara, A., Benbow, W.,.... Gasparyan, S.,...Sahakyan N.,.... Villata, M., The Great Markarian 421 Flare of 2010 February: Multiwavelength Variability and Corre-

lation Studies, The Astrophysical Journal, Volume 890, Issue 2, id.97, 2020, 21 pp.

- MAGIC Collaboration, Acciari V., Ansoldi S.,.... Gasparyan, S.,...Sahakyan N.,.... Lien, A., Multiwavelength variability and correlation studies of Mrk 421 during historically low X-ray and -ray activity in 2015-2016, Monthly Notices of the Royal Astronomical Society, DOI: 10.1093/mnras/staa3727

- MAGIC Collaboration, Acciari V., Ansoldi S.,.... Gasparyan, S.,...Sahakyan N.,.... Zari, D., The Great Markarian 421 Flare of 2010 February: Multiwavelength Variability and Correlation Studies, Astronomy and Astrophysics, Volume 635, id.A158, 2020, 10 pp.

- MAGIC Collaboration, Acciari V., Ansoldi S.,.... Gasparyan, S.,...Sahakyan N.,.... Lohfink A., New Hard-TeV Extreme Blazars Detected with the MAGIC Telescopes, The Astrophysical Journal Supplement Series, Volume 247, Issue 1, id.16, 2020, 24 p.

- MAGIC Collaboration, Acciari V., Ansoldi S.,.... Gasparyan, S.,...Sahakyan N.,.... Walker R., Monitoring of the radio galaxy M 87 during a low-emission state from 2012 to 2015 with MAGIC, Monthly Notices of the Royal Astronomical Society, Volume 492, Issue 4, 2020, p.5354-5365

- MAGIC Collaboration, Acciari V., Ansoldi S.,.... Gasparyan, S.,...Sahakyan N.,.... Tammi J., Study of the variable broadband emission of Markarian 501 during the most extreme Swift X-ray activity, Astronomy and Astrophysics, Volume 637, id.A86, 2020, 27 pp.

- MAGIC Collaboration, Acciari V., Ansoldi S.,.... Gasparyan, S.,...Sahakyan N.,.... Zari, D., A search for dark matter in Triangulum II with the MAGIC telescopes, Physics of the Dark Universe, Volume 28, article id. 100529, 2020.

- MAGIC Collaboration, Acciari V., Ansoldi S.,.... Gasparyan, S.,...Sahakyan N.,.... Zari, D., Broadband characterisation of the very intense TeV flares of the blazar 1ES 1959+650 in 2016, Astronomy and Astrophysics, Volume 638, id.A14, 2020, 16 pp.

- MAGIC Collaboration, Acciari V., Ansoldi S.,.... Gasparyan, S.,...Sahakyan N.,.... Reinthal R., Unraveling the Complex Behavior of Mrk 421 with Simultaneous X-Ray and VHE Observations during an Extreme Flaring Activity in 2013 April, The Astrophysical Journal Supplement Series, Volume 248, Issue 2, 2020, id.29

- MAGIC Collaboration, Acciari V., Ansoldi S.,.... Gasparyan, S.,...Sahakyan N.,.... Zheng W., An intermittent extreme BL Lac: MWL study of 1ES 2344+514 in an enhanced state, Monthly Notices of the Royal Astronomical Society, Volume 496, Issue 3, 2020, pp.3912-3928

- MAGIC Collaboration, Acciari V., Ansoldi S.,.... Gasparyan, S.,...Sahakyan N.,.... Zari, D., Studying the nature of the unidentified gamma-ray source HESS J1841-055 with the MAGIC telescopes, Monthly Notices of the Royal Astronomical Society, Volume 497, Issue 3, 2020, p. 3734-3745

- MAGIC Collaboration, Acciari V., Ansoldi S.,.... Gasparyan, S.,...Sahakyan N.,.... Zari, D., Bounds on Lorentz Invariance Violation from MAGIC Observation of GRB 190114C, Physical Review Letters, Volume 125, Issue 2, 2020, article id.021301

- MAGIC Collaboration, Acciari V., Ansoldi S.,.... Gasparyan, S.,...Sahakyan N.,.... Kehusmaa P., Testing two-component models on very high-energy gamma-ray-emitting BL Lac objects, Astronomy and Astrophysics, Volume 640, id.A132, 2020, 29 pp.

- MAGIC Collaboration, Acciari V., Ansoldi S.,.... Gasparyan, S.,...Sahakyan N.,.... Zari, D., MAGIC observations of the diffuse -ray emission in the vicinity of the Galactic center, Astronomy and Astrophysics, Volume 642, id.A190, 2020, 9 pp.

- MAGIC Collaboration, Acciari V., Ansoldi S.,.... Gasparyan, S.,...Sahakyan N.,.... Parkinson P., Detection of the Geminga pulsar with MAGIC hints at a power-law tail emission beyond 15 GeV, Astronomy and Astrophysics, Volume 643, id.L14, 2020, 6 p.

- V. Acciari,.....S. Gasparyan...N. Sahakyan, ... D. Zaric, "Testing emission models on the extreme blazar 2WHSP J073326.7+515354 detected at very high energies with the MAGIC telescopes", Monthly Notices of the Royal Astronomical Society, Volume 490, Issue 2, p.2284-2299, 2019.

- R. Ruffini, R. Moradi, J. Rueda, L. Becerra, C. Bianco, C. Cherubini, S. Filippi, Y. Chen, M. Karlica, N. Sahakyan, Y. Wang, S. Xue, "On the GeV Emission of the Type I BdHN GRB 130427A", The Astrophysical Journal, Volume 886, Issue 2, article id. 82, 13 pp., 2019.

- V. Acciari,.....S. Gasparyan...N. Sahakyan, ... D. Zaric, "Observation of inverse Compton emission from a long γ-ray burst", Nature, Volume 575, Issue 7783, p.459-463, 2019.

- V. Acciari,.....S. Gasparyan...N. Sahakyan, ... D. Zaric, "Teraelectronvolt emission from the -ray burst GRB 190114C", Nature, Volume 575, Issue 7783, p.455-458, 2019.

- N. Sahakyan, "Origin of the multiwavelength emission of PKS 0502+049", accepted for publication in Astronomy and Astrophysics, doi.org/10.1051/0004-6361/201936715, arXiv:1911.12087, 2019.

- V. Acciari,.....S. Gasparyan...N. Sahakyan, ... D. Zaric, "New hard-TeV extreme blazars detected with the MAGIC telescopes", accepted for publication in Astrophysical Journal Supplement, arXiv:1911.06680, 2019.

- P. Giommi, C. Brandt, U. Barres de Almeida, A. Pollock, F. Arneodo, Y. Chang, O. Civitarese, M. Angelis, V. DElia, J. Del Rio Vera, S. Di Pippo, R. Middei, A. Penacchioni, M. Perri, R. Ruffini, N. Sahakyan, S. Turriziani, "Open Universe for Blazars: a new generation of astronomical products based on 14 years of Swift-XRT data", Astronomy and Astrophysics, Volume 631, id.A116, 11 pp., 2019.

- T. Glauch, P. Padovani, P. Giommi, E. Resconi, B. Arsioli, N. Sahakyan, M. Huber, "Dissecting the region around IceCube-170922A: the blazar TXS 0506+056 as the first cosmic neutrino source", EPJ Web of Conferences, Volume 207, id.02003, 2019.

- V. Acciari,.....S. Gasparyan...N. Sahakyan, ... D. Zaric, "Constraints on Gamma-Ray and Neutrino Emission from NGC 1068 with the MAGIC Telescopes", The Astrophysical Journal, Volume 883, Issue 2, article id. 135, 9 pp., 2019.

- V. Acciari,.....S. Gasparyan...N. Sahakyan, ... D. Zaric, "Measurement of the extragalactic background light using MAGIC and Fermi-LAT gamma-ray observations of blazars up to z = 1", Monthly Notices of the Royal Astronomical Society, Volume 486, Issue 3, p.4233-4251, 2019.

- V. Acciari,.....S. Gasparyan...N. Sahakyan, ... D. Zaric, "Deep observations of the globular cluster M15 with the MAGIC telescopes", Monthly Notices of the Royal Astronomical Society, Volume 484, Issue 2, p.2876-2885, 2019.

- J. Rueda, R. Ruffini, Y. Wang, C. Bianco, J. Blanco-Iglesias, M. Karlica, P. Loren-Aguilar, R. Moradi, N. Sahakyan, "Electromagnetic emission of white dwarf binary mergers", Journal of Cosmology and Astroparticle Physics, Issue 03, article id. 044, 2019.

- N. Sahakyan, "Origin of the multiwavelength emission of PKS 0502+049", Astronomy and Astrophysics, Volume 622, id.A144, 10 pp. 2019.
- R. Ruffini, M. Karlica, N. Sahakyan, J. Rueda, Y. Wang, G. Mathews, C. Bianco, M. Muccino, "A GRB Afterglow Model Consistent with Hypernova Observations", The Astrophysical Journal, Volume 869, Issue 2, article id. 101, 9 pp. 2018.
- A. Abeysekara, ... N. Sahakyan, ... D. Zaric, "Periastron Observations of TeV Gamma-Ray Emission from a Binary System with a 50-year Period", The Astrophysical Journal Letters, Volume 867, Issue 1, article id. L19, 8 pp., 2018.
- P. Padovani, P. Giommi, E. Resconi, T. Glauch, B. Arsioli, N. Sahakyan, M. Huber, "Dissecting the region around IceCube-170922A: the blazar TXS 0506+056 as the first cosmic neutrino source", Monthly Notices of the Royal Astronomical Society, Volume 480, Issue 1, p.192-203, 2018.
- N. Sahakyan, "Lepto-hadronic γ-Ray and Neutrino Emission from the Jet of TXS 0506+056", The Astrophysical Journal, Volume 866, Issue 2, article id. 109, 6 pp. 2018.
- S. Gasparyan, N. Sahakyan, V. Baghmanyan, D. Zargaryan, "On the Multiwavelength Emission from CTA 102", The Astrophysical Journal, Volume 863, Issue 2, article id. 114, 11 pp., 2018.
- M. Aartsen, ... N. Sahakyan, ... T. Yuan, "Neutrino emission from the direction of the blazar TXS 0506+056 prior to the IceCube-170922A alert", Science, Volume 361, Issue 6398, pp. 147-151, 2018.
- V. Baghmanyan, M. Tumanyan, N. Sahakyan, Y. Vardanyan, "High-Energy γ -Ray Emission from PKS 0625-35", Astrophysics, Volume 61, Issue 2, pp.160-170, 2018.
- N. Sahakyan, V. Baghmanyan, D. Zargaryan, "Fermi-LAT observation of nonblazar AGNs", Astronomy & Astrophysics, Volume 614, id.A6, 11 pp., 2018.
- B. Fraga, U. Barres de Almeida, S. Gasparyan, P. Giommi, N. Sahakyan, "Time-Evolving SED of MKN421: a multi-band view and polarimetric signatures", Frontiers in Astronomy and Space Sciences, Volume 5, id.1, 2018.
- S. Gasparyan, N. Sahakyan, P. Chardonnet, "The origin of HE and VHE gamma-ray flares from FSRQs", International Journal of Modern Physics D, Volume 27, Issue 10, id. 1844007, 2018.

- D. Zargaryan, N. Sahakyan, H. Harutyunian, "Chandra observations of gamma-ray emitting radio galaxies", International Journal of Modern Physics D, Volume 27, Issue 10, id. 1844022, 2018.

- V. Baghmanyan, N. Sahakyan, "X-ray and γ-ray emissions from NLSy1 galaxies", International Journal of Modern Physics D, Volume 27, Issue 10, id. 1844001, 2018.

- D. Zargaryan, S. Gasparyan, V. Baghmanyan and N. Sahakyan, "Comparing 3C 120 jet emission at small and large scales", Astronomy & Astrophysics, Volume 608, id. A37, 10, 2017.

- U. Barres de Almeida, F. Bernardo, P. Giommi, N. Sahakyan, S. Gasparyann and C. Brandt, "Long-Term Multi-Band and Polarimetric View of Mkn 421: Motivations for an Integrated Open-Data Platform for Blazar Optical Polarimetry", Galaxies, vol. 5, issue 4, p. 90, 2017.

- V. Baghmanyan, S. Gasparyan and N. Sahakyan, "Rapid Gamma-Ray Variability of NGC 1275", The Astrophysical Journal, Volume 848, Issue 2, article id. 111, 8, 2017.

- N. Sahakyan and S. Gasparyan "High energy gamma-ray emission from PKS 1441+25", Monthly Notices of the Royal Astronomical Society, 470, 3, p.2861-2869, 2017.

- N. Sahakyan, V. Baghmanyan, and D. Zargaryan, "Gamma-ray Emission from Non-Blazar AGNs", AIP Conference Proceedings, Volume 1792, Issue 1, id.050002, 2017.

- N. Sahakyan and S. Gasparyan, "High Energy Gamma-Rays From PKS 1441+25", AIP Conference Proceedings, Volume 1792, Issue 1, id.050005, 2017.

- V. Baghmanyan, "Gamma-Ray Variability of NGC 1275", AIP Conference Proceedings, Volume 1792, Issue 1, id.050007, 2017.

- D. Zargaryan, "The Gamma-Ray Emission from Broad-Line Radio Galaxy 3C 120",AIP Conference Proceedings, Volume 1792, Issue 1, id.050008, 2017.

- N. Sahakyan, "Galactic sources of high energy neutrinos: Expectation from gamma-ray data", EPJ Web of Conferences, Volume 121, id.05005, 2016.

- Sahakyan, N., Zargaryan, D. and Baghmanyan, V. "On the gamma-ray emission from 3C 120", Astronomy & Astrophysics, Volume 574, id.A88, 5 pp., 2015.
- Sahakyan, N., Yang, R., Rieger, F., Aharonian, F. and de Ona-Wilhelmi, E. "High Energy Gamma Rays from Centaurus a" Proceedings of the MG13 Meeting on General Relativity ISBN 9789814623995, pp. 1028-1030, 2015.
- Sahakyan, N., Piano, G. and Tavani, M. "Hadronic Gamma-Ray and Neutrino Emission from Cygnus X-3", The Astrophysical Journal, Volume 780, Issue 1, article id. 29, 2014.
- Sahakyan, N., Rieger, F., Aharonian, F., Yang, R., and de Ona-Wilhelmi, E. "On the gamma-ray emission from the core and radio lobes of the radio galaxy Centaurus A", International Journal of Modern Physics: Conference Series, Volume 28, id. 1460182, 2014.
- Sahakyan, N., Yang, R. Aharonian, F. and Rieger, F., " Evidence for a Second Component in the High-energy Core Emission from Centaurus A?", The Astrophysical Journal Letters, Volume 770, Issue 1, L6, 2013.
- Yang, R.-Z., Sahakyan, N., de Ona Wilhelmi, E., Aharonian, F. and Rieger, F., "Deep observation of the giant radio lobes of Centaurus A with the Fermi Large Area Telescope", Astronomy & Astrophysics, 542, A19, 2012.
- Sahakyan, N., "High energy gamma-radiation from the core of radio galaxy Centaurus A", Astrophysics, 55, 14, 2012.
- Sahakyan, N., "On the Origin of High Energy Gamma-Rays from Giant Radio Lobes Centarus A", International Journal of Modern Physics Conference Series, 12, 224, 2012.

4 A thirteen-year-long broadband view of BL Lac

4.1 Introduction

Radio-loud Active Galactic Nuclei (AGNs) are characterized by two-sided narrow relativistic jets that originate from the central supermassive black hole. Blazars are the subclass of radio loud AGNs in which one of the jets happens to make a small angle ($< 10^{\circ}$) to the line of sight of the observer [257]. These jets transport a large amount of power in the form of particles, radiation and magnetic field and are strong sources of non-thermal emission. Due to the small viewing angle and the relativistic motion the emission in blazars is strongly Doppler boosted, a special situation that makes these sources detectable up to large redshifts [e.g., 12, 235] and is responsible for the observed extreme properties that characterizes them, like superluminal motion and rapid variability across the electromagnetic spectrum. Historically blazars are classified as BL Lacertae objects (BL Lacs), which exhibit an optical spectrum that is completely featureless or at most shows very weak emission lines (equivalent width $EW \leq 5\AA$), and as flat spectrum radio quasars (FSRQs) when the emission lines are stronger and quasar-like [257]. Blazars are generally assumed to be persistent sources, however a case of a transient blazar, 4FGL J1544.3-0649, was recently observed. This object remained below the sensitivity limits of X-ray and γ-ray instruments until May 2017 when it raised above detactability and for a few months it became one of the brightest X-ray blazars [232]. If this was not an isolated case, but rather a common phenomenon, it could have an impact on the real abundance and on our current understanding of blazars.

The broadband SED of blazars, in a $log(\nu F\nu)$ vs. $log(\nu)$ representation, shows two prominent broad components, one (low-energy component) peaking form far infrared frequencies to X-ray energies and another (high energy component) peaking at MeV/GeV energies. The peak of the low-energy component (ν_s) is used to further classify blazars as high synchrotron peaked BL Lacs (HBL when $\nu_s > 10^{15}$ Hz), intermediate synchrotron peaked BL Lacs (IBL when $10^{14} < \nu_s < 10^{15}$ Hz), or low synchrotron peaked BL Lacs (LBL when $\nu_s < 10^{14}$ Hz) objects [192, 5]. Sometimes the synchrotron peak can

reach energies as high as ∼1 keV, (∼ 2×10^{17} Hz) or beyond, showing what is considered to be extreme behaviour, even for these highly peculiar sources [e.g. 114, 74, 34]. Such a high synchrotron peak was first observed during a flare of Mkn 501 [205], and subsequently in many other objects [e.g., 73, 227]. Independently of the location of the peak, the low-energy part of the SED is generally interpreted as synchrotron emission from the relativistic electrons in the jet. A proton synchrotron origin of the high energy end of this component during X-ray flares has also been considered [171, 248]. The nature of the high energy (HE; $>$ 100 MeV) component is instead still under debate. Within one-zone leptonic scenarios, the second component originates from inverse Compton scattering of the synchrotron photons (SSC) by the electron population producing the low-energy component [104, 38, 163]. Depending on the location of the emission region, the photons external to the jet (e.g., photons from the disc, or those reprocessed from the broad-line region or those from the infrared torus) can up-scatter, producing the second component [external inverse Compton (EIC); 36, 105, 240]. On the other hand, the HE component can be also produced from the interaction of relativistic protons either from their synchrotron emission [179] or from the secondary particles from pion decay [160, 161, 179, 180, 43]. Recently, after associating TXS 0506+056 with the IceCube-170922A neutrino event [132, 130, 189] the lepto-hadronic scenarios, when both electrons and protons contribute to the HE emission, have become more attractive. These models also predict very high energy (VHE; $>$ 100 GeV) neutrinos observable by the IceCube detector [19, 141, 181, 189, 225, 221, 59, 226, 96, 99].

Blazars, being powerful sources of strongly variable non-thermal emission, are often targets of multiwavelength observations. The resulting data have been accumulating over time enriching the archives with very valuable information that can be used for detailed energy and time-domain investigations of the origin of their emission. BL Lacertae (BL Lac) is one of these frequently studied blazars; at $z = 0.069$ it is a prototype of the BL LAC subclass of blazars. BL Lac is usually classified as an LBL [184], but is sometimes listed as an IBL [11]. BL Lac is well known for its prominent variability in a wide energy range, especially in the optical [149, 14] and radio bands [261]. BL Lac has been a target of many multiwavelength campaigns ranging from the radio to the HE or VHE γ-ray bands [167, 212, 213, 157, 260] which resulted in a deep understanding of its properties in different bands. For example, in the X-ray band, BeppoSAX observations in June 1999 showed that the 0.3-2 keV flux of BL Lac doubled in $\sim$ 20 min and the spectrum was concave with a very hard component above 5-6 keV [216]. In the γ-ray band, the EGRET observations in 1995 showed an average γ-ray flux above 100 MeV of $(40 \pm 12) \times 10^{-8}$ *photon* $cm^{-2}\, s^{-1}$ [58] which increased up to $(171 \pm 42) \times 10^{-8}$ *photon* $cm^{-2}\, s^{-1}$ during the flare in 1997 [37]. Afterwards, the obser-

vations by the Large Area Telescope (LAT) on board the Fermi Gamma-ray Space Telescope (Fermi-LAT) showed that during flaring periods the average γ-ray flux above 100 MeV can reach above 10^{-6} $photon\,cm^{-2}\,s^{-1}$ [e.g., see 76, 67, 173, 187, 77]. VHE γ-rays above 1 TeV from BL Lac were initially reported by the Crimean Observatory in 1998 [183] and later, in 2005, the MAGIC telescope discovered a VHE γ-ray signal with an integral flux of 3% of the Crab Nebula flux above 200 GeV [16]. The source is flaring also in the VHE γ-ray band; for example, on June 28 2011, a very rapid TeV γ-ray flare was detected by VERITAS when the integral flux above 200 GeV reached roughly 125% of the Crab Nebula flux [21], or on June 15 2015 MAGIC detected a flare with a maximum flux of $(1.5 \pm 0.3) \times 10^{-10} photons\,cm^{-2}\,s^{-1}$ and halving time of 26 ± 8 min [157].

BL Lac shows a peculiar behavior both in terms of its classification and interpretation of the observed broadband SED. First, the observation of $H\alpha$ and $H\beta$ lines ($\sim 10^{41}$ $erg\,s^{-1}$) [72, 50] in different periods is quite unusual for this type of blazars. This might indeed indicate a presence of a broad-line region structure. On the other hand, the single-zone SSC models, usually successful for explaining the TeV BL Lac spectrum, have a difficulty in reproducing the variability of this source in different bands and taking into account the emission in all the bands. When the spectrum extends to the VHE γ-ray band or when a large Compton dominance is observed, the SED of BL Lac can be modeled only by considering an EIC component added to SSC or by using two-zone models [e.g., 37, 156, 42, 6, 157]. This illustrates that different models/components are contributing in the overall complex broadband spectrum of BL Lac.

Over the past decade, BL Lac was constantly monitored in the HE γ-ray band by Fermi-LAT [15] and AGILE [47] and frequently observed in the optical/UV and X-ray bands by *Neil Gehrels Swift Observatory* [102], (hereafter *Swift*). Together with the observations of other instruments (*NuSTAR*, MAGIC, VERITAS, etc.) this resulted in the accumulation of an extremely rich multifrequency data set mapping both emission components. The available data can be combined to build the broadband SED of BL Lac in many different periods with (quasi) contemporaneous data. The theoretical interpretation of these SEDs can help understanding the physical processes that dominate in different periods. For example, a similar study of the broadband emission of 3C 454.3 allowed us to estimate the main parameters describing the jet and emitting electrons as well as to investigate their evolution in time [229]. Moreover, BL Lac was in active flaring states from optical to γ-ray bands in October 2020 and January 2021 [e.g., 165, 164, 77, 80, 126, 81] when the brightest γ-ray flare from this source was also observed [173]; on October 6 2020, the daily averaged γ-ray flux of BL Lac was $(5 \pm 1) \times 10^{-6}$ $photons\,cm^{-2}\,s^{-1}$. The available multiwavelength data and the extraordinary flaring activity of

BL Lac in 2020/2021 motivated us to have a new look on the origin of the broadband emission from it.

In this paper, analyzing the data observed by Fermi-LAT, *Swift* X-ray Telescope (XRT) and Ultraviolet and Optical Telescope (UVOT) accumulated in the previous thirteen years, we perform an intense broadband study of BL Lac. The paper is organized as follows. The Fermi-LAT and *Swift* data collected for the analysis and its reduction methods are described in Section 4.2. The spectral changes in different bands and the broadband SED modeling is discussed in Section 4.3. The discussion is presented in Section 4.4 and the summary in Section 4.5.

4.2 Fermi-LAT Observations and Data Analysis

Since August 2008, BL Lac was constantly observed by Fermi-LAT providing unprecedented information on its emission in the γ-ray band. Fermi-LAT is a pair conversion telescope sensitive to γ-rays in the energy range from 100 MeV to 500 GeV. By default, it operates in all sky scanning mode, mapping the entire γ-ray sky every three hours. Further details on Fermi-LAT are given in **(author?)** [25].

For the current study, publicly available data accumulated between 04 August, 2008 and 01 March, 2021 are used (MET 239557417 - 636249605). The data have been analysed by using Fermi ScienceTools version 1.2.1. The Pass8 Source class events with a higher probability of being photons (evclass = 128, evtype=3) in the energy range from 100 MeV to 500 GeV were analyzed using P8R3_ SOURCE_ V3 instrument response function. The events were downloaded from a region of interest (ROI) defined as a circular region with 12° around the γ-ray position of BL Lac. The events are binned within a 16.9° $\times$ 16.9° square region into pixels of 0.1° $\times$ 0.1° and into 37 equal logarithmically spaced energy bins. The model was created using the Fermi-LAT fourth source catalog Data Release 2 [4FGL-DR2; 15] where all sources within 17° around the target as well as the Galactic (gll_ iem_ v07) and the isotropic (iso_ P8R3_ SOURCE _ V3_ v1) diffuse emission components are included. The spectral parameters of the background sources falling between 12° and 12°+5° were fixed to their catalog values, while the parameters of the other sources and background models were left free. Binned likelihood analysis was applied with gtlike tool to find the best matches between spectral models and the data. The source variability was investigated by dividing the entire period to three-day bins. During these short periods the source spectrum was modeled using a power-law function, and the photon flux and index were estimated by applying unbinned likelihood analysis with the appropriate quality cuts mentioned above. The light curves were computed by

fixing the spectral indices of all sources (except BL Lac) and the normalization of both the Galactic and isotropic components to the best-fit values obtained for the whole time period and then by allowing them to vary. In all cases the light-curves are fully consistent with each other and with the one available in the Fermi-LAT light curve repository [1]. In addition to the three-day binned light curve, an adaptively binned light curve was generated by adjusting the time bin widths so as to attain 20% uncertainty in the flux estimation above an optimal energy [see 155, for details]. This light curve with unequal time bins has been proven to be particularly efficient for the identification of flaring states [e.g., see 101, 230, 269, 26, 46, 215].

The adaptively binned (E $>$ 196.7 MeV) and three-day (E $>$ 100 MeV) γ-ray light curves are shown in Fig. 5.1 panels a) and b) respectively. The time-averaged γ-ray flux of BL Lac above 100 MeV is $(3.71 \pm 0.05) \times 10^{-7}$ *photon* $cm^{-2}\, s^{-1}$. Both light curves show the complex behaviour of BL Lac in the γ-ray band; the mean γ-ray flux of the source is 4.46×10^{-7} *photon* $cm^{-2}\, s^{-1}$ which increases up to $(4.39 \pm 1.01) \times 10^{-6}$ *photon* $cm^{-2}\, s^{-1}$ (above 196.7 MeV) observed on MJD 59231.34 (17 January 2021). Using the adaptively binned light curve in the considered thirteen years the source flux was above 10^{-6} *photon* $cm^{-2}\, s^{-1}$ in total for 41.5 days. The photon index variation in time is investigated using a 3-day binned light curve. The photon index is mostly soft with a mean value of $\Gamma_{mean} = 2.15$ but occasionally it hardened to $\Gamma < 2.0$. The hardest indexes of 1.48 ± 0.22 and 1.61 ± 0.17 were observed on MJD 57771.16 (18 January 2017) and 55782.16 (09 August 2011), respectively.

The time evolution of the γ-ray emission is also investigated by generating the SED at different times. When the SEDs are constructed for short periods (e.g., three-day bins or for the time intervals identified in the adaptive bins lightcurve) the spectrum can be measured only up to the moderate energies, not enough for a detailed study. Therefore, the Bayesian block algorithm [237] is used to divide the γ-ray light curve into optimal intervals which are represented by an approximately constant flux. By applying this algorithm, the points where the flux changes from one state to another will be identified, providing the γ-ray spectra of the source in different states. The Bayesian block algorithm applied to the adaptively binned light curve divides the entire period into 218 intervals with a similar flux level. The shortest period is 5.81 hours during a flare while in the low emission state the longest period is 278.74 days. The spectral analysis is applied by limiting the time for each interval selected based on the Bayesian block. During the analysis, the spectrum of BL Lac is assumed to be a power-law with spectral index and normalization left as free parameters. The best matches between the spectral

[1] `https://fermi.gsfc.nasa.gov/ssc/data/access/lat/LightCurveRepository/index.html`

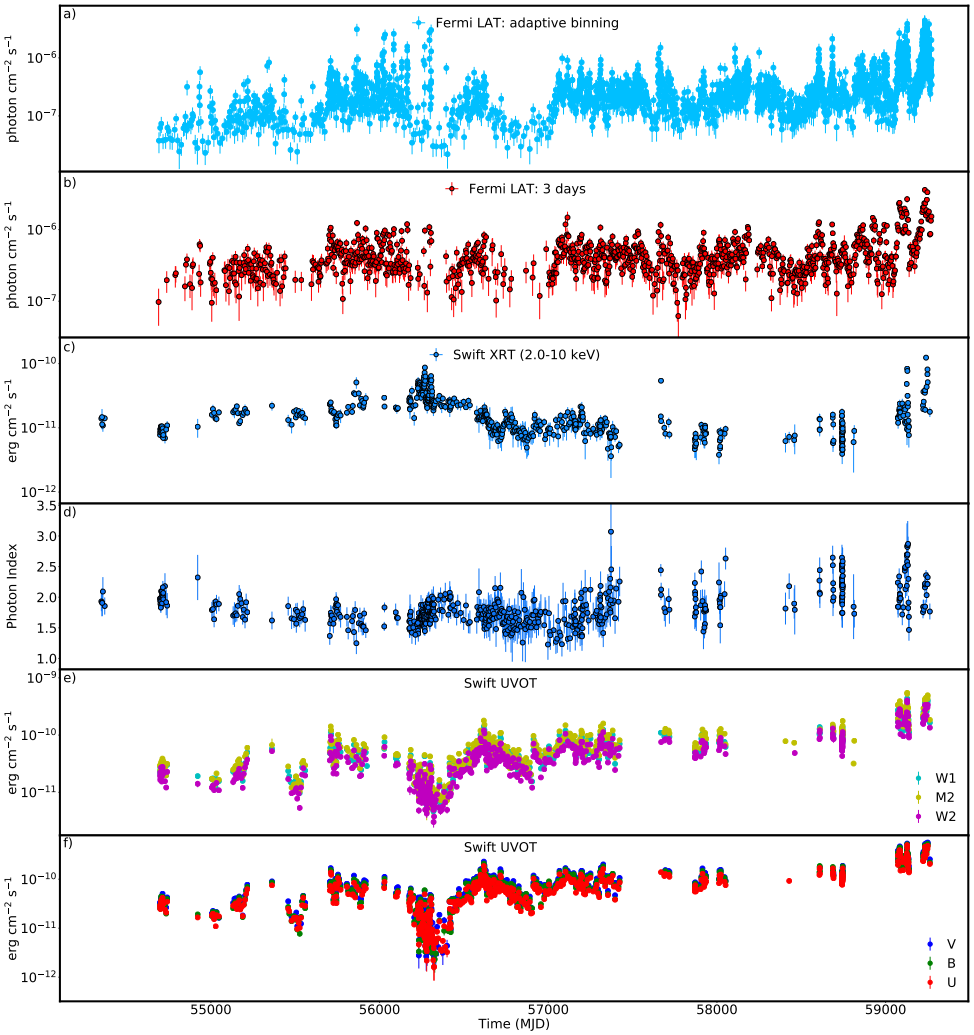

Figure 4.1 The multiwavelength light curve of BL Lac between August 04, 2008 and March 01, 2020. *a)* Adaptively binned γ-ray light curve ($>$ 196.7 MeV); *b)* 3-day binned γ-ray light curve ($>$ 100 MeV); *c) Swift* XRT light curve in the 2.0-10 keV range; *d)* 0.3-10.0 keV X-ray photon index; *e, f)* host galaxy corrected flux in W1, M2, W2, V, B, and U filters.

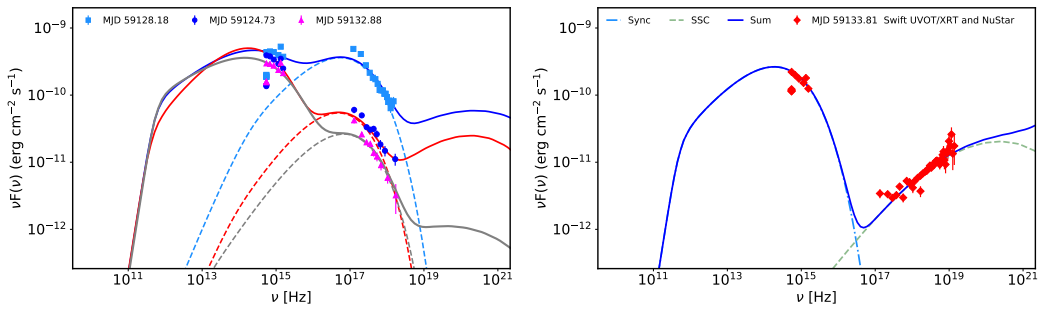

Figure 4.2 The SED of BL Lac in different periods. Left panel: The periods with a soft X-ray spectrum as modeled within the two-zone leptonic scenario. The dashed lines show the synchrotron emission from the second region and the solid lines are the sum of the contribution from both regions.Right panel: The usual hard X-ray spectrum (*Swift* XRT and *NuSTAR*) observed on MJD 59133.88 (11 October 2020).

models and events are obtained with an unbinned likelihood analysis implemented in gtlike. Depending on source intensity the spectrum of BL Lac is obtained by separately running the analysis for 4 or 7 energy bands of equal width in log scale.

4.2.1 Swift XRT

During the considered period, the *Swift* satellite observed BL Lac 610 times with single exposures ranging from 1.13 to 16.46 ks. All the data were downloaded and processed using Swift_xrtproc automatic tool for XRT data analysis developed within the Open Universe Initiative [116]. This tool automatically downloads the raw data and processes it using the XRTPIPELINE task adopting standard parameters and filtering criteria. For each observation, it extracts the source events from a circle with a radius of 20 pixels centered at the position of the source, while the background counts are taken from an annular ring centered at the source. The tool applies also pile-up correction when the source count rate is above 0.5 $counts\,s^{-1}$. Then it loads the ungrouped data in XSPEC (version 12.11) for spectral fitting using Cash statistics [57], modeling the source spectrum as a power-law and a log-parabola model with the Galactic absorption column density fixed to $2.7 \times 10^{21}\,cm^{-2}$ [e.g., 156, 260, 78].

The 2-10 keV X-ray flux variation is shown in Fig. 5.1 panel c). The baseline flux is around $2 \times 10^{-11}\,erg\,cm^{-2}\,s^{-1}$ although small amplitude changes are visible in different observations. In three periods, MJD 56300 (08 January 2013), MLD 59140 (18 October 2020) and MJD 59235 (21 January 2021),

the flux substantially increased reaching the maximum of $(1.41 \pm 0.06) \times 10^{-10}\, erg\, cm^{-2}\, s^{-1}$ on MJD 59128.18 (06 October 2020). This is the historical highest flux of BL Lac in the soft X-ray band.

The X-ray photon index in different observations is shown in Fig. 5.1 panel d). Most of the time, the photon index is hard ($\leq$ 2.0) implying that the X-ray emission is due to the rising part of the HE component in the SED of BL Lac. However, the photon index undergoes interesting modifications reaching 2.0 which corresponds to a flat distribution in $\nu f\nu$ vs ν representation. For example, such tendency can be noticed after the X-ray flare around MJD 56300 (08 January 2013). In the considered periods, also a significant softening of the photon index is observed; e.g., in 36 observations the X-ray photon index is $>$ 2.3 (considering only the observations when the number of counts was $>$ 100) which is unusual for BL Lac and more typical of HBL blazars. Examples of optical/UV and X-ray spectrum of BL Lac during such changes are shown in Fig 4.2. The X-ray component started to soften starting from MJD 59113.16 (21 September 2020) when an index of $\Gamma_X = 2.43 \pm 0.11$ was observed. Then, the photon index softens to $\Gamma_X = 2.84 \pm 0.03$ on MJD 59128.18 (06 October 2020) during the brightest X-ray emission state (light blue squares in Fig. 4.2). In this period the optical/UV flux increased substantially as well, showing that the low-energy component now extends to the X-ray band. Such soft X-ray emission with $\Gamma_X = 2.82 \pm 0.07$ and a flux of $F_{X(0.3-10\,keV)} = (7.68 \pm 0.47) \times 10^{-11}\, erg\, cm^{-2}\, s^{-1}$ (red circle in Fig.4.2) was also observed on MJD 59128.91 (06 October 2020). In the next two observations (MJD 59129.90 (07 October 2020) and 59131.83 [09 October 2020]), the X-ray flux was constantly decreasing and the photon index was $\Gamma_X = 2.52 - 2.70$. The softest photon index of $\Gamma_X = 2.87 \pm 0.11$ was observed on MJD 59132.88 (10 October 2020; magenta triangles in Fig. 4.2) when the source flux was $F_{X(0.3-10\,keV)} = (2.44 \pm 0.16) \times 10^{-11}\, erg\, cm^{-2}\, s^{-1}$. However, this component fades in the next observations (e.g., on MJD 59133.81 [11 October 2020]) and in the X-ray band the usual HE component is observed.There were additional periods when softening in the X-ray band was observed ($\Gamma_X \geq 2.5$); for example, on MJD 58685.98 (21 July 2019) and 58686.90 (22 July 2019) and between MJD 58740.42-58741.41 (14-15 September 2019) the X-ray photon index was $\Gamma_X = 2.51 - 2.64$ with a flux between $F_{X(0.3-10\,keV)} = (8.36 - 17.64) \times 10^{-12}\, erg\, cm^{-2}\, s^{-1}$.

The X-ray flux evolution was further investigated by comparing it with the photon index in different states. When considering the entire observational period with diverse X-ray emission properties, any trend (if present) will be smoothed out. For this reason, the X-ray photon index versus the flux was investigated by selecting the periods around two major flares visible in Fig. 5.1; namely within MJD 56160-56350 (21 August 2012- 27 February 2013) and

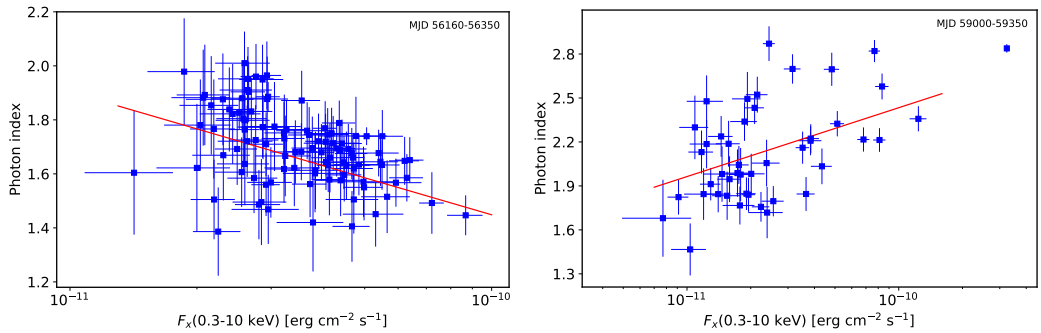

Figure 4.3 BL Lac X-ray photon index versus the flux during two major X-ray flares. The correlation trend is shown with a red line.

MJD 59000-59350 (31 May 2020- 16 May 2021). The results are shown in Fig. 4.3. The linear-Pearson correlation test applied to the data during the first flare (MJD 56160-56350; 21 August 2012- 27 February 2013) yields -0.45, the p-value being 1.6×10^{-6} for $N = 102$ observations, implying a negative correlation between the flux and photon index, i.e., when the source gets brighter, the photon index decreases (hardens). This behaviour has already been observed for many flaring blazars [e.g. 112]. On the other hand, for the second flare the linear-Pearson test results in 0.47 with a p-value of 0.001 for $N = 45$. This implies that during the X-ray flare the photon index softens, so a softer-when-brighter trend is observed. This shows that two major flares observed in the X-ray band for BL Lac are different by their nature and are caused by different processes. Similar behavior of the X-ray flux of BL Lac was already seen in the previous studies [e.g., 261, 260, 78].

4.2.2 Swift UVOT

UVOT observed BL Lac in all six filters, V (500-600 nm), B (380-500 nm), U (300- 400 nm), W1 (220-400 nm), M2 (200-280 nm) and W2 (180260 nm) simultaneously with the XRT. All single observations of BL Lac were downloaded and reduced using HEAsoft version 6.27 with the latest release of HEASARC CALDB. The data are reduced using standard procedures, by selecting source counts from a circular region of 5″ around the source, while the background counts were estimated from a 20″ region away from the source. Host galaxy contributions were subtracted following **(author?)** [213] and **(author?)** [211] by assuming a flux density of 2.89, 1.30, 0.36, 0.026, 0.020, and 0.017 mJy for the host galaxy in the V, B, U, W1, M2, W2 bands, respectively. For the considered source extraction radius, the host galaxy contribution is $\sim 50\%$ of the total galaxy flux, which is removed. uvotsource tool was used to derive the magnitudes which were converted to fluxes using the conversion factors pro-

vided by **(author?)** [206] which then were corrected for extinction using the reddening coefficient $E(B-V)$ from the Infrared Science Archive [2].

The optical/UV flux evolution in time is shown in Fig. 5.1 panel e) and f) separating the flux in V, B, U and W1, M2 and W2 filters. The source flux is relatively constant at the level of a few times $10^{-11}\,erg\,cm^{-2}\,s^{-1}$ up to MJD 56500 (27 July 2013). A flaring activity occurred around MJD 56617-56622 (21-26 November 2013) when the flux in all filters exceeded $10^{-10}\,erg\,cm^{-2}\,s^{-1}$. The major flaring activity started on MJD 59072 (11 August 2020) and the baseline flux level was above $10^{-10}\,erg\,cm^{-2}\,s^{-1}$. The maximum flux of $(5.80 \pm 0.14) \times 10^{-10}\,erg\,cm^{-2}\,s^{-1}$ was observed in the V band on MJD 59249.26 (04 February 2021). The maximum flux in B, U and M2 filters was also above $5 \times 10^{-10}\,erg\,cm^{-2}\,s^{-1}$ while that in W1 and W2 was around $4 \times 10^{-10}\,erg\,cm^{-2}\,s^{-1}$.

4.2.3 Archival data

To achieve as much as possible a complete view of the broad-band emission from BL Lac we have also considered all the available multi-frequency archival measurements alongside with the data from Fermi-LAT, *Swift* XRT and UVOT. These include a) optical data monitoring from the ASAS-SN Sky Patrol web site [3] [146], b) *NuSTAR* data from the observations of BL Lac on 11 December 2012 (MJD 56272), 14 September 2019 (MJD 58740) and 11 October 2020 (MHD 59133) from Middei et al. 2021, submitted, and c) any other multi-frequency measurements available from the VOU_BLazars tool [64] and the ASI Space Science Data Center (SSDC) archive [4]. In addition we also considered the observations of BL Lac carried out by VERITAS on June 11, 2011 [MJD 55740 21] and on October 5, 2016 [MJD 57697 8] and by MAGIC between June 15 and 28, 2015 [MJD 57188-57201 157]. The combination of all these data sets results in an unprecedented amount of observations of BL Lac covering the spectrum from radio frequencies to HE and VHE γ-ray bands over a period of nearly 13 years, from 2008 August to 2021 March.

4.3 Modeling the SEDs

In this section we use the data assembled as described above to investigate the evolution of the broadband spectrum of BL Lac between 2008 August and 2021 March. To this end we have generated a large number of quasi contemporaneous SEDs by plotting the computed γ-ray spectra together with

[2] http://irsa.ipac.caltech.edu/applications/DUST/
[3] https://asas-sn.osu.edu/
[4] https://www.ssdc.asi.it

the data available in all other energy bands in each of the Bayesian intervals defined in Sec. 4.2. To illustrate the temporal evolution of the broad band emission from BL Lac in a visually effective way we have combined these SEDs to form an animation that is available as Supplementary data and at the following link: youtube.com/L1yT105UGYM. Flux changes in the optical/UV, X-ray and γ-ray bands are evident. In the γ-ray band, the spectrum hardens together with the flux amplification, resulting in a shift of the peak of the second component to higher energy values. During the brightest X-ray state (on MJD 59128.18; 06 October 2020), the low-energy SED component extended to the X-ray band as a consequence of a significant change of the location of the synchrotron peak from the usual $\sim 10^{14}$ Hz to $\sim 10^{16}$ Hz, well into the HBL regime [192, 5]. Such a large modification, never observed before in BL Lac , marks the extraordinary nature of this flare, which has been studied also by **(author?)** [78] and **(author?)** [208].

The classical double-humped SED of BL Lac is usually interpreted within leptonic scenarios. The EGRET observations of BL Lac [236, 156] revealed that modeling of the HE data requires a component that extends beyond the SSC radiation generated in a single emission zone: one-zone leptonic modeling requires a very high Doppler factor (δ; $\delta \simeq \Gamma_{jet}$, where Γ_{jet} is the bulk Lorentz factor) or an extended emission region. Since then the SED of BL Lac has been conventionally modelled within two-zone scenarios [e.g. 6, 157] or assuming inverse Compton scattering of external (EIC) photons [e.g., 156, 43]. External Compton scenarios are favoured in BL Lac, considering the detection, although weak, of the $H\alpha$ line [72, 50], which points to the presence of a broad-line region (BLR). Even if this BLR is not large enough to absorb VHE γ-rays through $\gamma - \gamma$ interaction [e.g., 90], it can provide targets for inverse Compton up-scattering. For example, by modeling the SED of BL Lac, **(author?)** [6] showed that the SSC+ERC scenario provides reasonable modeling of the data also during the low state and the inverse Compton scattering of the BLR-reprocessed radiation strongly dominates over that directly from the disc.

In an effort to understand the processes dominating in the jet in different physical conditions we investigated the broadband emission from BL Lac by modeling the SEDs observed in different periods. From the SED/light curve animation discussed above we have selected all periods with sufficient multi-wavelength data, typically those with flux measurements in at least the optical/UV, X-ray and γ-ray bands. This allowed us to assemble 511 high-quality and quasi-simultaneous SEDs representing BL Lac in a variety of emission states. All these SEDs are modeled assuming that the emission region ('the blob') is a sphere with radius R, including a magnetic field of intensity B and a population of relativistic electrons following an energy distribution defined by a power law with an exponential cutoff, as expected from shock accelera-

tions:

$$N(\gamma') = N'_e \gamma'^{-p} \, Exp(-\gamma'/\gamma'_{cut}) \tag{4.3.1}$$

for $\gamma' > \gamma'_{min}$ where γ'_{min} and γ'_{cut} are the minimum and cut-off energy of the electrons, respectively. It is assumed that the emission region is located inside the BLR and the low energy SED component is interpreted as synchrotron emission of relativistic electrons, while the second SED component is due to inverse Compton up-scattering of photon fields from the jet itself [SSC model e.g., 163, 38] and those reprocessed from the BLR clouds [EIC BLR; 240]. The BLR is assumed to be spherical shell with an average radius of $R_{BLR} = 7 \times 10^{16}$ cm and lower and upper boundaries of $0.9 \times R_{BLR}$ and $1.2 \times R_{BLR}$, respectively [90]. The BLR reflects 10% of the disc luminosity whose emission is approximated as a mono-temperature black body with a luminosity of $L_d = 3 \times 10^{43} \, erg \, s^{-1}$. This luminosity was estimated with a requirement that the disc component does not overproduce the optical/UV data in any period. We note that R_{BLR} and L_d define the density of the external photon fields, so their small changes do not affect the results and only will result in moderate changes in the normalization of the electrons.

Our 511 SEDs represent an ample variety of different states of BL Lac and in some periods the simple one-zone model described above cannot explain the observed data. For example, when the X-ray spectrum softens neither the synchrotron component (defined by the optical/UV data) nor SSC component which has a rising shape cannot account for the X-ray flux. In these cases the SEDs were modeled considering two-zone scenarios, assuming that one region is within the BLR and the other is outside [e.g., see Fig. 2 panel c) in 250].

The broadband SEDs model fitting was carried out using the open source package JetSet [168, 254, 255, 256]. The free model parameters (p, γ_{cut}, γ_{min}, δ, R and B) are constrained by using the Minuit optimizer and then improved by Markov Chain Monte Carlo (MCMC) sampling of their distributions. The quality of the fits was checked by calculating the goodness-of-fit and by checking MCMC diagnostic plots. In principle, R can be constrained either from the variability consideration or from SED fitting. If high quality data are available, detailed variability studies may constrain the radius from the relation $R \leq \delta \, t \, c/(1+z)$. However, in the current case, due to the high number of the considered periods for the modeling (511), proper variability studies in each period are impossible. Therefore, in the SED fitting R is considered as a free parameter allowing to vary within the range defined by the applied model, i.e., the emission region is inside the BLR. When two-zone modeling was considered, to reduce the number of free parameters, different but fixed radii were used for the emitting regions.Since the TeV or X-ray observations in the bright states reveal that the flux varies on minute

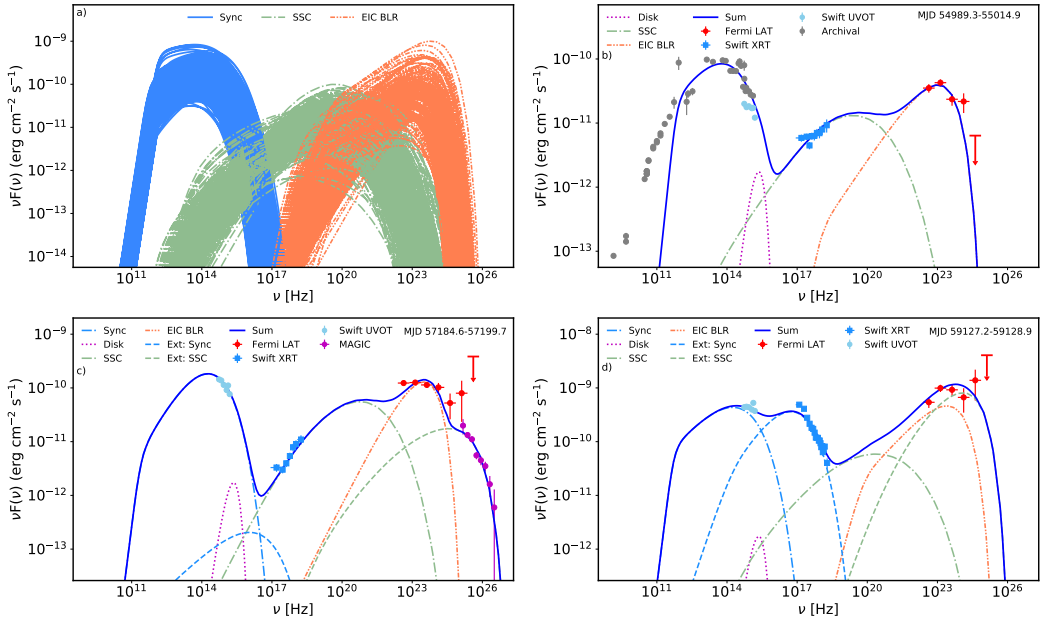

Figure 4.4 The broadband SEDs of BL Lac observed in different emission states. a) The emission components obtained from the modeling of all SEDs with contemporaneous data collected during 2008 August-2021 August. b) The SED of BL Lac in the normal emission state. c) BL Lac SED modeling with VHE γ-ray data from MAGIC observations [157]; corrected for extragalactic background light absorption using the model of **(author?)** [89]. d) The SED of BL Lac during the brightest X-ray period modeled within two-zone scenario.

scales, implying that the emitting region outside BLR should be very compact, $R = 10^{15}$ cm was assumed. On the other hand, the optical/UV and γ-ray fluxes vary albeit not on such short scales, so for the blob within the BLR $R = 10^{16}$ cm was used. Also, both emitting regions were assumed to have the same Doppler boosting factor. In principle, because of orientations those regions can have different Doppler boosting factors which, however, will introduce an additional free parameter.

4.3.1 SEDs modeling results

The animation of our 511 high-quality and quasi-contemporaneous SEDs of BL Lac together with the corresponding modeling is available as Supplementary data and at the following link `youtube.com/watch?v=f3a5CGukbbE`. In this animation, the sum of all model components is plotted as a solid blue line, while the SSC and EIC components appear as green and orange lines, respectively. The disc emission, approximated as a black body with inten-

sity that is always below the synchrotron component, is shown in magenta. Fig. 4.4 shows the emission components in all 511 SEDs (panel a) and some frames representing special states (panels b-d). The optical/UV data constrain the tail of the synchrotron component which peaks at $\sim 10^{14}$ Hz and, despite large flux variability, it remains almost unchanged as can be seen from Fig. 4.4 panel a) (blue curves; the bright and soft X-ray periods were not considered). The SSC emission of the synchrotron emitting electrons starts to dominate around 10^{17} Hz extending up to $\sim 10^{23}$ Hz (green dot-dashed lines in Fig. 4.4 panel a) while at higher frequencies EIC of BLR photons dominates (orange dot-dot-dashed lines in Fig. 4.4 panel a). The change of intensity of these components show high-amplitude variability of BL Lac emission in the optical/UV, X-ray and γ-ray bands. The variability in the radio band cannot be tested, as the data are missing for most of the cases. Moreover, the radio emission at lower frequencies can be produced, with significant time-lags, by the low-energy electrons in extended regions which is not associated with the emission in other bands.

The modeling provides estimates of the physical parameters describing the emission from BL Lac and allows us to investigate their changes in time. The evolution of the p, γ_{min}, γ_{cut}, δ and B parameters is shown in Fig. 4.5 panels a) to e). The minimum energy of electrons γ_{min} is mostly below 10 (Fig. 4.5 panel b) implying that even lower-energy electrons are efficiently accelerated. The power-law index (p) is mostly within $1.2 - 2.3$ (Fig. 4.5 panel a) and is defined by fitting the X-ray data with the SSC component. Its variation is in accordance with the changes of the X-ray photon index shown in Fig. 5.1 (panel d). The the cut-off energy obtained from the modeling of SEDs in different periods is shown in Fig. 4.5 panel c) which is defined mostly by the optical/UV and sometimes by γ-ray data; the minimal and maximal values of the cut-off energy are 311 ± 13 and 2438 ± 208, respectively. Despite such change in the cut-off energy, the low- and high- energy peaks in the SED do not deviate to higher frequencies; the peak positions are determined by the product of γ_{cut} and B. In this case, the magnetic field (see Fig. 4.5 panel e) varies in the range of $B = 0.80 - 14.65$ G but, in particular, when a high γ_{cut} was estimated, B was around its lower level (see Fig. 4.5). It is also interesting to investigate the evolution of the Doppler factor δ (Fig. 4.5 panel d) which was estimated under the assumption of a constant viewing angle. This parameter remained mostly below 20 but it reached the maximum value of $\delta = 63$ on MJD 59117.4 (25 september 2020) when the major γ-ray flares were observed.

An example of SED modeling during the period of MJD 54989.3-55014.9 (07 June- 02 July 2009), when the source was not flaring in any band, is shown in Fig. 4.4 panel b). The synchrotron emission of the accelerated electrons explains the archival (gray) and optical/UV (light blue) data, while the X-ray

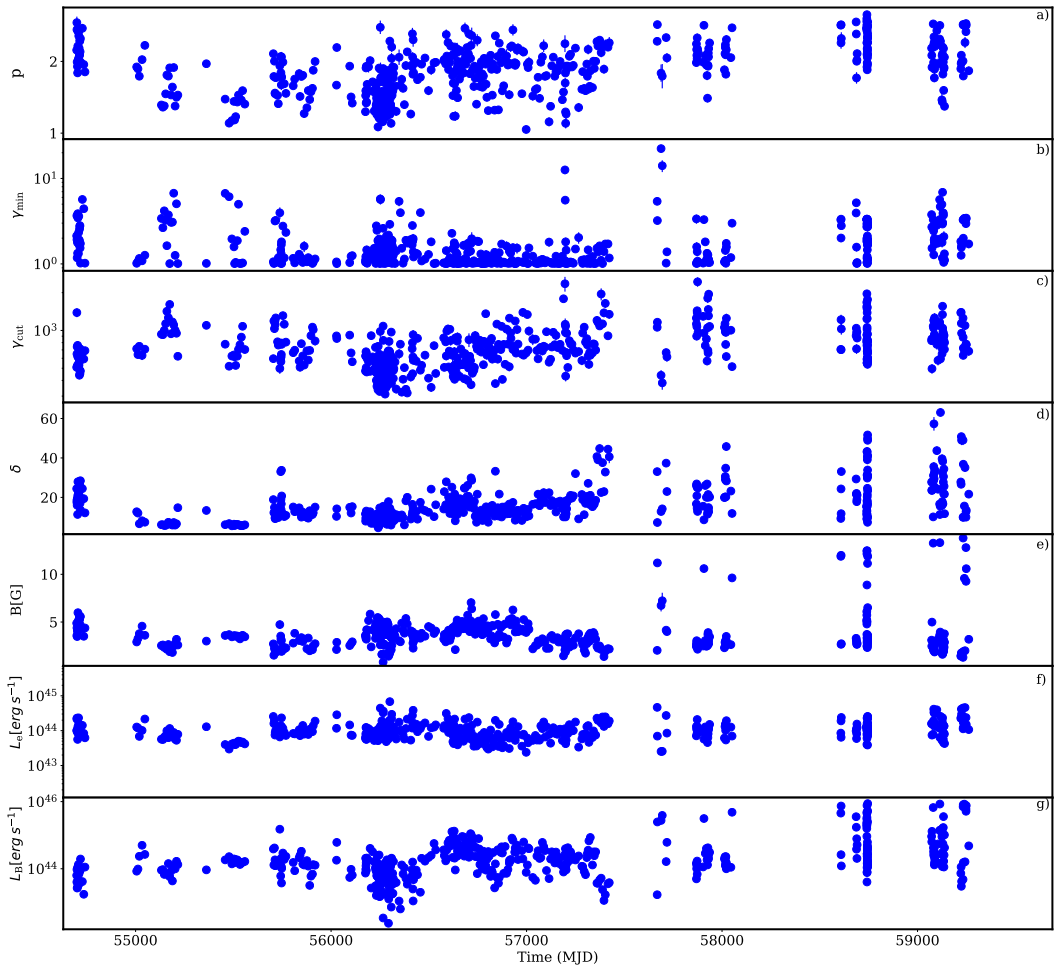

Figure 4.5 The evolution of electron parameters obtained from the modeling of 511 quasi-contemporaneous broadband SEDs of BL Lac. a) the power-law index of the emitting electrons, b) and c) minimum and cut-off energy of the emitting electrons, respectively. d) and e) Doppler factor and magnetic field estimated in different periods. f) and g) the jet luminosity in particles and in magnetic field.

emission (blue) is due to SSC emission. This SSC component extends up to 10^{20} Hz and the emission in the γ-ray band is dominated by the IC scattering of BLR photons. This shows that even in the quiescent state of the source, the external photon field (BLR) is necessary to explain HE γ-ray data. The power-law index of the emitting electrons is $p = 1.92 \pm 0.03$ and $\gamma_{cut} = 715 \pm 35$, while the emitting regions size is $R = 4.08 \times 10^{15}$ cm which moves with a Doppler factor of $\delta = 12.7$. The system is close to the equipartition $U_e/U_B \simeq 1.5$ with $B = 2.91 \pm 0.12$ G.

An example of the BL Lac SED modeling with VHE γ-ray data from MAGIC observations is shown in Fig. 4.4 panel c). When considering a one-zone scenario, the optical/UV data with a decreasing trend constrains the cut-off energy of the emitting electrons and the IC scattering of $1 - 5$ eV synchrotron or BLR photons on them will only reach the MeV/GeV band, unable to account for the VHE γ-ray data. These periods (8 among the considered SEDs) are modeled within two-zone scenarios, considering the emitting regions inside and outside the BLR. The emission observed in the radio to HE γ-ray bands is dominated by that from the region within the BLR, and the VHE γ-ray data are explained by the SSC emission from the compact region. In the extended region ($R = 10^{16}$ cm), $B = 1.87 \pm 0.08$ G and the emitting electrons have $\gamma'^{-1.28\pm0.02}$ distribution with $\gamma'_{cut} = 1082 \pm 36$. Instead, in the compact region, requiring that its synchrotron emission is lower than that from the other region, $B = 3.32 \times 10^{-2}$ G is estimated, implying that the electrons can be accelerated to higher energies, i.e., $\gamma'_{cut} = 1.39 \times 10^5$ was estimated in this case. The contribution of these electrons with $p = 2.17$ starts to dominate above $\sim$ 30 GeV when the spectrum of IC scattering of BLR photons decreases, explaining the data observed by MAGIC.

Similar two-zone models are also required when the soft component in the X-ray band is observed. The synchrotron component defined by the available optical/UV data effectively extends up to 10^{17} Hz ($\sim$ 400 eV), unable to account for the observed X-ray data. Thus, in the X-ray band an additional component is dominating. Among the selected periods, 38 SEDs with a soft X-ray spectrum were modeled within the two-zone scenario; an example of SED modeling when the brightest X-ray emission was observed is shown in Fig. 4.4 panel d). The Doppler boosting factor of both emitting regions is $\delta = 16.44$ but they are filled with different distributions of electrons. For example, the X-ray emitting electrons (the region outside BLR) have $\gamma^{-1.49}$ distribution above $\gamma_{min} = 761$ with a cut-off energy of 1.10×10^4. Instead, the electrons in the other region have a softer distribution with 2.02 ± 0.25 and are accelerated only up to moderate energies of $\gamma_{cut} = 1559 \pm 213$. The magnetic field in the region outside the BLR is stronger ($B = 7.28$ G) than that in the other region ($B = 1.71 \pm 0.02$ G) which is because i) the first region has a smaller radius and ii) the synchrotron emission should be at higher

frequencies, reaching up to the X-ray band.

4.4 Discussion

We performed a comprehensive investigation of the large and complex luminosity and spectral variability of BL Lac using the data taken by Fermi-LAT, *Swift*-XRT and *Swift*-UVOT between 2008 August and 2021 March. Using the unprecedented amount of the available multiwavelength data we performed an in-depth study of the origin of nonthermal emission from BL Lac.

In all the energy bands considered, the source shows multiple periods when the flux exceeds its average level by substantial amounts. The adaptively binned light curve, encapsulating more information, provides a detailed timing view of the γ-ray flares. The maximum γ-ray flux of $F_\gamma(> 196.7\ MeV) = (4.39 \pm 1.01) \times 10^{-6}\ photon\ cm^{-2}\ s^{-1}$ was observed on MJD 59231.34 (17 January 2021), associated with a flat spectral slope with photon index of 2.03 ± 0.21. This implies an energy flux, ϵF_ϵ, of $9.39 \times 10^{-9}\ erg\ cm^{-2}\ s^{-1}$ in the 0.1-300 GeV energy range, corresponding to an isotropic γ-ray luminosity of $L_\gamma = 4\,\pi\,d_L^2 \epsilon F_\epsilon = (1.06 \pm 0.24) \pm 10^{47}\ erg\ s^{-1}$ for a $\sim$ 307 Mpc distance. Assuming a Doppler factor of $\delta = 20$ this corresponds to $L_\gamma/\delta^2 \simeq 2 \times 10^{44}\ erg\ s^{-1}$ in the proper frame of the jet. This value largely exceeds the disc luminosity estimated under any reasonable assumption (e.g., $3 \times 10^{43}\ erg\ s^{-1}$ to not overproduce the observed optical/UV data) implying extreme energetics during the γ-ray flares [e.g., 108]. Unlike the flux, the photon index does not usually vary significantly, although it occasionally hardens to values < 2.0. Such hardening, for example, was noticed after the brightening observed on MJD 59247.4 (02 February 2021) when the γ-ray flux measured within three days was $(3.32 \pm 0.15) \times 10^{-6}\ photon\ cm^{-2}\ s^{-1}$; the photon index was within $1.79 - 1.89$ during MJD 59247.4-59256.4 (02-11 February 2021).

The *Swift*-XRT observations spanning different years showed an interesting behaviour of BL Lac. Although there can be seen flux variations in different observations, there are two major flaring activities on MJD 56268.65 (07 December 2012) and 59128.18 (06 October 2020) when the source was in an elevated state for a prolonged period. Even though during these flares the flux increased almost at the same level, the photon index was significantly different. During the first flare, when the 0.3-10 keV flux reached it maximum value of $(8.68 \pm 0.84) \times 10^{-11}\ erg\ cm^{-2}\ s^{-1}$ and the traditional harder-when-brighter trend was observed. In the X-ray band, this is a known behaviour for blazars [112, 274, 117]. On the other hand, during the second flare the linear-Pearson test resulted in 0.47 showing softer-when-brighter trend. Such a pattern was also observed in the X-ray emission of OJ 287 [e.g., 138, 116, 147]. During this flare, when the highest X-ray flux was observed

(on MJD 59128.18), the spectral index is 2.84 ± 0.03 - very different from the values normally observed in BL Lac (typically $\Gamma_X \leq 2.0$). There are 36 additional occasions when the X-ray spectrum softened ($\Gamma_X \geq 2.3$; see Fig. 5.1 panel d) but the exceptional softening during this flare was never observed for BL Lac.

The softening of the X-ray spectrum also affects the peak frequency of the synchrotron component. When the soft component is associated with a high X-ray flux (i.e., $F_{X(0.3-10\,keV)} > 10^{-11}\,erg\,cm^{-2}\,s^{-1}$) the peak of the SED low-energy component reaches frequencies of $\sim 10^{15}$ - 10^{16} Hz, instead of the usual $\sim 10^{14}$ Hz, temporarily placing BL Lac into the domain of HBL blazars. This component is present during the period MJD 59124.73-59132.88 (02-10 October 2020) when the flux rises from $F_{X(0.3-10\,keV)} = (4.83 \pm 0.40) \times 10^{-11}\,erg\,cm^{-2}\,s^{-1}$ with $\Gamma_X = 2.69 \pm 0.11$, and reaches $F_{X(0.3-10\,keV)} = (3.24 \pm 0.08) \times 10^{-10}\,erg\,cm^{-2}\,s^{-1}$ ($\Gamma_X = 2.84 \pm 0.03$) on MJD 59128.18 (06 October 2020). This component fades on MJD 59132.88 (10 October 2020) when the flux decreases to $F_{X(0.3-10\,keV)} = (2.44 \pm 0.12) \times 10^{-11}\,erg\,cm^{-2}\,s^{-1}$ ($\Gamma_X = 2.87 \pm 0.12$).

During these soft states (38 among the selected 511 periods) the source's X-ray emission is driven by a new HBL-like component, which significantly differs from the usual X-ray spectrum of BL Lac. Our modeling shows that this component may come from a separate emission zone with specific properties, like the size of the emission region, the population of electrons, etc. As an example, some of the SEDs observed during the soft X-ray emission period are shown in Fig. 4.2. The new soft component clearly goes beyond the synchrotron radiation constrained by the optical/UV data and is interpreted as synchrotron emission from the second region (dashed line) containing much more energetic particles. For example, the electrons should be accelerated up to $\gamma_{cut} = 1.76 \times 10^4$ with $p = 1.15$ to explain the data observed on MJD 59124.73 (02 October 2020; red line). Similar parameters obtained from the modeling of the SED on MJD 59128.18 (06 October 2020) are $\gamma_{cut} = 1.10 \times 10^4$ and $p = 1.49$ (blue line) but the magnetic field is 7.28 G, significantly higher compared to the previous case (1.65 G). Such a large magnetic field is required because of the increase in the X-ray flux (~ 6.11 times) which cannot be explained by changing γ_{cut}; p and γ_{cut} are also constrained by the γ-ray data. The X-ray flux variation impacts the magnetic field which decreases to $B = 0.27$ G on MJD 59132.88 (10 October 2020) when the soft X-ray component was with a low state. The electrons in the emitting region are still energetic with $\gamma_{cut} = 5.47 \times 10^4$ but their contribution starts to be subdominant. In fact, the usual hard X-ray component which is interpreted as SSC radiation from the blob inside the BLR dominates already on MJD 59133.81 (11 October 2020; Fig. 4.2 right panel). This implies that either the acceleration/injection

of the energetic electrons is not efficient anymore or due to the drop of the magnetic field these electrons cool down on longer time scales; for example, when $B = 0.1$ G the cooling of $\gamma = 5 \times 10^4$ electrons in the observer frame is $t_{cool} = 6\,\pi\,m_e\,c\,(1+z)/\sigma_T\,B^2\,\delta\gamma = 1.3\,(B/0.1\,G)^{-2}\,(\delta/15)^{-1}\,(\gamma/5\times10^4)^{-1}$ day.

The composition of the second emitting region (U_e/U_B) changes during the periods shown in Fig. 4.2. A slightly particle dominated region ($U_e/U_B \simeq 12.3$) is necessary to explain the SED on MJD 59124.73 (02 October 2020) while it should be magnetically dominated with $U_e/U_B \simeq 0.49$ to explain the data observed on MJD 59128.18 (06 October 2020) and it is strongly particle dominated on MJD 59132.88 (10 October 2020) with $U_e/U_B \simeq 3.1 \times 10^3$. This indicates that the X-ray flare was caused by the injection of new energetic particles and by sudden increase of the magnetic field. This is in agreement with the observation of the softer photon index during the bright X-ray state; due to the high magnetic field the electrons cool faster forming a soft spectrum with the increase of intensity.

The observed VHE γ-rays are also most likely produced from the second emission zone, although its composition is different. This region still contains energetic electrons with $\gamma_{cut} \simeq 10^5$ but the magnetic field is low ($0.02 - 0.1$ G), so the region is strongly particle dominated with $U_e/U_B \geq 10^3$. This makes the emission from these electrons significant in the VHE γ-ray band with no significant contribution at lower energies.

Our modeling shows that the overall emission from BL Lac from time to time is produced from two regions separated in the jet. We note that an excess of a new component in the X-ray band was already noticed in previous observations of BL Lac in 2007-2008: the XMM Newton observations showed that the X-ray spectrum was flat/concave producing a mild soft-X-ray excess, suggesting that two components are contributing in this band [212]. This excess was interpreted by the helical jet model of [258]. Also BeppoSAX observations indicated presence of two synchrotron components in the broadband SED of BL Lac [217]. The formation of the second emission region can be explained in the framework of other hypotheses as well. For example, it can be a local reconnection outflow in the jet in a jet scenario [110, 111]. The second population of energetic electrons can be formed also when the energetic protons interact in the jet; the electrons are produced from the decay of muons and are more energetic than the initial cooled electrons. The radiative signature of these electrons initially appears at HE, which in time is shifted to lower energies. In the scenario considered by [171] the second emission region could be where occasionally accelerated protons radiate X-ray photons via the synchrotron mechanism and interact with them via photomeson processes producing detectable high-energy neutrinos [248].

The extensive modeling of SEDs presented in this paper shows that ex-

cept for the cases when BL Lac was in a high and soft X-ray emission or a flaring VHE γ-ray state (46 in total), a one-zone leptonic model involving inverse Compton scattering of synchrotron and BLR-reprocessed photons gives a reasonable modeling of the data. The parameters values obtained from our modeling are similar to those typically estimated for blazars; their evolution in time is shown in Fig. 4.5. In some cases, the power-law index of the emitting electrons (panel a) on Fig. 4.5) should be hard (< 2.0) to account for the observed X-ray data. Such a hard injection index is difficult to obtain within standard shock accelerations, but it can be achieved when the particles are accelerated via magnetic reconnection [245]. For example, **(author?)** [121] using fully kinetic simulations demonstrated that in highly magnetized environments ($\sigma >> 1$) the spectral index of the particles approaches $p = 1.0$; the $\sigma >> 1$ condition is required so that the time scale over which particles are injected into the acceleration region is longer than the first-order Fermi acceleration time. The cut-off energy of the emitting electrons takes value between 311 ± 13 and 2438 ± 208 and shows that the electrons are efficiently accelerated up to ~ 1 GeV during the flares. The cut-off energy is naturally formed when the acceleration is limited by the cooling or dynamical time scale [e.g., 265, 275, 228, 28]. For example, when the particles are abruptly injected into the emitting region, they start to loose energy or escape the region, so the HE tail of the particle distribution steepens and a cut-off is formed. In principle, the cut-off energy values given in Fig. 4.5 panel c) can be obtained under a reasonable assumption for the injection and escape times. It should be noted that a similar cut-off feature in the electron spectrum will be formed also in the case of an episodic injection with an energy-dependent escape.

The comparison of the multiwavelength light curve shown in Fig. 5.1 with the Doppler boosting factor evolution in time given in Fig. 4.5 panel d) shows that it substantially increases when the source is bright in the γ-ray band. This is a consequence of the current interpretation the γ-ray data as inverse Compton scattering of the external photon field whose density transferred to the jet frame is $u^{'}_{ph} \sim \delta^2 \, u$. Therefore, any increase in the γ-ray luminosity would require a larger δ. Although the values estimated for BL Lac and shown in Fig. 4.5 are not physically unrealistic, in other interpretations, e.g., in two zone emission scenarios, a lower value of δ would be acceptable.

The modeling allows us to assess the luminosity of the jet in various periods. The evolution of the power (luminosity) carried by the jet in the form of electrons and magnetic field computed as $L_e = \pi c R_b^2 \Gamma^2 U_e$ and $L_B = \pi c R_b^2 \Gamma^2 U_B$ respectively, is shown in Fig. 4.5 panels f) and g), respectively. Both are relatively constant with a mean luminosity of $L_{e,mean} = 1.12 \times 10^{44} \, erg \, s^{-1}$ and $L_{B,mean} = 5.09 \times 10^{44} \, erg \, s^{-1}$, but they slightly increased during flaring periods. The jet is magnetically dominated in the periods when the optical/UV

data (defined by the synchrotron component) exceeds the X-ray data (defined by SSC), for the other cases $L_e/L_B > 1$ was estimated. The total luminosity ($L_{tot} = L_e + L_B$) varies within $(0.07 - 8.86) \times 10^{45}\, erg\, s^{-1}$ which is lower than the Eddington luminosity $4.75 \times 10^{46}\, erg\, s^{-1}$ for a black hole mass of $3.8 \times 10^8\, M_{BH}$ [262]; see also **(author?)** [92, 50, 107, 253]. Moreover, this condition will be still satisfied when considering the second emission region with $L_{tot} = (0.1 - 8.1) \times 10^{44}\, erg\, s^{-1}$, comparable to the luminosity of the other region.

The multiwavelength SED of BL Lac observed in different periods has been modeled within various scenarios [e.g., 156, 236, 216, 42, 6, 261, 157]. For example, in **(author?)** [6] the synchrotron/SSC, two-zone SSC and synchrotron/SSC plus EIC models were considered to fit the averaged (2008 August 20September 9) SED of BL Lac. The SSC and EIC emission of electrons initially injected with a 2.85 power-law index in the emitting region with a radius of 3×10^{15} cm which moves with a bulk Doppler factor of 15 can reproduce the observed data. This model is preferred also from the viewpoint of equipartition considerations, i.e., $L_B/L_e = 1.48$. Alternatively, **(author?)** [157] considered a two-zone scenario for modeling the VHE γ-ray flare of BL Lac, discussing a different setup for the emitting regions. Assuming a smoothed broken power-law distribution for the emitting electrons, correspondingly 2.0 and 3.2 (3.7) indices were estimated before and after the break for the compact (extended) emitting region. The minimum energy of the electrons is 50 and 3.0 for the compact (10^{15} cm) and extended (10^{17} cm) emitting regions, respectively, which move with a Doppler factor of 60 and 7, respectively. The parameters obtained here are not substantially different from those usually estimated for BL Lac. The long-term flux variability of BL Lac is also discussed in the context of the geometrical changes, i.e., in the jet the emitting regions have different orientations with respect to the line of sight [213].

4.5 Conclusion

In this paper we have presented a long-term (thirteen-year-long) multiwavelength study of the peculiar blazar BL Lac. Using an adaptive binning method for the generation of the γ-ray light curve a very different state of the source emission was identified and studied, revealing complex and high-amplitude variability. Thanks to the good X-ray coverage (610 *Swift* XRT observations), two major X-ray flaring activities were identified. Although X-ray flux variations are common in BL Lac, the observed flaring activities showed substantially different properties; during the flare observed on MJD 59128.18 (06 October 2020) the flux increase was associated to a X-ray photon index softening to 2.84 ± 0.03, resulting from the shift of the synchrotron peak to higher

frequencies. We investigated the evolution of the X-ray photon index in time and identified additional 38 periods when the X-ray photon index softens, extending the X-ray emission beyond the synchrotron component extrapolated from the optical/UV band.

We also performed a comprehensive modeling of BL Lac SEDs selected in different periods. Most of the time the broad-band emission of the source can be described within a simple one-zone scenario when the emission region is inside the BLR, considering the inverse-Compton up-scattering of both synchrotron and BLR reprocessed photons. However, in the periods when the X-ray emission is associated to a soft spectral index and when VHE γ-rays were observed, the data could be modeled only considering a second emitting region outside the BLR. The modeling shows that, depending on the magnetic field and the U_e/U_B ratio, the radiative signature of the second emitting region contributes to either the X-ray or VHE γ-ray bands. The model parameters estimated through fitting 511 broadband SEDs allow us to track the changes in the jet that are responsible for multiwavelength flares.

The accumulation of a large number of high-quality data from the observations in different bands provides an exceptional chance to investigate the dynamical evolution of jet radiation in time. Through this new comprehensive approach the main properties defining the jet physics can be compared and contrasted, helping to unveil the origin of the emission in different periods.

5 Modeling the time variable spectral energy distribution of the blazar CTA 102 from 2008 to 2022

5.1 Introduction

Active galactic nuclei powered by supermassive black holes with masses of 10^6-10^{10} $M_\odot$ are the most luminous persistent objects in the extragalactic sky. In some AGNs a relativistic jet is formed perpendicular to the accretion disc plane and it plays a crucial role in blazar classifications. According to the unification scheme developed by **(author?)** [257], an AGN is called a blazar when the jet is closely aligned with the line of sight of the observer. Blazars are characterized by high radio and optical polarization, apparent superluminal motion along with high-amplitude variability in all accessible bands of the electromagnetic spectrum. Usually, this variability is unpredictable and only for a few objects periodic variability is observed [e.g., see 10, 219]. Blazars are usually believed to be persistent sources, however recently a blazar showing a transient behaviour was observed. Namely, 4FGL J1544.3-0649 was never detected in the X-ray and γ-ray bands until May 2017 when it rose above the detectability level and for a few months became one of the brightest X-ray blazars [232]. Blazar emission is dominated by non-thermal emission from the jet which is significantly Doppler amplified since the jet with superluminal motion is viewed at small angles. Because of this, blazars even at higher redshift are observed [e.g., see 235].

The emission from blazars is observed in a wide frequency range, from radio to high energy (HE; $>$ 100 MeV) and very high energy (VHE; $>$ 100 GeV) γ-ray bands [188] displaying a double hump structure in their broadband spectral energy distribution (SED). The first component (low-energy) usually peaks between far infrared and X-rays while the second component (HE) is observed between X-rays and VHE γ-rays. The low-energy component is explained by the synchrotron emission of jet-accelerated electrons under the magnetic field while the origin of the HE component is discussed within

leptonic and hadronic models, depending on the type of emission initiating particles, e^-e^+ pairs or hadrons. According to the widely discussed leptonic scenario, the HE component is due to inverse Compton upscattering of photons by energetic electrons. Most common scenarios used in the literature are synchrotron self-Compton (SSC) model and the external Compton (EIC) model. According to the first scenario, the internal synchrotron photons are up-scattered to higher energies [104, 38, 163] whereas the latter model assumes the photons are produced external to the jet [36, 105, 240]. In alternative hadronic or lepto-hadronic scenarios, the protons co-accelerated with the electrons make a non-negligible contribution to the HE component. This contribution can be either directly from proton synchrotron radiation [179] or from secondaries produced in the proton-photon interactions or photo-pair productions [160, 161, 179, 180, 43, 199, 99]. Lately, the hadronic models [especially lepto-hadronic 99] have become more attractive after the detection of VHE neutrinos spatially coinciding with the direction of known blazars [132, 130, 189]. The initial association between TXS 0506+056 and IceCube-170922A event provided first multimessenger picture of blazar and opened a wider perspective for theoretical studies [19, 141, 181, 189, 225, 221, 59, 226, 96, 99]. The assumption that blazars are neutrino sources was further strengthened by the observation of multiple neutrino events from the direction of PKS 0735+178 when the source was undergoing a major flaring activity in the optical/UV, X-ray and γ-ray bands [234].

Commonly, the blazars are grouped based on their optical spectral properties. Namely, Flat Spectrum Radio Quasars (FSRQs) which show strong optical lines and BL Lacertae type objects (BL Lacs) which have very faint optical emission lines. Blazars are further classified based on the observed SEDs. Namely, based on the frequency where the synchrotron component peaks (ν_p), blazars are separated into low, intermediate and high-energy peaked sources [192, 5]; low synchrotron peaked sources (LSPs or LBLs) when $\nu_p < 10^{14}$ Hz, intermediate synchrotron peaked sources (ISPs or IBLs) when $10^{14}\,Hz < \nu_p < 10^{15}$ Hz and high synchrotron peaked sources (HSPs or HBLs) when $\nu_p > 10^{15}$ Hz. However, recently **(author?)** [118] showed that there are strong similarities between the properties of IBLs and HBLs and they show large differences from LBLs, so the classification can be refined into LBLs and intermediate-high-energy-peaked objects (IHBLs) when ν_p is below or above $10^{13.5}$ Hz.

CTA 102 is a FSRQ with a redshift of $z = 1.037$ [238]. Harboring a black hole with a mass of $8.5 \times 10^8\,M_{BH}$ [268], CTA 102 is one of the brightest FSRQs observed in the HE γ-ray band. It was initially observed by the Compton Gamma Ray Observatory mission having estimated a γ-ray flux of $(2.4 \pm 0.5) \times 10^{-7}\,photon\,cm^{-2}\,s^{-1}$ [186]. Then, CTA 102 was scanned continuously by the Fermi Large Area Telescope (Fermi-LAT) since mid-2008, initially show-

ing that the source is relatively weak in the γ-ray band. However, from 2016 to 2017 it underwent an unprecedented outburst in all the wavebands [55, 27, 65, 207, 70, 48, 71, 30, 176, 54]. For example, in the γ-ray band its flux was as high as $(3.55 \pm 0.55) \times 10^{-5}\ photon\, cm^{-2}\, s^{-1}$ [101] and in some active γ-ray periods its spectrum also deviated from simple power-law model [228]. During the γ-ray flares, the source was so bright that variability was investigated down to minute scales [239]. In December 2016, the source was also in an extreme optical and near-IR out-bursting state when the brightness increased up to six magnitudes with respect to the faint state of the source [210]. Various theoretical models were used to explain the flaring behaviour of CTA 102 which includes an inhomogeneous curved jet with different jet regions changing their orientation and consequently the Doppler factors [210], or a superluminal component crossing a recollimation shock [56], or leptohadronic processes when the gas cloud penetrates the jet [266, 267] or the activities were interpreted as change of the location of the emission region [e.g., 101, 209, 228], etc.

Due to the long-lasting and peculiar multiwavelength flaring activity, CTA 102 was frequently observed in different bands and became one of the most-studied blazars [151, 140, 79, 174, 66, 9, 223, 144, 103]. Although many studies have been conducted which lead to a better understanding of the CTA 102 jet, it is up to now not clear the origin of the multiwavelength flares of CTA 102, especially the changes in the jet that have led to prolonged flaring activities.

The monitoring of CTA 102 during its unprecedented outburst with various instruments resulted in accumulation of an extensive data set. In addition, before and after the outburst the source was also monitored in the γ-ray band with Fermi-LAT and observed in the optical/UV and X-ray bands by Neil Gehrels Swift Observatory [102], (hereafter Swift). This can be combined with other available data to build the broadband SEDs of CTA 102 in various (flaring or quiescent) periods with (quasi) contemporaneous data. These SEDs with various spectral properties represent an ample variety of source emission in different states and their modeling is crucial for understanding of the physical processes and their changes in time. In the broadband SEDs of blazars the changes are expected to be due to the variation of the parameters of the emitting electrons or the physical parameters of the emission region. Therefore, the modeling of the SEDs in different periods allows to connect the observational properties with the physical processes at work in jets. For example in **(author?)** [229] and **(author?)** [233] the modeling of a large number of contemporaneous SEDs of 3C 454.3 and BL Lac allowed to estimate the main parameters describing the emitting electrons and the emission region and investigate their evolution in time which was crucial for understanding of the observed spectral changes in them.

Motivated by the availability of multiwavelength data from CTA 102 obser-

vations before, during and after the large outburst, for furthering our knowledge of the emission processes dominating in the jet of CTA 102 we performed an intense broadband study of CTA 102 using the data accumulated during 2008-2022. We have systematically investigated the spectral and variability properties of the source emission in the optical/UV, X-ray and γ-ray bands. We performed a deep investigation of the origin of the source emission in various periods by generating as many SEDs of CTA 102 as possible that can be constructed with contemporaneous data and modeling them within the leptonic scenario. The paper is structured as follows. The broadband data analyses are described in Section 5.2. The multiwavelength variability is explored in Section 5.3. The modeling of broadband SED is described in Section 5.4. We present the discussion and results in Section 5.5 and the conclusions in Section 6.6.

5.2 Multiwavelength observations of CTA 102

Exhibiting interesting multiwavelength properties, CTA 102 was frequently observed in different bands. Below we report the data analyzed in this paper or extracted from public archives which was used in the current study.

5.2.1 Fermi-LAT observations of CTA 102

Operating since 2008, Fermi-LAT provides an exceptional view of the γ-ray sky, imaging the entire sky every three hours [25]. In the current paper the Fermi-LAT data accumulated between 04 August 2008 and 04 March 2022 in the 100 MeV300 GeV range were downloaded and analyzed using the Fermi ScienceTools version 2.0.8 and P8R3_SOURCE_V3 instrument response function. Events were extracted from a region of interest (ROI) with a 12° radius centered on the source position (RA: 338.15, DEC: 11.73). As recommended by the Fermi-LAT team, the cut evclass = 128 and evtype=3 was applied to select events with higher probability of being photons. Whereas, the filter $(DATA\_QUAL > 0)\&\&(LAT\_CONFIG == 1)$ was applied to update the good time interval based on spacecraft specifications. A maximum zenith angle cut of $> 90°$ is applied to reduce the contamination from Earth limb γ-rays. The model file was generated based on Fermi-LAT fourth source catalog Data Release 3 [4FGL-DR3; 15, 7] which includes point sources within the ROI and standard Galactic (gll_iem_v07) and the isotropic (iso_P8R3_SOURCE_V3_v1) diffuse emission components. The spectral parameters of the background sources falling between 12° and 12°+5° were fixed to the values published in the 4FGL-DR3 catalog, while the parameters of the other sources (within 12°) and background models were left free. The best match between

the source parameters and the data was obtained by applying standard binned likelihood analysis with gtlike tool.

After analyzing the data accumulated in the whole time interval, light curves were computed with different time bins to investigate the variability in the γ-ray band. Initially, the entire period was divided into three-day intervals (1653 in total) and for each single period the flux, photon index (CTA 102 spectrum was modeled with power-law distribution) and the Test Statistics [TS, defined as twice the difference between the log-likelihoods of the model computed with and without including the source; 172] were estimated.

Next, for a deeper investigation of the γ-ray flux variability, the light curve was generated with the help of the adaptive binning method [155]. As distinct from the fixed time interval light curve where the longer bins will smooth out the fast variation and in short time intervals the flux can be estimated only in the bright state of the source, in the adaptively binned light curve the bin width is defined by requiring a constant relative flux uncertainty above an optimal energy, so the time bins are longer during low flux levels and narrower when the source is in flaring state. This allows to track the evolution of the γ-ray flux in time, extract maximum possible information and identify flaring periods [e.g., see 101, 230, 231, 269, 26, 46, 215].

The spectral changes in the γ-ray band were further investigated by producing the source spectrum in different periods. For this purpose, the adaptively binned light curve is divided into piece-wise constant blocks [Bayesian blocks 237] representing optimal segmentation of the data into time intervals during which the flux is constant. By this approach, the considered period is divided into 347 intervals with the same flux level, whether flaring or quiescent. The spectrum of CTA 102 in each of the selected period is computed by applying unbinned likelihood analysis and running gtlike separately for 5 (when the source is in average or quiescent state) or 7 energy bins (when the source is in flaring state) of equal width in log scale.

5.2.2 Swift observations of CTA 102

In the optical/UV and X-ray bands there are available a total of 146 observations of CTA 102 with Swift XRT/UVOT instruments. All the XRT observations were individually downloaded and analyzed using Swift_xrtproc pipeline [119]. This tool developed within the Open Universe Initiative downloads the raw data and calibration files from one of the official Swift archives, processes it using the XRTPIPELINE task for each snapshot and for the entire Swift observation, applies pile-up correction when the source count rate is above 0.5 $counts\, s^{-1}$ and generates source (from a circle with a radius of 20 pixels centered at the position of the source) and background (an annu-

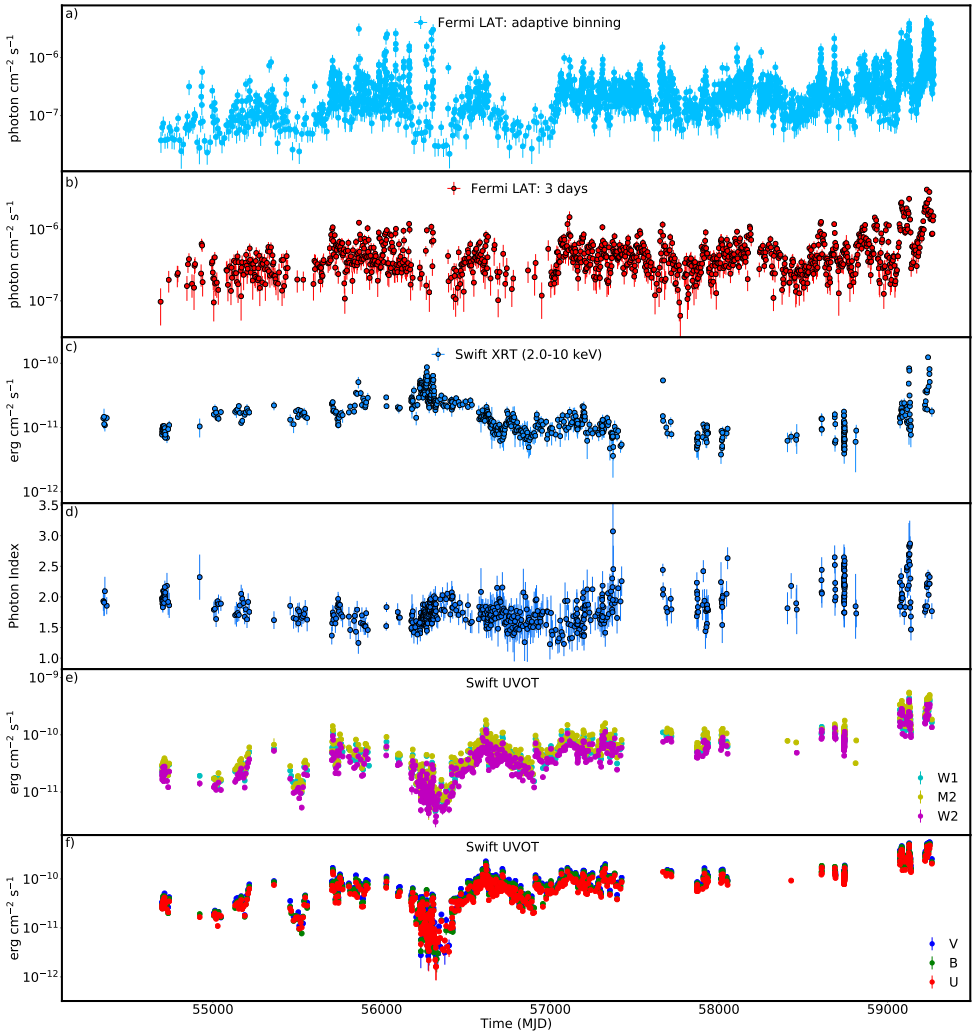

Figure 5.1 The multiwavelength light curve of CTA 102 between 2007 and 2022. *a)* Adaptively binned γ-ray light curve ($>$ 166.3 MeV) with the Bayesian blocks, *b)* 3-day binned γ-ray light curve, *c)* 2.0-10 keV X-ray flux, *d)* 0.3-10.0 keV X-ray photon index, *e)* flux in V, B, and U filters, *f)* flux in W1, M2 and W2 filters and *g)* V-band and R-band fluxes. The periods for which the SEDs have been modeled are highlighted in gray.

lar ring centered at the source) spectral files. It performs a spectral fitting with XSPEC (version 12.12.0) on the ungrouped data using Cash statistics [57], modeling CTA 102 spectrum as a power-law and a log-parabola. As a result, the tool generates SED data and estimates the flux and photon index in various bands. More details on Swift_xrtproc are given in **(author?)** [119].

The Swift-UVOT data in three optical filters (V, B, and U) and three UV filters (W1, M2, and W2) were downloaded and reduced using HEAsoft version 6.29 with the latest release of HEASARC CALDB. The source counts were extracted from a region of 5 arcsec radius centered at the source and the background counts from a region of 20 arcsec centered away from the source. uvotsource tool was used to obtain the magnitude which was corrected for reddening and galactic extinction using the reddening coefficient $E(B-V)$ from the Infrared Science Archive [1].

5.2.3 NuSTAR observations of CTA 102

NuSTAR with two focal plane modules [125], FPMA and FPMB, observed CTA 102 in the hard X-ray (3-79 keV) band on December 30, 2016 for a total exposure of 26.2 ksec. The NuStar data was processed with NuSTAR_ Spectra script which is a shell script based on the *NuSTAR* Data Analysis Software (NuSTARDAS) that automatically downloads calibrated and filtered event files from the SSDC repository, generates scientific products and carries out a complete spectral analysis. It uses *nuproducts* to generate the spectra from source counts extracted from a circular region whose radius is set to a value that is optimised depending on the source count rate (30″ in this case), while the background counts are from an annulus centered on the source. With the XSPEC, the spectral analysis is performed adopting Cash statistics for the energy range from 3 keV up to the maximum energy where the signal is still present, typically between 20 and 79 keV. NuSTAR_ Spectra script is presented and described in **(author?)** [175].

5.2.4 Archival optical data

In order to monitor the flux changes in the optical band, the light curves from several public archives were used. Namely, the optical data (V- and R- band) from Steward Observatory [246], V-band data from the All-Sky Automated Survey for Supernovae (ASAS-SN) [2] [146] and the V-band data from the Catalina Sky Survey [CSS; 91] were downloaded from the public archives.

[1] http://irsa.ipac.caltech.edu/applications/DUST/
[2] https://asas-sn.osu.edu/

5.3 Multiwavelength variability

The multiwavelength light curve of CTA 102 is shown in Fig. 5.1. The adaptively binned light curve above 166.3 MeV in Fig. 5.1 panel a) shows the continuous observation of the source in the γ-ray band and reveals the complex flux changes. During the considered periods several outbursts are observed. Until April 2011 the source flux was constant, not exceeding $10^{-7}\ photon\ cm^{-2}\ s^{-1}$. The first flare (when $F_\gamma > 15 \times F_{\gamma,min}$) occurred in April-June 2011 (MJD 55680-55730), when the flux increased up to $(2.55 \pm 0.62) \times 10^{-6}\ photon\ cm^{-2}\ s^{-1}$. Other enhancements were observed between September-October 2012 (MJD 56180-56230) and between March-April 2013 (MJD 56380-56400). Yet, a major flaring activity, when the source flux increased above $10^{-5}\ photon\ cm^{-2}\ s^{-1}$, was observed between December 2015- March 2016 (MJD 57370-57470). Then, the source entered a prolonged out-bursting state between November 2016 - June 2017 (MJD 57710-57910) when the highest flux of $(2.64 \pm 0.60) \times 10^{-5}\ photon\ cm^{-2}\ s^{-1}$ above 166.3 MeV was observed on MJD 57738.5. Another brightening of the source (although with lower amplitude) was observed between November 2017-March 2018 (MJD 58080-58180). During the considered period, the γ-ray flux of CTA 102 was above $10^{-5}\ photon\ cm^{-2}\ s^{-1}$ for 121.1 hours in total. The ratio between the highest and lowest fluxes is $\simeq 1137$ which again shows the high-amplitude variation of the γ-ray flux. The overall trends revealed in the γ-ray light curve generated by the adaptive binning method are also visible in the 3-day light curve (panel b) Fig. 5.1) but, as expected, the intra-day flux variability is smoothed out.

Together with the γ-ray flux, the photon index varies as well. The hardest photon index is $\Gamma_\gamma = 1.52 \pm 0.12$ observed on MJD 57752.5 when the source was in bright γ-ray state with a flux of $(1.02 \pm 0.20) \times 10^{-5}\ photon\ cm^{-2}\ s^{-1}$. The distribution of photon index estimated in all adaptively binned intervals is shown in Fig. 5.2 (light magenta). The mean of the photon index distribution 2.31 is the same as the time-averaged photon index of the source in 4FGL DR3 ($\sim$ 2.3). However, there are 353 periods when the photon index was significantly hard (< 1.9) which means that the peak of the HE component moved to HEs. In Fig. 5.2, the blue area corresponds to photon index distribution only when the γ-ray flux was $10^{-5}\ photon\ cm^{-2}\ s^{-1}$ which shows that in some of the bright states the photon index of the source was also hard.

The X-ray flux ($2 - 10$ keV) variation in time is shown in Fig. 5.1 panel c). There is significant variability of the X-ray flux in different XRT observations. During the prolonged flaring in the γ-ray band, the source was also in an active X-ray emission state, when the X-ray flux reached $F_{X-ray}[2 - 10\,keV] = (5.77 \pm 0.63) \times 10^{-11}\ erg\ cm^{-2}\ s^{-1}$. The NuSTAR observation shows that the source flux in the 3-10 keV band is $(4.46 \pm 0.02) \times 10^{-11}\ erg\ cm^{-2}\ s^{-1}$ in agree-

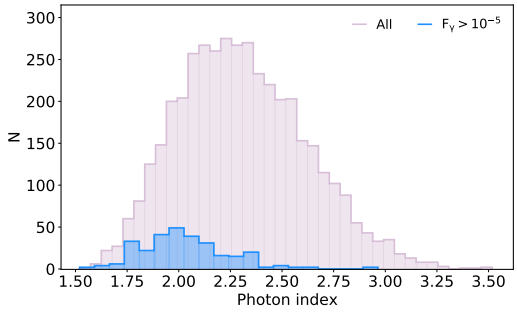

Figure 5.2 The distribution of the γ-ray photon index estimated in the adaptively binned intervals. The light red area shows the total distribution, while the blue is only when the γ-ray flux was above 10^{-5} $photon\ cm^{-2}\ s^{-1}$.

ment with the X-ray flux observed by Swift XRT on the same day ($F_{X-ray}[2-10\,keV] = (5.30 \pm 0.47) \times 10^{-11}\ erg\ cm^{-2}\ s^{-1}$). As the X-ray band corresponds to the rising part of the HE component, the flux in the 10-30 keV band increases being $(9.04 \pm 0.05) \times 10^{-11}\ erg\ cm^{-2}\ s^{-1}$. Also, the Swift XRT and NuSTAR observations reveal similar photon indexes in the 0.3-10 keV and 3-30 keV bands, 1.25 ± 0.08 and 1.30 ± 0.01, respectively.

In Fig. 5.1 panels e), f) and g), the flux variation in the optical/UV band is shown. In the optical band, the source's emission follows the same trend as in the γ-ray and X-ray bands. Namely, Swift UVOT, ASAS-SN, Steward (V and R band) and CSS observations show that the flux was relatively constant up to MJD 56000 and then increased several times around MJD 56200. However, long-lasting flaring activity was observed between MJD 57400-58000 when the flux in the optical band, as observed with all the considered instruments, was above $10^{-11}\ erg\ cm^{-2}\ s^{-1}$. The highest flux of $(6.38 \pm 0.19) \times 10^{-10}\ erg\ cm^{-2}\ s^{-1}$ was observed in the V-band on MJD 57751.84 by Swift UVOT. The Swift UVOT observations show that between MJD 57718-57768 (November 2016-January 2017), the source was in an extreme bright state in the optical/UV band when the flux was above $10^{-10}\ erg\ cm^{-2}\ s^{-1}$. This is in agreement with the results obtained from CTA 102 monitoring by the Whole Earth Blazar Telescope (WEBT) [210]. The ASAS-SN monitoring of the source shows that another flaring activity was observed on MJD 58741 and then the source's emission in the optical band was on its regular level.

5.4 Broadband SED modeling

One of the ways for investigation of the underlying physical processes in the jet is through broadband SED modeling. The SEDs constrained with con-

temporaneous or quasi-contemporaneous data contain valuable information on the emitting particle spectrum and on the condition of the plasma inside the jet. The evolution of the CTA 102 SEDs in time (SED/light curve animation) is shown here youtube.com/jFNkI_psAjo. These SEDs were generated by plotting the γ-ray spectra for each of the Bayesian blocks shown in Fig. 5.1 together with the data available in all other energy bands. In a visually effective way, the temporal changes in the CTA 102 spectra can be seen by going from one to another interval. This animation shows the high-amplitude and spectral changes in different periods, demonstrating dramatic changes of the CTA 102 during the prolonged out-bursting period.

In FSRQs, such as CTA 102, a one-zone synchrotron/synchrotron-self Compton (SSC) with an external radiation component is expected to produce the broadband emission. The origin of the external photons depends on the location of the emitting region [243] and photons directly emitted from the disc [86, 84], emitted from the BLR [240] or emitted from the dusty torus [36] can inverse Compton up-scatter and explain the second component in the broadband SED. In the current study we assume that the emitting region is at 10^{17} cm distance from the black hole within the BLR and the external photons are the photons emitted from the BLR. The SED modeling when different locations of the emitting region are considered is presented in **(author?)** [101] and **(author?)** [228].

Here, we consider a one-zone leptonic model of jet emission, assuming the accelerated electrons (protons) are injected in the spherical region of radius R. This magnetized region with a field strength of B moves along the jet with a bulk Lorentz factor of Γ_{jet} at an angle of θ relative to the observers line of sight. As the jet is almost aligned to the observer (small θ), the emission is Doppler boosting by a beaming factor of $\Gamma_{jet} = \delta$. It is assumed that the spectrum of the injected electrons is described by a power-law with an exponential cutoff energy distribution defined as

$$N(\gamma_e) = N_0 \, \gamma_e^{-p} \, Exp(-\gamma_e/\gamma_{cut}), \quad \gamma_e > \gamma_{min} \tag{5.4.1}$$

where γ_{cut} and γ_{min} are the cut-off and minimum energy of the electrons, respectively, and p is the power-law index of the electron energy distribution. The normalization constant N_0 defines the energy density of the electrons: $U_e = m_e c \int \gamma_e N(\gamma_e) d\gamma_e$.

In this scenario, the first peak in the SED is described by synchrotron radiation as a consequence of the interaction of relativistic electrons inside the emitting region with the magnetic field. Instead, the second peak (from X-ray to HE γ-rays) is formed by the contribution of inverse Compton scattering of synchrotron (SSC) and BLR emitted (EIC) photons. The BLR radius and luminosity of CTA 102 are $R_{BLR} = 6.73 \times 10^{17} \, cm$ and $L_{BLR} = 4.14 \times 10^{45} \, erg \, s^{-1}$

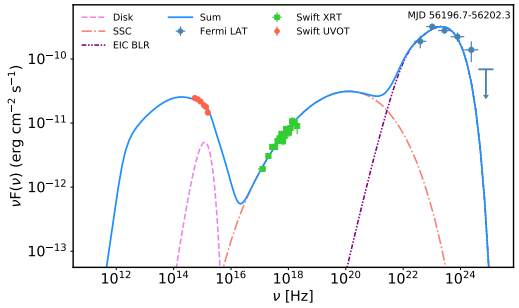

Figure 5.3 The multiwavelength SED of CTA 102 during MJD 56196.7-56202.3 constructed with the data from Swift UVOT, XRT and Fermi-LAT. The disc, SSC, EIC-BLR and the sum of all components are in dashed pink, dot-dashed orange, dot-dot-dashed purple and solid blue lines, respectively.

[204], respectively, and the BLR is modeled as a spherical shell with a lower boundary of $R_{in,BLR} = 0.9 \times R_{BLR} = 6.06 \times 10^{17}$ cm and an outer boundary of $R_{out,BLR} = 1.2 \times R_{BLR} = 8.08 \times 10^{17}$ cm. Assuming that the 10% of the disc luminosity is reprocessed into BLR radiation, the disc luminosity would be $L_{disc} = 4.14 \times 10^{46}\, erg\, s^{-1}$.

To model the broadband SED, a publicly available code, JetSet was used [168, 254, 255, 256]. JetSet fits the numerical models to observed data and is able to find the optimal values of parameters best describing the data. The multiwavelength SED of CTA 102 constrained with contemporaneous data observed during MJD 56196.7-56202.3 and modeled with JetSet is shown in Fig. 5.3. The dashed violet line shows the disc thermal emission approximated as a black body. The power-law index of the emitting electrons is $p = 1.61$ while the minimum and cut-off energies are $\gamma_{min} = 51.3$ and $\gamma_{cut} = 685.6$, respectively. The synchrotron emission of these electrons in the magnetic field of $B = 4.43$ G extends up to 10^{16} Hz explaining the observed data in the optical/UV bands. Then, the SSC component takes into account the X-ray data (dot-dashed orange curve in Fig. 5.3) dominating only up to 10^{22} Hz, failing to explain the γ-ray data. Instead, the inverse Compton upscattering of the BLR photons that have higher mean energy and number density in the jet frame can explain the γ-ray data (dot-dot-dashed purple curve in Fig. 5.3). The modeling allows to estimate the jet parameters such as size of the emission region, $R = 2.03 \times 10^{15}$ cm and the Doppler factor $\delta = 29.8$. The size of the emission region corresponds to the flux variability of the order of 1.3 hours, consistent with the rapid multi-band variability of CTA 102.

The modeling of the single snapshot SED shown in Fig. 5.3 permits to identify the parameters of the emitting region and the jet for a given period. How-

ever, in order to deeply investigate the multiwavelength emission processes in CTA 102 something beyond the single-epoch SED modeling is required. In **(author?)** [229] and **(author?)** [233] the multiwavelength emission from 3C 454.3 and BL Lac was investigated by modeling as many contemporaneous SEDs as possible constrained during the considered periods. As compared with the single snapshot SED modeling, the advantage of such an approach is that it allows to follow the changes also in the parameters over time, thus get a clue on the evolution of the processes that have lead to the emission in different states (e.g., flares). In addition, such modeling has diagnostic applications, i.e., by fitting many SEDs it is possible to identify periods when the source was characterized with peculiar emission properties that are not possible to explain within the considered model.

In order to model the SEDs of CTA 102 in different periods, from the SEDs generated for each Bayesian block there were selected all the periods with sufficient multiwavelength data, i.e., when the optical/UV data at least in two filters is available together with the γ-ray and X-ray data. In Fig. 5.1 the selected periods are shown in gray. As a result high-quality SEDs in 117 periods were assembled which represent various emitting sates of CTA 102 including periods when it was in a prolonged flaring state in the γ-rays. Therefore, this allows to understand the physical processes dominating in the jet of the source in its quiescent and flaring states. All the selected SEDs are modeled within the same one-zone scenario described above.

5.5 Results and Discussion

In this section, the implications of the data analysis are discussed, and the results from the broadband spectral fitting are presented. In the optical/UV, X-ray and γ-ray bands, CTA 102 exhibits complex flux changes showing multiple flaring periods. The highest amplitude changes are observed in the HE γ-ray band where the γ-ray luminosity of the source varies from $8.50 \times 10^{46}\ erg\,s^{-1}$ to $7.55 \times 10^{50}\ erg\,s^{-1}$ (assuming a distance of 7.1 Gpc) which makes CTA 102 one of the brightest sources in the extragalactic γ-ray sky.

The visual inspection of the multiwavelength light curves in Fig. 5.1 shows that fluxes in different bands change almost simultaneously. Possible correlation or anticorrelation between the fluxes in different bands shows whether or not the emission is produced by the same population of the particles and related mechanisms. In the case of one-zone leptonic scenario considered here, when the optical/UV photons are from synchrotron emission of the electrons while the emission in the X-ray and γ-ray bands is from the inverse Compton scattering of internal and external photon fields by the electrons in the same emitting region, one expects correlation between the photons at different fre-

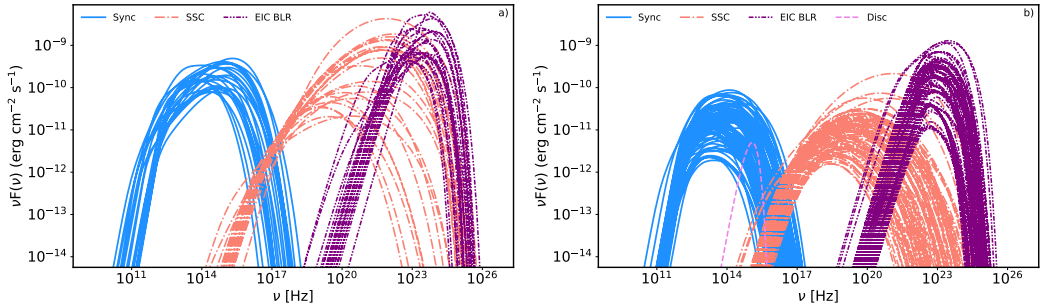

Figure 5.4 The Multiwavelength SED modeling in different periods. Panel a: Synchrotron, SSC and EIC components, blue, dot-dashed orange and dot-dot-dashed purple lines, respectively, when the source was in an active state in all the considered bands. Panel b: The same components in all other periods.

quencies as can be seen from Fig. 5.1 [e.g., 152, 159, 214].

5.5.1 Long-term broadband SED modeling

The one-zone leptonic model adopted here can adequately reproduce the observed data in almost all the considered periods. The datasets considered here, namely optical/UV, X-ray and γ-ray data, contain relevant information on the source emission in each band, but together they put a constraint on the shape of the emitting particle distribution. Except for the cases when the source is in a very low emission state and the optical/UV emission is (partly) dominated by the thermal emission from the disc, the decaying shape of the optical/UV data directly constrains the HE tail of the synchrotron component which controls the cut-off energy of the emitting electrons (γ_{cut}). Instead, the X-ray spectrum exhibiting rising shape allows to constrain p. Additional constraints on the γ_{cut} and p are provided from γ-ray observations: depending on the shape of the γ-ray spectrum, rising, steepening or flat, it defines either the distribution of the particles or their cut-off energy.

The time evolution of the selected SEDs modeling is available here `youtube.com/0H1IyNN9PSM`. In Fig. 5.4 the SED modeling results are shown for each case separating synchrotron (light blue), SSC (dot-dashed orange) and EIC (dot-dot-dashed purple) components. The models are shown by separating the periods when CTA 102 was in the active states in all the bands (panel a) and in all the other periods (panel b). The low-energy component peaks, as typical for FSRQs, is around $\sim 10^{14}$ Hz and is mostly defined by the synchrotron emission of the jet electrons. Although the flux of the synchrotron component varies largely, i.e., in the low state the peak flux can be as low as

$\sim 10^{-12}\,erg\,cm^{-2}\,s^{-1}$ but it can increase up to $\sim 10^{-10}\,erg\,cm^{-2}\,s^{-1}$ during the flares, the synchrotron peak frequency remains relatively unchanged. However, in several occasions (e.g., between MJD 55228-56190 and MJD 58297-58353) the disc thermal emission with a flux of $\sim 6.86 \times 10^{-11}\,erg\,cm^{-2}\,s^{-1}$ exceeds the synchrotron emission from the jet (violet dashed line in Fig. 5.4 panel b). As one can see from Fig. 5.1, in the mentioned periods the source was in a quiescent state in all the considered bands, so it is natural that bright accretion disc of CTA 102 overshines the synchrotron component. The relatively constant peak frequency of the synchrotron component limits also the highest energy of the synchrotron photons, and their inverse-Compton scattering steepens in the hard X-ray/soft γ-ray bands, unable to explain the observed γ-ray data (SSC; dot-dashed orange lines in Fig. 5.4). Instead, the Compton dominance (the ratio of the high-to-low components luminosity) and the γ-ray spectra are naturally explained by inverse Compton scattering of BLR photons (EIC; dot-dot-dashed purple lines in Fig. 5.4).

The models shown in panels a) and b) of Fig. 5.4 demonstrate different behaviour of the CTA 102 emission in active and other states. The brightening of the source substantially modifies different components affecting their flux and spectrum. For example, when modeling the SED in the bright X-ray state characterized by a hard X-ray photon index, the intensity of the SSC component increases and its spectrum hardens extending the peak of this component to higher energies (panel a) Fig. 5.4). However, for a harder photon index (hence a lower p), γ_{cut} should be lower not to violate the optical/UV data. So, even in those bright and hard X-ray states the SSC component has a decreasing shape in the GeV band, and again the Fermi-LAT observed data are interpreted as inverse-Compton up-scattering of BLR emitted photons. Similarly, the spectral variability in the MeV/GeV band affects the EIC component. As an example, the SED of CTA 102 during MJD 57872.9-57875.6 is shown in Fig. 5.5. During this period, the MeV/GeV spectrum is characterized by a nearly flat spectrum extending up to 58 GeV. The modeling shows that the distribution of the emitting electrons is described by $p = 1.87$ power-law index and the cut-off energy of $\gamma_{cut} = 306.4$. So, the inverse Compton scattering of BLR photons can reach only 2 GeV unable to explain the observed data in tens of GeV. The limit imposed by the emitting electron distribution prohibits the interpretation of GeV data within one-zone scenarios; the observed data can be account for only when the photons with higher mean energy are inverse Compton up-scattered on the same electrons. In the emitting region, except for BLR, the electron can interact with disc photon or the photons emitted from the dusty torus. The inverse Compton scattering of the disc photons will produce a peak comparable to that shown in Fig. 5.5 whereas in the case of the dusty torus photons with a lower mean energy will produce a peak at lower frequencies. The emission in the > 2

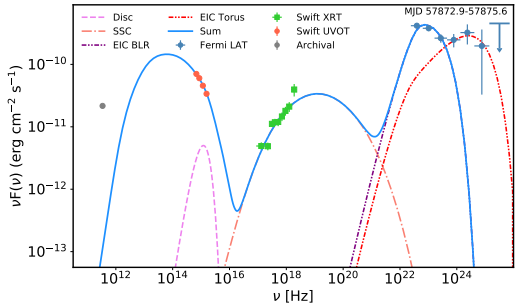

Figure 5.5 The multiwavelength SED of CTA 102 during MJD 57872.9-57875.6 when the γ-ray spectrum was flat, extending up to 58 GeV. The same color code as in Fig. 5.3 is adopted. The light red dot-dot-dashed line shows EIC torus component when the second emitting region is outside BLR.

GeV band is most likely produced from the second emission region containing more energetic electrons. As an example, in Fig. 5.5 the GeV data are modeled as emission from the second region which is assumed to be be outside the BLR. As the data are not sufficient to constrain the parameters, it is assumed that this region *i)* has the same Doppler boosting factor ($\delta = 29.4$) as the one inside the BLR (constrained from the fit), *ii)* is characterized by a significantly lower magnetic field (0.2 G as compared to 12.3 G estimated for the other region) not to overproduce the X-ray data which are from the region within the BLR and *iii)* contains more energetic electrons with $p = 1.80$ and $\gamma_{cut} = 1.10 \times 10^4$. As the emitting region is outside the BLR, the dominant photon field is IR photons from the dusty torus; the inverse Compton up-scattering of these photons is shown with a light red dashed line in Fig. 5.5 which extends up to GeV bands and accounts for the observed data. In principle, the second emission region can be a local structure in the jet where the particles are re-accelerated (e.g., a local reconnection outflow in the jet in a jet scenario [110, 111]) or there occurs an injection of fresh electrons. The modeling presented above is to show that the observed data in some cases (e.g., when the γ-ray spectrum is flat and extends to tens of GeV, two among the selected SEDs) cannot be reproduced in one-zone scenarios, so that more complex (e.g., two-zone) scenarios are required.

5.5.2 Energy distribution of the emitting electrons

The modeling of 117 high-quality SEDs of CTA 102 with diverse features allows to investigate the properties of the jet and emitting particles over time. In Fig. 5.6 the distribution of p, γ_{min}, γ_{cut}, B, L_e and L_B obtained from the modeling are shown. The wide distribution of the considered parameters

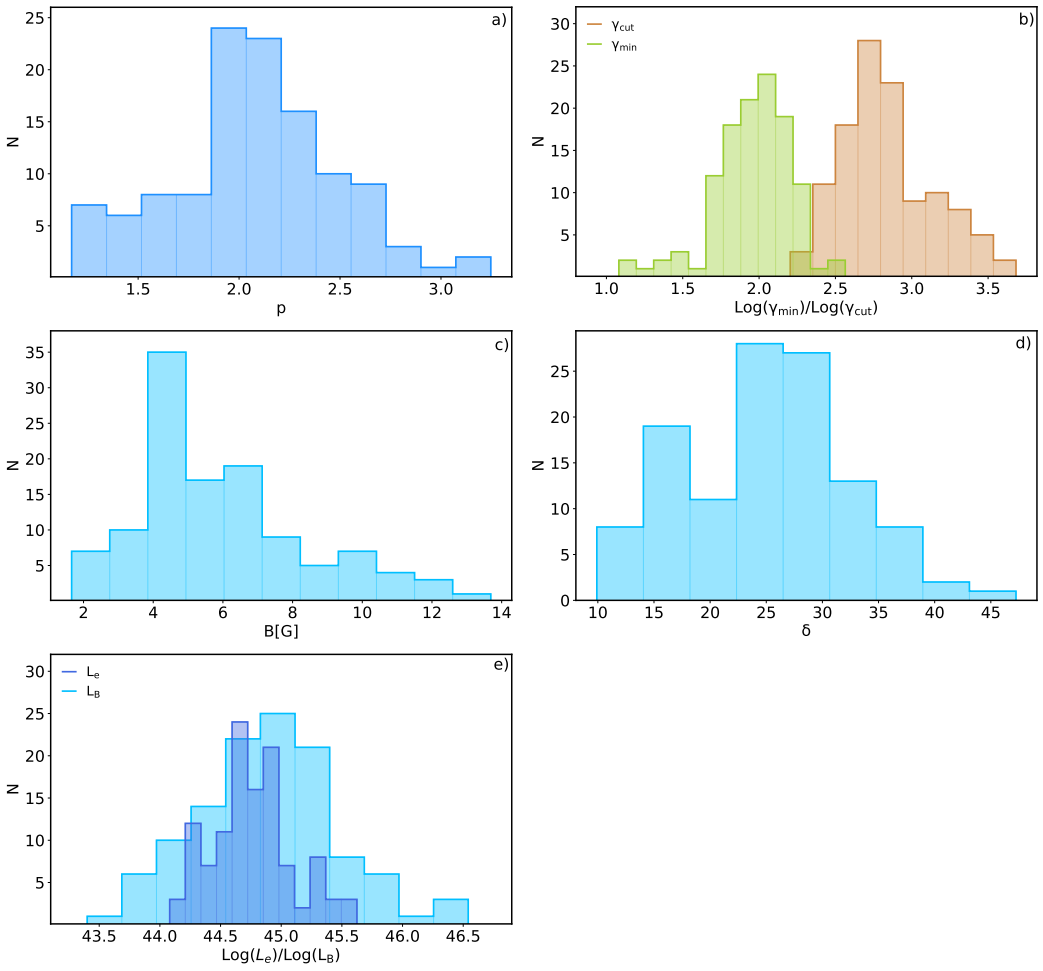

Figure 5.6 The distribution of the parameters obtained from the fitting of all data-sets composed with simultaneous data. *a)* The distribution of the emitting electron power-law index, *b)* the distribution of γ_{min} (green) and γ_{min} (orange), *c)* magnetic field distribution, *d)* Doppler factor distribution and *e)* the distribution of L_e (dark blue) and L_B (light blue).

once more shows the complex changes having taken place in the jet of CTA 102. The power-law index of the emitting electron distribution varies between $p = 1.17 - 3.25$ with a mean of $p_{mean} = 2.08$ (Fig. 5.6 panel a). This power-law index constrained by the X-ray and γ-ray data varies following the spectral changes in the X-ray and γ-ray bands; when a steep falling spectrum is observed in the γ-ray band, the emitting electron should also have a steep spectrum, while $p < 2.0$ are expected in bright active states that are characterized by a hard photon index. The distribution of γ_{min} and γ_{cut} is shown in Fig. 5.6 panel b). Both parameters have a narrow distribution peaking around $\gamma_{min,mean} = 104.6$ and $\gamma_{cut,mean} = 905.1$, respectively. The narrow distribution of γ_{cut} (between $(1.60 - 48.16) \times 10^2$) is probably due to stability of ν_{peak} but in general it depends also on p. The magnetic field estimated in different periods (Fig. 5.6 panel c), varies from $B = 1.66$ G to $B = 13.69$ G with a mean of $B_{mean} = 5.96$ G. For example, the highest magnetic field of $B = 13.69$ G was estimated from fitting the SED observed between MJD 57754-57756 when the source was in an elevated optical/UV emission state. So, the increase of the synchrotron component leads to an increase in B: large magnitude change of the synchrotron component can be seen from Fig. 5.4.

The distribution of δ in different periods is shown in Fig. 5.6 panel d). The high values of δ are mostly estimated during the flares in the γ-ray band, for example, the highest value of $\delta = 47.2$ was observed on MJD 57743.2 when the source was in a γ-ray active state. It should be noted that sometimes high values of δ have already been estimated for Fermi-LAT detected blazars [e.g., see 273] and are usually used to model the bright blazar flares observed in HE or VHE γ-ray bands [e.g., see 124, 150]. When δ increases, a lower electron density is required to produce the same level of synchrotron radiation, so the synchrotron photon density and the SSC component decrease but the external photon energy density in the jet frame becomes larger leading to the increase of the EIC component. For this reason, the enhancement in the γ-ray band results in higher δ.

The parameters distribution presented in Fig. 5.6 does not differ from that usually estimated for CTA 102 in different periods. For example, in **(author?)** [101] by considering different locations of the emission region it is found that SSC and EIC of BLR photons can explain the broadband SED in the low state when $p = 2.51 \pm 0.11$, $\gamma_{cut} = 1311.1 \pm 195$, $B = 5.40 \pm 0.13$ and $\delta = 10$. Whereas in the active state, the data can be explained when these parameters are: $p = 1.81 \pm 0.09$, $\gamma_{cut} = 724.1 \pm 78$, $B = 8.24 \pm 0.18$ and $\delta = 30$ [228]. Or in **(author?)** [209] by assuming a log-parabolic electrons injection spectrum, it is shown that in a pre-flare state the SED of CTA 102 can be modeled when the injection index of the electrons is 1.9 and the curvature is 0.08 but in the flaring states the index becomes 1.7 with a curvature of 0.02. The magnetic field is estimated to be around 4 G. Moreover, it should be noted that there are other

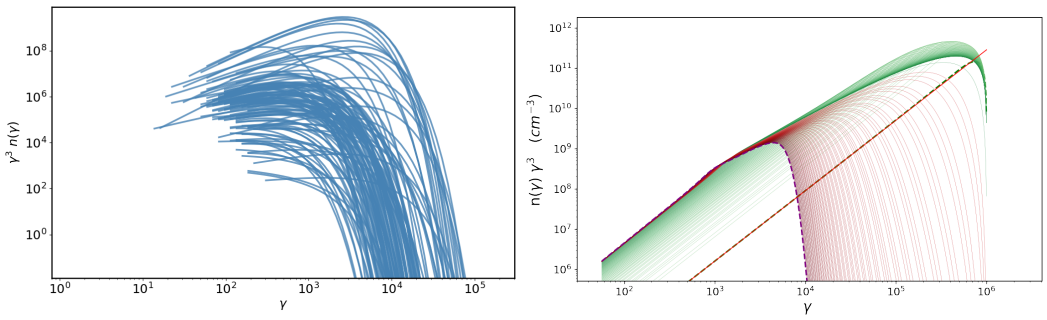

Figure 5.7 *U*pper panel: Electron energy distributions obtained from modeling of SEDs. *L*ower panel: The evolution of the energy spectrum of the electrons injected in the emitting region. Red and green lines show the electron spectrum in different steps and the final spectrum is shown in purple.

models which explain the flaring activity of CTA 102, e.g., those considering the ablation of a gas cloud penetrating the relativistic jet and computing the expected multiwavelength emission from the leptonic and hadronic interactions, see **(author?)** [266] and **(author?)** [267]. Also, the parameters estimated within these models are not significantly different from those presented in Fig. 5.6.

5.5.3 Formation of electron spectrum

The electron spectrum given in Eq. 5.4.1 is an ad-hoc assumption of the distribution of particle injected in the emitting region. This approach, however, ignores the formation of the particle spectrum which is governed by different cooling processes and gains through particle energization mechanisms. From the theoretical point of view, the mechanisms usually considered for the particle acceleration are shock acceleration [e.g., 247, 249, 28] or magnetic reconnection [e.g., 272, 245, 122]. However, all the considered mechanisms to some degree face difficulties to explain all the constraints imposed from the multiwavelength SED modelings. Here we do not attempt to discuss the exact mechanisms that have led to the particle acceleration and injection in the emitting region but instead we investigate whether or not the distribution of the electron spectrum necessary to model the broadband SEDs of CTA 102 can be formed under the physical conditions considered above. A more straightforward approach to gain much information on the particle acceleration and cooling mechanisms would be self-consistent consideration of particle spectrum from acceleration to cooling and comparing its radiative signature with the multiwavelength data. This will be studied in a future paper.

Fig. 5.7 upper panel shows the distributions of the electrons estimated from

the modeling of selected SEDs. This clearly demonstrates different properties of the emitting particles and their evolution in time. In particular, the spectrum of the electrons sometimes is hard ($p < 2.0$) and extends above $\gamma_e > 10^3$ however steep and narrow distributions were also obtained. The power-law index of the electron distribution directly points to the acceleration mechanisms which is unknown while γ_{cut} is due to the interplay of acceleration and cooling processes. In order to calculate the temporal evolution of the electron spectrum, an integro-differential equation that takes into account the injection, cooling (considering all the radiative fields) and escape of the particles should be solved [139]. This is done using JetTimeEvol class of the JetSet. This class numerically solves the kinetic equation and allows to evolve the particle distribution under any cooling process.

In the electron distribution the limiting factors constraining γ_{cut} are the efficiencies of the acceleration process (namely the acceleration/injection time t_{inj}) and the physical size of the accelerator. In other words, the electrons will not be accelerated beyond the energies when the radiative cooling time ($3/4\, c\, \sigma_T\, \frac{U_{tot}}{m_e\, c^2}\, \gamma^2$, where U_{tot} is the sum of magnetic and photon fields) is shorter than the acceleration time. In the one-zone scenario considered here when the emission region is within the BLR, the electrons are cooled through interaction with the magnetic and photon fields, so U_{tot} is synchrotron plus photon energy density, i.e. $U_{tot} = U_B + U_{SSC} + U_{EIC}$. In order to discuss the evolution of the particle distribution in time, we assume that power-law distributed electrons with $p = 1.25$ are injected into the emitting region where the magnetic field is 4.1 G and $\delta = 24.2$. These are chosen to be similar to the parameters estimated from the SED modeling observed during MJD 57715.6-57716.8 (see the SED modeling animation) when the source was in an active emission state. In this case, the synchrotron cooling time for the electrons with energy of $\gamma_e = 10^4$ is $t_{syn,cool} = 4 \times 10^3$ s. The evolution of the energy spectrum of electrons with a luminosity of $L_e = 1.74 \times 10^{45}\, erg\, s^{-1}$ injected into the emitting region with a radius of 2.38×10^{15} cm and without escape is shown in Fig. 5.7 lower panel. The red dashed line corresponds to the initial injection spectrum of the electrons. As the cooling time is inverse proportional to the energy of the electrons, initially only the highest energy electrons are cooled down, forming a turnover (cut-off) in the spectrum. In time, this cut-off energy gradually moves to lower energies and when the injection time is $\simeq 2.6 \times 10^3$ s the cut-off energy will be around 1.5×10^3 close to the value estimated from SED modeling. In time, however, this cut-off energy will move to lower ranges.

When the injected electrons start to cool, their radiative signature changes in time. The SEDs corresponding to electron spectra given in Fig. 5.7 lower panel are shown in Fig. 5.8. The SED of initially injected electrons (the sum

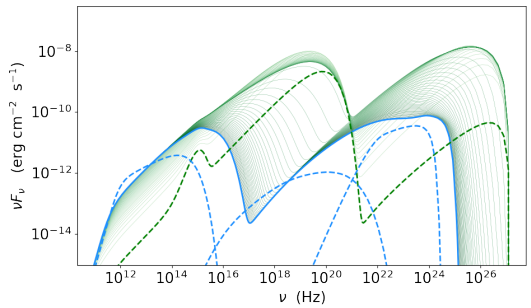

Figure 5.8 The SED evolution in time after the injection of the power-law electrons. The green dashed line shows the initial SED, the green solid lines show the SED in different steps while the final SED is in solid blue. The dashed blue line shows the SED for longer evolution of the system.

of synchrotron, SSC and EIC components) is shown with green dashed line. This spectrum modifies in time when the injected electrons start to cool; the green solid lines show the evolution of the sum of all component in time which shows that the synchrotron and inverse Compton peaks move to lower frequencies. By cooling, the highest energy electrons are transferred to lower energies, so the number of low-energy (i.e., not cooled) electrons changes and their synchrotron emission increases at lower frequencies (e.g., around 10^{12} Hz). Similarly, the SSC component increases in the X-ray band, while EIC dominates in the HE γ-ray band. The blue line in Fig. 5.8 is the final SED produced from the electron population with a spectrum shown by a purple line in Fig. 5.7 lower panel. It matches with that obtained from the modeling of SED observed on MJD 57715.6-57716.8 when using electron distribution given by Eq. 5.4.1. For later periods, the resulting spectrum decreases in intensity and moves to lower frequencies which is shown as a blue dashed line in Fig. 5.8. The resulting spectrum is more characteristic to source emission when it is in quiescent state. Therefore, the electron spectra obtained from the fitting of SEDs can be naturally formed in time.

5.5.4 Jet power

The modeling allows also to estimate the jet power carried by electrons (L_e) and magnetic field (L_B). The distribution of the luminosities computed as $L_e = \pi c R_b^2 \Gamma^2 U_e$ and $L_B = \pi c R_b^2 \Gamma^2 U_B$ is shown in Fig. 5.6 panel e). The mean of L_e and L_B is at $7.81 \times 10^{44}\, erg\, s^{-1}$ and $2.07 \times 10^{45}\, erg\, s^{-1}$, respectively. The distribution of L_B in the range $2.51 \times 10^{43} - 3.48 \times 10^{46}\, erg\, s^{-1}$ is broader than that of L_e between $1.20 \times 10^{44} - 4.21 \times 10^{45}\, erg\, s^{-1}$. The large variations of L_B are mostly due to the high-amplitude changes of the synchrotron component

in the SED of CTA 102. Instead, the high-amplitude increase of the γ-ray flux interpreted as EIC of BLR photons which would affect the electron content in the jet is compensated by increasing δ. The distribution of L_e and L_B in Fig. 5.6 panel e) shows that in some periods $L_e/L_B < 1$, i.e., the jet is magnetically dominated. Such a trend is observed when the synchrotron component (defined by optical/UV data) exceeds the SSC component (defined by X-ray data).

The estimated parameters allow also to asses the total kinetic energy of the jet, namely, assuming a proton-to-electron comoving number density ratio of $N_p/N_e \simeq 0.1$, the total kinetic luminosity defined as $L_{kin} = L_e + L_B + L_{p,cold}$ varies from $4.64 \times 10^{44}\, erg\, s^{-1}$ to $3.71 \times 10^{46}\, erg\, s^{-1}$. Similarly, when $N_p/N_e \simeq 0.01$ and $N_p/N_e \simeq 0.5$, L_{kin} varies from $2.72 \times 10^{44}\, erg\, s^{-1}$ to $3.66 \times 10^{46}\, erg\, s^{-1}$ and from $1.08 \times 10^{45}\, erg\, s^{-1}$ to $3.93 \times 10^{46}\, erg\, s^{-1}$, respectively. The central black hole mass in CTA 102 is estimated to be $8.5 \times 10^8\, M_{BH}$ [268], so the Eddington luminosity is $\simeq 1.1 \times 10^{47}\, erg\, s^{-1}$. Therefore, the kinetic power of the jet estimated in various periods is lower than the Eddington luminosity.

5.6 Conclusion

In this paper we studied the physical processes taking place in the jet of CTA 102 using the results from long-term (fourteen-year-long) multiwavelength observations. We systematically studied the features of the source emission in optical/UV, X-ray and γ-ray bands. Generating the γ-ray light curve with the help of an adaptive binning method, the high-amplitude, multiple flaring and complex variability of the source is investigated.

The broadband emission from CTA 102 was investigated by modeling 117 high-quality SEDs assembled during the considered period. This new comprehensive approach allowed to compare and contrast jet and emitting particle properties in different states of the source emission as well as follow the dynamical changes of the physical processes governing in the jet. The one-zone model, when the low energy emission is due to synchrotron radiation of electrons while HE is due to inverse Compton scattering of both synchrotron and BLR reprocessed photons, adequately explains the source emissions in different periods, except the cases when the γ-ray spectrum is flat, extending to tens of GeV (2 out of 117 periods). It is found that during the flaring periods the spectrum of the emitting electrons has a harder distribution and they are effectively accelerated up to $\gamma_{cut} = (1-4) \times 10^3$ as opposed to the other periods when the electrons have narrow energy distributions. By modeling also the jet kinetic power was assessed showing that it always remained

below the Eddington power.

6 Time-dependent lepto-hadronic modeling of the emission from blazar jets with SOPRANO: the case of TXS 0506+056, 3HSP J095507.9+355101 and 3C 279

6.1 Introduction

The discovery of the first cosmic very high energy (VHE; $>$ 100 GeV) neutrinos in 2013 by the IceCube experiment [128, 1, 2] has opened a new window on VHE sources such as gamma-ray bursts (hereafter GRBs), active galactic nuclei (AGNs) and tidal disruption events (TDEs). The lack of high confidence association between these neutrino events and a particular type of sources significantly complicated the interpretation of their origin. Potentially, they are produced in the sources where ultra-high energy cosmic rays (protons or nucleons with energy exceeding $10^{19}\,eV$) are accelerated. If the origin of these neutrinos remains an open question, the VHE neutrino event IceCube 170922A [131] and its 3.5σ association with the (simultaneously) flaring blazar TXS 0506+056 [133, 189] made clear that high energy (HE; $>$ 100 MeV) protons, neutrons and even possibly nucleons have an important role to play in the dynamics and the radiation of relativistic jets [31, 241, 24].

Blazars are a subclass of AGNs which have their jet aligned with or making a small angle to the observer [257]. Blazars are among the most luminous and energetic sources in the Universe. Based on optical emission lines blazars are sub-grouped as flat spectrum radio quasars (FSRQs) and BL Lacs: the emission lines are strong and quasar-like in FSRQs and weak or absent in BL lacs [257]. The emission from blazar jets, extending from radio to HE and VHE γ-ray bands [188], is characterized by rapid and high amplitude variability, especially in the HE and VHE γ-ray bands [e.g., 18, 13]. This variability suggests that the emission originates from a compact relativistically moving region. Since the γ-ray emission has been detected even from blazars at very high redshift, $z > 3.1$, [e.g., 196, 12, 235], they are unique objects to study

the evolution of jet power, morphology and emission processes in different cosmic epochs.

The broadband spectral energy distribution (SED) of blazars typically exhibit a double hump distribution, the first one peaking at optical/UV or X-ray bands (low energy component) and the other one in the HE or VHE γ-ray bands (HE component). The low energy component is usually explained by synchrotron radiation of relativistic electrons in the jet magnetic field. The origin of the HE component is still under debate, mostly between two main scenarios. In leptonic scenarios, the HE component is due to inverse Compton scattering of low energy seed photons by the relativistic electrons in the blazar jet [104, 162, 38]. The nature of the seed photons depends on the location of the emission region and can be produced either inside or outside the jet [e.g., 244]. In the alternative hadronic scenarios, synchrotron radiation from protons, see *e.g.* **(author?)** [179], and secondaries generated in photo-pion and photo-pair interactions produce the emission from the X-ray to the HE γ-rays bands [160, 161, 180]. In addition, inelastic pp scattering could be involved when the highly energetic protons of the jet interact with a dense proton target, such as clouds in the broad line region or surrounding stars (*e.g.* **(author?)** [82, 29, 20]).

Protons are unavoidably accelerated with the electrons in the jet, but a direct test of their presence and energy cannot be done when only considering electromagnetic data. Except for the cases when the leptonic models face severe problems to account for the observed data, usually both leptonic and hadronic models give equally good representation of the data [e.g., 43]. Indirect test of proton content and a proof of the hadronic origin of the HE and VHE emission can only be given by the observation of VHE neutrinos. Indeed, when protons interact within the jet, the energy they lose is nearly equally divided into electromagnetic and neutrinos components. The produced neutrinos escape the emitting region, carrying information about the protons in the jet and their distribution function.

Multimessenger observations have long been considered the next major breakthrough required for the study of extra-galactic objects. The recent association of IceCube 170922A [131] with TXS 0506+056 provided the first ever possibility to perform a direct multimessenger study of a blazar jet. In addition, an analysis of the IceCube archival data revealed a ~ 13 neutrinos excess within a 110 day period, between September 2014 and March 2015, in the direction of TXS 0506+056. Those two pieces of information together suggests that TXS 0506+056 is indeed the source of those HE neutrinos. Moreover, a second possible association between the muon track event IceCube 200107A [129] and the blazar 3HSP J095507.9+355101 in a flaring state was reported based on the small angular distance (0.62°) between 3HSP J095507.9+355101 and the best-fit position of IceCube 200107A [115, 195]. These two associ-

ations provide unprecedented data allowing to constrain the hadronic processes in relativistic jets.

In order to exploit multiwavelength and multimessenger data-sets, several groups have developed numerical models to estimate leptons, hadron and photon distribution functions, either under the steady state approximation [23, 44, 61, 271], or in a fully time dependent approach [169, 198, 32, 259, 88, 87, 98, 137, 135] and use them to model the broadband SED of blazars and other relativistic transients. Time-dependent modeling of blazars, both leptonic and hadronic is required to understand the time evolution of particle distribution functions, for instance during a flare, see *e.g.* [45].

Time-dependent hadronic modeling is challenging as many different particles are involved. The time evolution of the initial particle populations, as well as that of the secondaries, should be treated with a set of kinetic equations, where the energy is conserved in a self-consistent manner, i.e., the energy lost by a particle is exactly transferred to the energy of other particles. In this paper, we present and use a new fully time-dependent hadronic code, *SOPRANO*[1], standing for Simulator of Processes in Relativistic AstroNomical Objects, which takes into account all relevant processes (leptonic and hadronic) and allows to compute the SED in any given period. The code solves the time dependent isotropic kinetic equations and preserves the total energy of the system as well as the number of particles where needed. The code structure is modular such that processes can be easily added (or removed). *SOPRANO* is implicit so numerical stability is achieved at all time. The code is designed in a such manner that by changing the initial conditions, the lepto-hadronic processes can be investigated in blazar jets, GRBs and other relativistic astrophysical sources where protons are hypothesized to be efficiently accelerated.

The paper is organised as follow. Section 6.2 gives a short description of our kinetic code *SOPRANO*. The kinetic processes included in our numerical code and their cross-sections are detailed in Appendix .1. The numerical discretization in energy and in time is provided in Appendix .2. The analytical estimates of several key model parameters are provided in Section 6.3 whereas the code is applied to model the broadband SEDs of TXS 0506+056, 3HSP J095507.9+355101 and 3C 279 in Section 6.4. The discussion is in Section 6.5, whereas the conclusion is summarized in Section 6.6. Throughout the paper, we use the definition $X = X_x \times 10^x$ where a quantity X is given in cgs units. Moreover, the following cosmological constants are adopted: Ω_M = 0.3, Ω_Λ = 0.7, and H_0 = 70 km s^{-1} Mpc^{-1} [95].

[1] `https://www.amsdc.am/soprano`

6.2 SOPRANO: Simulator Of Processes in Relativistic AstroNomical Objects

Investigation of hadronic processes in galactic sources, such as supernovae remnants and pulsar wind nebulae, as well as extra-galactic objects, such as AGNs and GRBs, has always been an interesting but challenging task. Primarily, it is related with the desire to identify the sources in which cosmic rays and ultra-high energy cosmic rays are accelerated, and to understand the processes responsible for the broadband emission. Such studies are especially timely after the recent IceCube observations of cosmic neutrinos and their association with blazars. Indeed, for the first time, it is possible to constrain the emission process using a different window than that of electromagnetic observations.

In order to interpret the observed data and constrain the models that can explain the observed VHE neutrinos, it is necessary to perform self-consistent simulations of the time evolution of the distribution functions of all interacting particles: protons, neutrons, photons, electrons and positrons, as well as of the secondaries produced in photohadronic interactions, such as pions, muons and neutrinos. This is a challenging task since i) there is a large number of distribution functions (fourteen even though some are trivial), ii) all equations describing the time evolution of particle distribution functions are coupled in a non-trivial and non-linear way by many complex processes that iii) have very different time scales, requiring an implicit time discretization. The high number of distribution functions is necessary to compute the cooling and emission of charged secondaries, pions and muons. This requirement also prevents the use of semi-analytical expressions for the production rate of neutrinos, as given in *e.g.* [143]

For blazars, the magnetic field is expected to be around or smaller than 1G for leptonic models [see *e.g.* 94, 106, 251, 100], while hadronic models usually require the magnetic field to be larger, in the range of few tens to few hundreds Gauss [220, 271], see however **(author?)** [148]. This magnetic field is too low to observe a substantial modification of the neutrino spectrum [49]. However, synchrotron cooling of secondaries produces photons, which form pairs, which in turn will radiate, effectively shifting the spectrum to lower-energies for which strong constraints are given by X-ray observatories. In fact, X-ray observations are believed to be the most constraining ones for hadronic models of blazars. In particular, they strongly challenge any models attempting to explain the neutrino emission of TSX 0506+056 [142, 60, 97, 263].

With the goal to model the multiwavelength and multimessenger SED of relativistic sources (e.g., AGNs and GRBs), we have developed a numerical

code which computes the temporal evolution of particle distribution functions by solving the relevant kinetic equations. This code, *SOPRANO*, relies on two underlying assumptions : *i)* the space is homogeneous and *ii)* particle distribution functions are isotropic. In its current version, *SOPRANO* uses implicit time discretization to evolve the distribution functions of the following particles:

1. photons,
2. electrons and positrons, considered as a single particle type,
3. protons,
4. neutrons,
5. charged (π^+, π^-) and neutral pions (π^0) separately
6. muons
7. neutrinos and anti-neutrinos, all species separately.

The processes considered for the above listed particles are:

1. synchrotron emission and cooling of all charged particles (protons, electrons and positrons, charged pions and muons),
2. inverse Compton scattering of photons by electrons and positrons,
3. Bethe-Heitler photo-pair production and corresponding proton cooling,
4. photo-pion production and corresponding cooling of protons and neutrons,
5. pion and muon decay,
6. neutrino production.

Detailed expression for the interactions kernel and all terms appearing in the kinetic equations for all particle species are given in Appendix .1.

The energy discretization of the fourteen coupled partial differential equations is presented in Appendix .2. It follows from the prescription of finite volume allowing us to conserve particle number to machine accuracy for all processes which conserve particle number. For instance, for pion decay, there are as many muons and neutrinos created as pions that decay. Our numerical implementation ensures that $\partial n_\pi/\partial t = -\partial n_\mu/\partial t = -\partial n_\nu/\partial t$. Energy conservation is also enforced by specific choices for the fluxes for diffusion-like terms or redistribution of particles between adjacent energy cells. The

difficulty in our numerical implementation is in the computation of the 3- to 5-dimensional integrals which approximate the rates on each energy bin. Each of those integrals are computed to a relative accuracy of 10^{-4} with locally adaptive Gauss-Kronrod method. They only need to be computed one time for a given grid and since we do not change the energy grid, they remain the same for all the results presented here.

The largely varying time-scale of the processes and the large energy span of particle and photon grids require using an implicit scheme for the time integration. The code uses a semi-implicit version of the backward Euler method, that is to say that for the evaluation of photo-pion and photo-pair collisional terms, the photon spectrum is assumed to be explicit, while the proton and neutron distribution functions are solved for implicitly. This assumption makes the kinetic equation for all hadrons linear by decoupling their evolution from that of the photons and pairs. In practice, it means that the rate of photo-pair and photo-pion interactions might be underestimated, unless the time step is carefully chosen. We have studied how the time step of the integration method should be chosen to minimise the impact on the solution. Then, the kinetic equations describing the evolution of leptons are solved fully implicitly. The product terms $n_{ph}n_e$ and $n_{ph}n_{ph}$ appearing in Compton scattering and pair production make the problem non-linear and the coupled kinetic equations are solved with the Newton-Raphson method. We have checked that our code is able to properly account for particle cooling as well as to reproduce semi-analytical examples. Those tests are presented in Appendix .3.

6.3 Model Setup: Analytical estimation of model parameters

The broadband spectrum of blazars extends from radio to the HE or VHE γ-ray bands, covering a large 10^{20} Hz frequency range [e.g., 188]. The observed nonthermal emission is produced in the jet and can be explained by different models. The primary dichotomy is the split between leptonic and hadronic models, depending on the type of particles (electron-positron pairs or hadrons) initiating the emission. On the one hand, leptonic models are solely based on the synchrotron emission of relativistic electrons at low energy, while the HE peak is explained either by synchrotron self-Compton, hereinafter SSC, or by external Compton process. These models assume that proton emission has a negligible contribution to the overall SED, and therefore lack the ability to produce a significant amount of VHE neutrinos ($\sim 10^{15}$eV) as detected by the IceCube observatory [128, 1]. In contrast, the so-

called hadronic models assume that protons are also efficiently accelerated in the jet and contribute to the multiwavelength spectrum either by the synchrotron process, or by the radiation from the secondaries produced in photo-pair and photo-pion interactions.

The modeling of the observed SEDs, be it leptonic, hadronic or lepto-hadronic, is a regular approach and is a unique way to investigate the physical processes taking place in jets. The particle spectra are defined by the acceleration and cooling processes within the jet, which may vary from source to source. In this work, we assume that particles are instantaneously accelerated and injected in the emission zone where they radiate their energy. The particle injection spectrum is usually assumed to be a simple power-law, a power-law with an exponential cutoff or a broken power-law. Additionally, the emitting region can contain broad external photon fields which interact with the relativistic particles in the jet. For instance, photons emitted by the dusty torus or reflected by the broad line region play a crucial role in shaping the multiwavelength emission of FSRQs [e.g., order of minutes, 244, 242, 106]. Moreover an arbitrary distributed photon field can be considered as well, which is necessary for complex scenarios such as the multi-zones or the spine-sheath layer models [252]. *SOPRANO* is designed to work with arbitrary injection particle spectrum as well as arbitrary external photon field, and proceed to compute the evolution of particle spectrum. This makes *SOPRANO* an ideal code to investigate the emission processes in different astrophysical environment.

Within the leptonic and hadronic interpretation of the blazar SEDs, it is assumed that the emission is produced in a spherical blob of comoving size R' that moves towards the observer with a bulk Lorentz factor $\Gamma \sim \delta$, where δ is the Doppler factor. Accelerated leptons and hadrons are injected in the emitting region, which is uniformly filled with a magnetic field of strength B. The magnetic jet luminosity is

$$L_B = \pi c R'^2 \delta^2 \frac{B^2}{8\pi}, \tag{6.3.1}$$

where c is the speed of light. We assume that protons are injected in the comoving frame with a power-law spectrum:

$$Q'_p(\gamma_p) = Q'_{0,p} \gamma_p^{-\alpha_p} \qquad \gamma_p < \gamma_{p,max}. \tag{6.3.2}$$

The normalization factor $Q'_{0,p}$ is linked to the proton luminosity as

$$L_p = \pi R'^2 \delta^2 m_p c^3 \int \gamma_p Q'_p(\gamma_p) \gamma_p, \tag{6.3.3}$$

where m_p is the proton mass. We assume that the injection electron spectrum is given by a power-law with an exponential cut-off :

$$Q'_e(\gamma_e) = \begin{cases} Q'_0 \gamma_e^{-\alpha_e} \exp\left(-\frac{\gamma_e}{\gamma_{e,cut}}\right) & \gamma_{e,min} \leq \gamma_e \leq \gamma_{e,max}, \\ 0 & otherwise, \end{cases} \tag{6.3.4}$$

where $\gamma_{e,min}$ is the minimum injection Lorentz factor. The electron luminosity is then given by

$$L_e = \pi R'^2 \delta^2 m_e c^3 \int \gamma_e \, Q'_e(\gamma_e) \, d\gamma_e, \tag{6.3.5}$$

where m_e is the electron mass. In general $\gamma_{e,cut}$ should be defined by the equality of the acceleration and cooling time-scales. However, in order to have a broad inference of the physical processes in the jet, $\gamma_{e,cut}$ is considered a free parameter which will be constrained by the data. The distribution functions of protons and electrons evolve via cooling and via interaction with photons, producing different signatures in the broadband spectrum. Our aim is to identify those signatures and use them to constrain the emission mechanism within the framework of different scenarios.

In one dynamical time-scale, $t'_d \sim R'/c$, electrons and positrons cool to Lorentz factor

$$\gamma_{e,c} = \frac{6\pi m_e c^2}{B^2 R' \sigma_T} \sim 2.3 \times 10^3 B^{-2} R'^{-1}_{16}, \tag{6.3.6}$$

where σ_T is the Thompson cross-section. The associated observed synchrotron characteristic frequency is

$$\nu_{e,c} = \frac{48\pi\delta c^3 m_e q}{B^3 R'^2 \sigma_T^2} \sim 4.0 \times 10^{14} \delta_1 B^{-3} R'^{-2}_{16} \quad Hz, \tag{6.3.7}$$

where q is the elementary charge. The frequency $\nu_{e,c}$ is usually associated to the peak frequency of the low energy component in the SED. The injection frequency corresponding to electrons with Lorentz factor $\gamma_{e,min}$ is given by

$$\nu_{e,m} = \frac{4}{3\pi} \frac{qB\delta\gamma^2_{e,min}}{m_e c} \sim 7.5 \times 10^{15} B_0 \delta_1 \gamma^2_{e,min,4} \quad Hz. \tag{6.3.8}$$

Another turnover in the synchrotron spectrum is at the self-absorption frequency ν_{SSA}. Synchrotron self-absorption dominates at low frequency, specifically in the radio band, and introduces a cut-off like modification around the

frequency ν_{SSA} [182]:

$$\nu'_{SSA} \approx \frac{1}{3}\left(\frac{eB'}{m_e^3 c}\right)^{1/7} \frac{L'^{2/7}_{syn}}{R'^{4/7}} \tag{6.3.9}$$

where L'_{syn} is the synchrotron energy distribution peak luminosity.

The interaction between the photons of the low energy hump and the electrons and positrons producing this hump via synchrotron radiation can produce the second peak in the broadband spectrum (SSC). The peak frequency of this component depends on the the cooling regime of the electrons and on the peak frequency of the synchrotron component. It is given by

$$\begin{aligned} \nu_{IC} &= \begin{cases} 2\gamma^2_{e,min}\nu_{e,m} & \nu_{e,c} < \nu_{e,m} \\ 2\gamma^2_{e,c}\nu_{e,c} & \nu_{e,m} < \nu_{e,c} \end{cases} \\ &\sim \begin{cases} 1.5 \times 10^{24} B\delta_1 \gamma^4_{e,min,4}\ Hz, & \nu_{e,c} < \nu_{e,m} \\ 4.3 \times 10^{21} \delta_1 B^{-7} R'^4_{16}\ Hz, & \nu_{e,m} < \nu_{e,c} \end{cases} \end{aligned} \tag{6.3.10}$$

for fast and slow cooling respectively. Similarly, the ratio of luminosities of the synchrotron L_s and the inverse self-Compton L_{IC} components can be approximated by

$$\frac{L_{SSC}}{L_{syn}} \sim \begin{cases} \frac{2}{3}\tau\gamma^2_{e,c}\left(\frac{\gamma_{e,c}}{\gamma_{e,min}}\right)^{1-\alpha_e} & \nu_{e,c} > \nu_{e,m} \\ \frac{2}{3}\tau\gamma_{e,c}\gamma_{e,min} & \nu_{e,c} < \nu_{e,m} \end{cases} \tag{6.3.11}$$

where $\tau = \sigma_T R^{'} n'_e$ is the opacity of the source for the Compton process and n'_e is the comoving electron density. It is computed assuming that the Thomson regime is achieved for the peak, which might not always be the case.

For hadronic models (hereinafter HM), and more specifically for proton synchrotron models, the HE component of the SED is dominated by the proton synchrotron radiation rather than by the inverse Compton scattering. This model requires that a substantial number of protons are accelerated in the jet to very large Lorentz factor[2]. In this case, the required magnetic field is larger than in leptonic models, with B in the order of hundred Gauss. The

[2]In principle, the maximum proton energy γ_p could be estimated by assuming an acceleration time of the form $t_{acc} \sim \gamma_p m_p c^2/(\eta c q B)$, where $\eta \sim 1$ is the acceleration efficiency. This time is then compared to the different cooling time scale to obtain an estimate of $\gamma_{p,max}$.

peak frequency of proton synchrotron emission is at:

$$\nu_s^p = 4.1 \times 10^{24} B_2 \delta_1 \gamma_{p,max,9}^2 \, Hz, \tag{6.3.12}$$

where we did not consider cooling. In general, hadronic models necessitate much more energetic jets since they require a large magnetic field, as well as a significant amount of energy in relativistic protons. We further discuss these constraints in Section 6.5. In addition to synchrotron loses, relativistic protons of the jet also lose energy by photo-pion and Bethe-Heithler photo-pair interactions with the photons.

For hybrid models, a subclass of hadronic models, the low and high energy peaks are explained by leptonic processes and proton synchrotron emission is required to be subdominant. The requirement on proton content is obtained by maximizing the neutrino flux at PeV energies, which is constrained by the radiation from the secondaries produced by the Bethe-Heithler and photo-pion processes. Indeed, it has long been speculated that efficient neutrino production is associated with efficient Bethe-Heithler process, creating a population of HE pairs, which can over-shine the tight constraints in the X-ray band [e.g., order of minutes, 200].

In order to produce PeV neutrinos, protons should have a comoving energy larger than $E'_p > 10^{15}/\delta_1$ eV. Assuming for simplicity that the Bethe-Heithler process creates pairs with Lorentz factor $\gamma_\pm = \gamma_p/5$[3], the pairs created by the protons producing PeV neutrinos are in the fast cooling regime, see Equation (6.3.6). Therefore, the energy produced in the Bethe-Heitler process is efficiently radiated by synchrotron radiation. For an electron or positron to radiate in X-ray, its Lorentz factor should be

$$\gamma_\pm^{1keV} = \sqrt{\frac{3\pi\nu c m_e}{4B\delta q_e}} \sim 5.7 \times 10^3 \nu_{1keV}^{\frac{1}{2}} B_2^{-\frac{1}{2}} \delta_1^{-\frac{1}{2}}. \tag{6.3.13}$$

which is smaller than the Lorentz factor of the pairs from the protons producing PeV neutrinos. Therefore, synchrotron radiation from the Bethe-Heitler pairs contributes to the X-ray band. We now estimates the Bethe-Heitler pair spectrum. The Bethe-Heitler pair yield is

$$\frac{\partial n_\pm}{\partial t}(\gamma_\pm) = 2c \int_0^\infty dx n_{ph}(x) \int_1^\infty d\gamma_p N_p \frac{d\sigma_\pm}{d\gamma_\pm}. \tag{6.3.14}$$

where $x = h\nu/(m_e c^2)$ is the photon energy normalised to the electron rest

[3]This assumptions requires the inelasticity to be $\kappa_e \sim 10^{-4}$. [170] computed the inelasticity and finds that it steadily decreases from 10^{-3} for increasing $\gamma_p x$, where $x = h\nu/(m_e c^2)$, with h the Planck constant.

mass. Under the head-on approximation and if the photon energy is small enough to neglect proton recoil, the differential pair rate can be written as [75]

$$\frac{d\sigma_{\pm}}{d\gamma_{\pm}} \sim \frac{\alpha\sigma_T}{2x\gamma_{\pm}^2} \qquad\qquad \frac{1}{2x} \leq \gamma_{\pm} \leq \frac{\gamma_p}{2}, \tag{6.3.15}$$

where α is the fine structure constant. We further assume that the photon spectrum is well approximated by $n_\gamma(\epsilon) = n_{\gamma,0}\epsilon^{-\alpha_{ph}}$, which is realistic since the synchrotron emission from the electrons forming the low energy bump can be well approximated by a succession of power-laws with indexes $\alpha_{ph} = 2/3,\ 3/2,\ (\alpha_e+1)/2$, where we neglected self-absorption and specialised to the fast cooling scenario, usually appropriate for HM. We also further assume that protons do not cool substantially such that their distribution function is $N_p = N_{p,0}\gamma_p^{-\alpha_p}$ for $\gamma_p < \gamma_{p,max}$, then the integral of Equation 6.3.14 yields

$$\frac{\partial n_{\pm}}{\partial t}(\gamma_{\pm}) \simeq \alpha c\sigma_T 2^{\alpha_{ph}+2-\alpha_p}\frac{n_0}{\alpha_{ph}}\frac{N_0}{\alpha_p-1}\gamma_{\pm}^{\alpha_{ph}-\alpha_p-1} \tag{6.3.16}$$

Therefore, the pair injection spectrum will be formed of three smoothly connected power-laws with indexes $\alpha_{ph}-\alpha_p-1$, where $\alpha_{ph} = 2/3,\ 3/2,\ (\alpha_e+1)/2$. Since these pairs are in the fast cooling regime, their distribution function is well approximated by smoothly connected power-laws with indexes $q = \alpha_{ph}-\alpha_p-2$. From [224], the resulting photon flux is well approximated by three smoothly connected power-laws $F_\nu \propto \nu^{-q/2}$.

In proton synchrotron models, when the proton injection index is $\alpha_p \sim 2$, the specific spectral power νF_ν of the synchrotron emission from the Bethe-Heithler pairs is nearly flat with indexes $-2/3, -1/4, -(\alpha_e-3)/4$. The spectrum extends up to energies

$$\nu_{\pm,max} \sim \left(\frac{\gamma_{\pm}}{\gamma_{p,max}}\right)^2\frac{m_p}{m_e}\nu_s^p \sim 3.0\times10^{26}B_2\delta_1\gamma_{p,9}^2\ Hz. \tag{6.3.17}$$

where we used Equation (6.3.12) for the synchrotron frequency associated to the highest energy protons with Lorentz factor $\gamma_{p,max}$. Yet, because the pair synchrotron emission peaks at such a large frequency, its contribution to the X-ray is likely to be small and not constraining for proton synchrotron models. However, this is not the case for hybrid models when the peak frequency for synchrotron radiation from the pairs will be

$$\nu_{\pm,max} \sim 3.0\times10^{19}B_{-1}\delta_1\gamma_{p,7}^2\ Hz, \tag{6.3.18}$$

around the X-ray frequency, in agreements with the estimates from [200]. It is clear that increasing the neutrino flux requires to increase the density of protons or of photons. This leads to an increase of the production rate of pairs, and as a result, a larger synchrotron flux in the X-ray band, which becomes critical for constraining this type of models [200, 97, 218].

6.4 Modeling of Blazar SEDs

The code *SOPRANO*, described in Section 6.2, is used to model the multiwavelength SEDs of TXS 0506+056, 3HSP J095507.9+355101 and 3C 279. Two of these sources, TXS 0506+056 and 3HSP J095507.9+355101, coincide in space and time with the IceCube 170922A and IceCube 200107A events, respectively. The other source, 3C 279, shows a prominent flare in the γ-ray band.

It is assumed that protons and electrons are injected in the emitting region with energy distributions given by Equations (6.3.2) and (6.3.4), respectively. We also assume that the injection power-law indexes are such that $\alpha_e = \alpha_p$. Once injected in the emitting region, particles interact with the magnetic field and with the photons, producing secondary particles, which themselves interact, radiate and decay, shaping the broadband SED. The low energy component is interpreted as the synchrotron emission of the primary electrons while the HE component is formed by joint contributions of inverse Compton scattering of primary electrons and of synchrotron radiation from the protons, as well as secondary particles from photo-hadronic interactions. The system of kinetic equations is evolved for one dynamical time scale $t'_{dyn} \sim R'/c$ considering the magnetic field to be constant, and taking into account all relevant processes for particles interactions.

6.4.1 Modeling of TXS 0506+056 SED

After the observations of neutrinos from the direction of TXS 0506+056 [131, 133], hadronic processes in its jet have been extensively studied. The multiwavelength emission and neutrino production were discussed for the $p\gamma$ [19, 141, 181, 59, 96, 221, 202] and pp [225, 154] interaction scenarios. The current modeling consensus is that the applied one zone models predict, albeit low, but still consistent results with the observation of one neutrino event in 2017. However, the neutrino flare in 20142015 cannot be explained when both the neutrinos and the electromagnetic emission are produced from the same region.

Panels a) and b) of Figure 6.1 show the SED of TXS 0506+056 when the neutrino event was observed. The multiwavelength data from **(author?)** [131] are modeled within a HM scenario in panel a). The corresponding model

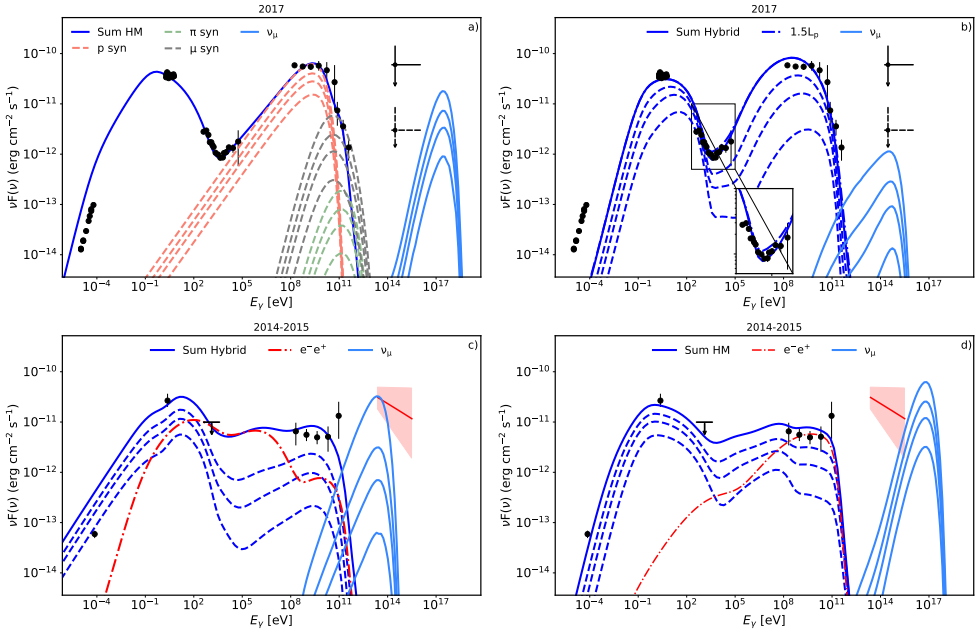

Figure 6.1 The multiwavelength SED of TXS 0506+056 during the neutrino emission in 2017 (upper panels) and during the neutrino flare in 2014-2015 (lower panels) modeled within the hadronic and lepto-hadronic hybrid scenarios. The solid blue line in all plots represents the sum of all components which has been corrected for EBL absorption considering the model of **(author?)** [89].

Table 6.1 Parameter sets used for modeling the SEDs of TXS 0506+056, observed in 2017 and during the neutrino flare in 2014-2015. The electon, proton and magnetic luminosities are also given.

	TXS 0506+056			
	2017		2014-2015	
	Hadronic	Lepto-hadronic	Hadronic	Lepto-hadronic
δ	20	20	15	10
$R/10^{15}\,cm$	2.5	10	1	100
$B[G]$	80	0.57	35	0.65
$\gamma_{e,min}$	100	1000	2×10^2	9×10^3
$\gamma_{e,cut}$	2.4×10^3	4.5×10^4	10^4	$=\gamma_{e,max}$
$\gamma_{e,max}$	3×10^4	6×10^4	8×10^4	8×10^4
α_e	2.1	2.0	2.0	2.0
$\alpha_p = \alpha_e$	2.1	2.0	2.0	2.0
$\gamma_{p,min}$	1	1	1	1
$\gamma_{p,max}$	10^9	10^6	2×10^8	1.2×10^5
$L_e\,(erg\,s^{-1})$	2.2×10^{44}	9.3×10^{44}	2.8×10^{44}	5.3×10^{44}
$L_B\,(erg\,s^{-1})$	6.0×10^{46}	4.9×10^{43}	10^{45}	1.6×10^{45}
$L_p\,(erg\,s^{-1})$	2.1×10^{47}	2.6×10^{50}	3.4×10^{47}	4.9×10^{52}

parameters are given in Table 6.1. The sum of all components, represented by the blue line in the top left panel of Figure 6.1, satisfactorily explains the observed data. The model over-predicts the radio data, but when taking the synchrotron self-absorption into account via Equation (6.3.9), which is significant below the energies $\approx 10^{-3}$ eV ($\approx 3 \times 10^{11}$ Hz) the model is in agreement with the data. Under the guise of our modeling, the data up to the soft X-ray band are produced by synchrotron emission of electrons, which are in the fast-cooling regime. Indeed the magnetic field is required to be high, $B = 80$G, to explain the HE peak with proton synchrotron emission, shown by the red dashed line in panel a) of Figure 6.1, with a contribution of muon synchrotron emission at HEs, represented by the gray dashed line. The contribution of pion synchrotron emission is negligible and does not contribute substantially to the flux observed by the MAGIC telescopes [19]. The emission in the transition region between the low and high energy components, in the X-ray band, is dominated by proton synchrotron emission, with little contribution from the cascade emission of the secondary pairs produced from the absorption of VHE γ-rays and by the emission of pairs from the Bethe-Heithler process.

The modeling parameters given in the first column of Table 6.1 are in the range of similar estimations for blazars in general and for TXS 0506+056 in

particular. A Doppler factor $\delta = 20$ and a radius $R' = 2.5 \times 10^{15}$ cm were used in our modeling. This is in agreement with the limits on the variability time of 10^5s presented in [142] and in [190]. We note that when $\delta = 10$ or 15, the data can also be well reproduced by the model. The radius, which defines the density of interacting particles and photons, is a crucial quantity in defining the type of model. The initial injection power-law index of the emitting electrons is $\alpha_e = 2.1$, a value that can be formed by shock accelerations, *e.g.* [35]. Due to the high magnetic field, $B = 80$ G, electrons are in the fast cooling regime and their distribution function is a power-law with index $\alpha_e + 1$. The initial electron distribution extends up to $\gamma_{cut} = 2.4 \times 10^3$ ($\sim$ 1 GeV) which is representative of the acceleration and cooling time scales. Instead, protons cool less efficiently and they could be accelerated up to much higher energies, *i.e.* $\gamma_{max} = 10^9$ (9.4×10^{17} eV), see the discussion in Section 6.5.

Previous modelings of TXS 0506+056 have shown that hybrid models can be good alternatives to proton synchrotron or leptonic models [59, 97]. They are found to be favourable from the point of view of neutrino observations. The SED of TXS 0506+056, now modeled within the framework of a hybrid lepto-hadronic scenario, is shown in panel b) of Figure 6.1. The model parameters are given in the second column of Table 6.1. The blue dashed lines represent the time evolution of the spectrum in selected numerical steps, which builds and forms the overall SED, represented by the solid blue line after one dynamical time scale.

The synchrotron component peaking between 1-10 eV is up-scattered by the relativistic electrons to produce the HE and VHE component. The magnetic field in the emitting region is $B = 0.57$G significantly lower than for the proton synchrotron modeling. Therefore, electrons with Lorentz factor $\gamma_{e,min} = 10^3$ are not substantially cooled in one dynamical time scale. The electron distribution function is a broken power-law with an exponential cut-off, $\gamma_e^{-\alpha_e}$ and $\gamma_e^{-\alpha_e+1} \exp[-\gamma_e/\gamma_{e,cut}]$, with a break at Lorentz factor $\gamma_{e,c} = 7 \times 10^3$, where we used Equation (6.3.6). In order for the neutrino spectrum to peak around the energy of the observed neutrino (290 TeV), the comoving proton distribution function should extend at least up to $\gamma_{p,max} = 10^6 \delta_1^{-1}$. This Lorentz factor is lower than what is usually used in pure HM models. For this hybrid model, protons do not directly contribute to the observed SED. Their radiative signature is due to the emission of the secondaries of photo-pion and photo-pair interactions. Their contribution dominate in the X-ray band, which constrains the proton luminosity and as a consequence the neutrino luminosity. For example, if one increases by 1.5 times theproton luminosity, the model would overshoot the X-ray data, as shown by the dotted-dashed blue line in panel b) of Figure 6.1.

We now present our results of the SED modeling obtained during the his-

torical neutrino flare of TXS 0506+056. Unfortunately, when 13 ± 5 neutrinos were observed between October 2014 and March 2015 [133], the multiwavelength coverage is scarce. Yet, the flux upper limit of $F < 9.12 \times 10^{-12}\, erg\, cm^{-2}\, s^{-1}$ derived from Swift BAT observations [218] introduces substantial difficulties for a one-zone modeling. Indeed, the predicted number of neutrino events cannot be matched to the IceCube observations. **(author?)** [218] and **(author?)** [222] have shown that only few neutrino events could be detected under different optimistic considerations for the emitting region and for the target photon field (internal or external to the jet). Matching together the observed multiwavelength data and the neutrino data seems to require two zone models with more free parameters [218, 222].

To accommodate the X-ray limit and try to account for the neutrino flux during this flare, two different assumptions on the proton distribution function are made. On the one hand, radiation from the secondaries can be constrained to be dominant in the MeV band, in which there are no observational constraint. On the other hand, radiation from the secondaries could be dominant in the GeV band and produce the second HE hump. The SEDs of these two models are respectively shown in panels c) and d) of Figure 6.1, with data from **(author?)** [222]. Those two models lead to two very different sets of parameters for the emitting region, see column 3 and 4 of Table 6.1. The first model requires a large radius $R' = 10^{17} cm$ and a slowly moving jet with Doppler factor $\delta = 10$, while the second model necessitates those parameters to be $R' = 10^{15} cm$ and $\delta = 15$. The required magnetic field also significantly differs between these two models with $B = 35$G for the first model, to be compared to $B = 0.65$G for the second one. The first model tends to reproduce the neutrino flux, albeit produces the peak at lower energies. The second model puts the neutrino peak at larger energy, but is not able to reproduce the observed neutrino number. In both interpretations, it is clear that the upper limit in the X-ray band imposes strong constraints on the photon spectrum, which in turn limits the proton content in the jet. Considering larger proton luminosity would lead to over-estimate both the observed γ-ray flux and the X-ray upper limit.

6.4.2 Modeling of 3HSP J095507.9+355101 SED

The blazar 3HSP J095507.9+355101 is another interesting source to study within a hadronic scenario. Indeed, it is a nearby blazar at redshift $z = 0.55703$ [193], and it lies in the error region of the neutrino event IC 200107A [113]. The multiwavelength campaign, which started after the neutrino detection in January 2020, showed that 3HSP J095507.9+355101 was in a bright X-ray emission state with a synchrotron peak frequency of 5×10^{17} Hz [115]. This is a typical

Table 6.2 Parameters used to model the multiwavelength SEDs of 3HSP J095507.9+355101 and 3C 279. The electron, proton and magnetic luminosity is also displayed.

	3HSP J095507.9+355101				3C 279
	January 8th		January 10th		
	Hadronic	Lepto-hadronic	Hadronic	Lepto-hadronic	Hadronic
δ	15	30	15	30	55
$R/10^{15}\,cm$	0.3	10	0.3	10	0.32
$B[G]$	45	0.11	45	0.08	70
$\gamma_{e,min}$	10^4	100	5×10^3	100	1
$\gamma_{e,cut}$	6×10^5	2×10^6	2×10^5	7×10^5	2.4×10^2
$\gamma_{e,max}$	9×10^5	6×10^6	5×10^5	6×10^6	4×10^2
α_e	1.9	2.0	1.9	2	1.8
$\alpha_p = \alpha_e$	1.9	2.0	1.9	2	1.8
$\gamma_{p,min}$	1	1	1	1	1
$\gamma_{p,max}$	9×10^8	10^6	9×10^8	10^6	2.1×10^8
$L_e\,(erg\,s^{-1})$	1.2×10^{44}	1.6×10^{44}	7.3×10^{43}	2.1×10^{44}	1.9×10^{44}
$L_B\,(erg\,s^{-1})$	1.5×10^{44}	4.1×10^{42}	1.5×10^{44}	2.2×10^{42}	5.7×10^{45}
$L_p\,(erg\,s^{-1})$	3.2×10^{46}	8.0×10^{50}	3.2×10^{46}	1.8×10^{51}	1.3×10^{49}

value for extreme peak blazars [74]. It is the first time that the jet of an extreme blazar is associated with a neutrino event, straightening the assumption that the jets of this blazar type are potential sites for cosmic rays and even ultra-high energy cosmic ray acceleration [191]. The multimessenger emission from 3HSP J095507.9+355101 was interpreted within various leptonic and lepto-hadronic models by [203] and [195]. **(author?)** [203] showed that a change of the X-ray flux above 1 keV does not significantly affect the neutrino flux. The expected number of neutrinos during the 44-day period is 6×10^{-4} with a low probability of ~ 0.06 % to detect one or more neutrinos. Alternatively, **(author?)** [195] investigated the effects of the external photon fields to enhance the neutrino production.

The SED of 3HSP J095507.9+355101 is shown in Figure 6.2, where the multiwavelength data are from **(author?)** [115]. Optical, UV and X-ray data were acquired on the 8^{th}, 10^{th} and 11^{th} of January. However, since the data taken on the 8^{th} and 11^{th} of January seem to have the same flux and spectral shape [203], we only model the data from the 8^{th}. The lack of available multiwavelength data does not allow to constrain the low and high energy peaks, which hardens the estimation of the model free parameters. A hint of a $20 - 30$ minutes variability has been found in the NICER and NuSTAR data, but only at the $\sim 3.5\,\sigma$ level [195]. Therefore, the compactness of the emitting region

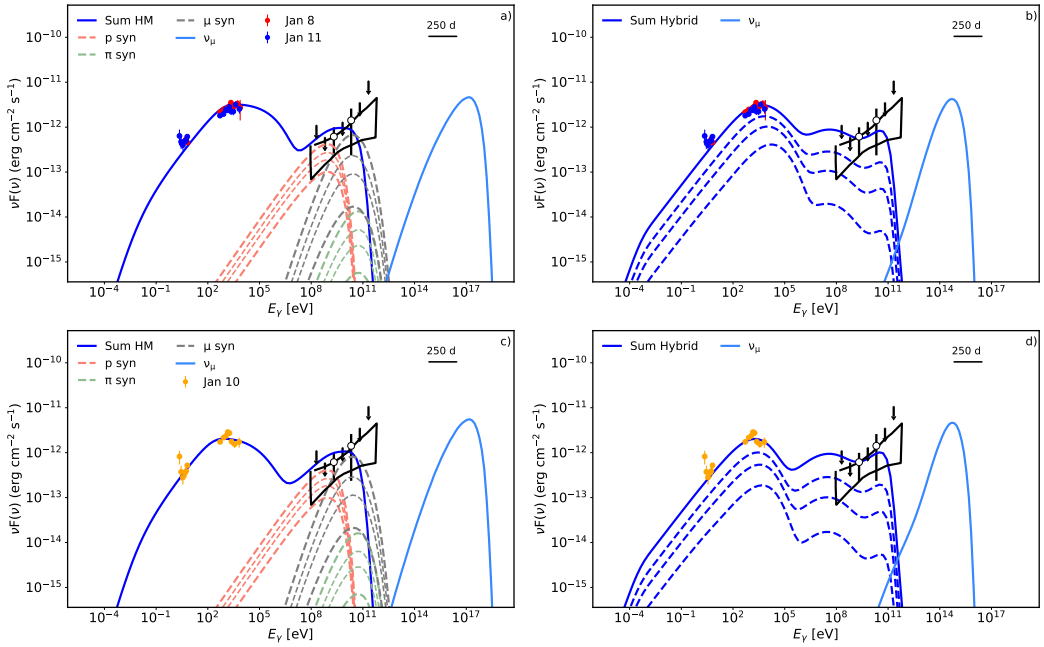

Figure 6.2 The multiwavelength SEDs of 3HSP J095507.9+355101 on the the 8^{th} and the 11^{th} of January (panels a) and b) on the top raw) and on the 10^{th} of January (panels c) and d) on the bottom raw). The data are taken from **(author?)** [115, 203]. The observed spectrum including all processes is shown by the solid blue line. All models (solid blue lines) have been corrected for EBL absorption considering the model of **(author?)** [89].

cannot be constrained. **(author?)** [203] investigated the blob radiusDoppler factor relation for a wide range of photo-pion production efficiency and for several set of parameters. In order to keep the generality, in the current study, the SED of 3HSP J095507.9+355101 is modeled for two different parameter configurations. For the HM, we consider $R' = 3 \times 10^{14}$ cm and $\delta = 15$, while for the lepto-hadronic model we assume $R' \simeq 10^{16}$ cm and $\delta = 30$.

In our hadronic modeling, the HE component is mainly due to the synchrotron emission of protons, shown by the red dashed line in panel a) of Figure 6.2. Protons are assumed to have an energy distribution $N_p \propto \gamma_p^{-1.9}$ and to be accelerated up to $\gamma_{p,max} = 9 \times 10^8$, corresponding to 8.4×10^{17} eV. At VHEs, the largest contribution is due to muon synchrotron radiation, represented by the gray dashed line in panel a) of Figure 6.2. The high synchrotron peak at $\sim 10^4$ eV can be reproduced when $\gamma_{e,cut} = 6 \times 10^5$ and $B = 45$ G. The minimal energy of the accelerated electrons is relatively high, $\gamma_{e,min} = 10^4$, but still in the range of parameters usually estimated for ultra-high-frequency-peaked blazars, see *e.g.* **(author?)** [62]. For the hybrid lepto-hadronic modeling, shown in panel b) of Figure 6.2, the emitting electrons should be accelerated up to $\gamma_{e,cut} = 2 \times 10^6$ so the SSC component extends to the GeV band to explain the observed data. In this model, a lower magnetic field of 0.11 G is required because of the larger radius of the emitting region ($R' = 10^{16}$ cm). The emission of the secondary pairs from protons accelerated up to $\gamma_{p,max} = 10^6$ dominates in the sub-MeV band.

The hadronic and hybrid modeling of the SED observed on the 10^{th} of January 2020, is displayed in panel c) and d) of Figure 6.2, respectively. Since the peak of the low energy component, defined by the X-ray data, is at lower energies than for observations performed on the 8^{th} of January, the modeling requires a three times smaller cutoff energy, *i.e.* $\gamma_{e,cut} = 2 \times 10^5$ and $\gamma_{e,cut} = 7 \times 10^5$ for the hadronic and lepto-hadronic modelings, respectively. The other parameters are given in Table 6.2 and are similar with these obtained from modeling the data observed on the 8^{th} of January.

6.4.3 Modeling of 3C 279 SED during the 2015 flare

The emission from the powerful FSRQs 3C 279 at redshift $z = 0.536$ has been detected in all possible spectral bands. Its broadband emission is characterized by high amplitude variability almost in all energy bands [e.g., order of minutes, 17] and in particular in the HE γ-ray band, which present the fastest variability. On the 16^{th} of June 2015, Fermi LAT observations showed that 3C 279 was in an exceptionally bright state. The flux increased up to 3.6×10^{-5} *photon* $cm^{-2}\, s^{-1}$ with a flux doubling time on the order of 5 minutes [13]. IceCube performed a time-dependent neutrino signal search corre-

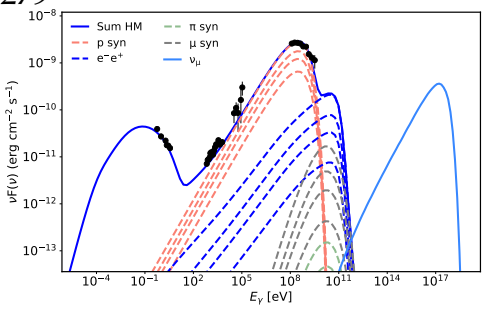

Figure 6.3 The multiwavelength SED of 3C 279 during the exceptional flaring activity in 2015. The contribution of different particle emission is shown by dashed lines whereas the thick solid line represents the observed spectrum, corrected for EBL absorption considering the model of **(author?)** [89].

lated with this γ-ray flare but no evidence for a signal was found [4]. We use *SOPRANO* to model the SED of 3C 279 during its flare to infer the neutrino flux. We consider a HM and explain the second peak with proton synchrotron emission. The parameters of our modeling are given in Table 6.2.

Figure 6.3 shows the multiwavelength SED of 3C 279 taken from **(author?)** [41], alongside with the results of our modeling. During the brightening, the X-ray emission of the source appears with a hard photon index < 1.50, smoothly connecting with the INTEGRAL data, described by a power-law with index 1.08 [41]. In the HE γ-ray band, the spectrum presents a power-law with photon index 2.21 with a turn over [194]. We make the hypothesis that the HE component is produced from a single mechanism. In our modeling it is interpreted as proton synchrotron emission, represented by the red dashed lines in Figure 6.3. This interpretation requires that protons are accelerated up to $\gamma_{p,max} = 2.1 \times 10^8$, see Table 6.2. The compactness of the emitting region implies a high efficiency for photo-pion and photo-pair interactions, which inject energetic secondary pairs. The contribution of these pairs dominates above $\sim$ 10 GeV and peak at $\sim$ 100 GeV, as can be seen by the blue dashed line in Figure 6.3. The synchrotron radiation of the primary electrons peaks at $\sim$ 0.1 eV and its HE tail accounts for the observed optical/UV data. These data constrain the cut-off energy to be relatively low, $\gamma_{e,cut} = 2.4 \times 10^2$, otherwise, for $B = 70$ G and $\delta = 55$, the synchrotron radiation would overshoot the observed flux in optical and UV bands. A similar hadronic modeling for this flare is presented in [41] and in [201].

6.5 Discussion

The primary class of objects to be studied in the multimessenger context are blazars which are associated with neutrino events observed by IceCube. Even if the associations are not at the 5σ significance level, the observations by IceCube put some constraints on the physical processes taking place in relativistic jets. Using the hadronic time-dependent model constrained by their neutrino emission, the broadband SEDs of two blazars, namely TXS 0506+056 and 3HSP J095507.9+355101, respectively associated to the neutrino events IC 170922A and IC 200107A, are studied. We also analysed the SED of 3C 279 during its 2015 γ-ray flaring period. For each source, we present several modelings assuming that different components dominate in the HE γ-ray band. For the sources studied in this paper, we find that the proton synchrotron model, the secondaries emission model and the hybrid lepto-hadronic model can explain the observed SEDs under sensible assumptions for the particle energy distributions.

Some of our modelings require a compact emitting region, with $R' \lesssim 10^{15}$cm. In principle, the maximum energy of the particles, and specifically of the protons, is limited by requiring their Larmor radius, given by $r_{p,L} = \gamma_p m_p c^2/(qB)$, to be smaller than the emission region. All our models are consistent with this requirement, and therefore protons can be accelerated to the maximum energy as given in Tables 6.1 and 6.2. The strongest constraints are obtained for the hadronic model of 3HSP J095507.9+355101 for which the protons with $\gamma_{p,max} = 9 \times 10^8$ have Larmor radius $r_L = 6.3 \times 10^{13}$cm, while the emitting region has size $R = 3 \times 10^{14}$cm. The maximum particle energy can also be limited by synchrotron cooling. Specifically, [83] balanced acceleration timescales for shock and gyroresonant acceleration with cooling time scale via the synchrotron process to find that the electrons can be accelerated up to

$$\gamma_e^{max} \sim 4 \times 10^7 B^{-\frac{1}{2}}. \tag{6.5.1}$$

For all our modelings, we have $\gamma_{e,max} < \gamma_e^{max}$. Only the lepto-hadronic modeling of 3HSP J095507.9+355101 is marginally consistent with this limit. Such constraints are highly dependent on the acceleration mechanism and vary for alternative scenarios, such as particle acceleration by magnetic reconnection or in shear layers.

The power-law index of the accelerated particles, assumed to be equal for protons and electrons, is found to be in the range $\alpha = 1.8 - 2.1$, a value in agreement with prediction of shock acceleration theories [e.g., order of minutes, 145, 249]. This index is defined by the acceleration processes, and we note that protons and electrons could have different indexes. In fact, if particles are accelerated by shocks, the properties of their acceleration depend

on the direction of the shock with the magnetic field: quasi-parallel shocks accelerate both ions and electrons, while quasi-perpendicular shocks only accelerate electrons [51, 52, 53, 197, 123]. It is worth noting that magnetic reconnection could be the mechanism accelerating particles in blazar jets, see *e.g.* **(author?)** [109], in which case it is also expected that the power-law of accelerated electrons and protons be slightly different [e.g., order of minutes, 120]).

An important quantity allowing to compare and contrast the models is the luminosity carried out by electrons, protons and the magnetic field. They are respectively computed with Equations (6.3.1), (6.3.3) and (6.3.5) and are given in Table 6.1 for TXS 0506+056 and Table 6.2 for 3HSP J095507.9+355101 and 3C 279. In all our models, the total luminosity of the jet is defined by the proton content. This is expected since our models are designed to produce a high neutrino flux. Specifically, in the case of TXS 0506+056, for the proton synchrotron model, shown on panel a) of Figure 6.1, the required luminosity for the jet is $L_{tot} = L_p + L_e + L_B = 2.7 \times 10^{47}\, erg\, s^{-1}$. The energy budget in the emitting region is dominated by the particles $(L_p + L_e)/L_B \simeq 3.5$, yet the system is closed to equipartition. For this model, the required luminosity exceeds by one order of magnitude the Eddington luminosity of $\simeq 4 \times 10^{46} erg\, s^{-1}$ for a black hole mass of $3 \times 10^8\, M_\odot$, as estimated for TXS 0506+056 using the absolute R-band magnitude [190]. This is in agreement with previous studies suggesting that in the case of proton synchrotron models or models producing a high neutrino flux, the required jet luminosity exceeds that of the Eddington limit [264]. Within a lepto-hadronic model, matching the neutrino flux with the neutrino event of TXS 0506+056, displayed on panel b) of Figure 6.1, requires the jet luminosity to be $\sim 10^{50}\, erg\, s^{-1}$, significantly exceeding that of the Eddington luminosity. Although the Eddington luminosity is not a strict limit and super-Eddington luminosities were previously reported [134], this value is extremely large. On the other hand, for the neutrino flare in 2014-2015, when assuming that the emission from the secondary pairs solely dominates in the X-ray and γ-ray bands, an unrealistically high luminosity of $\sim 10^{52}\, erg\, s^{-1}$ is obtained. Indeed, matching the high neutrino flux with the large radius (10^{17} cm) imposed by the modeling in this case, requires a large protons density, hence the too large proton luminosity. In the alternative interpretation, when the emission from the secondary pairs dominates in the GeV band, a modest luminosity of $3.4 \times 10^{47}\, erg\, s^{-1}$ is estimated.

For 3HSP J095507.9+355101, the situation is identical to that of TXS 0506+056. For the HM, a luminosity of $3.2 \times 10^{46}\, erg\, s^{-1}$ is estimated while the lepto-hadronic modeling requires the jet luminosity to be $\sim 10^{51}\, erg\, s^{-1}$. The black hole mass of 3HSP J095507.9+355101 was estimated, using two different methods, to be $3 \times 10^8\, M_\odot$ [193] or $\sim 8 \times 10^8\, M_\odot$ [195]. Therefore, the luminosity estimated from the hadronic modeling is compatible with the Eddington lu-

minosity $(4-10)\times10^{46}$ erg s^{-1}. In principle, the proton contribution to the overall jet luminosity can be decreased by assuming that protons have a softer energy distribution, $\alpha_p > 2.0$, different than that of the electrons. However, this introduces a new free parameter for the modeling, and the difference for the proton luminosity would only be a factor of a few.

For 3C 279, the hadronic interpretation of the SED observed in 2015 is natural, considering the difficulties encountered by the leptonic models. Indeed, when considering external inverse Compton scenario, the interpretation of the observed large Compton dominance ($\sim$ 70, the luminosity ratio of the high- and low -energy components) requires a strongly matter dominated jet [22]. In the alternative hadronic modeling, the data from the X-ray band to the γ-ray band can be well reproduced by proton synchrotron emission, provided they are efficiently accelerated up to energy 2×10^{17} eV with a power-law index -1.8. The modeling requires a relatively high jet total luminosity $\sim 10^{49}\,erg\,s^{-1}$, which exceeds the Eddington luminosity ($\sim 10^{47}\,erg\,s^{-1}$) for a black hole mass of $8\times10^{8}\,M_{\odot}$ [185]. However, this required luminosity is not a strong argument to disfavour the hadronic origin of 3C 279 emission during the 2015 flare considering that the source was in an exceptionally bright state.

Having estimated the model parameters of each blazar SEDs, the corresponding neutrino flux can be derived. The flux of muon neutrino, $F_{\nu_\mu}(E_{\nu_\mu})$, in all considered scenarios is shown by the light blue line in Figures 6.1-6.3. When available, the neutrino flux is compared with the limit imposed by the IceCube detector. This flux can be transformed to the expected observed number of neutrinos in the IceCube detector using its averaged effective area $A_{eff}(E_\mu)$, which is mostly a function of the incident neutrino energy. For 3HSP J095507.9+355101 and 3C 279, the average area from **(author?)** [3] was cosidered, while for TXS 0506+056 we used the area released after the observation of IceCube-170922A [4]. The effective area increases with energy and reaches its maximal value for energies above several hundreds of PeV. The expected number of muon neutrinos and anti-neutrinos is computed through

$$N_{\nu_\mu+\bar{\nu}_\mu} = t_{exp}\int_{E_{min,\nu_\mu}}^{E_{max,\nu_\mu}} F_{\nu_\mu}(E_{\nu_\mu})\,A_{eff}(E_{\nu_\mu})\,dE_{\nu_\mu} \tag{6.5.2}$$

where the minimum and maximum energy of the neutrinos are $E_{min,\nu_\mu} = 100$ GeV and $E_{max,\nu_\mu} = 10^9$ GeV, respectively, chosen to correspond the limits for the effective area. The expected number of neutrino events depends on the duration of the source activity, t_{exp}, over which the neutrinos are emitted. The neutrino oscillation, within the quasi-two neutrino oscillation assumption, is

[4] https://icecube.wisc.edu/science/data-releases/

taken into account by

$$N_{\nu_\mu}^{obs} = 0.575 N_{\nu_\mu} + 0.425 N_{\nu_e}, \tag{6.5.3}$$

where $N_{\nu_\mu}^{obs}$ is the observable distribution of muon neutrinos, while, N_{ν_μ} and N_{ν_e} are the emitted muon and electron neutrino distributions [93].

The expected number of neutrinos during the 6 months flare of TXS 0506+056 is 0.43 and 0.23 for the hadronic and the lepto-hadronic scenarios, respectively. During the 2014-2015 neutrino flare, our most optimistic model predict 3.0-3.3 neutrinos for a 6 months exposure time (note however that the IceCube observational window was $\sim$ 110 days). However, this lepto-hadronic modeling requires the jet luminosity to reach unrealistic values, $4.9 \times 10^{52}\, erg\, s^{-1}$, significantly exceeding the Eddington limit. By slightly varying the model parameters, a higher neutrino event count can be estimated, but it always remains below the 13 ± 5 events mark. The neutrino flux directly depends on the proton content in the jet, which is limited by the upper limit of the X-ray luminosity. Our results are in agreement with previous estimations for TXS 0506+056 and confirm that within a one-zone scenarios, 13 ± 5 events from the direction of TXS 0506+056 cannot be explained [218, 222].

In the case of 3HSP J095507.9+355101, the muon neutrino rate, $N_{\nu_\mu+\bar{\nu}_\mu}/t_{exp}$, is within $6 \times 10^{-4} - 4.8 \times 10^{-3}$ per day. This implies that under this rate of emission, the expected number of neutrinos to be detected by IceCube in a time corresponding to the duration of the flare is very low. By exploring different parameter sets, **(author?)** [203] concluded that in the most promising scenarios, there is a $\sim$ 1% to $\sim$ 3% to observe one neutrino over the time characteristic of the long-term emission of 3HSP J095507.9+355101 (years). As the neutrino emission seems to coincide with extreme behaviour of 3HSP J095507.9+355101 in the X-ray band, in principle, a large number of neutrinos could be expected if such an activity continues for a longer period. However, this is not the case for 3HSP J095507.9+355101. Similarly, when considering the flaring activity of 3C 279, a neutrino daily rate as high as 0.15 per day is estimated. However, for a relatively short period of the source activity, from minutes to one day, no neutrino events in the IceCube detector are expected, in agreement with [4].

6.6 Conclusion

Extensive multiwavelength data campaigns from radio to TeV energy bands and simultaneous observations of VHE neutrinos by increasingly more precise experiments pave the way towards a better understanding of highly energetic sources, both in terms of emission mechanism and dynamics. The un-

derstanding of the broad SED and neutrino emission requires detailed time-dependent numerical models of the interactions between leptons, photons and hadrons. We have presented a new kinetic model of photo-hadronic and leptonic interactions aiming at studying the emission of optically thin (for Compton scattering) scenarios of relativistic sources (e.g., AGNs and GRBs). Our numerical solution of the kinetic equations for protons, neutrons, pions, muons, neutrinos, pairs, and photons conserves the total energy of the system as well as the number of particles where required. The code takes as an input the spectral injection rate of the particles (e.g., electrons and/or protons), and compute the time evolution of all relevant particles, including the secondaries, as they interact and cool, allowing the computation of the broadband emission spectrum at any given period.

In this paper, we have applied *SOPRANO* to model the SEDs of three blazars, two of which are potentially associated to neutrino emission observed by IceCube. We have assumed different models for the production of the HE component and compute in all cases the expected number of muon neutrinos. The time-dependent nature of the code allowed to follow the evolution of all particles in one dynamical time scale and then assess the proton content in the jet by using the radiative spectrum of either secondaries or initial particles. This is necessary for the estimation of the expected number of neutrinos. Such time-dependent treatment of the particle evolution enabled us to constrain different scenarios of neutrino production by using the limits imposed by the observations in different bands.

.1 Physical processes in Soprano and their kinetic equations

In the current version of *SOPRANO*, the isotropic kinetic equations for photons, electrons and positrons (considered as one species, see below), protons, neutrons, charged and neutral pions, muons, neutrino and anti-neutrino of all relevant[5] flavors are evolved in time. For the photon distribution function, we assign n_{ph} to be the number of photons per unit volume per hertz. We further define N_i to be the number of particles of i species per unit volume per unit Lorentz factor of particle i. Here, i can be all leptons and all hadrons. Finally, we define N_{ν_i} as the number of neutrinos of i flavour per unit volume per GeV. In our numerical approach, all hadrons and leptons are considered relativistic with $\gamma_i \geq 1$. This appendix gives an overview of the kinetic equations, of the cross-sections and of the kinetic equations used in *SOPRANO* for all considered interactions. In Appendix .2, we detail the numerical prescription.

.1.1 Kinetic equations for all particles

Here, we summarize all terms appearing in the kinetic equations for all particle species. We denote Q, S and C as the source, sink and cooling terms, respectively. The contribution of inverse Compton scattering is denoted by R_{IC} for the photons and it is a cooling term for the leptons. Detailed expressions for the interaction kernels are given in the next subsections of this appendix.

- *Photons* are produced by the synchrotron radiation of all charged particles and by the decay of neutral pions, π_0. They are absorbed by pair production and redistributed in energy by inverse Compton scattering. We neglect the absorption of photons in the photo-pion and photo-pair processes. We did not consider synchrotron self-absorption and are planning to include it in the next version. The resulting kinetic equation takes the form

$$\frac{\partial n_{ph}}{\partial t} = -S_{\gamma\gamma\to e^+e^-} + Q_{\pi_0} + R_{IC} + \sum_{i\in[p,\mu^\pm,\pi^\pm,e^\pm]} Q^i_{synch}, \qquad (.1.1.1)$$

  where the last sum runs on all charged particles.

- *Leptons* (electrons and positrons) are considered as a single species. They are created by muon decay, Bethe-Heitler photo-pair production and

[5] τ neutrino cannot be produced by photo-hadronic interactions.

two photons recombination. They also undergo synchrotron cooling such that the final kinetic equation reads as

$$\frac{\partial N_{e^\pm}}{\partial t} = Q_{\mu^\pm} + Q_{p\gamma\to e^+e^-} + Q_{\gamma\gamma\to e^+e^-} + C_{IC} + C_{synch}. \tag{.1.1.2}$$

- *Protons* are loosing energy by synchrotron emission, photo-pair and photo-pion interactions. Protons are produced through photo-hadronic interactions between photons and neutrons, and are turned to neutrons for a substantial fraction of photo-pion interactions. The kinetic equation takes the form

$$\frac{\partial N_p}{\partial t} = C_{p\gamma\to p\pi} + C_{p\gamma\to e^+e^-} + C_{synch} - S_{\gamma p\to n\pi} + Q_{\gamma n\to p\pi}. \tag{.1.1.3}$$

- *Neutrons* are produced in photo-pion interactions and turned to protons by the same process. The kinetic equation takes the form

$$\frac{\partial N_n}{\partial t} = -S_{n\gamma\to p\pi} + Q_{p\gamma\to n\pi} + C_{n\gamma\to n\pi}. \tag{.1.1.4}$$

  In the current version of the code, we do not include neutron decay. Indeed, for the very large particle Lorentz factor involved, neutrons would escape the source before decaying. In principle, neutrinos produced by neutron decay should contribute to the observed overall signal. But since we are considering models in which the neutron number is always much smaller than the proton number, we can safely neglect this contribution. Note that numerically investigating a model similar to that of [24] would require a proper treatment of neutron decay.

- *Charged pions*, π_+ and π_-, are produced by photo-pion interactions. Then, they cool via synchrotron emission and decay. The kinetic equation for both species takes the form

$$\frac{\partial N_{\pi_\pm}}{\partial t} = Q_{p\gamma\to\pi} + Q_{n\gamma\to\pi} - S_\pi + C_{synch}. \tag{.1.1.5}$$

  The kinetic equations were solved independently for π^+ and π^- since the branching ratio in photo-pion production is different for negative and positive pions. This impacts the production ratio between the different neutrino species further.

- *Neutral pions* have a kinetic equation similar to that of charged pions but without synchrotron cooling.

- *Muons* are produced from the decay of charged pions. They lose energy by synchrotron radiation and decay. Therefore, the kinetic equation is

$$\frac{\partial N_{\mu_\pm}}{\partial t} = Q_{\pi_\pm} - S_{\mu_\pm} + C_{synch}. \tag{.1.1.6}$$

- *Muon and electron neutrinos and anti-neutrinos* are produced in the decay of pions and muons. We consider the two flavours independently, but neutrino and anti-neutrinos of the same flavour are combined.

$$\frac{\partial N_\nu}{\partial t} = Q_{\pi_\pm} + Q_{\mu_\pm}. \tag{.1.1.7}$$

For each of the processes, the details of the terms Q, S, C and R are given in the next subsections of Appendix .1 together with the cross-sections used in *SOPRANO*.

.1.2 Synchrotron emission and cooling

In *SOPRANO*, all charged particles lose their energy by synchrotron radiation as soon as a magnetic field is specified. Our current treatment does not include synchotron self-absorption, which will be added in a future update. For each charged particles, we describe the evolution of the distribution function due to synchrotron loses by a diffusion equation in energy space

$$\frac{\partial N_i}{\partial t} = \frac{1}{m_i c^2}\frac{\partial}{\partial \gamma_i}\left(N_i \int_0^\infty j_{synch}(\nu, \gamma_i) d\nu\right), \tag{.1.2.1}$$

while the photon kinetic equation is given by an integro-differential type equation:

$$\frac{\partial n_{ph}}{\partial t} = \int_1^\infty N_i(\gamma_i)\frac{j_{synch}}{h\nu}(\nu, \gamma_i) d\gamma_i. \tag{.1.2.2}$$

The synchrotron emissivity j_{synch} is given in the relativistic approximation by

$$j_{synch}(\nu) = \frac{\sqrt{3} q^3 B}{m_i c^2}\int_0^{\pi/2} \sin(\theta_p) F(X) d\theta_p \tag{.1.2.3}$$

with $X = \nu/\nu_c$,

$$\nu_c = \frac{3}{4\pi}\gamma_i^2 \frac{qB}{m_i c}\sin(\theta_p), \tag{.1.2.4}$$

and

$$F(X) = X\int_X^\infty K_{5/3}(\xi) d\xi \tag{.1.2.5}$$

with $K_{5/3}$ the modified Bessel function. This expression fails when the particle Lorentz factor tends towards one, in which case expression suitable with cyclo-synchrotron should be used [158, 166]. Therefore, in our numerical models, synchrotron emission due to mildly-relativistic particles is inaccurate. In practice, this parameter space is not relevant for blazars or for optically thin emission models of GRBs.

.1.3 Inverse Compton scattering.

For the rate of Compton scattering of an electron with Lorentz factor γ interacting with an isotropic distribution of photons of energy $x_1 = h\nu_1/(m_e c^2)$, we consider the relativistic approximation given by [136]

$$R(\gamma, x_1 \to x_2) \equiv \frac{dN}{dtdx_2} = \frac{3c}{4}\frac{\sigma_T}{x_1\gamma^2}\left[2q\ln(q) + (1+2q)(1-q) + \frac{1}{2}\frac{(4x_1\gamma q)^2}{1+4x_1\gamma q}(1-q)\right], \tag{.1.3.1}$$

where $x_2 = h\nu_2/(m_e c^2)$ is the energy of the scattered photons, and

$$q = \frac{x_2}{4x_1\gamma^2\left(1-\frac{x_2}{\gamma}\right)}, \tag{.1.3.2}$$

is limited to $q < 1$ and $q > 1/(4\gamma^2)$. This approximation to the exact cross-section is often used for blazar modeling. It it is accurate for large electron Lorentz factors, relevant for those objects. This approximation also implies that electrons can only lose energy and photons can only gain energy. Therefore, it is not suitable to describe the heating of electrons by the photon field.

For the relativistic electrons considered in *SOPRANO*, the kinetic equation takes the form of a diffusion equation

$$\frac{\partial}{\partial t}\left(N_{e^\pm}\right) = \frac{1}{m_e c^2}\frac{\partial}{\partial \gamma_e}\left(P_c N_{e^\pm}\right), \tag{.1.3.3}$$

where the power radiated by Compton scattering is

$$P_c(\gamma) = m_e c^2 \int_{x_1}\int_{x_2} dx_1 dx_2 R(\gamma, x_1 \to x_2)\, n_{ph}(x_1)(x_2 - x_1). \tag{.1.3.4}$$

On the other hand, we preserve the full integro-differential expression for the photon kinetic equations since for each inverse Compton scattering off relativistic electrons, photons gain a large amount of energy compared to their

initial energy :

$$\frac{\partial n_{ph}}{\partial t}(x_2) = \int_\gamma \int_{x_1} d\gamma dx_1 R(\gamma, x_1 \to x_2) N_{e^\pm}(\gamma) n_{ph}(x_1) - n_{ph}(x_2) \int_\gamma \int_{x_1} d\gamma dx_1 R(\gamma, x_2 \to x_1) N_{e^\pm}(\gamma) \tag{.1.3.5}$$

The first term represent the redistribution of photons of energy x_1 to x_2 and the second term represent the redistribution of photons of energy x_2 to all other possible energies.

.1.4 Pair production

For the pairs, the kinetic equation of the photon-photon annihilation process reads

$$\frac{\partial N_e}{\partial t} = c \int_{x_1} \int_{x_2} n_{ph}(x_1) n_{ph}(x_2) \sigma_{2\gamma \to e^\pm}(x_1, x_2 \to \gamma) dx_1 dx_2. \tag{.1.4.1}$$

For the photons, the kinetic equation can be written

$$\frac{\partial n_{ph}}{\partial t}(x_1) = -n_\gamma(x_1) \int_{x_2} n_{ph}(x_2) \sigma^0_{2\gamma \to e^\pm}(x_1, x_2) dx_2, \tag{.1.4.2}$$

where

$$\sigma^0_{2\gamma \to e^\pm} = 2 \int_\gamma \sigma_{2\gamma \to e^\pm}(x_1, x_2, \gamma) d\gamma. \tag{.1.4.3}$$

For the cross-section, we use the formula given by [40]. It is recall here for convenience

$$\sigma_{2\gamma \to e^\pm}(x_1, x_2 \to \gamma) = \frac{3}{4} \frac{\sigma_T c}{x_1^2 x_2^2} \left(\frac{\sqrt{E^2 - 4\alpha_{cm}^2}}{4} + H_+ + H_- \right) \Bigg|_{\alpha_{cm}^L}^{\alpha_{cm}^U}, \tag{.1.4.4}$$

where the center of mass energy α_{cm} is given by

$$\alpha_{cm} = \sqrt{\frac{x_1 x_2}{2}}, \tag{.1.4.5}$$

and

$$\begin{cases} E = x_1 + x_2 \\ c_\pm = (x_{1,2} - \gamma)^2 - 1 \\ d_\pm = x_{1,2}^2 + x_1 x_2 \pm \gamma(x_2 - x_1) \\ \alpha_{cm}^{a,b} = \sqrt{1/2}\sqrt{\gamma(E-\gamma) + 1 \pm \sqrt{[\gamma(E-\gamma)+1]^2 - E^2}} \\ \alpha_{cm}^{U} = \min\left(\sqrt{x_1 x_2}, \alpha_{cm}^{a}\right) \\ \alpha_{cm}^{L} = \max\left(1, \alpha_{cm}^{b}\right) \end{cases} \tag{.1.4.6}$$

Finally for $c \neq 0$, the H functions are defined by

$$H_\pm = -\frac{\alpha_{cm}}{8\sqrt{x_1 x_2 + c_\pm \alpha_{cm}^2}}\left(\frac{d_\pm}{x_1 x_2} + \frac{2}{c_\pm}\right) + \frac{1}{4}\left(2 - \frac{x_1 x_2 - 1}{c_\pm}\right) I_\pm + \frac{\sqrt{x_1 x_2 + c_\pm \alpha_{cm}^2}}{4}\left(\frac{\alpha_{cm}}{c_\pm} + \frac{\alpha_{cm}}{\alpha_{cm}}\right. \tag{.1.4.7}$$

where

$$I_\pm = \begin{cases} \dfrac{1}{\sqrt{c_\pm}} \ln\left(\alpha_{cm}\sqrt{c_\pm} + \sqrt{x_1 x_2 + c_\pm \alpha_{cm}^2}\right) & c_\pm > 0, \\ \dfrac{1}{\sqrt{c_\pm}} \arcsin\left(\alpha_{cm}\sqrt{-\dfrac{c_\pm}{x_1 x_2}}\right) & c_\pm < 0, \end{cases} \tag{.1.4.8}$$

while for $c_\pm = 0$, we have

$$H_\pm = \left(\frac{\alpha_{cm}^3}{12} - \frac{\alpha_{cm} d_\pm}{8}\right)\frac{1}{(x_1 x_2)^{3/2}} + \left(\frac{\alpha_{cm}^2}{6} + \frac{\alpha_{cm}}{2} + \frac{1}{4\alpha_{cm}}\right)\frac{1}{\sqrt{x_1 x_2}}. \tag{.1.4.9}$$

.1.5 Bethe-Heitler pair production

Photo-pair production, also called Bethe-Heitler process, is the creation of an electron positron pair by the interaction between a proton and a photon. The cross section of this process is given by the formula 3D-2000 of [177], see also

[39] and [143], which we recall here for convenience:

$$\frac{d^2\sigma}{dE_- d\mu} = \left(\frac{\alpha Z^2 r_0^2 p_- p_+}{2k^3}\right)\left[-4\sin^2(\theta)\frac{2E_-^2+1}{p_-^2\Delta_-^4} + \frac{5E_-^2 - 2E_+E_- + 3}{p_-^2\Delta_-^2} + \frac{p_-^2 - k^2}{T^2\Delta_-^2} + \frac{2E_+}{p_-^2\Delta_-}\right.$$
$$+\frac{Y}{p_- p_+}\left(2E_-\sin^2(\theta)\frac{3k + p_-^2 E_+}{\Delta_-^4} + \frac{2E_-^2(E_-^2+E_+^2) - (7E_-^2 + 3E_+E_- + E_+^2) + 1}{\Delta_-^2} + \frac{k(E_-^2 - E}{\Delta}\right. \tag{.1.5.1}$$
$$\left.\left. - \frac{\delta_+}{p_+ T}\left(\frac{2}{\Delta_-^2} - \frac{3k}{\Delta_-} - \frac{k(p_-^2 - k^2)}{T^2\Delta_-}\right) - \frac{2y_+}{\Delta_-}\right],$$

where

$$E_+ = k - E_- \qquad p_+ = \sqrt{p_+^2 - 1} \quad p_- = \sqrt{E_-^2 - 1} \tag{.1.5.2}$$

$$T = \sqrt{k^2 + p_-^2 - 2kp_-\cos(\theta)} \qquad Y = \frac{2}{p_-^2}\ln\left(\frac{E_+E_- + p_+p_- + 1}{k}\right) \tag{.1.5.3}$$

$$y_+ = \frac{1}{p_+}\ln\left(\frac{E_+ + p_+}{E_+ - p_+}\right) \qquad \delta_+ = \ln\left(\frac{T + p_+}{T - p_+}\right). \tag{.1.5.4}$$

The kinetic equation for the production of pairs is given by

$$\frac{\partial}{\partial t}\left(N_{e^\pm}(\gamma_e)\right) = c\int_{\gamma_p m_p > \gamma_e m_e} dE_p N_p \frac{dN_e}{dE_e}. \tag{.1.5.5}$$

The pair spectrum is given by [143]

$$\frac{dN_e^-}{dE_e} = \frac{1}{2\gamma_p^3}\int_{x=\frac{(\gamma_p+E_e)^2}{4\gamma_p^2 E_e}}^{\infty}\int_{\omega=\frac{(\gamma_p+E_e)^2}{2\gamma_p E_e}}^{2\gamma_p x} \times \int_{E_-=\frac{\gamma_p^2+E_e^2}{2\gamma_p E_e}}^{\omega-1}\frac{dE_- d\omega dx}{p_-}\frac{n_{ph}(x)}{x^2}W(\omega, E_-, \xi), \tag{.1.5.6}$$

where ϵ is the photon energy in unit of electron rest mass energy. The kinetic equation for the protons is obtained from consideration of energy conservation

$$\frac{\partial N_p(\gamma_p)}{\partial t} = \frac{\partial\left(P_{BH}N_p\right)}{\partial\gamma_p} \tag{.1.5.7}$$

where the power emitted by Bethe-Heitler is given by

$$P_{BH} = \int \gamma_e m_e c^2 \frac{dN_{e^\pm}}{dt} \tag{.1.5.8}$$

.1.6 Photo-hadronic interaction : pion production

Photo-pion production is the interaction between a proton and a photon mostly producing pions. This interaction can be divided into four channels : resonance, direct production, multi-production and fragmentation. In the following, we neglect the contribution from fragmentation and plan its inclusion for future studies. For the sake of presentation, in this subsection only, we change the energy unit of the photon distribution from frequency ν to energy ϵ in GeV. Following [127], the spectral production rate of each pion species (π^+, π^- and π^0) can be written as

$$\frac{dN_\pi}{dt} = \sum_{IT} M_{IT} \int_{\gamma_p} \int_{\epsilon} d\gamma_p d\epsilon N_p n_{ph} R_{IT}(\gamma_p, \nu \to \gamma_\pi), \tag{.1.6.1}$$

where the index IT spams all resonances, the two direct production channels, and multi production channels. In this equation M^{IT} is the multiplicity of each interaction. This coefficient takes a different value for each interaction and each pion species. Finally, the rate of interaction is given by [143]

$$R_{IT} = \frac{c}{2\gamma_p^2 \beta_p \epsilon^2} \int_{\epsilon_{th}}^{2\gamma_p \epsilon} d\epsilon_r \epsilon_r \int_{\psi} d\psi \frac{\partial \sigma_{p\gamma}(\epsilon_r, \psi)}{\partial \psi} \delta(E_\pi - \xi), \tag{.1.6.2}$$

where the threshold energy ϵ_{th} is constrained by the kinematics of the reaction, ϵ_r is the energy of the photon in the frame comoving with the proton, ψ is the cosine of the comoving (in the proton rest-frame) angle between the photon direction and the axis representing the direction of the proton in the lab frame, the differential represent the angular distribution of the reaction and ξ is the pion energy obtained from the kinematics. For a detailed discussion, on the kinematics, see **(author?)** [31, 33] and **(author?)** [127].

Photo-pion production : resonances

For the cross-section of the nine resonances considered in this work, we consider the Breit-Wigner approximation

$$\sigma^{IT}(\epsilon_r) = B^{IT} \frac{s}{\epsilon_r^2} \frac{\sigma_0^{IT} \left(\Gamma^{IT}\right)^2 s}{\left(s - \left(M^{IT}\right)^2\right)^2 + \left(\Gamma^{IT}\right)^2 s}, \tag{.1.6.3}$$

where $s = m_p^2 + 2m_p\epsilon_r$ is the total energy in the center of mass. The parameters σ^{IT}, B^{IT}, Γ^{IT} and M^{IT} are given by **(author?)** [178, 127] and in the review of Particle Data Group [276]. The nine resonances used are the ones of **(author?)** [178]. Contrary to the simple model used by [127], we include the angular dependence of the Δ meson decay for R_1 type resonances, as given by table 3 of [178].

Photo-pion production : direct production

For the direct production, we use the parametric cross-sections given by [178]

$$\sigma_{N\pi}(\epsilon_r) = 92.7\mathfrak{P}(\epsilon_r, 0.152, 0.25, 2) + 40\exp\left(-\frac{(\epsilon_r - 0.29)^2}{0.002}\right) - 15\exp\left(-\frac{(\epsilon_r - 0.37^2)}{0.002}\right), \tag{.1.6.4}$$

$$\sigma_{\Delta\pi}(\epsilon_r) = 37.7\mathfrak{P}(\epsilon_r, 0.4, 0.6, 2), \tag{.1.6.5}$$

where the function $\mathfrak{P}$ is 0 if $\epsilon_r \leq \epsilon_{th}$ and

$$\mathfrak{P}(\epsilon_r, \epsilon_{th}, \epsilon_{max}, \alpha) = \left(\frac{\epsilon_r - \epsilon_{th}}{\epsilon_{max} - \epsilon_{th}}\right)^{A-\alpha}\left(\frac{\epsilon_r}{\epsilon_{max}}\right)^{-A} \tag{.1.6.6}$$

otherwise. Here, $A = \alpha\epsilon_{max}/\epsilon_{th}$. We also include the angular dependence coming from the distribution of the t-Mandelstam variable as explaned in [178].

Photo-pion production : multi-pion production

For the multi-production channel, it is not possible to resort to simple integral expressions. Therefore, we use the approximation developed by [127]. It provides a simple and convenient form for the pion spectrum, while the multiplicities are approximated from results of Sophia [178].

For completeness, we give here the expressions of the pion spectrum:

$$\frac{\partial N_\pi}{\partial E_\pi} = \frac{cm_p}{E_\pi}\sum_{IT} N_p\left(\frac{E_\pi}{\xi^{IT}}\right)\int_{\epsilon_{th}}^{\infty} dy n_\gamma\left(\frac{m_p y \xi^{IT}}{E_\pi}\right) M^{IT} f^{IT}(y), \tag{.1.6.7}$$

where

$$f^{IT} = \begin{cases} 0 & 2y < \epsilon_{min}^{IT} \\ \frac{\sigma^{IT}}{(4y^2)}(4y^2 - {\epsilon_{min}^{IT}}^2) & \epsilon_{min}^{IT} \leq 2y < \epsilon_{max}^{IT} \\ \frac{\sigma^{IT}}{(4y^2)}({\epsilon_{max}^{IT}}^2 - {\epsilon_{min}^{IT}}^2) & \epsilon_{max}^{IT} \leq 2y. \end{cases} \tag{.1.6.8}$$

The parameters for the 14 interactions making the approximation are given in Table 6 of [127].

.1.7 Particle decay

We consider the decay of charged pions

$$\begin{cases} \pi^+ \to \mu^+ + \nu_\mu, \\ \pi^- \to \mu^- + \bar{\nu}_\mu, \end{cases} \tag{.1.7.1}$$

of neutral pions

$$\pi^0 \to 2\gamma, \tag{.1.7.2}$$

and of muons

$$\begin{cases} \mu^- \to e^- + \nu_e + \bar{\nu}_\mu, \\ \mu^+ \to e^+ + \bar{\nu}_e + \nu_\mu. \end{cases} \tag{.1.7.3}$$

The kinetic equation of the decaying particle is given by

$$\frac{\partial N_i}{\partial t} = -\frac{N_i}{\tau_i \gamma_i} \tag{.1.7.4}$$

where τ_i is the mean-life time of the particle which decays, and γ_i its Lorentz factor. The kinetic equation for the daughter particle is given by

$$\frac{\partial N_j}{\partial t}\left(E_j\right) = \int_{E_i > E_j}^{\infty} \frac{N_i}{\tau_i \gamma_i} F(E_i, E_j) dE_i, \tag{.1.7.5}$$

where $F(E_i, E_j)$ is the spectrum of particle j at energy E_j produced by a parent particle of energy E_i.

The neutrino spectrum from charged pion decay is given by [153]

$$F(E_\pi, E_\nu) = \frac{1}{E_\pi}\frac{1}{1-r_\pi} H\left(1 - r_\pi - \frac{E_\nu}{E_\pi}\right), \tag{.1.7.6}$$

where $r_\pi = (m_\mu/m_\pi)^2$.

The photon spectrum obtained from neutral pion decay is given by

$$F(E_{\pi_0}, E_\gamma) = \frac{2}{E_{\pi^0}}, \tag{.1.7.7}$$

where the factor 2 comes from the fact that two photons are created in the decay.

For the electron and neutrino spectra, we do not use the expression given by [270], but resort to the simpler relativistic approximation of [153]

$$F_{\nu_e}(E_{\nu_e}, E_\mu) = \frac{2 - 6x^2 + 4x^3}{E_\mu}, \tag{.1.7.8}$$

$$F_{\nu_\mu}(E_{\nu_\mu}, E_\mu) = F_e(E_e, E_\mu) = \frac{\frac{5}{3} - 3x^2 + \frac{4}{3}x^3}{E_\mu}, \tag{.1.7.9}$$

where $x = E_i/E_\mu$ for each particle species i.

.1.8 Photon and particle escape

When dealing with a one-zone model, since the emitting region is assumed to be shaped like a blob, all effects due to photon transport are neglected. Moreover, since we are considering optically thin plasma, photons cannot accumulate in the emission region for an arbitrarily large amount of time. Indeed, they would escape the region in which they are produced in a time of the order of the crossing time

$$t_{ph}^{esc} \sim \frac{2R}{3c}, \tag{.1.8.1}$$

where R is the comoving size. In principle, charged particles could remain longer inside the emitting region. Therefore, particle escape can be treated by

adding a term to the kinetic equation of the form

$$\frac{\partial N_i}{\partial t} = \frac{N_i}{\mathfrak{T}_i t_{ph}^{esc}} \tag{.1.8.2}$$

$$\frac{\partial n_{ph}}{\partial t} = \frac{n_\gamma}{t_{ph}^{esc}} \tag{.1.8.3}$$

where $\mathfrak{T}_i = t_i^{esc}/t_{ph}^{esc}$ is a parameter that is specified for each runs. It represents the time increase it takes for a particle to escape the system as compared to a photon. In other words, particle escape is used to crudely represent the finiteness of the emitting region. In this work, we did not consider particle escape. Instead, we evolve the distributions until a comoving time equal to the dynamical time scale.

.2 Numerical discretization and prescription in SOPRANO

In order to numerically integrate the kinetic equations presented in Section .1, a numerical grid for the energy of all particles is introduced. In this work, *SOPRANO* uses a grid of bins equally space in logarithmic of the energy[6]. Table .3 gives the grid characteristics for each types of particle, that is to say the number of energy bins, together with the minimum and maximum energies. For the energy discretization, we use the approach of the discontinuous Galerkin method, that we restrain to first order for this paper[7]. On each energy cell I, we approximate the distribution function by a polynomial, while we use for basis the Legendre polynomial basis. Therefore, on each energy cell I, the distribution function is approximated by

$$N_i^I(t,x) = N_{i,0}^I(t) L_0^I(x) \tag{.2.1}$$

[6]Note that our numerical method does not require a uniform grid. Since, it is based on finite volume, we can refine the grid in one or several energy bands of interest (static mesh refinement). In this way, we can provide more detailed results in those specific bands, while the rest of the domain is coarse for faster numerical estimation. This numerical technique will be used in future works, in which we will study the shape of the spectral peaks.

[7]We have implemented some of the processes with reconstruction up to order 2, but this numerical technique is not included in the current paper

Particle	Number of energy cells	Minimum of the grid	Maximum of the grid
Photons :	150	$\nu = 10^{-2}$Hz	$\nu = 10^{30}$ Hz
Leptons :	130	$\gamma_{e^\pm} = 1.2$	$\gamma_{e^\pm} 5 \times 10^{13}$
Hadrons :	100	$\gamma_h = 1.2$	$\gamma_h = 10^{11}$
Neutrinos :	100	$E_\nu = 10^{-3}$ GeV	$E_\nu = 10^{11}$ Gev

Table .3 Characteristics of the numerical grids used by *SOPRANO* for the numerical models of this work. The cells are equally space in logarithmic scale.

where the first order Legendre polynomial on the energy cell I is

$$L_0^I = \frac{1}{\sqrt{x_{I+\frac{1}{2}} - x_{I-\frac{1}{2}}}} \equiv \frac{1}{\sqrt{||I||}} \tag{.2.2}$$

Here $x_{I\pm(1/2)}$ are the energy boundaries of cell I and where we introduced the additional notation $||I|| = (x_{I+1/2} - x_{I-1/2})$. In the following we will use interchangeably $N_i^I \equiv N_{i,0}^I$.

We seek the weak formulation of all kinetic equations presented in Appendix .1 on each energy interval I. For this, we multiply both sides of any of the kinetic equation by L_0 and integrate over I. After simplification, we obtain a system of differential equations for all $N_{i,0}^I$. This specific discretization and the structure of the kinetic equation allows us to retrieve a numerical method which conserves energy and the number of particles when they are conserved. Time discretization is achieved via implicit first order Euler method. leptonic processes, which involved terms of the form $n_i n_j$. Below, we give details on the numerical discretisation on a couple of example and give additional details for specific processes when needed.

For the sake of the example, consider the synchrotron process and its associated kinetic equations. Without synchrotron self-absorption, the treatment of synchrotron losses and photon production is heavily simplified. We start by the photon given by Equation .1.2.1. Multiplying both side by L_0^J and integrating gives

$$\frac{\partial n_{ph}^I}{\partial t} = \frac{1}{h\sqrt{||J||}} \sum_K \frac{N_i^K}{\sqrt{||K||}} \int_K \int_I \frac{j_{synch}^i(\nu, \gamma_i)}{\nu} d\nu d\gamma_i, \tag{.2.3}$$

where N_i represent any charged particle. We follow the same procedure for the charge particle equation and after an integration by part, the kinetic equa-

tion can be put into the form

$$\frac{\partial N_i^K}{\partial t} = \int_K L_0^K \frac{\partial}{\partial \gamma_k}\left[P_{synch} N_i^K L_0^K\right] d\gamma_i = \int \frac{\partial L_0^K}{\partial \gamma_i}\left[P_{synch} N_i^K L_0^K\right] d\gamma_i - \frac{1}{\sqrt{K}}\left[F_{K+\frac{1}{2}} - F_{K-\frac{1}{2}}\right]. \tag{.2.4}$$

In this last expression, only the second term is non-null. In order to obtain an expression for the numerical fluxes $F_{K+1/2}$ on the right-hand side, we consider the energy lost by particles and that gain by the photons. The total energy gain by the photons is

$$\frac{\partial E_{ph}}{\partial t} = \frac{\partial}{\partial t}\left(\sum_J \int_J n_{ph}^J L_0^J h\nu d\nu\right) = \sum_J \frac{\nu_{J+\frac{1}{2}} - \nu_{J-\frac{1}{2}}}{2||J||} \sum_K \frac{N_i^K}{\sqrt{||K||}} \int_K \int_J \frac{j_{synch}(\nu, \gamma_i)}{\nu} d\gamma_i d\nu, \tag{.2.5}$$

where the last equality is obtained after using Equation .2.3. Turning to the energy lost by the charged particles, we have

$$\frac{\partial E_i}{\partial t} = m_i c^2 \sum_K \frac{\partial N_i^K}{\partial t} \frac{\gamma_{i,K+\frac{1}{1}}^2 - \gamma_{i,K-\frac{1}{1}}^2}{2\sqrt{||K||}}. \tag{.2.6}$$

Inserting the expression for the time derivative of the distribution function coefficients, and reorganising the summation it comes

$$\frac{\partial E_i}{\partial t} = m_i c^2 \left[-\frac{\gamma_{i,\frac{1}{2}}^2 - \gamma_{i,-\frac{1}{2}}^2}{2(\gamma_{i,\frac{1}{2}} - \gamma_{i,-\frac{1}{2}})} F_{-\frac{1}{2}} + \frac{\gamma_{i,\xi+\frac{1}{2}}^2 - \gamma_{i,\xi-\frac{1}{2}}^2}{2(\gamma_{i,\xi+\frac{1}{2}} - \gamma_{i,\xi-\frac{1}{2}})} F_{\xi+\frac{1}{2}} + \sum_K \left(\frac{\gamma_{i,K+\frac{1}{2}}^2 - \gamma_{i,K-\frac{1}{2}}^2}{(\gamma_{i,K+\frac{1}{2}} - \gamma_{i,K-\frac{1}{2}})} - \frac{\gamma_{i,K+\frac{3}{2}}^2}{(\gamma_{i,K+\frac{3}{2}}} \right. \right. \tag{.2.7}$$

where in this specific equation ξ represent the number of cells of the grid for particle species i. We assume that no particle diffuse out of the energy grid. This gives $F_\xi = F_{-\frac{1}{2}} = 0$. Inverting the summation order in Equation .2.5, and identifying the term gives the expression of the fluxes

$$\mathcal{F}_{K+\frac{1}{2}} = \frac{1}{m_i c^2} \frac{N_{i,0}^{K+1} / \sqrt{\gamma_{i,K+\frac{3}{2}} - \gamma_{i,K+\frac{1}{2}}}}{\left[\frac{\gamma_{i,K+\frac{1}{2}}^2 - \gamma_{i,K-\frac{1}{2}}^2}{\gamma_{i,K+\frac{1}{2}} - \gamma_{i,K-\frac{1}{2}}}\right] - \left[\frac{\gamma_{i,K+3/2}^2 - \gamma_{i,K+\frac{1}{2}}^2}{\gamma_{i,K+\frac{3}{2}} - \gamma_{i,K+\frac{1}{2}}}\right]} \times \sum_J \frac{\nu_{J+\frac{1}{2}}^2 - \nu_{J-\frac{1}{2}}^2}{\nu_{J+\frac{1}{2}} - \nu_{J-\frac{1}{2}}} \int_J \int_{K+1} \frac{j_{synch}(\nu, \gamma_i)}{\nu} d\gamma_i d\nu. \tag{.2.8}$$

This choice of the flux preserves the total energy of the system, while the

particle number conservation is ensured by the structure of Equation .2.4. However, this choice of numerical discretization leads to numerical diffusion, see .3.1, in which the current scheme is compared to the classical Chang and Cooper scheme [63].

For the Compton scattering process, the weak formulation is trivially obtained and does not require the use of integration by part, since the kinetic equation does not take the form of a diffusion equation. For all other processes, their respective kinetic equation takes either the same form as that of synchrotron mechanism or of Compton scattering. Therefore, all energy discretization can be easily obtained following the same procedure outlined above. We note, that we use redistribution of particles in integro-differential equation type to preserve simultaneously total particle number (when required by the process) and total energy.

Before discussing the temporal discretization, we note that the equation are non-linear in the distribution function for Compton scattering, pair production, photo-pion and photo-pair processes. We decided to linearize the kinetic equations of photo-pion and photo-pair processes by assuming that the target photon-field is equal to the one at the previous time step, effectively making those process linear in the distribution functions. For all leptonic processes, we preserve the non-linearity of the kinetic equations and solve at each time step a non-linear system via the Newton-Raphson method. Since the gradients can be computed analytically, we do not need to use numerical estimates for the Jacobian. The temporal evolution of the distribution function is performed with the first order implicit Euler method.

One time step of the code takes the following form

1. solve the linear kinetic equation to obtain the protons and neutrons spectra at time $t + dt$, assuming that the photon distribution function is given at time t for photo-pion and photo-pair processes. The pairs and photons created in those two processes and by the proton synchrotron process are saved to be use as a source term in the leptonic computation.

2. compute the decay and cooling (when required) of pions and muons. The pairs and photons created in the muon and pion decay, as well as their synchrotron radiation are saved to be used as source terms in the leptonic computation.

3. perform the non-linear implicit leptonic computation with the source terms computed in the two previous steps.

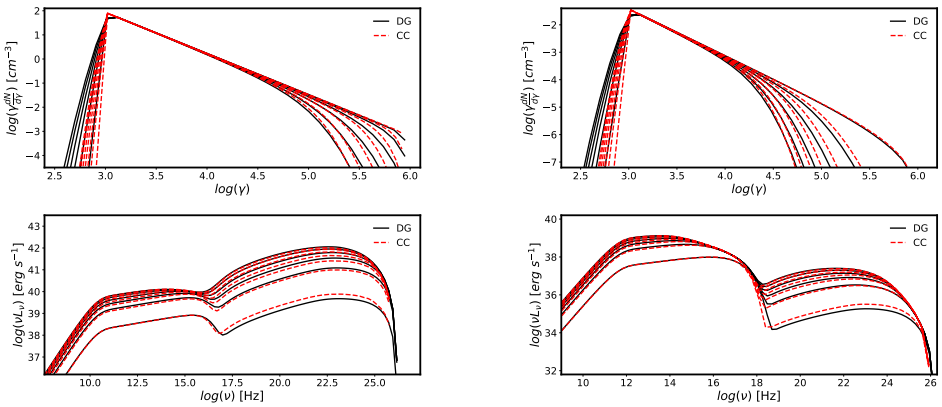

Figure .4 Comparison between the **(author?)** [63] scheme and *SOPRANO* for Compton scattering and synchrotron radiation in two different regimes, whose parameters are given in Table .4. Left − inverse Compton dominates. Right − synchrotron cooling dominates. The plots show the time evolution of the electron (top) and photon (bottom) distribution functions up to dynamical time scale, in the comoving frame. Electron number conservation is satisfied to machine accuracy (10^{-16}) while the energy is conserved to an accuracy better than 10^{-11}.

.3 Code tests and examples

.3.1 Synchrotron and inverse Compton cooling for electrons

In this section, we present two tests performed for the synchrotron and inverse Compton radiation processes. First, the results from *SOPRANO* are compared to the results obtain with our implementation of the [63] scheme, which is widely spread and used in time-dependent application, see *e.g.* **(author?)** [68, 98]. We consider a situation in which electrons are continuously injected into the radiating zone in the form of a power-law between $\gamma_{min} = 10^3$ and $\gamma_{max} = 9 \times 10^5$. The properties of the radiating zone are such that for one test, inverse Compton cooling dominates over synchrotron cooling, while for the other test it is the opposite. The parameter are summarized in Table .4.

Figure .4 shows the results. It is clear that the agreement between the Chang and Cooper scheme and *SOPRANO* is very good for both the electron and the photon distribution functions. We notice that *SOPRANO* is more diffusive at low energy below the peak of the electron distribution function. This is mostly because of the scheme used to preserve the total energy of the system in *SOPRANO*, which induces extra diffusion. However, despite these

	IC dominance	Syn dominance
$R/10^{17}\ cm$	1	1
$B[G]$	0.005	0.1
$\gamma_{e,min}$	10^3	10^3
$\gamma_{e,max}$	9×10^5	9×10^5
α_e	2.7	2.7
U_e/U_B	10^5	0.1

Table .4 Parameters used for our numerical comparison between *SOPRANO* and the Chang and Cooper scheme [63]. The corresponding evolution of the photon and electron distribution functions is given on Figure .4.

differences for the electron distribution function, the photon spectra are in very good agreement.

.3.2 Proton cooling on black-body photons by photo-pair and photo-pion interaction

We start by computing the proton cooling time in photo-pion production. [24] presented a simple model for the cross-section and inelasticity for the photon-pion interaction. The model is such that the product of the cross-section with the inelasticity is constant for all energies larger than the threshold energy in the center of mass frame. It gives a simple estimate of the cooling time for a proton of Lorentz factor γ_p interacting with an isotropic photon field with the spectrum of a black-body withe temperature θ. From [85], it reads

$$t_{p\gamma}^{-1}(\gamma_p) = \frac{8\pi c\sigma K\theta^3}{\lambda_c^3}\int_\omega^\infty dy \frac{y^2-\omega^2}{\exp(y)-1}, \tag{.3.1}$$

where λ_c is the Compton wavelength, $\sigma K \sim 70\mu$b and

$$\omega = \frac{\epsilon_{th}}{2\gamma_p\theta}. \tag{.3.2}$$

In Figure .5, we present the mean free path in Mpc as a function of proton Lorentz factor for an hypothetical radiation field with temperature $10^4 T_{CMB}$, with the temperature of the cosmic microwave background $T_{CMB} = 2.725$K. To obtain this plot, we considered a δ-function in each of the proton energy grid bins. We see that the agreement is quite good. We remark that the contribution of the multi-production channel has a sharp increase at large Lorentz factor. This is not physical and is a grid effect. Indeed, the proton cooling is computed by summation over all created pions. Because both the pion and

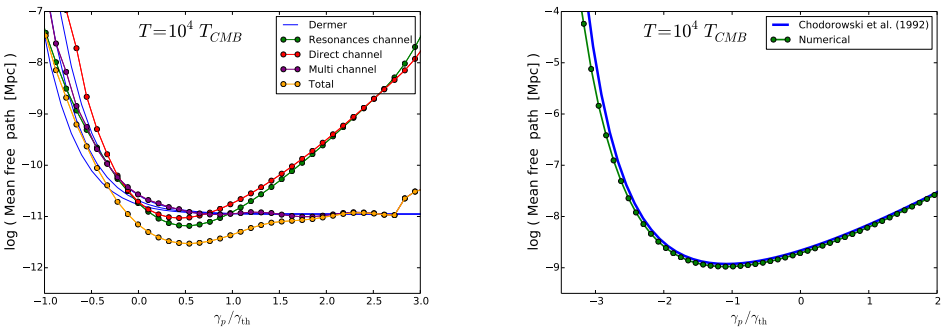

Figure .5 Right : Proton mean free path as a function of their Lorentz factor for the photon-pion process. The photon temperature is $T = 10^4 T_{CMB}$. Blue : mean free path computed by using Equation .3.1 for the lower boundary center and upper boundary of an energy cell. The Lorentz factor is normalized by $\gamma_{th} = \epsilon_{th}/(2k_B\theta) \sim 3.2 \times 10^7$. Right : Proton mean free path as a function of the Lorentz factor for the photo-pair process. Green - *SOPRANO*. Blue with the approximation of **(author?)** [69]. For easy comparison, the proton Lorentz factor is also normalized by γ_{th}.

proton energy grid have the same maximum Lorentz factor, protons at the highest energies in our grid do not interact substantially, since they cannot create pions of the correct energy.

We now turn to the photo-pair process. The energy loss rate for this process can be written as

$$\frac{dE}{dt} = \alpha_f r_e^2 c m_e c^2 \int_2^\infty d\epsilon n_{ph} \left(\frac{\epsilon}{2\gamma_p}\right) \frac{\phi(\epsilon}{\epsilon^2}. \tag{.3.3}$$

[69] gives a convenient approximation for the differential cross-section $\phi(\epsilon)$, see their appendix. It is therefore easy to compute the energy loss pathlength $r = c[(dE/dt)/E]^{-1}$. A comparison between this semi-analytical approach and our numerical discretization is given by the right part of Figure .5. We see that the agreement is excellent.

.3.3 Decay time

We show in this subsection how particles decay in our code with the examples of pion decay. We inject pions with a specific Lorentz factor and simulate the evolution of the system as they decay, producing neutrinos and muons. The initial pions Lorentz factor are $\gamma_\pi = 10^7,\ 10^8,\ 10^9$. In this section only, we assume that muons cannot decay. Figure .6 shows the evolution of the

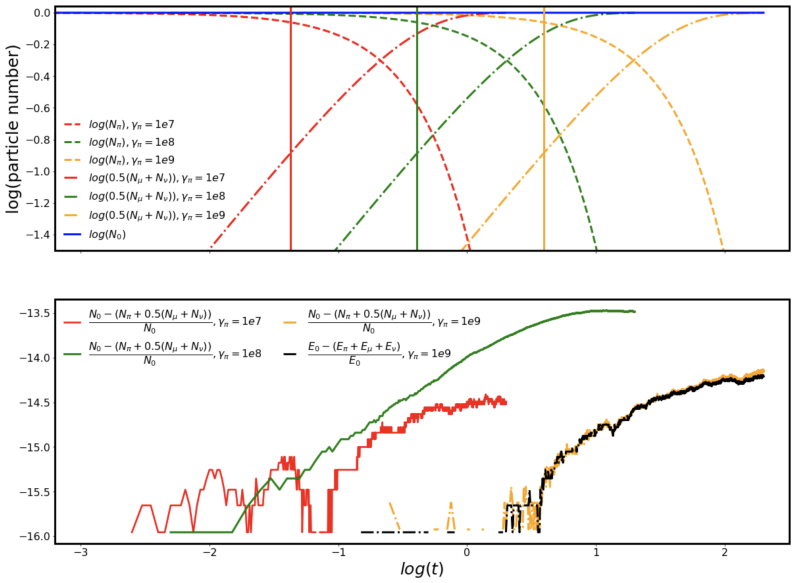

Figure .6 Top - evolution of the pion, neutrino and muon numbers as a function of time for the pion decay process. The vertical lines correspond to the decay time of the corresponding particle Lorentz factor. Obviously the decay time is properly respected. Bottom - temporal evolution of the particle number conservation and energy conservation. The total energy conservation is only shown for $\gamma_p i = 10^9$, but similar results are obtained for other particle energy.

pion, neutrino and muon numbers as time evolve. The muon and neutrino number is obtained by summing over their respective distribution function. The same figure also shows the evolution of particle number and total energy of the system, which can be seen to be satisfied to accuracy better than 10^{-13} after 4×10^3 iterations.

Bibliography

[1] M. G. Aartsen, R. Abbasi, Y. Abdou, M. Ackermann, J. Adams, J. A. Aguilar, M. Ahlers, D. Altmann, J. Auffenberg, X. Bai, and et al. First Observation of PeV-Energy Neutrinos with IceCube. *Physical Review Letters*, 111(2):021103, July 2013.

[2] M. G. Aartsen, M. Ackermann, J. Adams, J. A. Aguilar, M. Ahlers, M. Ahrens, C. Alispach, K. Andeen, T. Anderson, I. Ansseau, G. Anton, C. Argüelles, J. Auffenberg, S. Axani, P. Backes, H. Bagherpour, X. Bai, A. Balagopal V., A. Barbano, S. W. Barwick, B. Bastian, V. Baum, S. Baur, R. Bay, J. J. Beatty, K.-H. Becker, J. Becker Tjus, S. BenZvi, D. Berley, E. Bernardini, D. Z. Besson, G. Binder, D. Bindig, E. Blaufuss, S. Blot, C. Bohm, S. Böser, O. Botner, J. Böttcher, E. Bourbeau, J. Bourbeau, F. Bradascio, J. Braun, S. Bron, J. Brostean-Kaiser, A. Burgman, J. Buscher, R. S. Busse, T. Carver, C. Chen, E. Cheung, D. Chirkin, S. Choi, K. Clark, L. Classen, A. Coleman, G. H. Collin, J. M. Conrad, P. Coppin, P. Correa, D. F. Cowen, R. Cross, P. Dave, C. De Clercq, J. J. DeLaunay, H. Dembinski, K. Deoskar, S. De Ridder, P. Desiati, K. D. de Vries, G. de Wasseige, M. de With, T. DeYoung, A. Diaz, J. C. Díaz-Vélez, H. Dujmovic, M. Dunkman, E. Dvorak, B. Eberhardt, T. Ehrhardt, P. Eller, R. Engel, P. A. Evenson, S. Fahey, A. R. Fazely, J. Felde, K. Filimonov, C. Finley, D. Fox, A. Franckowiak, E. Friedman, A. Fritz, T. K. Gaisser, J. Gallagher, E. Ganster, S. Garrappa, L. Gerhardt, K. Ghorbani, T. Glauch, T. Glüsenkamp, A. Goldschmidt, J. G. Gonzalez, D. Grant, T. Grégoire, Z. Griffith, S. Griswold, M. Günder, M. Gündüz, C. Haack, A. Hallgren, R. Halliday, L. Halve, F. Halzen, K. Hanson, A. Haungs, D. Hebecker, D. Heereman, P. Heix, K. Helbing, R. Hellauer, F. Henningsen, S. Hickford, J. Hignight, G. C. Hill, K. D. Hoffman, R. Hoffmann, T. Hoinka, B. Hokanson-Fasig, K. Hoshina, F. Huang, M. Huber, T. Huber, K. Hultqvist, M. Hünnefeld, R. Hussain, S. In, N. Iovine, A. Ishihara, M. Jansson, G. S. Japaridze, M. Jeong, K. Jero, B. J. P. Jones, F. Jonske, R. Joppe, D. Kang, W. Kang, A. Kappes, D. Kappesser, T. Karg, M. Karl, A. Karle, U. Katz, M. Kauer, J. L. Kelley, A. Kheirandish, J. Kim, T. Kintscher, J. Kiryluk, T. Kittler,

S. R. Klein, R. Koirala, H. Kolanoski, L. Köpke, C. Kopper, S. Kopper, D. J. Koskinen, M. Kowalski, K. Krings, G. Krückl, N. Kulacz, N. Kurahashi, A. Kyriacou, J. L. Lanfranchi, M. J. Larson, F. Lauber, J. P. Lazar, K. Leonard, M. Lesiak-Bzdak, A. Leszczyńska, M. Leuermann, Q. R. Liu, E. Lohfink, C. J. Lozano Mariscal, L. Lu, F. Lucarelli, J. Lünemann, W. Luszczak, Y. Lyu, W. Y. Ma, J. Madsen, G. Maggi, K. B. M. Mahn, Y. Makino, P. Mallik, K. Mallot, S. Mancina, I. C. Mariş, R. Maruyama, K. Mase, R. Maunu, F. McNally, K. Meagher, M. Medici, A. Medina, M. Meier, S. Meighen-Berger, G. Merino, T. Meures, J. Micallef, D. Mockler, G. Momenté, T. Montaruli, R. W. Moore, R. Morse, M. Moulai, P. Muth, R. Nagai, U. Naumann, G. Neer, H. Niederhausen, M. U. Nisa, S. C. Nowicki, D. R. Nygren, A. Obertacke Pollmann, M. Oehler, A. Olivas, A. O'Murchadha, E. O'Sullivan, T. Palczewski, H. Pandya, D. V. Pankova, N. Park, P. Peiffer, C. Pérez de los Heros, S. Philippen, D. Pieloth, S. Pieper, E. Pinat, A. Pizzuto, M. Plum, A. Porcelli, P. B. Price, G. T. Przybylski, C. Raab, A. Raissi, M. Rameez, L. Rauch, K. Rawlins, I. C. Rea, A. Rehman, R. Reimann, B. Relethford, M. Renschler, G. Renzi, E. Resconi, W. Rhode, M. Richman, S. Robertson, M. Rongen, C. Rott, T. Ruhe, D. Ryckbosch, D. Rysewyk, I. Safa, S. E. Sanchez Herrera, A. Sandrock, J. Sandroos, M. Santander, S. Sarkar, S. Sarkar, K. Satalecka, M. Schaufel, H. Schieler, P. Schlunder, T. Schmidt, A. Schneider, J. Schneider, F. G. Schröder, L. Schumacher, S. Sclafani, D. Seckel, S. Seunarine, S. Shefali, M. Silva, R. Snihur, J. Soedingrekso, D. Soldin, M. Song, G. M. Spiczak, C. Spiering, J. Stachurska, M. Stamatikos, T. Stanev, R. Stein, J. Stettner, A. Steuer, T. Stezelberger, R. G. Stokstad, A. Stößl, N. L. Strotjohann, T. Stürwald, T. Stuttard, G. W. Sullivan, I. Taboada, F. Tenholt, S. Ter-Antonyan, A. Terliuk, S. Tilav, K. Tollefson, L. Tomankova, C. Tönnis, S. Toscano, D. Tosi, A. Trettin, M. Tselengidou, C. F. Tung, A. Turcati, R. Turcotte, C. F. Turley, B. Ty, E. Unger, M. A. Unland Elorrieta, M. Usner, J. Vandenbroucke, W. Van Driessche, D. van Eijk, N. van Eijndhoven, J. van Santen, S. Verpoest, M. Vraeghe, C. Walck, A. Wallace, M. Wallraff, N. Wandkowsky, T. B. Watson, C. Weaver, A. Weindl, M. J. Weiss, J. Weldert, C. Wendt, J. Werthebach, B. J. Whelan, N. Whitehorn, K. Wiebe, C. H. Wiebusch, L. Wille, D. R. Williams, L. Wills, M. Wolf, J. Wood, T. R. Wood, K. Woschnagg, G. Wrede, D. L. Xu, X. W. Xu, Y. Xu, J. P. Yanez, G. Yodh, S. Yoshida, T. Yuan, and M. Zöcklein.

Characteristics of the Diffuse Astrophysical Electron and Tau Neutrino Flux with Six Years of IceCube High Energy Cascade Data.

Phys. Rev. Lett., 125:121104, Sep 2020.

[3] M. G. Aartsen, M. Ackermann, J. Adams, J. A. Aguilar, M. Ahlers, M. Ahrens, D. Altmann, K. Andeen, T. Anderson, I. Ansseau, G. Anton, C. Argüelles, J. Auffenberg, S. Axani, P. Backes, H. Bagherpour, X. Bai, A. Barbano, J. P. Barron, S. W. Barwick, V. Baum, R. Bay, J. J. Beatty, J. Becker Tjus, K. H. Becker, S. BenZvi, D. Berley, E. Bernardini, D. Z. Besson, G. Binder, D. Bindig, E. Blaufuss, S. Blot, C. Bohm, M. Börner, F. Bos, S. Böser, O. Botner, E. Bourbeau, J. Bourbeau, F. Bradascio, J. Braun, H. P. Bretz, S. Bron, J. Brostean-Kaiser, A. Burgman, R. S. Busse, T. Carver, C. Chen, E. Cheung, D. Chirkin, K. Clark, L. Classen, G. H. Collin, J. M. Conrad, P. Coppin, P. Correa, D. F. Cowen, R. Cross, P. Dave, M. Day, J. P. A. M. de André, C. De Clercq, J. J. DeLaunay, H. Dembinski, K. Deoskar, S. De Ridder, P. Desiati, K. D. de Vries, G. de Wasseige, M. de With, T. DeYoung, J. C. Díaz-Vélez, H. Dujmovic, M. Dunkman, E. Dvorak, B. Eberhardt, T. Ehrhardt, B. Eichmann, P. Eller, P. A. Evenson, S. Fahey, A. R. Fazely, J. Felde, K. Filimonov, C. Finley, A. Franckowiak, E. Friedman, A. Fritz, T. K. Gaisser, J. Gallagher, E. Ganster, S. Garrappa, L. Gerhardt, K. Ghorbani, W. Giang, T. Glauch, T. Glüsenkamp, A. Goldschmidt, J. G. Gonzalez, D. Grant, Z. Griffith, C. Haack, A. Hallgren, L. Halve, F. Halzen, K. Hanson, D. Hebecker, D. Heereman, K. Helbing, R. Hellauer, S. Hickford, J. Hignight, G. C. Hill, K. D. Hoffman, R. Hoffmann, T. Hoinka, B. Hokanson-Fasig, K. Hoshina, F. Huang, M. Huber, K. Hultqvist, M. Hünnefeld, R. Hussain, S. In, N. Iovine, A. Ishihara, E. Jacobi, G. S. Japaridze, M. Jeong, K. Jero, B. J. P. Jones, P. Kalaczynski, W. Kang, A. Kappes, D. Kappesser, T. Karg, A. Karle, U. Katz, M. Kauer, A. Keivani, J. L. Kelley, A. Kheirandish, J. Kim, T. Kintscher, J. Kiryluk, T. Kittler, S. R. Klein, R. Koirala, H. Kolanoski, L. Köpke, C. Kopper, S. Kopper, D. J. Koskinen, M. Kowalski, K. Krings, M. Kroll, G. Krückl, S. Kunwar, N. Kurahashi, A. Kyriacou, M. Labare, J. L. Lanfranchi, M. J. Larson, F. Lauber, K. Leonard, M. Leuermann, Q. R. Liu, E. Lohfink, C. J. Lozano Mariscal, L. Lu, J. Lünemann, W. Luszczak, J. Madsen, G. Maggi, K. B. M. Mahn, Y. Makino, S. Mancina, I. C. Mariş, R. Maruyama, K. Mase, R. Maunu, K. Meagher, M. Medici, M. Meier, T. Menne, G. Merino, T. Meures, S. Miarecki, J. Micallef, G. Momenté, T. Montaruli, R. W. Moore, M. Moulai, R. Nagai, R. Nahnhauer, P. Nakarmi, U. Naumann, G. Neer, H. Niederhausen, S. C. Nowicki, D. R. Nygren, A. Obertacke Pollmann, A. Olivas, A. O'Murchadha, E. O'Sullivan, T. Palczewski, H. Pandya, D. V. Pankova, P. Peiffer, C. Pérez de los Heros, D. Pieloth, E. Pinat, A. Pizzuto, M. Plum, P. B. Price, G. T. Przybylski, C. Raab,

M. Rameez, L. Rauch, K. Rawlins, I. C. Rea, R. Reimann, B. Relethford, G. Renzi, E. Resconi, W. Rhode, M. Richman, S. Robertson, M. Rongen, C. Rott, T. Ruhe, D. Ryckbosch, D. Rysewyk, I. Safa, S. E. Sanchez Herrera, A. Sandrock, J. Sandroos, M. Santander, S. Sarkar, S. Sarkar, K. Satalecka, M. Schaufel, P. Schlunder, T. Schmidt, A. Schneider, J. Schneider, S. Schöneberg, L. Schumacher, S. Sclafani, D. Seckel, S. Seunarine, J. Soedingrekso, D. Soldin, M. Song, G. M. Spiczak, C. Spiering, J. Stachurska, M. Stamatikos, T. Stanev, A. Stasik, R. Stein, J. Stettner, A. Steuer, T. Stezelberger, R. G. Stokstad, A. Stößl, N. L. Strotjohann, T. Stuttard, G. W. Sullivan, M. Sutherland, I. Taboada, F. Tenholt, S. Ter-Antonyan, A. Terliuk, S. Tilav, M. N. Tobin, C. Tönnis, S. Toscano, D. Tosi, M. Tselengidou, C. F. Tung, A. Turcati, R. Turcotte, C. F. Turley, B. Ty, E. Unger, M. A. Unland Elorrieta, M. Usner, J. Vandenbroucke, W. Van Driessche, D. van Eijk, N. van Eijndhoven, S. Vanheule, J. van Santen, M. Vraeghe, C. Walck, A. Wallace, M. Wallraff, F. D. Wandler, N. Wandkowsky, T. B. Watson, C. Weaver, M. J. Weiss, C. Wendt, J. Werthebach, S. Westerhoff, B. J. Whelan, N. Whitehorn, K. Wiebe, C. H. Wiebusch, L. Wille, D. R. Williams, L. Wills, M. Wolf, J. Wood, T. R. Wood, E. Woolsey, K. Woschnagg, G. Wrede, D. L. Xu, X. W. Xu, Y. Xu, J. P. Yanez, G. Yodh, S. Yoshida, and T. Yuan.
Search for steady point-like sources in the astrophysical muon neutrino flux with 8 years of IceCube data.
European Physical Journal C, 79(3):234, March 2019.

[4] R. Abbasi, M. Ackermann, J. Adams, J. A. Aguilar, M. Ahlers, M. Ahrens, C. Alispach, Jr. Alves, A. A., N. M. Amin, K. Andeen, T. Anderson, I. Ansseau, G. Anton, C. Argüelles, S. Axani, X. Bai, A. Balagopal V., A. Barbano, S. W. Barwick, B. Bastian, V. Basu, V. Baum, S. Baur, R. Bay, J. J. Beatty, K. H. Becker, J. Becker Tjus, C. Bellenghi, S. BenZvi, D. Berley, E. Bernardini, D. Z. Besson, G. Binder, D. Bindig, E. Blaufuss, S. Blot, S. Böser, O. Botner, J. Böttcher, E. Bourbeau, J. Bourbeau, F. Bradascio, J. Braun, S. Bron, J. Brostean-Kaiser, A. Burgman, R. S. Busse, M. A. Campana, C. Chen, D. Chirkin, S. Choi, B. A. Clark, K. Clark, L. Classen, A. Coleman, G. H. Collin, J. M. Conrad, P. Coppin, P. Correa, D. F. Cowen, R. Cross, P. Dave, C. De Clercq, J. J. DeLaunay, H. Dembinski, K. Deoskar, S. De Ridder, A. Desai, P. Desiati, K. D. de Vries, G. de Wasseige, M. de With, T. DeYoung, S. Dharani, A. Diaz, J. C. Díaz-Vélez, H. Dujmovic, M. Dunkman, M. A. DuVernois, E. Dvorak, T. Ehrhardt, P. Eller, R. Engel, J. Evans, P. A. Evenson, S. Fahey, A. R. Fazely, S. Fiedlschuster, A. T. Fienberg, K. Fil-

imonov, C. Finley, L. Fischer, D. Fox, A. Franckowiak, E. Friedman, A. Fritz, P. Fürst, T. K. Gaisser, J. Gallagher, E. Ganster, S. Garrappa, L. Gerhardt, A. Ghadimi, C. Glaser, T. Glauch, T. Glüsenkamp, A. Goldschmidt, J. G. Gonzalez, S. Goswami, D. Grant, T. Grégoire, Z. Griffith, S. Griswold, M. Gündüz, C. Haack, A. Hallgren, R. Halliday, L. Halve, F. Halzen, M. Ha Minh, K. Hanson, J. Hardin, A. A. Harnisch, A. Haungs, S. Hauser, D. Hebecker, K. Helbing, F. Henningsen, E. C. Hettinger, S. Hickford, J. Hignight, C. Hill, G. C. Hill, K. D. Hoffman, R. Hoffmann, T. Hoinka, B. Hokanson-Fasig, K. Hoshina, F. Huang, M. Huber, T. Huber, K. Hultqvist, M. Hünnefeld, R. Hussain, S. In, N. Iovine, A. Ishihara, M. Jansson, G. S. Japaridze, M. Jeong, B. J. P. Jones, R. Joppe, D. Kang, W. Kang, X. Kang, A. Kappes, D. Kappesser, T. Karg, M. Karl, A. Karle, U. Katz, M. Kauer, M. Kellermann, J. L. Kelley, A. Kheirandish, J. Kim, K. Kin, T. Kintscher, J. Kiryluk, S. R. Klein, R. Koirala, H. Kolanoski, L. Köpke, C. Kopper, S. Kopper, D. J. Koskinen, P. Koundal, M. Kovacevich, M. Kowalski, K. Krings, G. Krückl, N. Kurahashi, A. Kyriacou, C. Lagunas Gualda, J. L. Lanfranchi, M. J. Larson, F. Lauber, J. P. Lazar, K. Leonard, A. Leszczyńska, Y. Li, Q. R. Liu, E. Lohfink, C. J. Lozano Mariscal, L. Lu, F. Lucarelli, A. Ludwig, W. Luszczak, Y. Lyu, W. Y. Ma, J. Madsen, K. B. M. Mahn, Y. Makino, P. Mallik, S. Mancina, I. C. Mariş, R. Maruyama, K. Mase, F. McNally, K. Meagher, A. Medina, M. Meier, S. Meighen-Berger, J. Merz, J. Micallef, D. Mockler, G. Momenté, T. Montaruli, R. W. Moore, R. Morse, M. Moulai, R. Naab, R. Nagai, U. Naumann, J. Necker, L. V. Nguyn, H. Niederhausen, M. U. Nisa, S. C. Nowicki, D. R. Nygren, A. Obertacke Pollmann, M. Oehler, A. Olivas, E. O'Sullivan, H. Pandya, D. V. Pankova, N. Park, G. K. Parker, E. N. Paudel, P. Peiffer, C. Pérez de los Heros, S. Philippen, D. Pieloth, S. Pieper, A. Pizzuto, M. Plum, Y. Popovych, A. Porcelli, M. Prado Rodriguez, P. B. Price, B. Pries, G. T. Przybylski, C. Raab, A. Raissi, M. Rameez, K. Rawlins, I. C. Rea, A. Rehman, R. Reimann, M. Renschler, G. Renzi, E. Resconi, S. Reusch, W. Rhode, M. Richman, B. Riedel, S. Robertson, G. Roellinghoff, M. Rongen, C. Rott, T. Ruhe, D. Ryckbosch, D. Rysewyk Cantu, I. Safa, S. E. Sanchez Herrera, A. Sandrock, J. Sandroos, M. Santander, S. Sarkar, S. Sarkar, K. Satalecka, M. Scharf, M. Schaufel, H. Schieler, P. Schlunder, T. Schmidt, A. Schneider, J. Schneider, F. G. Schröder, L. Schumacher, S. Sclafani, D. Seckel, S. Seunarine, S. Shefali, M. Silva, B. Smithers, R. Snihur, J. Soedingrekso, D. Soldin, G. M. Spiczak, C. Spiering, J. Stachurska, M. Stamatikos, T. Stanev, R. Stein, J. Stettner, A. Steuer, T. Stezelberger, R. G. Stokstad, T. Stut-

tard, G. W. Sullivan, I. Taboada, F. Tenholt, S. Ter-Antonyan, S. Tilav, F. Tischbein, K. Tollefson, L. Tomankova, C. Tönnis, S. Toscano, D. Tosi, A. Trettin, M. Tselengidou, C. F. Tung, A. Turcati, R. Turcotte, C. F. Turley, J. P. Twagirayezu, B. Ty, M. A. Unland Elorrieta, J. Vandenbroucke, D. van Eijk, N. van Eijndhoven, D. Vannerom, J. van Santen, S. Verpoest, M. Vraeghe, C. Walck, A. Wallace, T. B. Watson, C. Weaver, A. Weindl, M. J. Weiss, J. Weldert, C. Wendt, J. Werthebach, M. Weyrauch, B. J. Whelan, N. Whitehorn, K. Wiebe, C. H. Wiebusch, D. R. Williams, M. Wolf, K. Woschnagg, G. Wrede, J. Wulff, X. W. Xu, Y. Xu, J. P. Yanez, S. Yoshida, T. Yuan, Z. Zhang, and IceCube Collaboration.
A Search for Time-dependent Astrophysical Neutrino Emission with IceCube Data from 2012 to 2017.
ApJ, 911(1):67, April 2021.

[5] A. A. Abdo, M. Ackermann, I. Agudo, M. Ajello, H. D. Aller, M. F. Aller, E. Angelakis, A. A. Arkharov, M. Axelsson, U. Bach, L. Baldini, J. Ballet, G. Barbiellini, D. Bastieri, B. M. Baughman, K. Bechtol, R. Bellazzini, E. Benitez, A. Berdyugin, B. Berenji, R. D. Bland ford, E. D. Bloom, M. Boettcher, E. Bonamente, A. W. Borgland, J. Bregeon, A. Brez, M. Brigida, P. Bruel, T. H. Burnett, D. Burrows, S. Buson, G. A. Caliandro, L. Calzoletti, R. A. Cameron, M. Capalbi, P. A. Caraveo, D. Carosati, J. M. Casand jian, E. Cavazzuti, C. Cecchi, Ö. Çelik, E. Charles, S. Chaty, A. Chekhtman, W. P. Chen, J. Chiang, G. Chincarini, S. Ciprini, R. Claus, J. Cohen-Tanugi, S. Colafrancesco, L. R. Cominsky, J. Conrad, L. Costamante, S. Cutini, F. D'ammando, R. Deitrick, V. D'Elia, C. D. Dermer, A. de Angelis, F. de Palma, S. W. Digel, I. Donnarumma, E. do Couto e. Silva, P. S. Drell, R. Dubois, D. Dultzin, D. Dumora, A. Falcone, C. Farnier, C. Favuzzi, S. J. Fegan, W. B. Focke, E. Forné, P. Fortin, M. Frailis, L. Fuhrmann, Y. Fukazawa, S. Funk, P. Fusco, J. L. Gómez, F. Gargano, D. Gasparrini, N. Gehrels, S. Germani, B. Giebels, N. Giglietto, P. Giommi, F. Giordano, A. Giuliani, T. Glanzman, G. Godfrey, I. A. Grenier, C. Gronwall, J. E. Grove, L. Guillemot, S. Guiriec, M. A. Gurwell, D. Hadasch, Y. Hanabata, A. K. Harding, M. Hayashida, E. Hays, S. E. Healey, J. Heidt, D. Hiriart, D. Horan, E. A. Hoversten, R. E. Hughes, R. Itoh, M. S. Jackson, G. Jóhannesson, A. S. Johnson, W. N. Johnson, S. G. Jorstad, M. Kadler, T. Kamae, H. Katagiri, J. Kataoka, N. Kawai, J. Kennea, M. Kerr, G. Kimeridze, J. Knödlseder, M. L. Kocian, E. N. Kopatskaya, E. Koptelova, T. S. Konstantinova, Y. Y. Kovalev, Yu. A. Kovalev, O. M. Kurtanidze, M. Kuss, J. Lande, V. M. Larionov, L. La-

tronico, P. Leto, E. Lindfors, F. Longo, F. Loparco, B. Lott, M. N. Lovellette, P. Lubrano, G. M. Madejski, A. Makeev, P. Marchegiani, A. P. Marscher, F. Marshall, W. Max-Moerbeck, M. N. Mazziotta, W. McConville, J. E. McEnery, C. Meurer, P. F. Michelson, W. Mitthumsiri, T. Mizuno, A. A. Moiseev, C. Monte, M. E. Monzani, A. Morselli, I. V. Moskalenko, S. Murgia, I. Nestoras, K. Nilsson, N. A. Nizhelsky, P. L. Nolan, J. P. Norris, E. Nuss, T. Ohsugi, R. Ojha, N. Omodei, E. Orlando, J. F. Ormes, J. Osborne, M. Ozaki, L. Pacciani, P. Padovani, C. Pagani, K. Page, D. Paneque, J. H. Panetta, D. Parent, M. Pasanen, V. Pavlidou, V. Pelassa, M. Pepe, M. Perri, M. Pesce-Rollins, S. Piranomonte, F. Piron, C. Pittori, T. A. Porter, S. Puccetti, F. Rahoui, S. Rainò, C. Raiteri, R. Rando, M. Razzano, A. Reimer, O. Reimer, T. Reposeur, J. L. Richards, S. Ritz, L. S. Rochester, A. Y. Rodriguez, R. W. Romani, J. A. Ros, M. Roth, P. Roustazadeh, F. Ryde, H. F. W. Sadrozinski, A. Sadun, D. Sanchez, A. Sander, P. M. Saz Parkinson, J. D. Scargle, A. Sellerholm, C. Sgrò, M. S. Shaw, L. A. Sigua, E. J. Siskind, D. A. Smith, P. D. Smith, G. Spandre, P. Spinelli, J. L. Starck, M. Stevenson, G. Stratta, M. S. Strickman, D. J. Suson, H. Tajima, H. Takahashi, T. Takahashi, L. O. Takalo, T. Tanaka, J. B. Thayer, J. G. Thayer, D. J. Thompson, L. Tibaldo, D. F. Torres, G. Tosti, A. Tramacere, Y. Uchiyama, T. L. Usher, V. Vasileiou, F. Verrecchia, N. Vilchez, M. Villata, V. Vitale, A. P. Waite, P. Wang, B. L. Winer, K. S. Wood, T. Ylinen, J. A. Zensus, G. V. Zhekanis, and M. Ziegler.
The Spectral Energy Distribution of Fermi Bright Blazars.
ApJ, 716(1):30–70, June 2010.

[6] A. A. Abdo, M. Ackermann, M. Ajello, E. Antolini, L. Baldini, J. Ballet, G. Barbiellini, D. Bastieri, K. Bechtol, R. Bellazzini, B. Berenji, R. D. Blandford, E. Bonamente, A. W. Borgland, J. Bregeon, A. Brez, M. Brigida, P. Bruel, R. Buehler, S. Buson, G. A. Caliandro, R. A. Cameron, A. Cannon, P. A. Caraveo, S. Carrigan, J. M. Casandjian, C. Cecchi, Ö. Çelik, E. Charles, A. Chekhtman, C. C. Cheung, J. Chiang, S. Ciprini, R. Claus, J. Cohen-Tanugi, J. Conrad, L. Costamante, S. Cutini, C. D. Dermer, F. de Palma, D. Donato, E. do Couto e. Silva, P. S. Drell, R. Dubois, L. Escande, C. Favuzzi, S. J. Fegan, J. Finke, W. B. Focke, P. Fortin, M. Frailis, Y. Fukazawa, S. Funk, P. Fusco, F. Gargano, D. Gasparrini, N. Gehrels, S. Germani, N. Giglietto, F. Giordano, M. Giroletti, T. Glanzman, G. Godfrey, I. A. Grenier, S. Guiriec, D. Hadasch, M. Hayashida, E. Hays, R. E. Hughes, R. Itoh, G. Jóhannesson, A. S. Johnson, W. N. Johnson, T. Kamae, H. Katagiri, J. Kataoka, J. Knödlseder, M. Kuss, J. Lande, S. Larsson,

L. Latronico, S. H. Lee, M. Llena Garde, F. Longo, F. Loparco, B. Lott, M. N. Lovellette, P. Lubrano, A. Makeev, M. N. Mazziotta, J. E. McEnery, J. Mehault, P. F. Michelson, T. Mizuno, C. Monte, M. E. Monzani, A. Morselli, I. V. Moskalenko, S. Murgia, T. Nakamori, M. Naumann-Godo, S. Nishino, P. L. Nolan, J. P. Norris, E. Nuss, T. Ohsugi, A. Okumura, N. Omodei, E. Orlando, J. F. Ormes, M. Ozaki, D. Paneque, J. H. Panetta, D. Parent, V. Pelassa, M. Pepe, M. Pesce-Rollins, F. Piron, T. A. Porter, S. Rainò, R. Rando, M. Razzano, A. Reimer, O. Reimer, S. Ritz, M. Roth, H. F. W. Sadrozinski, D. Sanchez, A. Sander, F. K. Schinzel, C. Sgrò, E. J. Siskind, P. D. Smith, K. V. Sokolovsky, G. Spandre, P. Spinelli, M. S. Strickman, D. J. Suson, H. Takahashi, T. Tanaka, J. B. Thayer, J. G. Thayer, D. J. Thompson, L. Tibaldo, D. F. Torres, G. Tosti, A. Tramacere, T. Uehara, T. L. Usher, J. Vandenbroucke, V. Vasileiou, N. Vilchez, V. Vitale, A. P. Waite, E. Wallace, P. Wang, B. L. Winer, K. S. Wood, Z. Yang, T. Ylinen, M. Ziegler, A. Berdyugin, M. Boettcher, A. Carramiñana, L. Carrasco, E. de la Fuente, C. Diltz, T. Hovatta, V. Kadenius, Y. Y. Kovalev, A. Lähteenmäki, E. Lindfors, A. P. Marscher, K. Nilsson, D. Pereira, R. Reinthal, P. Roustazadeh, T. Savolainen, A. Sillanpää, L. O. Takalo, and M. Tornikoski.

The First Fermi Multifrequency Campaign on BL Lacertae: Characterizing the Low-activity State of the Eponymous Blazar.

ApJ, 730(2):101, April 2011.

[7] S. Abdollahi, F. Acero, L. Baldini, J. Ballet, D. Bastieri, R. Bellazzini, B. Berenji, A. Berretta, E. Bissaldi, R. D. Blandford, E. Bloom, R. Bonino, A. Brill, R. J. Britto, P. Bruel, T. H. Burnett, S. Buson, R. A. Cameron, R. Caputo, P. A. Caraveo, D. Castro, S. Chaty, C. C. Cheung, G. Chiaro, N. Cibrario, S. Ciprini, J. Coronado-Blázquez, M. Crnogorcevic, S. Cutini, F. D'Ammando, S. De Gaetano, S. W. Digel, N. Di Lalla, F. Dirirsa, L. Di Venere, A. Domínguez, V. Fallah Ramazani, S. J. Fegan, E. C. Ferrara, A. Fiori, H. Fleischhack, A. Franckowiak, Y. Fukazawa, S. Funk, P. Fusco, G. Galanti, V. Gammaldi, F. Gargano, S. Garrappa, D. Gasparrini, F. Giacchino, N. Giglietto, F. Giordano, M. Giroletti, T. Glanzman, D. Green, I. A. Grenier, M. H. Grondin, L. Guillemot, S. Guiriec, M. Gustafsson, A. K. Harding, E. Hays, J. W. Hewitt, D. Horan, X. Hou, G. Jóhannesson, C. Karwin, T. Kayanoki, M. Kerr, M. Kuss, D. Landriu, S. Larsson, L. Latronico, M. Lemoine-Goumard, J. Li, I. Liodakis, F. Longo, F. Loparco, B. Lott, P. Lubrano, S. Maldera, D. Malyshev, A. Manfreda, G. Martí-Devesa, M. N. Mazziotta, I. Mereu, M. Meyer, P. F. Michelson, N. Mirabal, W. Mitthumsiri, T. Mizuno, A. A. Moiseev,

M. E. Monzani, A. Morselli, I. V. Moskalenko, M. Negro, E. Nuss, N. Omodei, M. Orienti, E. Orlando, D. Paneque, Z. Pei, J. S. Perkins, M. Persic, M. Pesce-Rollins, V. Petrosian, R. Pillera, H. Poon, T. A. Porter, G. Principe, S. Rainò, R. Rando, B. Rani, M. Razzano, S. Razzaque, A. Reimer, O. Reimer, T. Reposeur, M. Sánchez-Conde, P. M. Saz Parkinson, L. Scotton, D. Serini, C. Sgrò, E. J. Siskind, D. A. Smith, G. Spandre, P. Spinelli, K. Sueoka, D. J. Suson, H. Tajima, D. Tak, J. B. Thayer, D. J. Thompson, D. F. Torres, E. Troja, J. Valverde, K. Wood, and G. Zaharijas.
Incremental Fermi Large Area Telescope Fourth Source Catalog.
ApJSS, 260(2):53, June 2022.

[8] A. U. Abeysekara, W. Benbow, R. Bird, T. Brantseg, R. Brose, M. Buchovecky, J. H. Buckley, V. Bugaev, M. P. Connolly, W. Cui, M. K. Daniel, A. Falcone, Q. Feng, J. P. Finley, L. Fortson, A. Furniss, G. H. Gillanders, I. Gunawardhana, M. Hütten, D. Hanna, O. Hervet, J. Holder, G. Hughes, T. B. Humensky, C. A. Johnson, P. Kaaret, P. Kar, M. Kertzman, F. Krennrich, M. J. Lang, T. T. Y. Lin, S. McArthur, P. Moriarty, R. Mukherjee, S. O'Brien, R. A. Ong, A. N. Otte, N. Park, A. Petrashyk, M. Pohl, E. Pueschel, J. Quinn, K. Ragan, P. T. Reynolds, G. T. Richards, E. Roache, C. Rulten, I. Sadeh, M. Santander, G. H. Sembroski, K. Shahinyan, S. P. Wakely, A. Weinstein, R. M. Wells, P. Wilcox, D. A. Williams, B. Zitzer, VERITAS Collaboration, S. G. Jorstad, A. P. Marscher, M. L. Lister, Y. Y. Kovalev, A. B. Pushkarev, T. Savolainen, I. Agudo, S. N. Molina, J. L. Gómez, V. M. Larionov, G. A. Borman, A. A. Mokrushina, M. Tornikoski, A. Lähteenmäki, W. Chamani, S. Enestam, S. Kiehlmann, T. Hovatta, P. S. Smith, and P. Pontrelli.
Multiwavelength Observations of the Blazar BL Lacertae: A New Fast TeV Gamma-Ray Flare.
ApJ, 856(2):95, April 2018.

[9] Atreya Acharyya, Paula M. Chadwick, and Anthony M. Brown.
Locating the gamma-ray emission region in the brightest Fermi-LAT flat-spectrum radio quasars.
MNRAS, 500(4):5297–5321, January 2021.

[10] M. Ackermann, M. Ajello, A. Albert, W. B. Atwood, L. Baldini, J. Ballet, G. Barbiellini, D. Bastieri, J. Becerra Gonzalez, R. Bellazzini, E. Bissaldi, R. D. Blandford, E. D. Bloom, R. Bonino, E. Bottacini, J. Bregeon, P. Bruel, R. Buehler, S. Buson, G. A. Caliandro, R. A. Cameron, R. Caputo, M. Caragiulo, P. A. Caraveo, E. Cavazzuti, C. Cecchi, A. Chekhtman, J. Chiang, G. Chiaro, S. Ciprini,

J. Cohen-Tanugi, J. Conrad, S. Cutini, F. D'Ammando, A. de Angelis, F. de Palma, R. Desiante, L. Di Venere, A. Domínguez, P. S. Drell, C. Favuzzi, S. J. Fegan, E. C. Ferrara, W. B. Focke, L. Fuhrmann, Y. Fukazawa, P. Fusco, F. Gargano, D. Gasparrini, N. Giglietto, P. Giommi, F. Giordano, M. Giroletti, G. Godfrey, D. Green, I. A. Grenier, J. E. Grove, S. Guiriec, A. K. Harding, E. Hays, J. W. Hewitt, A. B. Hill, D. Horan, T. Jogler, G. Jóhannesson, A. S. Johnson, T. Kamae, M. Kuss, S. Larsson, L. Latronico, J. Li, L. Li, F. Longo, F. Loparco, B. Lott, M. N. Lovellette, P. Lubrano, J. Magill, S. Maldera, A. Manfreda, W. Max-Moerbeck, M. Mayer, M. N. Mazziotta, J. E. McEnery, P. F. Michelson, T. Mizuno, M. E. Monzani, A. Morselli, I. V. Moskalenko, S. Murgia, E. Nuss, M. Ohno, T. Ohsugi, R. Ojha, N. Omodei, E. Orlando, J. F. Ormes, D. Paneque, T. J. Pearson, J. S. Perkins, M. Perri, M. Pesce-Rollins, V. Petrosian, F. Piron, G. Pivato, T. A. Porter, S. Rainò, R. Rando, M. Razzano, A. Readhead, A. Reimer, O. Reimer, A. Schulz, C. Sgrò, E. J. Siskind, F. Spada, G. Spandre, P. Spinelli, D. J. Suson, H. Takahashi, J. B. Thayer, D. J. Thompson, L. Tibaldo, D. F. Torres, G. Tosti, E. Troja, Y. Uchiyama, G. Vianello, K. S. Wood, M. Wood, S. Zimmer, A. Berdyugin, R. H. D. Corbet, T. Hovatta, E. Lindfors, K. Nilsson, R. Reinthal, A. Sillanpää, A. Stamerra, L. O. Takalo, and M. J. Valtonen.

Multiwavelength Evidence for Quasi-periodic Modulation in the Gamma-Ray Blazar PG 1553+113.

ApJL, 813(2):L41, November 2015.

[11] M. Ackermann, M. Ajello, A. Allafort, E. Antolini, W. B. Atwood, M. Axelsson, L. Baldini, J. Ballet, G. Barbiellini, D. Bastieri, K. Bechtol, R. Bellazzini, B. Berenji, R. D. Blandford, E. D. Bloom, E. Bonamente, A. W. Borgland, E. Bottacini, A. Bouvier, J. Bregeon, M. Brigida, P. Bruel, R. Buehler, T. H. Burnett, S. Buson, G. A. Caliandro, R. A. Cameron, P. A. Caraveo, J. M. Casandjian, E. Cavazzuti, C. Cecchi, E. Charles, C. C. Cheung, J. Chiang, S. Ciprini, R. Claus, J. Cohen-Tanugi, J. Conrad, L. Costamante, S. Cutini, A. de Angelis, F. de Palma, C. D. Dermer, S. W. Digel, E. do Couto e. Silva, P. S. Drell, R. Dubois, L. Escande, C. Favuzzi, S. J. Fegan, E. C. Ferrara, J. Finke, W. B. Focke, P. Fortin, M. Frailis, Y. Fukazawa, S. Funk, P. Fusco, F. Gargano, D. Gasparrini, N. Gehrels, S. Germani, B. Giebels, N. Giglietto, P. Giommi, F. Giordano, M. Giroletti, T. Glanzman, G. Godfrey, I. A. Grenier, J. E. Grove, S. Guiriec, M. Gustafsson, D. Hadasch, M. Hayashida, E. Hays, S. E. Healey, D. Horan, X. Hou, R. E. Hughes, G. Iafrate,

G. Jóhannesson, A. S. Johnson, W. N. Johnson, T. Kamae, H. Katagiri, J. Kataoka, J. Knödlseder, M. Kuss, J. Lande, S. Larsson, L. Latronico, F. Longo, F. Loparco, B. Lott, M. N. Lovellette, P. Lubrano, G. M. Madejski, M. N. Mazziotta, W. McConville, J. E. McEnery, P. F. Michelson, W. Mitthumsiri, T. Mizuno, A. A. Moiseev, C. Monte, M. E. Monzani, E. Moretti, A. Morselli, I. V. Moskalenko, S. Murgia, T. Nakamori, M. Naumann-Godo, P. L. Nolan, J. P. Norris, E. Nuss, M. Ohno, T. Ohsugi, A. Okumura, N. Omodei, M. Orienti, E. Orlando, J. F. Ormes, M. Ozaki, D. Paneque, D. Parent, M. Pesce-Rollins, M. Pierbattista, S. Piranomonte, F. Piron, G. Pivato, T. A. Porter, S. Rainò, R. Rando, M. Razzano, S. Razzaque, A. Reimer, O. Reimer, S. Ritz, L. S. Rochester, R. W. Romani, M. Roth, D. A. Sanchez, C. Sbarra, J. D. Scargle, T. L. Schalk, C. Sgrò, M. S. Shaw, E. J. Siskind, G. Spandre, P. Spinelli, A. W. Strong, D. J. Suson, H. Tajima, H. Takahashi, T. Takahashi, T. Tanaka, J. G. Thayer, J. B. Thayer, D. J. Thompson, L. Tibaldo, M. Tinivella, D. F. Torres, G. Tosti, E. Troja, Y. Uchiyama, J. Vandenbroucke, V. Vasileiou, G. Vianello, V. Vitale, A. P. Waite, E. Wallace, P. Wang, B. L. Winer, D. L. Wood, K. S. Wood, and S. Zimmer.

The Second Catalog of Active Galactic Nuclei Detected by the Fermi Large Area Telescope.

ApJ, 743(2):171, December 2011.

[12] M. Ackermann, M. Ajello, L. Baldini, J. Ballet, G. Barbiellini, D. Bastieri, J. Becerra Gonzalez, R. Bellazzini, E. Bissaldi, R. D. Blandford, E. D. Bloom, R. Bonino, E. Bottacini, J. Bregeon, P. Bruel, R. Buehler, S. Buson, R. A. Cameron, M. Caragiulo, P. A. Caraveo, E. Cavazzuti, C. Cecchi, C. C. Cheung, J. Chiang, G. Chiaro, S. Ciprini, J. Conrad, D. Costantin, F. Costanza, S. Cutini, F. D'Ammando, F. de Palma, R. Desiante, S. W. Digel, N. Di Lalla, M. Di Mauro, L. Di Venere, A. Domínguez, P. S. Drell, C. Favuzzi, S. J. Fegan, E. C. Ferrara, J. Finke, W. B. Focke, Y. Fukazawa, S. Funk, P. Fusco, F. Gargano, D. Gasparrini, N. Giglietto, F. Giordano, M. Giroletti, D. Green, I. A. Grenier, L. Guillemot, S. Guiriec, D. H. Hartmann, E. Hays, D. Horan, T. Jogler, G. Jóhannesson, A. S. Johnson, M. Kuss, G. La Mura, S. Larsson, L. Latronico, J. Li, F. Longo, F. Loparco, M. N. Lovellette, P. Lubrano, J. D. Magill, S. Maldera, A. Manfreda, L. Marcotulli, M. N. Mazziotta, P. F. Michelson, N. Mirabal, W. Mitthumsiri, T. Mizuno, M. E. Monzani, A. Morselli, I. V. Moskalenko, M. Negro, E. Nuss, T. Ohsugi, R. Ojha, N. Omodei, M. Orienti, E. Orlando, J. F. Ormes, V. S. Paliya, D. Paneque, J. S. Perkins, M. Persic, M. Pesce-Rollins, F. Piron, T. A. Porter, G. Principe, S. Rainò,

R. Rando, B. Rani, M. Razzano, S. Razzaque, A. Reimer, O. Reimer, R. W. Romani, C. Sgrò, D. Simone, E. J. Siskind, F. Spada, G. Spandre, P. Spinelli, C. S. Stalin, L. Stawarz, D. J. Suson, M. Takahashi, K. Tanaka, J. B. Thayer, D. J. Thompson, D. F. Torres, E. Torresi, G. Tosti, E. Troja, G. Vianello, and K. S. Wood.
Gamma-Ray Blazars within the First 2 Billion Years.
ApJL, 837(1):L5, March 2017.

[13] M. Ackermann, R. Anantua, K. Asano, L. Baldini, G. Barbiellini, D. Bastieri, J. Becerra Gonzalez, R. Bellazzini, E. Bissaldi, R. D. Blandford, E. D. Bloom, R. Bonino, E. Bottacini, P. Bruel, R. Buehler, G. A. Caliandro, R. A. Cameron, M. Caragiulo, P. A. Caraveo, E. Cavazzuti, C. Cecchi, C. C. Cheung, J. Chiang, G. Chiaro, S. Ciprini, J. Cohen-Tanugi, F. Costanza, S. Cutini, F. D'Ammando, F. de Palma, R. Desiante, S. W. Digel, N. Di Lalla, M. Di Mauro, L. Di Venere, P. S. Drell, C. Favuzzi, S. J. Fegan, E. C. Ferrara, Y. Fukazawa, S. Funk, P. Fusco, F. Gargano, D. Gasparrini, N. Giglietto, F. Giordano, M. Giroletti, I. A. Grenier, L. Guillemot, S. Guiriec, M. Hayashida, E. Hays, D. Horan, G. Jóhannesson, S. Kensei, D. Kocevski, M. Kuss, G. La Mura, S. Larsson, L. Latronico, J. Li, F. Longo, F. Loparco, B. Lott, M. N. Lovellette, P. Lubrano, G. M. Madejski, J. D. Magill, S. Maldera, A. Manfreda, M. Mayer, M. N. Mazziotta, P. F. Michelson, N. Mirabal, T. Mizuno, M. E. Monzani, A. Morselli, I. V. Moskalenko, K. Nalewajko, M. Negro, E. Nuss, T. Ohsugi, E. Orlando, D. Paneque, J. S. Perkins, M. Pesce-Rollins, F. Piron, G. Pivato, T. A. Porter, G. Principe, R. Rando, M. Razzano, S. Razzaque, A. Reimer, J. D. Scargle, C. Sgrò, M. Sikora, D. Simone, E. J. Siskind, F. Spada, P. Spinelli, L. Stawarz, J. B. Thayer, D. J. Thompson, D. F. Torres, E. Troja, Y. Uchiyama, Y. Yuan, and S. Zimmer.
Minute-timescale ¿100 MeV γ-Ray Variability during the Giant Outburst of Quasar 3C 279 Observed by Fermi-LAT in 2015 June.
ApJL, 824(2):L20, June 2016.

[14] Aditi Agarwal and Alok C. Gupta.
Multiband optical variability studies of BL Lacertae.
MNRAS, 450(1):541–551, June 2015.

[15] M. Ajello, R. Angioni, M. Axelsson, J. Ballet, G. Barbiellini, D. Bastieri, J. Becerra Gonzalez, R. Bellazzini, E. Bissaldi, E. D. Bloom, R. Bonino, E. Bottacini, P. Bruel, S. Buson, F. Cafardo, R. A. Cameron, E. Cavazzuti, S. Chen, C. C. Cheung, S. Ciprini, D. Costantin, S. Cutini, F. D'Ammando, P. de la Torre Luque, R. de Menezes, F. de Palma, A. Desai, N. Di Lalla, L. Di Venere, A. Domínguez,

F. Fana Dirirsa, E. C. Ferrara, J. Finke, A. Franckowiak, Y. Fukazawa, S. Funk, P. Fusco, F. Gargano, S. Garrappa, D. Gasparrini, N. Giglietto, F. Giordano, M. Giroletti, D. Green, I. A. Grenier, S. Guiriec, S. Harita, E. Hays, D. Horan, R. Itoh, G. Jóhannesson, M. Kovac'evic', F. Krauss, M. Kreter, M. Kuss, S. Larsson, C. Leto, J. Li, I. Liodakis, F. Longo, F. Loparco, B. Lott, M. N. Lovellette, P. Lubrano, G. M. Madejski, S. Maldera, A. Manfreda, G. Martí-Devesa, F. Massaro, M. N. Mazziotta, I. Mereu, M. Meyer, G. Migliori, N. Mirabal, T. Mizuno, M. E. Monzani, A. Morselli, I. V. Moskalenko, M. Negro, R. Nemmen, E. Nuss, L. S. Ojha, R. Ojha, N. Omodei, M. Orienti, E. Orlando, J. F. Ormes, V. S. Paliya, Z. Pei, H. Peña-Herazo, M. Persic, M. Pesce-Rollins, L. Petrov, F. Piron, H. Poon, G. Principe, S. Rainò, R. Rando, B. Rani, M. Razzano, S. Razzaque, A. Reimer, O. Reimer, F. K. Schinzel, D. Serini, C. Sgrò, E. J. Siskind, G. Spandre, P. Spinelli, D. J. Suson, Y. Tachibana, D. J. Thompson, D. F. Torres, E. Torresi, E. Troja, J. Valverde, P. van Zyl, and M. Yassine.
The Fourth Catalog of Active Galactic Nuclei Detected by the Fermi Large Area Telescope.
ApJ, 892(2):105, April 2020.

[16] J. Albert, E. Aliu, H. Anderhub, P. Antoranz, A. Armada, C. Baixeras, J. A. Barrio, H. Bartko, D. Bastieri, J. K. Becker, W. Bednarek, K. Berger, C. Bigongiari, A. Biland, R. K. Bock, P. Bordas, V. Bosch-Ramon, T. Bretz, I. Britvitch, M. Camara, E. Carmona, A. Chilingarian, J. A. Coarasa, S. Commichau, J. L. Contreras, J. Cortina, M. T. Costado, V. Curtef, V. Danielyan, F. Dazzi, A. De Angelis, C. Delgado, R. de los Reyes, B. De Lotto, E. Domingo-Santamaría, D. Dorner, M. Doro, M. Errando, M. Fagiolini, D. Ferenc, E. Fernández, R. Firpo, J. Flix, M. V. Fonseca, L. Font, M. Fuchs, N. Galante, R. García-López, M. Garczarczyk, M. Gaug, M. Giller, F. Goebel, D. Hakobyan, M. Hayashida, T. Hengstebeck, A. Herrero, D. Höhne, J. Hose, C. C. Hsu, P. Jacon, T. Jogler, R. Kosyra, D. Kranich, R. Kritzer, A. Laille, E. Lindfors, S. Lombardi, F. Longo, J. López, M. López, E. Lorenz, P. Majumdar, G. Maneva, K. Mannheim, O. Mansutti, M. Mariotti, M. Martínez, D. Mazin, C. Merck, M. Meucci, M. Meyer, J. M. Miranda, R. Mirzoyan, S. Mizobuchi, A. Moralejo, K. Nilsson, J. Ninkovic, E. Oña-Wilhelmi, N. Otte, I. Oya, D. Paneque, M. Panniello, R. Paoletti, J. M. Paredes, M. Pasanen, D. Pascoli, F. Pauss, R. Pegna, M. Persic, L. Peruzzo, A. Piccioli, M. Poller, E. Prandini, N. Puchades, A. Raymers, W. Rhode, M. Ribó, J. Rico, M. Rissi, A. Robert, S. Rügamer, A. Sag-

gion, A. Sánchez, P. Sartori, V. Scalzotto, V. Scapin, R. Schmitt, T. Schweizer, M. Shayduk, K. Shinozaki, S. N. Shore, N. Sidro, A. Sillanpää, D. Sobczynska, A. Stamerra, L. S. Stark, L. Takalo, P. Temnikov, D. Tescaro, M. Teshima, N. Tonello, D. F. Torres, N. Turini, H. Vankov, V. Vitale, R. M. Wagner, T. Wibig, W. Wittek, F. Zandanel, R. Zanin, and J. Zapatero.

Discovery of Very High Energy γ-Ray Emission from the Low-Frequency-peaked BL Lacertae Object BL Lacertae.

ApJL, 666(1):L17–L20, September 2007.

[17] J. Aleksić, S. Ansoldi, L. A. Antonelli, P. Antoranz, A. Babic, P. Bangale, U. Barres de Almeida, J. A. Barrio, J. Becerra González, W. Bednarek, K. Berger, E. Bernardini, A. Biland, O. Blanch, R. K. Bock, S. Bonnefoy, G. Bonnoli, F. Borracci, T. Bretz, E. Carmona, A. Carosi, D. Carreto Fidalgo, P. Colin, E. Colombo, J. L. Contreras, J. Cortina, S. Covino, P. Da Vela, F. Dazzi, A. De Angelis, G. De Caneva, B. De Lotto, C. Delgado Mendez, M. Doert, A. Domínguez, D. Dominis Prester, D. Dorner, M. Doro, S. Einecke, D. Eisenacher, D. Elsaesser, E. Farina, D. Ferenc, M. V. Fonseca, L. Font, K. Frantzen, C. Fruck, R. J. García López, M. Garczarczyk, D. Garrido Terrats, M. Gaug, G. Giavitto, N. Godinović, A. González Muñoz, S. R. Gozzini, D. Hadasch, A. Herrero, D. Hildebrand, J. Hose, D. Hrupec, W. Idec, V. Kadenius, H. Kellermann, M. L. Knoetig, K. Kodani, Y. Konno, J. Krause, H. Kubo, J. Kushida, A. La Barbera, D. Lelas, N. Lewandowska, E. Lindfors, S. Lombardi, M. López, R. López-Coto, A. López-Oramas, E. Lorenz, I. Lozano, M. Makariev, K. Mallot, G. Maneva, N. Mankuzhiyil, K. Mannheim, L. Maraschi, B. Marcote, M. Mariotti, M. Martínez, D. Mazin, U. Menzel, M. Meucci, J. M. Miranda, R. Mirzoyan, A. Moralejo, P. Munar-Adrover, D. Nakajima, A. Niedzwiecki, K. Nilsson, K. Nishijima, N. Nowak, R. Orito, A. Overkemping, S. Paiano, M. Palatiello, D. Paneque, R. Paoletti, J. M. Paredes, X. Paredes-Fortuny, S. Partini, M. Persic, F. Prada, P. G. Prada Moroni, E. Prandini, S. Preziuso, I. Puljak, R. Reinthal, W. Rhode, M. Ribó, J. Rico, J. Rodriguez Garcia, S. Rügamer, A. Saggion, T. Saito, K. Saito, M. Salvati, K. Satalecka, V. Scalzotto, V. Scapin, C. Schultz, T. Schweizer, S. N. Shore, A. Sillanpää, J. Sitarek, I. Snidaric, D. Sobczynska, F. Spanier, V. Stamatescu, A. Stamerra, T. Steinbring, J. Storz, S. Sun, T. Surić, L. Takalo, H. Takami, F. Tavecchio, P. Temnikov, T. Terzić, D. Tescaro, M. Teshima, J. Thaele, O. Tibolla, D. F. Torres, T. Toyama, A. Treves, P. Vogler, R. M. Wagner, F. Zandanel, and R. Zanin.

MAGIC observations and multifrequency properties of the flat spec-

trum radio quasar ¡ASTROBJ¿3C 279¡/ASTROBJ¿ in 2011.
A&A, 567:A41, July 2014.

[18] J. Aleksić, S. Ansoldi, L. A. Antonelli, P. Antoranz, A. Babic, P. Bangale, J. A. Barrio, J. Becerra González, W. Bednarek, E. Bernardini, B. Biasuzzi, A. Biland, O. Blanch, S. Bonnefoy, G. Bonnoli, F. Borracci, T. Bretz, E. Carmona, A. Carosi, P. Colin, E. Colombo, J. L. Contreras, J. Cortina, S. Covino, P. Da Vela, F. Dazzi, A. De Angelis, G. De Caneva, B. De Lotto, E. de Oña Wilhelmi, C. Delgado Mendez, D. Dominis Prester, D. Dorner, M. Doro, S. Einecke, D. Eisenacher, D. Elsaesser, M. V. Fonseca, L. Font, K. Frantzen, C. Fruck, D. Galindo, R. J. García López, M. Garczarczyk, D. Garrido Terrats, M. Gaug, N. Godinović, A. González Muñoz, S. R. Gozzini, D. Hadasch, Y. Hanabata, M. Hayashida, J. Herrera, D. Hildebrand, J. Hose, D. Hrupec, W. Idec, V. Kadenius, H. Kellermann, K. Kodani, Y. Konno, J. Krause, H. Kubo, J. Kushida, A. La Barbera, D. Lelas, N. Lewandowska, E. Lindfors, S. Lombardi, F. Longo, M. López, R. López-Coto, A. López-Oramas, E. Lorenz, I. Lozano, M. Makariev, K. Mallot, G. Maneva, N. Mankuzhiyil, K. Mannheim, L. Maraschi, B. Marcote, M. Mariotti, M. Martínez, D. Mazin, U. Menzel, J. M. Miranda, R. Mirzoyan, A. Moralejo, P. Munar-Adrover, D. Nakajima, A. Niedzwiecki, K. Nilsson, K. Nishijima, K. Noda, R. Orito, A. Overkemping, S. Paiano, M. Palatiello, D. Paneque, R. Paoletti, J. M. Paredes, X. Paredes-Fortuny, M. Persic, J. Poutanen, P. G. Prada Moroni, E. Prandini, I. Puljak, R. Reinthal, W. Rhode, M. Ribó, J. Rico, J. Rodriguez Garcia, S. Rügamer, T. Saito, K. Saito, K. Satalecka, V. Scalzotto, V. Scapin, C. Schultz, T. Schweizer, S. N. Shore, A. Sillanpää, J. Sitarek, I. Snidaric, D. Sobczynska, F. Spanier, V. Stamatescu, A. Stamerra, T. Steinbring, J. Storz, M. Strzys, L. Takalo, H. Takami, F. Tavecchio, P. Temnikov, T. Terzić, D. Tescaro, M. Teshima, J. Thaele, O. Tibolla, D. F. Torres, T. Toyama, A. Treves, M. Uellenbeck, P. Vogler, R. Zanin, M. Kadler, R. Schulz, E. Ros, U. Bach, F. Krauß, and J. Wilms.
Black hole lightning due to particle acceleration at subhorizon scales.
Science, 346(6213):1080–1084, November 2014.

[19] S. Ansoldi, L. A. Antonelli, C. Arcaro, D. Baack, A. Babić, B. Banerjee, P. Bangale, U. Barres de Almeida, J. A. Barrio, J. Becerra González, W. Bednarek, E. Bernardini, R. C. Berse, A. Berti, J. Besenrieder, W. Bhattacharyya, C. Bigongiari, A. Biland, O. Blanch, G. Bonnoli, R. Carosi, G. Ceribella, A. Chatterjee, S. M. Colak, P. Colin,

E. Colombo, J. L. Contreras, J. Cortina, S. Covino, P. Cumani, V. D'Elia, P. Da Vela, F. Dazzi, A. De Angelis, B. De Lotto, M. Delfino, J. Delgado, F. Di Pierro, A. Domínguez, D. Dominis Prester, D. Dorner, M. Doro, S. Einecke, D. Elsaesser, V. Fallah Ramazani, A. Fattorini, A. Fernández-Barral, G. Ferrara, D. Fidalgo, L. Foffano, M. V. Fonseca, L. Font, C. Fruck, S. Gallozzi, R. J. García López, M. Garczarczyk, M. Gaug, P. Giammaria, N. Godinović, D. Guberman, D. Hadasch, A. Hahn, T. Hassan, M. Hayashida, J. Herrera, J. Hoang, D. Hrupec, S. Inoue, K. Ishio, Y. Iwamura, Y. Konno, H. Kubo, J. Kushida, A. Lamastra, D. Lelas, F. Leone, E. Lindfors, S. Lombardi, F. Longo, M. López, C. Maggio, P. Majumdar, M. Makariev, G. Maneva, M. Manganaro, K. Mannheim, L. Maraschi, M. Mariotti, M. Martínez, S. Masuda, D. Mazin, K. Mielke, M. Minev, J. M. Miranda, R. Mirzoyan, A. Moralejo, V. Moreno, E. Moretti, V. Neustroev, A. Niedzwiecki, M. Nievas Rosillo, C. Nigro, K. Nilsson, D. Ninci, K. Nishijima, K. Noda, L. Nogués, S. Paiano, J. Palacio, D. Paneque, R. Paoletti, J. M. Paredes, G. Pedaletti, P. Peñil, M. Peresano, M. Persic, K. Pfrang, P. G. Prada Moroni, E. Prandini, I. Puljak, J. R. Garcia, W. Rhode, M. Ribó, J. Rico, C. Righi, A. Rugliancich, L. Saha, T. Saito, K. Satalecka, T. Schweizer, J. Sitarek, I. Šnidarić, D. Sobczynska, A. Stamerra, M. Strzys, T. Surić, F. Tavecchio, P. Temnikov, T. Terzić, M. Teshima, N. Torres-Albá, S. Tsujimoto, G. Vanzo, M. Vazquez Acosta, I. Vovk, J. E. Ward, M. Will, D. Zarić, and M. Cerruti.
The Blazar TXS 0506+056 Associated with a High-energy Neutrino: Insights into Extragalactic Jets and Cosmic-Ray Acceleration.
ApJL, 863:L10, August 2018.

[20] A. T. Araudo, V. Bosch-Ramon, and G. E. Romero.
Gamma-ray emission from massive stars interacting with active galactic nuclei jets.
MNRAS, 436(4):3626–3639, December 2013.

[21] T. Arlen, T. Aune, M. Beilicke, W. Benbow, A. Bouvier, J. H. Buckley, V. Bugaev, A. Cesarini, L. Ciupik, M. P. Connolly, W. Cui, R. Dickherber, J. Dumm, M. Errando, A. Falcone, S. Federici, Q. Feng, J. P. Finley, G. Finnegan, L. Fortson, A. Furniss, N. Galante, D. Gall, S. Griffin, J. Grube, G. Gyuk, D. Hanna, J. Holder, T. B. Humensky, P. Kaaret, N. Karlsson, M. Kertzman, Y. Khassen, D. Kieda, H. Krawczynski, F. Krennrich, G. Maier, P. Moriarty, R. Mukherjee, T. Nelson, A. O'Faoláin de Bhróithe, R. A. Ong, M. Orr, N. Park, J. S. Perkins, A. Pichel, M. Pohl, H. Prokoph, J. Quinn, K. Ragan, L. C.

Reyes, P. T. Reynolds, E. Roache, D. B. Saxon, M. Schroedter, G. H. Sembroski, D. Staszak, I. Telezhinsky, G. Tešić, M. Theiling, K. Tsurusaki, A. Varlotta, S. Vincent, S. P. Wakely, T. C. Weekes, A. Weinstein, R. Welsing, D. A. Williams, B. Zitzer, VERITAS Collaboration, S. G. Jorstad, N. R. MacDonald, A. P. Marscher, P. S. Smith, R. C. Walker, T. Hovatta, J. Richards, W. Max-Moerbeck, A. Readhead, M. L. Lister, Y. Y. Kovalev, A. B. Pushkarev, M. A. Gurwell, A. Lähteenmäki, E. Nieppola, M. Tornikoski, and E. Järvelä.
Rapid TeV Gamma-Ray Flaring of BL Lacertae.
ApJ, 762(2):92, January 2013.

[22] Katsuaki Asano and Masaaki Hayashida.
The Most Intensive Gamma-Ray Flare of Quasar 3C 279 with the Second-order Fermi Acceleration.
ApJL, 808(1):L18, July 2015.

[23] Katsuaki Asano and Susumu Inoue.
Prompt GeV-TeV Emission of Gamma-Ray Bursts Due to High-Energy Protons, Muons, and Electron-Positron Pairs.
ApJ, 671(1):645–655, December 2007.

[24] Armen M. Atoyan and Charles D. Dermer.
Neutral Beams from Blazar Jets.
ApJ, 586(1):79–96, Mar 2003.

[25] W. B. Atwood, A. A. Abdo, M. Ackermann, W. Althouse, B. Anderson, M. Axelsson, L. Baldini, J. Ballet, D. L. Band, G. Barbiellini, J. Bartelt, D. Bastieri, B. M. Baughman, K. Bechtol, D. Bédérède, F. Bellardi, R. Bellazzini, B. Berenji, G. F. Bignami, D. Bisello, E. Bissaldi, R. D. Blandford, E. D. Bloom, J. R. Bogart, E. Bonamente, J. Bonnell, A. W. Borgland, A. Bouvier, J. Bregeon, A. Brez, M. Brigida, P. Bruel, T. H. Burnett, G. Busetto, G. A. Caliandro, R. A. Cameron, P. A. Caraveo, S. Carius, P. Carlson, J. M. Casandjian, E. Cavazzuti, M. Ceccanti, C. Cecchi, E. Charles, A. Chekhtman, C. C. Cheung, J. Chiang, R. Chipaux, A. N. Cillis, S. Ciprini, R. Claus, J. Cohen-Tanugi, S. Condamoor, J. Conrad, R. Corbet, L. Corucci, L. Costamante, S. Cutini, D. S. Davis, D. Decotigny, M. DeKlotz, C. D. Dermer, A. de Angelis, S. W. Digel, E. do Couto e Silva, P. S. Drell, R. Dubois, D. Dumora, Y. Edmonds, D. Fabiani, C. Farnier, C. Favuzzi, D. L. Flath, P. Fleury, W. B. Focke, S. Funk, P. Fusco, F. Gargano, D. Gasparrini, N. Gehrels, F. X. Gentit, S. Germani, B. Giebels, N. Giglietto, P. Giommi, F. Giordano, T. Glanzman, G. Godfrey, I. A. Grenier, M. H. Grondin, J. E. Grove, L. Guillemot, S. Guiriec, G. Haller, A. K.

Harding, P. A. Hart, E. Hays, S. E. Healey, M. Hirayama, L. Hjalmarsdotter, R. Horn, R. E. Hughes, G. Jóhannesson, G. Johansson, A. S. Johnson, R. P. Johnson, T. J. Johnson, W. N. Johnson, T. Kamae, H. Katagiri, J. Kataoka, A. Kavelaars, N. Kawai, H. Kelly, M. Kerr, W. Klamra, J. Knödlseder, M. L. Kocian, N. Komin, F. Kuehn, M. Kuss, D. Landriu, L. Latronico, B. Lee, S. H. Lee, M. Lemoine-Goumard, A. M. Lionetto, F. Longo, F. Loparco, B. Lott, M. N. Lovellette, P. Lubrano, G. M. Madejski, A. Makeev, B. Marangelli, M. M. Massai, M. N. Mazziotta, J. E. McEnery, N. Menon, C. Meurer, P. F. Michelson, M. Minuti, N. Mirizzi, W. Mitthumsiri, T. Mizuno, A. A. Moiseev, C. Monte, M. E. Monzani, E. Moretti, A. Morselli, I. V. Moskalenko, S. Murgia, T. Nakamori, S. Nishino, P. L. Nolan, J. P. Norris, E. Nuss, M. Ohno, T. Ohsugi, N. Omodei, E. Orlando, J. F. Ormes, A. Paccagnella, D. Paneque, J. H. Panetta, D. Parent, M. Pearce, M. Pepe, A. Perazzo, M. Pesce-Rollins, P. Picozza, L. Pieri, M. Pinchera, F. Piron, T. A. Porter, L. Poupard, S. Rainò, R. Rando, E. Rapposelli, M. Razzano, A. Reimer, O. Reimer, T. Reposeur, L. C. Reyes, S. Ritz, L. S. Rochester, A. Y. Rodriguez, R. W. Romani, M. Roth, J. J. Russell, F. Ryde, S. Sabatini, H. F. W. Sadrozinski, D. Sanchez, A. Sander, L. Sapozhnikov, P. M. Saz Parkinson, J. D. Scargle, T. L. Schalk, G. Scolieri, C. Sgrò, G. H. Share, M. Shaw, T. Shimokawabe, C. Shrader, A. Sierpowska-Bartosik, E. J. Siskind, D. A. Smith, P. D. Smith, G. Spandre, P. Spinelli, J. L. Starck, T. E. Stephens, M. S. Strickman, A. W. Strong, D. J. Suson, H. Tajima, H. Takahashi, T. Takahashi, T. Tanaka, A. Tenze, S. Tether, J. B. Thayer, J. G. Thayer, D. J. Thompson, L. Tibaldo, O. Tibolla, D. F. Torres, G. Tosti, A. Tramacere, M. Turri, T. L. Usher, N. Vilchez, V. Vitale, P. Wang, K. Watters, B. L. Winer, K. S. Wood, T. Ylinen, and M. Ziegler.
The Large Area Telescope on the Fermi Gamma-Ray Space Telescope Mission.
ApJ, 697(2):1071–1102, June 2009.

[26] V. Baghmanyan, S. Gasparyan, and N. Sahakyan.
Rapid Gamma-Ray Variability of NGC 1275.
ApJ, 848(2):111, October 2017.

[27] T. J. Balonek, S. Zhang, and et al.
Blazar CTA 102 Reaches Historic Optical Maximum During Current Extended Period of Activity.
The Astronomer's Telegram, 9732, November 2016.

[28] Matthew G. Baring, Markus Böttcher, and Errol J. Summerlin.

Probing acceleration and turbulence at relativistic shocks in blazar jets.
MNRAS, 464(4):4875–4894, February 2017.

[29] J. H. Beall and W. Bednarek.
On the Hadronic Beam Model for Gamma-Ray Production in Blazars.
ApJ, 510(1):188–196, January 1999.

[30] J. Becerra, B. Carpenter, and S. Cutini.
Fermi-LAT detection of strong flaring activity from the FSRQ CTA 102.
The Astronomer's Telegram, 8722, February 2016.

[31] M. C. Begelman, B. Rudak, and M. Sikora.
Consequences of relativistic proton injection in active galactic nuclei.
ApJ, 362:38–51, October 1990.

[32] R. Belmont, J. Malzac, and A. Marcowith.
Simulating radiation and kinetic processes in relativistic plasmas.
A&A, 491:617–631, November 2008.

[33] V. S. Berezinsky and A. Z. Gazizov.
Production of high-energy cosmic neutrinos in pγ and nγ scattering. I. Neutrino yields for power-law spectra of protons and neutrons.
Phys. Rev. D, 47:4206–4216, May 1993.

[34] J. Biteau, E. Prandini, L. Costamante, M. Lemoine, P. Padovani, E. Pueschel, E. Resconi, F. Tavecchio, A. Taylor, and A. Zech.
Progress in unveiling extreme particle acceleration in persistent astrophysical jets.
Nature Astronomy, 4:124–131, February 2020.

[35] Roger Blandford and David Eichler.
Particle acceleration at astrophysical shocks: A theory of cosmic ray origin.
Phys. Rep., 154(1):1–75, October 1987.

[36] M. Błażejowski, M. Sikora, R. Moderski, and G. M. Madejski.
Comptonization of Infrared Radiation from Hot Dust by Relativistic Jets in Quasars.
ApJ, 545:107–116, December 2000.

[37] S. D. Bloom, D. L. Bertsch, R. C. Hartman, P. Sreekumar, D. J. Thompson, T. J. Balonek, E. Beckerman, S. M. Davis, K. Whitman, H. R. Miller, A. D. Nair, Jr. Roberts, L. C., G. Tosti, E. Massaro, R. Nesci, M. Maesano, F. Montagni, M. Jang, H. A. Bock, M. Dietrich, M. Herter, K. Otterbein, M. Pfeiffer, T. Seitz, and S. Wagner.

Observations of a Correlated Gamma-Ray and Optical Flare for BL Lacertae.
ApJL, 490(2):L145–L148, December 1997.

[38] S. D. Bloom and A. P. Marscher.
An Analysis of the Synchrotron Self-Compton Model for the Multi–Wave Band Spectra of Blazars.
ApJ, 461:657, April 1996.

[39] G. R. Blumenthal.
Energy Loss of High-Energy Cosmic Rays in Pair-Producing Collisions with Ambient Photons.
Phys. Rev. D, 1:1596–1602, March 1970.

[40] M. Boettcher and R. Schlickeiser.
The pair production spectrum from photon-photon annihilation.
A&A, 325:866–870, September 1997.

[41] Eugenio Bottacini, Markus Böttcher, Elena Pian, and Werner Collmar.
3C 279 in Outburst in 2015 June: A Broadband SED Study Based on the INTEGRAL Detection.
ApJ, 832(1):17, November 2016.

[42] M. Böttcher and S. D. Bloom.
Analyzing the Multiwavelength Spectrum of BL Lacertae during the 1997 July Outburst.
AJ, 119(2):469–477, February 2000.

[43] M. Böttcher, A. Reimer, K. Sweeney, and A. Prakash.
Leptonic and Hadronic Modeling of Fermi-detected Blazars.
ApJ, 768:54, May 2013.

[44] M. Böttcher, A. Reimer, K. Sweeney, and A. Prakash.
Leptonic and Hadronic Modeling of Fermi-detected Blazars.
ApJ, 768(1):54, May 2013.

[45] Markus Böttcher and Matthew G. Baring.
Multi-wavelength Variability Signatures of Relativistic Shocks in Blazar Jets.
ApJ, 887(2):133, December 2019.

[46] Richard J. Britto, Eugenio Bottacini, Benoît Lott, Soebur Razzaque, and Sara Buson.
Fermi-LAT Observations of the 2014 May-July Outburst from 3C 454.3.
ApJ, 830(2):162, October 2016.

[47] A. Bulgarelli, V. Fioretti, N. Parmiggiani, F. Verrecchia, C. Pittori, F. Lucarelli, M. Tavani, A. Aboudan, M. Cardillo, A. Giuliani, P. W. Cattaneo, A. W. Chen, G. Piano, A. Rappoldi, L. Baroncelli, A. Argan, L. A. Antonelli, I. Donnarumma, F. Gianotti, P. Giommi, M. Giusti, F. Longo, A. Pellizzoni, M. Pilia, M. Trifoglio, A. Trois, S. Vercellone, and A. Zoli.
Second AGILE catalogue of gamma-ray sources.
A&A, 627:A13, July 2019.

[48] A. Bulgarelli, F. Verrecchia, and et al.
AGILE detects renewed gamma-ray emission from the FSRQ CTA 102.
The Astronomer's Telegram, 9788, November 2016.

[49] Mauricio Bustamante and Irene Tamborra.
Using High-Energy Neutrinos As Cosmic Magnetometers.
arXiv e-prints, page arXiv:2009.01306, September 2020.

[50] A. Capetti, C. M. Raiteri, and S. Buttiglione.
Is BL Lacertae an "orphan" AGN?. Multiband and spectroscopic constraints on the parent population.
A&A, 516:A59, June 2010.

[51] D. Caprioli and A. Spitkovsky.
Simulations of Ion Acceleration at Non-relativistic Shocks. I. Acceleration Efficiency.
ApJ, 783:91, March 2014.

[52] D. Caprioli and A. Spitkovsky.
Simulations of Ion Acceleration at Non-relativistic Shocks. II. Magnetic Field Amplification.
ApJ, 794:46, October 2014.

[53] D. Caprioli and A. Spitkovsky.
Simulations of Ion Acceleration at Non-relativistic Shocks. III. Particle Diffusion.
ApJ, 794:47, October 2014.

[54] L. Carrasco, J. Miramon, E. Recillas, A. Porras, V. Chavushyan, and A. Carraminana.
A NIR Flare of the QSO PKS0306+102.
The Astronomer's Telegram, 8574, January 2016.

[55] C. Casadio, J. L. Gómez, and et al.
A Multi-wavelength Polarimetric Study of the Blazar CTA 102 during a Gamma-Ray Flare in 2012.

ApJ, 813:51, November 2015.

[56] Carolina Casadio, Alan P. Marscher, Svetlana G. Jorstad, Dmitry A. Blinov, Nicholas R. MacDonald, Thomas P. Krichbaum, Biagina Boccardi, Efthalia Traianou, José L. Gómez, Iván Agudo, Bong-Won Sohn, Michael Bremer, Jeffrey Hodgson, Juha Kallunki, Jae-Young Kim, Karen E. Williamson, and J. Anton Zensus.
The magnetic field structure in CTA 102 from high-resolution mm-VLBI observations during the flaring state in 2016-2017.
A&A, 622:A158, February 2019.

[57] W. Cash.
Parameter estimation in astronomy through application of the likelihood ratio.
ApJ, 228:939–947, March 1979.

[58] M. Catanese, C. W. Akerlof, S. D. Biller, P. Boyle, J. H. Buckley, D. A. Carter-Lewis, M. F. Cawley, V. Connaughton, B. L. Dingus, D. J. Fegan, C. E. Fichtel, J. P. Finley, J. A. Gaidos, W. K. Gear, R. C. Hartman, A. M. Hillas, F. Krennrich, R. C. Lamb, R. W. Lessard, Y. C. Lin, J. E. McEnery, A. P. Marscher, G. Mohanty, R. Mukherjee, J. Quinn, E. I. Robson, A. J. Rodgers, H. J. Rose, F. W. Samuelson, G. Sembroski, M. S. Schubnell, J. A. Stevens, H. Teräsranta, D. J. Thompson, T. C. Weekes, C. Wilson, and J. Zweerink.
Detection of Gamma Rays with E ¿ 100 MeV from BL Lacertae.
ApJ, 480(2):562–567, May 1997.

[59] M. Cerruti, A. Zech, C. Boisson, G. Emery, S. Inoue, and J.-P. Lenain.
Leptohadronic single-zone models for the electromagnetic and neutrino emission of TXS 0506+056.
MNRAS, 483:L12–L16, February 2019.

[60] M. Cerruti, A. Zech, C. Boisson, G. Emery, S. Inoue, and J. P. Lenain.
Leptohadronic single-zone models for the electromagnetic and neutrino emission of TXS 0506+056.
MNRAS, 483(1):L12–L16, February 2019.

[61] M. Cerruti, A. Zech, C. Boisson, and S. Inoue.
A hadronic origin for ultra-high-frequency-peaked BL Lac objects.
MNRAS, 448:910–927, March 2015.

[62] M. Cerruti, A. Zech, C. Boisson, and S. Inoue.
A hadronic origin for ultra-high-frequency-peaked BL Lac objects.
MNRAS, 448(1):910–927, March 2015.

[63] JS Chang and G Cooper.
A practical difference scheme for Fokker-Planck equations.
Journal of Computational Physics, 6(1):1–16, 1970.

[64] Y. L. Chang, C. H. Brandt, and P. Giommi.
The Open Universe VOU-Blazars tool.
Astronomy and Computing, 30:100350, January 2020.

[65] K. J. Chapman, A. Sabyr, R. W. Stahlin, S. Zhang, and T. J. Balonek.
A Spectacular, Unprecedented Optical Flare in the Blazar CTA 102.
The Astronomer's Telegram, 9756, November 2016.

[66] Vahram Chavushyan, Victor M. Patiño-Álvarez, Raúl A. Amaya-Almazán, and Luis Carrasco.
Flare-like Variability of the Mg II λ2798 Å Emission Line and UV Fe II Band in the Blazar CTA 102.
ApJ, 891(1):68, March 2020.

[67] C. C. Cheung.
Fermi-LAT detection of a gamma-ray flare of the blazar BL Lacertae coincident with an optical flare.
The Astronomer's Telegram, 13933:1, August 2020.

[68] Marco Chiaberge and Gabriele Ghisellini.
Rapid variability in the synchrotron self-Compton model for blazars.
MNRAS, 306(3):551–560, Jul 1999.

[69] Michal J. Chodorowski, Andrzej A. Zdziarski, and Marek Sikora.
Reaction Rate and Energy-Loss Rate for Photopair Production by Relativistic Nuclei.
ApJ, 400:181, Nov 1992.

[70] S. Ciprini.
Fermi LAT observation of renewed and strong GeV gamma-ray activity from blazar CTA 102.
The Astronomer's Telegram, 9869, December 2016.

[71] S. Ciprini.
Yet another strong GeV gamma-ray outburst of blazar CTA 102 observed by the Fermi LAT.
The Astronomer's Telegram, 10292, April 2017.

[72] E. A. Corbett, A. Robinson, D. J. Axon, J. H. Hough, R. D. Jeffries, M. R. Thurston, and S. Young.
The appearance of broad Hα in BL Lacertae.

MNRAS, 281(3):737–749, August 1996.

[73] L. Costamante, G. Bonnoli, F. Tavecchio, G. Ghisellini, G. Tagliaferri, and D. Khangulyan.
The NuSTAR view on hard-TeV BL Lacs.
MNRAS, 477(3):4257–4268, July 2018.

[74] L. Costamante, G. Ghisellini, P. Giommi, G. Tagliaferri, A. Celotti, M. Chiaberge, G. Fossati, L. Maraschi, F. Tavecchio, A. Treves, and A. Wolter.
Extreme synchrotron BL Lac objects. Stretching the blazar sequence.
A&A, 371:512–526, May 2001.

[75] P. Crumley and P. Kumar.
Hadronic models for Large Area Telescope prompt emission observed in Fermi gamma-ray bursts.
MNRAS, 429(4):3238–3251, Mar 2013.

[76] S. Cutini.
Fermi-LAT detection of increasing of gamma-ray activity of BL Lacertae.
The Astronomer's Telegram, 4028:1, April 2012.

[77] Sara Cutini.
Fermi-LAT gamma-ray flare in BL Lacertae contemporaneous with optical flaring activity.
The Astronomer's Telegram, 14330:1, January 2021.

[78] F. D'Ammando.
NICER, NuSTAR and swift follow-up observations of the γ-ray flaring blazar BL Lacertae in 2020 August-October.
MNRAS, September 2021.

[79] F. D'Ammando, C. M. Raiteri, M. Villata, J. A. Acosta-Pulido, I. Agudo, A. A. Arkharov, R. Bachev, G. V. Baida, E. Benítez, G. A. Borman, W. Boschin, V. Bozhilov, M. S. Butuzova, P. Calcidese, M. I. Carnerero, D. Carosati, C. Casadio, N. Castro-Segura, W. P. Chen, G. Damljanovic, A. Di Paola, J. Echevarría, N. V. Efimova, Sh A. Ehgamberdiev, C. Espinosa, A. Fuentes, A. Giunta, J. L. Gómez, T. S. Grishina, M. A. Gurwell, D. Hiriart, H. Jermak, B. Jordan, S. G. Jorstad, M. Joshi, G. N. Kimeridze, E. N. Kopatskaya, K. Kuratov, O. M. Kurtanidze, S. O. Kurtanidze, A. Lähteenmäki, V. M. Larionov, E. G. Larionova, L. V. Larionova, C. Lázaro, C. S. Lin, M. P. Malmrose, A. P. Marscher, K. Matsumoto, B. McBreen, R. Michel,

B. Mihov, M. Minev, D. O. Mirzaqulov, S. N. Molina, J. W. Moody, D. A. Morozova, S. V. Nazarov, A. A. Nikiforova, M. G. Nikolashvili, J. M. Ohlert, N. Okhmat, E. Ovcharov, F. Pinna, T. A. Polakis, C. Protasio, T. Pursimo, F. J. Redondo-Lorenzo, N. Rizzi, G. Rodriguez-Coira, K. Sadakane, A. C. Sadun, M. R. Samal, S. S. Savchenko, E. Semkov, L. Sigua, B. A. Skiff, L. Slavcheva-Mihova, P. S. Smith, I. A. Steele, A. Strigachev, J. Tammi, C. Thum, M. Tornikoski, Yu V. Troitskaya, I. S. Troitsky, A. A. Vasilyev, O. Vince, WEBT Collaboration, T Hovatta, S. Kiehlmann, W. Max-Moerbeck, A. C. S. Readhead, R. Reeves, T. J. Pearson, OVRO Team, T Mufakharov, Yu V. Sotnikova, and M. G. Mingaliev.
Investigating the multiwavelength behaviour of the flat spectrum radio quasar CTA 102 during 2013-2017.
MNRAS, 490(4):5300–5316, December 2019.

[80] Filippo D'Ammando.
NICER follow-up observations of the flaring blazar BL Lacertae.
The Astronomer's Telegram, 14342:1, January 2021.

[81] Filippo D'Ammando.
Swift follow-up observations of BL Lacertae during a new flaring activity.
The Astronomer's Telegram, 14350:1, January 2021.

[82] Arnon Dar and Ari Laor.
Hadronic Production of TeV Gamma-Ray Flares from Blazars.
ApJL, 478(1):L5–L8, March 1997.

[83] O. C. de Jager, A. K. Harding, P. F. Michelson, H. I. Nel, P. L. Nolan, P. Sreekumar, and D. J. Thompson.
Gamma-Ray Observations of the Crab Nebula: A Study of the Synchro-Compton Spectrum.
ApJ, 457:253, January 1996.

[84] C. D. Dermer, R. Schlickeiser, and A. Mastichiadis.
High-energy gamma radiation from extragalactic radio sources.
A&A, 256:L27–L30, March 1992.

[85] Charles D. Dermer and Govind Menon.
High Energy Radiation from Black Holes: Gamma Rays, Cosmic Rays, and Neutrinos.
2009.

[86] Charles D. Dermer and Reinhard Schlickeiser.

Model for the High-Energy Emission from Blazars.
ApJ, 416:458, October 1993.

[87] C. Diltz, M. Böttcher, and G. Fossati.
Time Dependent Hadronic Modeling of Flat Spectrum Radio Quasars.
ApJ, 802:133, April 2015.

[88] S. Dimitrakoudis, A. Mastichiadis, R. J. Protheroe, and A. Reimer.
The time-dependent one-zone hadronic model. First principles.
A&A, 546:A120, October 2012.

[89] A. Domínguez, J. R. Primack, D. J. Rosario, F. Prada, R. C. Gilmore, S. M. Faber, D. C. Koo, R. S. Somerville, M. A. Pérez-Torres, P. Pérez-González, J. S. Huang, M. Davis, P. Guhathakurta, P. Barmby, C. J. Conselice, M. Lozano, J. A. Newman, and M. C. Cooper.
Extragalactic background light inferred from AEGIS galaxy-SED-type fractions.
MNRAS, 410(4):2556–2578, February 2011.

[90] Alina-C. Donea and R. J. Protheroe.
Radiation fields of disk, BLR and torus in quasars and blazars: implications for $/\gamma$-ray absorption.
Astroparticle Physics, 18(4):377–393, January 2003.

[91] A. J. Drake, S. G. Djorgovski, A. Mahabal, E. Beshore, S. Larson, M. J. Graham, R. Williams, E. Christensen, M. Catelan, A. Boattini, A. Gibbs, R. Hill, and R. Kowalski.
First Results from the Catalina Real-Time Transient Survey.
ApJ, 696(1):870–884, May 2009.

[92] Renato Falomo, Nicoletta Carangelo, and Aldo Treves.
Host galaxies and black hole masses of low- and high-luminosity radio-loud active nuclei.
MNRAS, 343(2):505–511, August 2003.

[93] Guido Fantini, Andrea Gallo Rosso, Francesco Vissani, and Vanessa Zema.
The formalism of neutrino oscillations: an introduction.
arXiv e-prints, page arXiv:1802.05781, February 2018.

[94] J. D. Finke, C. D. Dermer, and M. Böttcher.
Synchrotron Self-Compton Analysis of TeV X-Ray-Selected BL Lacertae Objects.
ApJ, 686:181–194, October 2008.

[95] Wendy L. Freedman, Barry F. Madore, Brad K. Gibson, Laura Ferrarese, Daniel D. Kelson, Shoko Sakai, Jeremy R. Mould, Jr. Kennicutt, Robert C., Holland C. Ford, John A. Graham, John P. Huchra, Shaun M. G. Hughes, Garth D. Illingworth, Lucas M. Macri, and Peter B. Stetson.
Final Results from the Hubble Space Telescope Key Project to Measure the Hubble Constant.
ApJ, 553(1):47–72, May 2001.

[96] S. Gao, A. Fedynitch, W. Winter, and M. Pohl.
Modelling the coincident observation of a high-energy neutrino and a bright blazar flare.
Nature Astronomy, 3:88–92, January 2019.

[97] Shan Gao, Anatoli Fedynitch, Walter Winter, and Martin Pohl.
Modelling the coincident observation of a high-energy neutrino and a bright blazar flare.
Nature Astronomy, 3:88–92, January 2019.

[98] Shan Gao, Martin Pohl, and Walter Winter.
On the Direct Correlation between Gamma-Rays and PeV Neutrinos from Blazars.
ApJ, 843(2):109, July 2017.

[99] S. Gasparyan, D. Bégué, and N. Sahakyan.
Time-dependent lepto-hadronic modelling of the emission from blazar jets with SOPRANO: the case of TXS 0506 + 056, 3HSP J095507.9 + 355101, and 3C 279.
MNRAS, 509(2):2102–2121, January 2022.

[100] S. Gasparyan, N. Sahakyan, V. Baghmanyan, and D. Zargaryan.
On the multi-wavelength Emission from CTA 102.
ArXiv e-prints, July 2018.

[101] S. Gasparyan, N. Sahakyan, V. Baghmanyan, and D. Zargaryan.
On the Multiwavelength Emission from CTA 102.
ApJ, 863(2):114, August 2018.

[102] N. Gehrels, G. Chincarini, P. Giommi, K. O. Mason, J. A. Nousek, A. A. Wells, N. E. White, S. D. Barthelmy, D. N. Burrows, L. R. Cominsky, K. C. Hurley, F. E. Marshall, P. Mészáros, P. W. A. Roming, L. Angelini, L. M. Barbier, T. Belloni, S. Campana, P. A. Caraveo, M. M. Chester, O. Citterio, T. L. Cline, M. S. Cropper, J. R. Cummings, A. J. Dean, E. D. Feigelson, E. E. Fenimore, D. A. Frail, A. S.

Fruchter, G. P. Garmire, K. Gendreau, G. Ghisellini, J. Greiner, J. E. Hill, S. D. Hunsberger, H. A. Krimm, S. R. Kulkarni, P. Kumar, F. Lebrun, N. M. Lloyd-Ronning, C. B. Markwardt, B. J. Mattson, R. F. Mushotzky, J. P. Norris, J. Osborne, B. Paczynski, D. M. Palmer, H. S. Park, A. M. Parsons, J. Paul, M. J. Rees, C. S. Reynolds, J. E. Rhoads, T. P. Sasseen, B. E. Schaefer, A. T. Short, A. P. Smale, I. A. Smith, L. Stella, G. Tagliaferri, T. Takahashi, M. Tashiro, L. K. Townsley, J. Tueller, M. J. L. Turner, M. Vietri, W. Voges, M. J. Ward, R. Willingale, F. M. Zerbi, and W. W. Zhang.
The Swift Gamma-Ray Burst Mission.
ApJ, 611(2):1005–1020, August 2004.

[103] Xiongfei Geng, Nan Ding, Gang Cao, Yang Liu, Biwen Bao, Celine Chidiac, Pankaj Kushwaha, Zahir Shah, Zhijie Zhang, Xiongbang Yang, Tao Wen, Zejun Jiang, Li Zhang, Wei Zeng, Xiaohui Wu, Yao Qin, Meng Zhou, and Benzhong Dai.
Exploring γ-Ray Flares in the Long-term Light Curves of CTA 102 at GeV Energies.
ApJSS, 260(2):48, June 2022.

[104] G. Ghisellini, L. Maraschi, and A. Treves.
Inhomogeneous synchrotron-self-Compton models and the problem of relativistic beaming of BL Lac objects.
A&A, 146:204–212, May 1985.

[105] G. Ghisellini and F. Tavecchio.
Canonical high-power blazars.
MNRAS, 397:985–1002, August 2009.

[106] G. Ghisellini and F. Tavecchio.
Canonical high-power blazars.
MNRAS, 397:985–1002, August 2009.

[107] G. Ghisellini, F. Tavecchio, L. Foschini, G. Ghirlanda, L. Maraschi, and A. Celotti.
General physical properties of bright Fermi blazars.
MNRAS, 402(1):497–518, February 2010.

[108] G. Ghisellini, F. Tavecchio, L. Maraschi, A. Celotti, and T. Sbarrato.
The power of relativistic jets is larger than the luminosity of their accretion disks.
Nature, 515(7527):376–378, November 2014.

[109] D. Giannios and D. A. Uzdensky.

GRB and blazar jets shining through their stripes.
MNRAS, 484:1378–1389, March 2019.

[110] Dimitrios Giannios, Dmitri A. Uzdensky, and Mitchell C. Begelman.
Fast TeV variability in blazars: jets in a jet.
MNRAS, 395(1):L29–L33, May 2009.

[111] Dimitrios Giannios, Dmitri A. Uzdensky, and Mitchell C. Begelman.
Fast TeV variability from misaligned minijets in the jet of M87.
MNRAS, 402(3):1649–1656, March 2010.

[112] P. Giommi, P. Barr, B. Garilli, D. Maccagni, and A. M. T. Pollock.
A Study of BL Lacertae–Type Objects with EXOSAT. I. Flux Correlations, Luminosity, Variability, and Spectral Variability.
ApJ, 356:432, June 1990.

[113] P. Giommi, T. Glauch, and E. Resconi.
Swift observation of a flaring very extreme blazar in the error region of the high-energy neutrino Ice-Cube 200107A.
The Astronomer's Telegram, 13394:1, January 2020.

[114] P Giommi, M T Menna, and P Padovani.
The Sedentary Multi-Frequency Survey . I . arXiv : astro-ph / 9907014v1 1 Jul 1999.
MNRAS, 310:465–475, 1999.

[115] P. Giommi, P. Padovani, F. Oikonomou, T. Glauch, S. Paiano, and E. Resconi.
3HSP J095507.9+355101: A flaring extreme blazar coincident in space and time with IceCube-200107A.
A&A, 640:L4, August 2020.

[116] P. Giommi, M. Perri, M. Capalbi, V. D'Elia, U. Barres de Almeida, C. H. Brandt, A. M. T. Pollock, F. Arneodo, A. Di Giovanni, Y. L. Chang, O. Civitarese, M. De Angelis, C. Leto, F. Verrecchia, N. Ricard, S. Di Pippo, R. Middei, A. V. Penacchioni, R. Ruffini, N. Sahakyan, D. Israyelyan, and S. Turriziani.
X-ray spectra, light-curves and SEDs of blazars frequently observed by Swift.
arXiv e-prints, page arXiv:2108.07255, August 2021.

[117] P. Giommi, S. Piranomonte, M. Perri, and P. Padovani.
The sedentary survey of extreme high energy peaked BL Lacs.
A&A, 434(1):385–396, April 2005.

[118] Paolo Giommi and Paolo Padovani.
Astrophysical Neutrinos and Blazars.
Universe, 7(12):492, December 2021.

[119] Paolo Giommi, M. Perri, M. Capalbi, V. D'Elia, U. Barres de Almeida, C. H. Brandt, A. M. T. Pollock, F. Arneodo, A. Di Giovanni, Y. L. Chang, O. Civitarese, M. De Angelis, C. Leto, F. Verrecchia, N. Ricard, S. Di Pippo, R. Middei, A. V. Penacchioni, R. Ruffini, N. Sahakyan, D. Israyelyan, and S. Turriziani.
X-ray spectra, light curves and SEDs of blazars frequently observed by Swift.
MNRAS, 507(4):5690–5702, November 2021.

[120] F. Guo, X. Li, H. Li, W. Daughton, B. Zhang, N. Lloyd-Ronning, Y.-H. Liu, H. Zhang, and W. Deng.
Efficient Production of High-energy Nonthermal Particles during Magnetic Reconnection in a Magnetically Dominated Ion-Electron Plasma.
ApJL, 818:L9, February 2016.

[121] Fan Guo, Hui Li, William Daughton, and Yi-Hsin Liu.
Formation of Hard Power Laws in the Energetic Particle Spectra Resulting from Relativistic Magnetic Reconnection.
Phys. Rev. Lett., 113(15):155005, October 2014.

[122] Fan Guo, Yi-Hsin Liu, William Daughton, and Hui Li.
Particle Acceleration and Plasma Dynamics during Magnetic Reconnection in the Magnetically Dominated Regime.
ApJ, 806(2):167, June 2015.

[123] Xinyi Guo, Lorenzo Sironi, and Ramesh Narayan.
Non-thermal Electron Acceleration in Low Mach Number Collisionless Shocks. I. Particle Energy Spectra and Acceleration Mechanism.
ApJ, 794(2):153, October 2014.

[124] H. E. S. S. Collaboration, H. Abdalla, R. Adam, F. Aharonian, F. Ait Benkhali, E. O. Angüner, M. Arakawa, C. Arcaro, C. Armand, H. Ashkar, M. Backes, V. Barbosa Martins, M. Barnard, Y. Becherini, D. Berge, K. Bernlöhr, R. Blackwell, M. Böttcher, C. Boisson, J. Bolmont, S. Bonnefoy, J. Bregeon, M. Breuhaus, F. Brun, P. Brun, M. Bryan, M. Büchele, T. Bulik, T. Bylund, M. Capasso, S. Caroff, A. Carosi, S. Casanova, M. Cerruti, T. Chand, S. Chandra, A. Chen, S. Colafrancesco, M. Curyło, I. D. Davids, C. Deil, J. Devin, P. deWilt, L. Dirson, A. Djannati-Ataï, A. Dmytriiev, A. Donath,

V. Doroshenko, L. O. 'C. Drury, J. Dyks, K. Egberts, G. Emery, J. P. Ernenwein, S. Eschbach, K. Feijen, S. Fegan, A. Fiasson, G. Fontaine, S. Funk, M. Füßling, S. Gabici, Y. A. Gallant, F. Gaté, G. Giavitto, D. Glawion, J. F. Glicenstein, D. Gottschall, M. H. Grondin, J. Hahn, M. Haupt, G. Heinzelmann, G. Henri, G. Hermann, J. A. Hinton, W. Hofmann, C. Hoischen, T. L. Holch, M. Holler, D. Horns, D. Huber, H. Iwasaki, M. Jamrozy, D. Jankowsky, F. Jankowsky, A. Jardin-Blicq, I. Jung-Richardt, M. A. Kastendieck, K. Katarzyński, M. Katsuragawa, U. Katz, D. Khangulyan, B. Khélifi, J. King, S. Klepser, W. Kluźniak, Nu. Komin, K. Kosack, D. Kostunin, M. Kraus, G. Lamanna, J. Lau, A. Lemière, M. Lemoine-Goumard, J. P. Lenain, E. Leser, C. Levy, T. Lohse, I. Lypova, J. Mackey, J. Majumdar, D. Malyshev, V. Marandon, A. Marcowith, A. Mares, C. Mariaud, G. Martí-Devesa, R. Marx, G. Maurin, P. J. Meintjes, A. M. W. Mitchell, R. Moderski, M. Mohamed, L. Mohrmann, C. Moore, E. Moulin, J. Muller, T. Murach, S. Nakashima, M. de Naurois, H. Ndiyavala, F. Niederwanger, J. Niemiec, L. Oakes, P. O'Brien, H. Odaka, S. Ohm, E. de Ona Wilhelmi, M. Ostrowski, I. Oya, M. Panter, R. D. Parsons, C. Perennes, P. O. Petrucci, B. Peyaud, Q. Piel, S. Pita, V. Poireau, A. Priyana Noel, D. A. Prokhorov, H. Prokoph, G. Pühlhofer, M. Punch, A. Quirrenbach, S. Raab, R. Rauth, A. Reimer, O. Reimer, Q. Remy, M. Renaud, F. Rieger, L. Rinchiuso, C. Romoli, G. Rowell, B. Rudak, E. Ruiz-Velasco, V. Sahakian, S. Saito, D. A. Sanchez, A. Santangelo, M. Sasaki, R. Schlickeiser, F. Schüssler, A. Schulz, H. Schutte, U. Schwanke, S. Schwemmer, M. Seglar-Arroyo, M. Senniappan, A. S. Seyffert, N. Shafi, K. Shiningayamwe, R. Simoni, A. Sinha, H. Sol, A. Specovius, M. Spir-Jacob, L. Stawarz, R. Steenkamp, C. Stegmann, C. Steppa, T. Takahashi, T. Tavernier, A. M. Taylor, R. Terrier, D. Tiziani, M. Tluczykont, C. Trichard, M. Tsirou, N. Tsuji, R. Tuffs, Y. Uchiyama, D. J. van der Walt, C. van Eldik, C. van Rensburg, B. van Soelen, G. Vasileiadis, J. Veh, C. Venter, P. Vincent, J. Vink, F. Voisin, H. J. Völk, T. Vuillaume, Z. Wadiasingh, S. J. Wagner, R. White, A. Wierzcholska, R. Yang, H. Yoneda, M. Zacharias, R. Zanin, A. A. Zdziarski, A. Zech, A. Ziegler, J. Zorn, N. Żywucka, and M. Meyer.

Constraints on the emission region of ¡ASTROBJ¿3C 279¡/ASTROBJ¿ during strong flares in 2014 and 2015 through VHE γ-ray observations with H.E.S.S.

A&A, 627:A159, July 2019.

[125] Fiona A. Harrison, William W. Craig, Finn E. Christensen, Charles J.

Hailey, William W. Zhang, Steven E. Boggs, Daniel Stern, W. Rick Cook, Karl Forster, Paolo Giommi, Brian W. Grefenstette, Yunjin Kim, Takao Kitaguchi, Jason E. Koglin, Kristin K. Madsen, Peter H. Mao, Hiromasa Miyasaka, Kaya Mori, Matteo Perri, Michael J. Pivovaroff, Simonetta Puccetti, Vikram R. Rana, Niels J. Westergaard, Jason Willis, Andreas Zoglauer, Hongjun An, Matteo Bachetti, Nicolas M. Barrière, Eric C. Bellm, Varun Bhalerao, Nicolai F. Brejnholt, Felix Fuerst, Carl C. Liebe, Craig B. Markwardt, Melania Nynka, Julia K. Vogel, Dominic J. Walton, Daniel R. Wik, David M. Alexander, Lynn R. Cominsky, Ann E. Hornschemeier, Allan Hornstrup, Victoria M. Kaspi, Greg M. Madejski, Giorgio Matt, Silvano Molendi, David M. Smith, John A. Tomsick, Marco Ajello, David R. Ballantyne, Mislav Baloković, Didier Barret, Franz E. Bauer, Roger D. Blandford, W. Niel Brandt, Laura W. Brenneman, James Chiang, Deepto Chakrabarty, Jerome Chenevez, Andrea Comastri, Francois Dufour, Martin Elvis, Andrew C. Fabian, Duncan Farrah, Chris L. Fryer, Eric V. Gotthelf, Jonathan E. Grindlay, David J. Helfand, Roman Krivonos, David L. Meier, Jon M. Miller, Lorenzo Natalucci, Patrick Ogle, Eran O. Ofek, Andrew Ptak, Stephen P. Reynolds, Jane R. Rigby, Gianpiero Tagliaferri, Stephen E. Thorsett, Ezequiel Treister, and C. Megan Urry.
The Nuclear Spectroscopic Telescope Array (NuSTAR) High-energy X-Ray Mission.
ApJ, 770(2):103, June 2013.

[126] R. Hosokawa, K. L. Murata, M. Niwano, S. Wang, R. Adachi, F. Ogawa, N. Nakamura, N. Ito, S. Ogata, H. Takamatsu, H. Hara, Y. Yatsu, and N. Kawai.
Multicolor-optical observation of the flaring blazar BL Lacertae.
The Astronomer's Telegram, 14334:1, January 2021.

[127] S. Hümmer, M. Rüger, F. Spanier, and W. Winter.
Simplified Models for Photohadronic Interactions in Cosmic Accelerators.
ApJ, 721:630–652, September 2010.

[128] IceCube Collaboration.
Evidence for High-Energy Extraterrestrial Neutrinos at the IceCube Detector.
Science, 342:1242856, November 2013.

[129] IceCube Collaboration.

IceCube-200107A: IceCube observation of a high-energy neutrino candidate event.
GRB Coordinates Network, 26655:1, January 2020.

[130] IceCube Collaboration, M. G. Aartsen, M. Ackermann, J. Adams, J. A. Aguilar, M. Ahlers, M. Ahrens, I. Al Samarai, D. Altmann, K. Andeen, T. Anderson, I. Ansseau, G. Anton, C. Argüelles, J. Auffenberg, S. Axani, H. Bagherpour, X. Bai, J. P. Barron, S. W. Barwick, V. Baum, R. Bay, J. J. Beatty, J. Becker Tjus, K. H. Becker, S. Ben-Zvi, D. Berley, E. Bernardini, D. Z. Besson, G. Binder, D. Bindig, E. Blaufuss, S. Blot, C. Bohm, M. Börner, F. Bos, S. Böser, O. Botner, E. Bourbeau, J. Bourbeau, F. Bradascio, J. Braun, M. Brenzke, H. P. Bretz, S. Bron, J. Brostean-Kaiser, A. Burgman, R. S. Busse, T. Carver, E. Cheung, D. Chirkin, A. Christov, K. Clark, L. Classen, S. Coenders, G. H. Collin, J. M. Conrad, P. Coppin, P. Correa, D. F. Cowen, R. Cross, P. Dave, M. Day, J. P. A. M. de André, C. De Clercq, J. J. DeLaunay, H. Dembinski, S. De Ridder, P. Desiati, K. D. de Vries, G. de Wasseige, M. de With, T. DeYoung, J. C. Díaz-Vélez, V. di Lorenzo, H. Dujmovic, J. P. Dumm, M. Dunkman, E. Dvorak, B. Eberhardt, T. Ehrhardt, B. Eichmann, P. Eller, P. A. Evenson, S. Fahey, A. R. Fazely, J. Felde, K. Filimonov, C. Finley, S. Flis, A. Franckowiak, E. Friedman, A. Fritz, T. K. Gaisser, J. Gallagher, L. Gerhardt, K. Ghorbani, T. Glauch, T. Glüsenkamp, A. Goldschmidt, J. G. Gonzalez, D. Grant, Z. Griffith, C. Haack, A. Hallgren, F. Halzen, K. Hanson, D. Hebecker, D. Heereman, K. Helbing, R. Hellauer, S. Hickford, J. Hignight, G. C. Hill, K. D. Hoffman, R. Hoffmann, T. Hoinka, B. Hokanson-Fasig, K. Hoshina, F. Huang, M. Huber, K. Hultqvist, M. Hünnefeld, R. Hussain, S. In, N. Iovine, A. Ishihara, E. Jacobi, G. S. Japaridze, M. Jeong, K. Jero, B. J. P. Jones, P. Kalaczynski, W. Kang, A. Kappes, D. Kappesser, T. Karg, A. Karle, U. Katz, M. Kauer, A. Keivani, J. L. Kelley, A. Kheirandish, J. Kim, M. Kim, T. Kintscher, J. Kiryluk, T. Kittler, S. R. Klein, R. Koirala, H. Kolanoski, L. Köpke, C. Kopper, S. Kopper, J. P. Koschinsky, D. J. Koskinen, M. Kowalski, K. Krings, M. Kroll, G. Krückl, S. Kunwar, N. Kurahashi, T. Kuwabara, A. Kyriacou, M. Labare, J. L. Lanfranchi, M. J. Larson, F. Lauber, K. Leonard, M. Lesiak-Bzdak, M. Leuermann, Q. R. Liu, C. J. Lozano Mariscal, L. Lu, J. Lünemann, W. Luszczak, J. Madsen, G. Maggi, K. B. M. Mahn, S. Mancina, R. Maruyama, K. Mase, R. Maunu, K. Meagher, M. Medici, M. Meier, T. Menne, G. Merino, T. Meures, S. Miarecki, J. Micallef, G. Momenté, T. Montaruli, R. W. Moore, S, R. Morse, M. Moulai, R. Nahnhauer, P. Nakarmi, U. Naumann, G. Neer,

H. Niederhausen, S. C. Nowicki, D. R. Nygren, A. Obertacke Pollmann, A. Olivas, A. O'Murchadha, E. O'Sullivan, T. Palczewski, H. Pandya, D. V. Pankova, P. Peiffer, J. A. Pepper, C. Pérez de los Heros, D. Pieloth, E. Pinat, M. Plum, P. B. Price, G. T. Przybylski, C. Raab, L. Rädel, M. Rameez, L. Rauch, K. Rawlins, I. C. Rea, R. Reimann, B. Relethford, M. Relich, E. Resconi, W. Rhode, M. Richman, S. Robertson, M. Rongen, C. Rott, T. Ruhe, D. Ryckbosch, D. Rysewyk, I. Safa, T. Sälzer, S. E. Sanchez Herrera, A. Sandrock, J. Sandroos, M. Santander, S. Sarkar, S. Sarkar, K. Satalecka, P. Schlunder, T. Schmidt, A. Schneider, S. Schoenen, S. Schöneberg, L. Schumacher, S. Sclafani, D. Seckel, S. Seunarine, J. Soedingrekso, D. Soldin, M. Song, G. M. Spiczak, C. Spiering, J. Stachurska, M. Stamatikos, T. Stanev, A. Stasik, R. Stein, J. Stettner, A. Steuer, T. Stezelberger, R. G. Stokstad, A. Stößl, N. L. Strotjohann, T. Stuttard, G. W. Sullivan, M. Sutherland, I. Taboada, J. Tatar, F. Tenholt, S. Ter-Antonyan, A. Terliuk, S. Tilav, P. A. Toale, M. N. Tobin, C. Toennis, S. Toscano, D. Tosi, M. Tselengidou, C. F. Tung, A. Turcati, C. F. Turley, B. Ty, E. Unger, M. Usner, J. Vandenbroucke, W. Van Driessche, D. van Eijk, N. van Eijndhoven, S. Vanheule, J. van Santen, E. Vogel, M. Vraeghe, C. Walck, A. Wallace, M. Wallraff, F. D. Wandler, N. Wandkowsky, A. Waza, C. Weaver, M. J. Weiss, C. Wendt, J. Werthebach, S. Westerhoff, B. J. Whelan, N. Whitehorn, K. Wiebe, C. H. Wiebusch, L. Wille, D. R. Williams, L. Wills, M. Wolf, J. Wood, T. R. Wood, K. Woschnagg, D. L. Xu, X. W. Xu, Y. Xu, J. P. Yanez, G. Yodh, S. Yoshida, T. Yuan, Fermi-LAT Collaboration, S. Abdollahi, M. Ajello, R. Angioni, L. Baldini, J. Ballet, G. Barbiellini, D. Bastieri, K. Bechtol, R. Bellazzini, B. Berenji, E. Bissaldi, R. D. Blandford, R. Bonino, E. Bottacini, J. Bregeon, P. Bruel, R. Buehler, T. H. Burnett, E. Burns, S. Buson, R. A. Cameron, R. Caputo, P. A. Caraveo, E. Cavazzuti, E. Charles, S. Chen, C. C. Cheung, J. Chiang, G. Chiaro, S. Ciprini, J. Cohen-Tanugi, J. Conrad, D. Costantin, S. Cutini, F. D'Ammando, F. de Palma, S. W. Digel, N. Di Lalla, M. Di Mauro, L. Di Venere, A. Domínguez, C. Favuzzi, A. Franckowiak, Y. Fukazawa, S. Funk, P. Fusco, F. Gargano, D. Gasparrini, N. Giglietto, M. Giomi, P. Giommi, F. Giordano, M. Giroletti, T. Glanzman, D. Green, I. A. Grenier, M. H. Grondin, S. Guiriec, A. K. Harding, M. Hayashida, E. Hays, J. W. Hewitt, D. Horan, G. Jóhannesson, M. Kadler, S. Kensei, D. Kocevski, F. Krauss, M. Kreter, M. Kuss, G. La Mura, S. Larsson, L. Latronico, M. Lemoine-Goumard, J. Li, F. Longo, F. Loparco, M. N. Lovellette, P. Lubrano, J. D. Magill, S. Maldera, D. Malyshev, A. Manfreda, M. N. Mazziotta, J. E. McEnery, M. Meyer, P. F. Michelson, T. Mizuno, M. E. Mon-

zani, A. Morselli, I. V. Moskalenko, M. Negro, E. Nuss, R. Ojha, N. Omodei, M. Orienti, E. Orlando, M. Palatiello, V. S. Paliya, J. S. Perkins, M. Persic, M. Pesce-Rollins, F. Piron, T. A. Porter, G. Principe, S. Rainò, R. Rando, B. Rani, M. Razzano, S. Razzaque, A. Reimer, O. Reimer, N. Renault-Tinacci, S. Ritz, L. S. Rochester, P. M. Saz Parkinson, C. Sgrò, E. J. Siskind, G. Spandre, P. Spinelli, D. J. Suson, H. Tajima, M. Takahashi, Y. Tanaka, J. B. Thayer, D. J. Thompson, L. Tibaldo, D. F. Torres, E. Torresi, G. Tosti, E. Troja, J. Valverde, G. Vianello, M. Vogel, K. Wood, M. Wood, G. Zaharijas, MAGIC Collaboration, M. L. Ahnen, S. Ansoldi, L. A. Antonelli, C. Arcaro, D. Baack, A. Babić, B. Banerjee, P. Bangale, U. Barres de Almeida, J. A. Barrio, J. Becerra González, W. Bednarek, E. Bernardini, A. Berti, W. Bhattacharyya, A. Biland, O. Blanch, G. Bonnoli, A. Carosi, R. Carosi, G. Ceribella, A. Chatterjee, S. M. Colak, P. Colin, E. Colombo, J. L. Contreras, J. Cortina, S. Covino, P. Cumani, P. Da Vela, F. Dazzi, A. De Angelis, B. De Lotto, M. Delfino, J. Delgado, F. Di Pierro, A. Domínguez, D. Dominis Prester, D. Dorner, M. Doro, S. Einecke, D. Elsaesser, V. Fallah Ramazani, A. Fernández-Barral, D. Fidalgo, L. Foffano, K. Pfrang, M. V. Fonseca, L. Font, A. Franceschini, C. Fruck, D. Galindo, S. Gallozzi, R. J. García López, M. Garczarczyk, M. Gaug, P. Giammaria, N. Godinović, D. Gora, D. Guberman, D. Hadasch, A. Hahn, T. Hassan, M. Hayashida, J. Herrera, J. Hose, D. Hrupec, S. Inoue, K. Ishio, Y. Konno, H. Kubo, J. Kushida, D. Lelas, E. Lindfors, S. Lombardi, F. Longo, M. López, C. Maggio, P. Majumdar, M. Makariev, G. Maneva, M. Manganaro, K. Mannheim, L. Maraschi, M. Mariotti, M. Martínez, S. Masuda, D. Mazin, M. Minev, J. M. M, R. Mirzoyan, A. Moralejo, V. Moreno, E. Moretti, T. Nagayoshi, V. Neustroev, A. Niedzwiecki, M. Nievas Rosillo, C. Nigro, K. Nilsson, D. Ninci, K. Nishijima, K. Noda, L. Nogués, S. Paiano, J. Palacio, D. Paneque, R. Paoletti, J. M. Paredes, G. Pedaletti, M. Peresano, M. Persic, P. G. Prada Moroni, E. Prandini, I. Puljak, J. Rodriguez Garcia, I. Reichardt, W. Rhode, M. Ribó, J. Rico, C. Righi, A. Rugliancich, T. Saito, K. Satalecka, T. Schweizer, J. Sitarek, I. Šnidaric , D. Sobczynska, A. Stamerra, M. Strzys, T. Surić, M. Takahashi, F. Tavecchio, P. Temnikov, T. Terzić, M. Teshima, N. Torres-Albà, A. Treves, S. Tsujimoto, G. Vanzo, M. Vazquez Acosta, I. Vovk, J. E. Ward, M. Will, S, D. Zaric , AGILE Team, F. Lucarelli, M. Tavani, G. Piano, I. Donnarumma, C. Pittori, F. Verrecchia, G. Barbiellini, A. Bulgarelli, P. Caraveo, P. W. Cattaneo, S. Colafrancesco, E. Costa, G. Di Cocco, A. Ferrari, F. Gianotti, A. Giuliani, P. Lipari, S. Mereghetti, A. Morselli, L. Pacciani, F. Paoletti, N. Parmiggiani,

A. Pellizzoni, P. Picozza, M. Pilia, A. Rappoldi, A. Trois, S. Vercellone, V. Vittorini, ASAS-SN Team, A. Franckowiak K. Z. Stanek, C. S. Kochanek, J. F. Beacom, T. A. Thompson, T. W. S. Holoien, S. Dong, J. L. Prieto, B. J. Shappee, S. Holmbo, HAWC Collaboration, A. U. Abeysekara, A. Albert, R. Alfaro, C. Alvarez, R. Arceo, J. C. Arteaga-Velázquez, D. Avila Rojas, H. A. Ayala Solares, A. Becerril, E. Belmont-Moreno, A. Bernal, K. S. Caballero-Mora, T. Capistrán, A. Carramiñana, S. Casanova, M. Castillo, U. Cotti, J. Cotzomi, S. Coutiño de León, C. De León, E. De la Fuente, R. Diaz Hernandez, S. Dichiara, B. L. Dingus, M. A. DuVernois, J. C. Díaz-Vélez, R. W. Ellsworth, K. Engel, D. W. Fiorino, H. Fleischhack, N. Fraija, J. A. García-González, F. Garfias, A. González Muñoz, M. M. González, J. A. Goodman, Z. Hampel-Arias, J. P. Harding, S. Hernand ez, B. Hona, F. Hueyotl-Zahuantitla, C. M. Hui, P. Hüntemeyer, A. Iriarte, A. Jardin-Blicq, V. Joshi, S. Kaufmann, G. J. Kunde, A. Lara, R. J. Lauer, W. H. Lee, D. Lennarz, H. León Vargas, J. T. Linnemann, A. L. Longinotti, G. Luis-Raya, R. Luna-García, K. Malone, S. S. Marinelli, O. Martinez, I. Martinez-Castellanos, J. Martínez-Castro, H. Martínez-Huerta, J. A. Matthews, P. Miranda-Romagnoli, E. Moreno, M. Mostafá, A. Nayerhoda, L. Nellen, M. Newbold, M. U. Nisa, R. Noriega-Papaqui, R. Pelayo, J. Pretz, E. G. Pérez-Pérez, Z. Ren, C. D. Rho, C. Rivière, D. Rosa-González, M. Rosenberg, E. Ruiz-Velasco, E. Ruiz-Velasco, F. Salesa Greus, A. Sandoval, M. Schneider, H. Schoorlemmer, G. Sinnis, A. J. Smith, R. W. Springer, P. Surajbali, O. Tibolla, K. Tollefson, I. Torres, L. Villaseñor, T. Weisgarber, F. Werner, T. Yapici, Y. Gaurang, A. Zepeda, H. Zhou, J. D. Álvarez, H. E. S. S. Collaboration, H. Abdalla, E. O. Angüner, C. Armand, M. Backes, Y. Becherini, D. Berge, M. Böttcher, C. Boisson, J. Bolmont, S. Bonnefoy, P. Bordas, F. Brun, M. Büchele, T. Bulik, S. Caroff, A. Carosi, S. Casanova, M. Cerruti, N. Chakraborty, S. Chandra, A. Chen, S. Colafrancesco, I. D. Davids, C. Deil, J. Devin, A. Djannati-Ataï, K. Egberts, G. Emery, S. Eschbach, A. Fiasson, G. Fontaine, S. Funk, M. Füßling, Y. A. Gallant, F. Gaté, G. Giavitto, D. Glawion, J. F. Glicenstein, D. Gottschall, M. H. Grondin, M. Haupt, G. Henri, J. A. Hinton, C. Hoischen, T. L. Holch, D. Huber, M. Jamrozy, D. Jankowsky, F. Jankowsky, L. Jouvin, I. Jung-Richardt, D. Kerszberg, B. Khélifi, J. King, S. Klepser, W. Kluz niak, Nu. Komin, M. Kraus, J. Lefaucheur, A. Lemière, M. Lemoine-Goumard, J. P. Lenain, E. Leser, T. Lohse, R. López-Coto, M. Lorentz, I. Lypova, V. Marandon, G. Guillem Martí-Devesa, G. Maurin, A. M. W. Mitchell, R. Moderski, M. Mohamed, L. Mohrmann, E. Moulin, T. Murach, M. de Naurois, F. Nieder-

wanger, J. Niemiec, L. Oakes, P. O'Brien, S. Ohm, M. Ostrowski, I. Oya, M. Panter, R. D. Parsons, C. Perennes, Q. Piel, S. Pita, V. Poireau, A. Priyana Noel, H. Prokoph, G. Pühlhofer, A. Quirrenbach, S. Raab, R. Rauth, M. Renaud, F. Rieger, L. Rinchiuso, C. Romoli, G. Rowell, B. Rudak, D. A. Sasaki, M. Sanchez, R. Schlickeiser, F. Schüssler, A. Schulz, U. Schwanke, M. Seglar-Arroyo, N. Shafi, R. Simoni, H. Sol, C. Stegmann, C. Steppa, T. Tavernier, A. M. Taylor, D. Tiziani, C. Trichard, M. Tsirou, C. van Eldik, C. van Rensburg, B. van Soelen, J. Veh, P. Vincent, F. Voisin, S. J. Wagner, R. M. Wagner, A. Wierzcholska, R. Zanin, A. A. Zdziarski, A. Zech, A. Ziegler, J. Zorn, N. Żywucka, INTEGRAL Team, V. Savchenko, C. Ferrigno, A. Bazzano, R. Diehl, E. Kuulkers, P. Laurent, S. Mereghetti, L. Natalucci, F. Panessa, J. Rodi, P. Ubertini, Kiso Kanata, Subaru Observing Teams, T. Morokuma, K. Ohta, Y. T. Tanaka, H. Mori, M. Yamanaka, K. S. Kawabata, Y. Utsumi, T. Nakaoka, M. Kawabata, H. Nagashima, M. Yoshida, Y. Matsuoka, R. Itoh, Kapteyn Team, W. Keel, Liverpool Telescope Team, C. Copperwheat, I. Steele, Swift/NuSTAR Team, S. B. Cenko, D. F. Cowen, J. J. DeLaunay, P. A. Evans, D. B. Fox, A. Keivani, J. A. Kennea, F. E. Marshall, J. P. Osborne, M. Santander, A. Tohuvavohu, C. F. Turley, VERITAS Collaboration, A. U. Abeysekara, A. Archer, W. Benbow, R. Bird, A. Brill, R. Brose, M. Buchovecky, J. H. Buckley, V. Bugaev, J. L. Christiansen, M. P. Connolly, W. Cui, M. K. Daniel, M. Errando, A. Falcone, Q. Feng, J. P. Finley, L. Fortson, A. Furniss, O. Gueta, M. Hütten, O. Hervet, G. Hughes, T. B. Humensky, C. A. Johnson, P. Kaaret, P. Kar, N. Kelley-Hoskins, M. Kertzman, D. Kieda, M. Krause, F. Krennrich, S. Kumar, M. J. Lang, T. T. Y. Lin, G. Maier, S. McArthur, P. Moriarty, R. Mukherjee, D. Nieto, S. O'Brien, R. A. Ong, A. N. Otte, N. Park, A. Petrashyk, M. Pohl, A. Popkow, S. E. Pueschel, J. Quinn, K. Ragan, P. T. Reynolds, G. T. Richards, E. Roache, C. Rulten, I. Sadeh, M. Santander, S. S. Scott, G. H. Sembroski, K. Shahinyan, I. Sushch, S. Trépanier, J. Tyler, V. V. Vassiliev, S. P. Wakely, A. Weinstein, R. M. Wells, P. Wilcox, A. Wilhelm, D. A. Williams, B. Zitzer, VLA/B Team, A. J. Tetarenko, A. E. Kimball, J. C. A. Miller-Jones, and G. R. Sivakoff.

Multimessenger observations of a flaring blazar coincident with high-energy neutrino IceCube-170922A.

Science, 361(6398):eaat1378, July 2018.

[131] IceCube Collaboration, M. G. Aartsen, M. Ackermann, J. Adams, J. A. Aguilar, M. Ahlers, M. Ahrens, I. Al Samarai, D. Altmann, K. Andeen, and et al.

Multimessenger observations of a flaring blazar coincident with high-energy neutrino IceCube-170922A.
Science, 361:eaat1378, July 2018.

[132] IceCube Collaboration, M. G. Aartsen, M. Ackermann, J. Adams, J. A. Aguilar, M. Ahlers, M. Ahrens, I. Al Samarai, D. Altmann, K. Andeen, T. Anderson, I. Ansseau, G. Anton, C. Argüelles, B. Arsioli, J. Auffenberg, S. Axani, H. Bagherpour, X. Bai, J. P. Barron, S. W. Barwick, V. Baum, R. Bay, J. J. Beatty, J. Becker Tjus, K. H. Becker, S. BenZvi, D. Berley, E. Bernardini, D. Z. Besson, G. Binder, D. Bindig, E. Blaufuss, S. Blot, C. Bohm, M. Börner, F. Bos, S. Böser, O. Botner, E. Bourbeau, J. Bourbeau, F. Bradascio, J. Braun, M. Brenzke, H. P. Bretz, S. Bron, J. Brostean-Kaiser, A. Burgman, R. S. Busse, T. Carver, E. Cheung, D. Chirkin, A. Christov, K. Clark, L. Classen, S. Coenders, G. H. Collin, J. M. Conrad, P. Coppin, P. Correa, D. F. Cowen, R. Cross, P. Dave, M. Day, J. P. A. M. de André, C. De Clercq, J. J. DeLaunay, H. Dembinski, S. DeRidder, P. Desiati, K. D. de Vries, G. de Wasseige, M. de With, T. DeYoung, J. C. Díaz-Vélez, V. di Lorenzo, H. Dujmovic, J. P. Dumm, M. Dunkman, E. Dvorak, B. Eberhardt, T. Ehrhardt, B. Eichmann, P. Eller, P. A. Evenson, S. Fahey, A. R. Fazely, J. Felde, K. Filimonov, C. Finley, S. Flis, A. Franckowiak, E. Friedman, A. Fritz, T. K. Gaisser, J. Gallagher, L. Gerhardt, K. Ghorbani, P. Giommi, T. Glauch, T. Glüsenkamp, A. Goldschmidt, J. G. Gonzalez, D. Grant, Z. Griffith, C. Haack, A. Hallgren, F. Halzen, K. Hanson, D. Hebecker, D. Heereman, K. Helbing, R. Hellauer, S. Hickford, J. Hignight, G. C. Hill, K. D. Hoffman, R. Hoffmann, T. Hoinka, B. Hokanson-Fasig, K. Hoshina, F. Huang, M. Huber, K. Hultqvist, M. Hünnefeld, R. Hussain, S. In, N. Iovine, A. Ishihara, E. Jacobi, G. S. Japaridze, M. Jeong, K. Jero, B. J. P. Jones, P. Kalaczynski, W. Kang, A. Kappes, D. Kappesser, T. Karg, A. Karle, U. Katz, M. Kauer, A. Keivani, J. L. Kelley, A. Kheirandish, J. Kim, M. Kim, T. Kintscher, J. Kiryluk, T. Kittler, S. R. Klein, R. Koirala, H. Kolanoski, L. Köpke, C. Kopper, S. Kopper, J. P. Koschinsky, D. J. Koskinen, M. Kowalski, B. Krammer, K. Krings, M. Kroll, G. Krückl, S. Kunwar, N. Kurahashi, T. Kuwabara, A. Kyriacou, M. Labare, J. L. Lanfranchi, M. J. Larson, F. Lauber, K. Leonard, M. Lesiak-Bzdak, M. Leuermann, Q. R. Liu, C. J. Lozano Mariscal, L. Lu, J. Lünemann, W. Luszczak, J. Madsen, G. Maggi, K. B. M. Mahn, S. Mancina, R. Maruyama, K. Mase, R. Maunu, K. Meagher, M. Medici, M. Meier, T. Menne, G. Merino, T. Meures, S. Miarecki, J. Micallef, G. Momenté, T. Montaruli, R. W. Moore, R. Morse, M. Moulai, R. Nahnhauer, P. Nakarmi, U. Nau-

mann, G. Neer, H. Niederhausen, S. C. Nowicki, D. R. Nygren, A. Obertacke Pollmann, A. Olivas, A. O'Murchadha, E. O'Sullivan, P. Padovani, T. Palczewski, H. Pand ya, D. V. Pankova, P. Peiffer, J. A. Pepper, C. Pérez de los Heros, D. Pieloth, E. Pinat, M. Plum, P. B. Price, G. T. Przybylski, C. Raab, L. Rädel, M. Rameez, K. Rawlins, I. C. Rea, R. Reimann, B. Relethford, M. Relich, E. Resconi, W. Rhode, M. Richman, S. Robertson, M. Rongen, C. Rott, T. Ruhe, D. Ryckbosch, D. Rysewyk, I. Safa, N. Sahakyan, T. Sälzer, S. E. Sanchez Herrera, A. Sandrock, J. Sandroos, M. Santander, S. Sarkar, S. Sarkar, K. Satalecka, P. Schlunder, T. Schmidt, A. Schneider, S. Schoenen, S. Schöneberg, L. Schumacher, S. Sclafani, D. Seckel, S. Seunarine, J. Soedingrekso, D. Soldin, M. Song, G. M. Spiczak, C. Spiering, J. Stachurska, M. Stamatikos, T. Stanev, A. Stasik, J. Stettner, A. Steuer, T. Stezelberger, R. G. Stokstad, A. Stößl, N. L. Strotjohann, T. Stuttard, G. W. Sullivan, M. Sutherland, I. Taboada, J. Tatar, F. Tenholt, S. Ter-Antonyan, A. Terliuk, S. Tilav, P. A. Toale, M. N. Tobin, C. Toennis, S. Toscano, D. Tosi, M. Tselengidou, C. F. Tung, A. Turcati, C. F. Turley, B. Ty, E. Unger, M. Usner, J. Vandenbroucke, W. Van Driessche, D. van Eijk, N. van Eijndhoven, S. Vanheule, J. van Santen, E. Vogel, M. Vraeghe, C. Walck, A. Wallace, M. Wallraff, F. D. Wandler, N. Wand kowsky, A. Waza, C. Weaver, M. J. Weiss, C. Wendt, J. Werthebach, S. Westerhoff, B. J. Whelan, N. Whitehorn, K. Wiebe, C. H. Wiebusch, L. Wille, D. R. Williams, L. Wills, M. Wolf, J. Wood, T. R. Wood, K. Woschnagg, D. L. Xu, X. W. Xu, Y. Xu, J. P. Yanez, G. Yodh, S. Yoshida, and T. Yuan.
Neutrino emission from the direction of the blazar TXS 0506+056 prior to the IceCube-170922A alert.
Science, 361(6398):147–151, July 2018.

[133] IceCube Collaboration, M. G. Aartsen, M. Ackermann, J. Adams, J. A. Aguilar, M. Ahlers, M. Ahrens, I. Al Samarai, D. Altmann, K. Andeen, T. Anderson, I. Ansseau, G. Anton, C. Argüelles, B. Arsioli, J. Auffenberg, S. Axani, H. Bagherpour, X. Bai, J. P. Barron, S. W. Barwick, V. Baum, R. Bay, J. J. Beatty, J. Becker Tjus, K. H. Becker, S. BenZvi, D. Berley, E. Bernardini, D. Z. Besson, G. Binder, D. Bindig, E. Blaufuss, S. Blot, C. Bohm, M. Börner, F. Bos, S. Böser, O. Botner, E. Bourbeau, J. Bourbeau, F. Bradascio, J. Braun, M. Brenzke, H. P. Bretz, S. Bron, J. Brostean-Kaiser, A. Burgman, R. S. Busse, T. Carver, E. Cheung, D. Chirkin, A. Christov, K. Clark, L. Classen, S. Coenders, G. H. Collin, J. M. Conrad, P. Coppin, P. Correa, D. F. Cowen, R. Cross, P. Dave, M. Day, J. P. A. M. de André, C. De Clercq, J. J. DeLaunay, H. Dembinski, S. DeRidder, P. Desiati, K. D.

de Vries, G. de Wasseige, M. de With, T. DeYoung, J. C. Díaz-Vélez, V. di Lorenzo, H. Dujmovic, J. P. Dumm, M. Dunkman, E. Dvorak, B. Eberhardt, T. Ehrhardt, B. Eichmann, P. Eller, P. A. Evenson, S. Fahey, A. R. Fazely, J. Felde, K. Filimonov, C. Finley, S. Flis, A. Franckowiak, E. Friedman, A. Fritz, T. K. Gaisser, J. Gallagher, L. Gerhardt, K. Ghorbani, P. Giommi, T. Glauch, T. Glüsenkamp, A. Goldschmidt, J. G. Gonzalez, D. Grant, Z. Griffith, C. Haack, A. Hallgren, F. Halzen, K. Hanson, D. Hebecker, D. Heereman, K. Helbing, R. Hellauer, S. Hickford, J. Hignight, G. C. Hill, K. D. Hoffman, R. Hoffmann, T. Hoinka, B. Hokanson-Fasig, K. Hoshina, F. Huang, M. Huber, K. Hultqvist, M. Hünnefeld, R. Hussain, S. In, N. Iovine, A. Ishihara, E. Jacobi, G. S. Japaridze, M. Jeong, K. Jero, B. J. P. Jones, P. Kalaczynski, W. Kang, A. Kappes, D. Kappesser, T. Karg, A. Karle, U. Katz, M. Kauer, A. Keivani, J. L. Kelley, A. Kheirandish, J. Kim, M. Kim, T. Kintscher, J. Kiryluk, T. Kittler, S. R. Klein, R. Koirala, H. Kolanoski, L. Köpke, C. Kopper, S. Kopper, J. P. Koschinsky, D. J. Koskinen, M. Kowalski, B. Krammer, K. Krings, M. Kroll, G. Krückl, S. Kunwar, N. Kurahashi, T. Kuwabara, A. Kyriacou, M. Labare, J. L. Lanfranchi, M. J. Larson, F. Lauber, K. Leonard, M. Lesiak-Bzdak, M. Leuermann, Q. R. Liu, C. J. Lozano Mariscal, L. Lu, J. Lünemann, W. Luszczak, J. Madsen, G. Maggi, K. B. M. Mahn, S. Mancina, R. Maruyama, K. Mase, R. Maunu, K. Meagher, M. Medici, M. Meier, T. Menne, G. Merino, T. Meures, S. Miarecki, J. Micallef, G. Momenté, T. Montaruli, R. W. Moore, R. Morse, M. Moulai, R. Nahnhauer, P. Nakarmi, U. Naumann, G. Neer, H. Niederhausen, S. C. Nowicki, D. R. Nygren, A. Obertacke Pollmann, A. Olivas, A. O'Murchadha, E. O'Sullivan, P. Padovani, T. Palczewski, H. Pand ya, D. V. Pankova, P. Peiffer, J. A. Pepper, C. Pérez de los Heros, D. Pieloth, E. Pinat, M. Plum, P. B. Price, G. T. Przybylski, C. Raab, L. Rädel, M. Rameez, K. Rawlins, I. C. Rea, R. Reimann, B. Relethford, M. Relich, E. Resconi, W. Rhode, M. Richman, S. Robertson, M. Rongen, C. Rott, T. Ruhe, D. Ryckbosch, D. Rysewyk, I. Safa, N. Sahakyan, T. Sälzer, S. E. Sanchez Herrera, A. Sandrock, J. Sandroos, M. Santander, S. Sarkar, S. Sarkar, K. Satalecka, P. Schlunder, T. Schmidt, A. Schneider, S. Schoenen, S. Schöneberg, L. Schumacher, S. Sclafani, D. Seckel, S. Seunarine, J. Soedingrekso, D. Soldin, M. Song, G. M. Spiczak, C. Spiering, J. Stachurska, M. Stamatikos, T. Stanev, A. Stasik, J. Stettner, A. Steuer, T. Stezelberger, R. G. Stokstad, A. Stößl, N. L. Strotjohann, T. Stuttard, G. W. Sullivan, M. Sutherland, I. Taboada, J. Tatar, F. Tenholt, S. Ter-Antonyan, A. Terliuk, S. Tilav, P. A. Toale, M. N. Tobin, C. Toennis, S. Toscano, D. Tosi, M. Tselengidou, C. F.

Tung, A. Turcati, C. F. Turley, B. Ty, E. Unger, M. Usner, J. Vandenbroucke, W. Van Driessche, D. van Eijk, N. van Eijndhoven, S. Vanheule, J. van Santen, E. Vogel, M. Vraeghe, C. Walck, A. Wallace, M. Wallraff, F. D. Wandler, N. Wand kowsky, A. Waza, C. Weaver, M. J. Weiss, C. Wendt, J. Werthebach, S. Westerhoff, B. J. Whelan, N. Whitehorn, K. Wiebe, C. H. Wiebusch, L. Wille, D. R. Williams, L. Wills, M. Wolf, J. Wood, T. R. Wood, K. Woschnagg, D. L. Xu, X. W. Xu, Y. Xu, J. P. Yanez, G. Yodh, S. Yoshida, and T. Yuan.
Neutrino emission from the direction of the blazar TXS 0506+056 prior to the IceCube-170922A alert.
Science, 361(6398):147–151, July 2018.

[134] Yan-Fei Jiang, James M. Stone, and Shane W. Davis.
Super-Eddington Accretion Disks around Supermassive Black Holes.
ApJ, 880(2):67, August 2019.

[135] Bruno Jiménez Fernández and Hendrik van Eerten.
Katu: a fast open-source full lepto-hadronic kinetic code suitable for Bayesian inference modelling of blazars.
arXiv e-prints, page arXiv:2104.08207, April 2021.

[136] F. C. Jones.
Calculated Spectrum of Inverse-Compton-Scattered Photons.
Physical Review, 167:1159–1169, March 1968.

[137] D. Kantzas, S. Markoff, T. Beuchert, M. Lucchini, A. Chhotray, C. Ceccobello, A. J. Tetarenko, J. C. A. Miller-Jones, M. Bremer, J. A. Garcia, V. Grinberg, P. Uttley, and J. Wilms.
A new lepto-hadronic model applied to the first simultaneous multi-wavelength data set for Cygnus X-1.
MNRAS, October 2020.

[138] B. Kapanadze, S. Vercellone, P. Romano, P. Hughes, M. Aller, H. Aller, S. Kapanadze, and L. Tabagari.
Strong X-ray flaring activity of the BL Lacertae source OJ 287 in 2016 October-2017 April.
MNRAS, 480(1):407–430, October 2018.

[139] N. S. Kardashev.
Nonstationarity of Spectra of Young Sources of Nonthermal Radio Emission.
, 6:317, December 1962.

[140] Navpreet Kaur and Kiran S. Baliyan.

CTA 102 in exceptionally high state during 2016-2017.
A&A, 617:A59, September 2018.

[141] A. Keivani, K. Murase, M. Petropoulou, D. B. Fox, S. B. Cenko, S. Chaty, A. Coleiro, J. J. DeLaunay, S. Dimitrakoudis, P. A. Evans, J. A. Kennea, F. E. Marshall, A. Mastichiadis, J. P. Osborne, M. Santander, A. Tohuvavohu, and C. F. Turley.
A Multimessenger Picture of the Flaring Blazar TXS 0506+056: Implications for High-energy Neutrino Emission and Cosmic-Ray Acceleration.
ApJ, 864:84, September 2018.

[142] A. Keivani, K. Murase, M. Petropoulou, D. B. Fox, S. B. Cenko, S. Chaty, A. Coleiro, J. J. DeLaunay, S. Dimitrakoudis, P. A. Evans, J. A. Kennea, F. E. Marshall, A. Mastichiadis, J. P. Osborne, M. Santander, A. Tohuvavohu, and C. F. Turley.
A Multimessenger Picture of the Flaring Blazar TXS 0506+056: Implications for High-energy Neutrino Emission and Cosmic-Ray Acceleration.
ApJ, 864:84, September 2018.

[143] SR Kelner and FA Aharonian.
Energy spectra of gamma rays, electrons, and neutrinos produced at interactions of relativistic protons with low energy radiation.
Physical Review D, 78(3):034013, 2008.

[144] Sang-Hyun Kim, Sang-Sung Lee, Jee Won Lee, Jeffrey A. Hodgson, Sincheol Kang, Juan-Carlos Algaba, Jae-Young Kim, Mark Hodges, Ivan Agudo, Antonio Fuentes, Juan Escudero, Ioannis Myserlis, Efthalia Traianou, Anne Lähteenmäki, Merja Tornikoski, Joni Tammi, Venkatessh Ramakrishnan, and Emilia Järvelä.
Magnetic field strengths of the synchrotron self-absorption region in the jet of CTA 102 during radio flares.
MNRAS, 510(1):815–833, February 2022.

[145] J. G. Kirk, A. W. Guthmann, Y. A. Gallant, and A. Achterberg.
Particle Acceleration at Ultrarelativistic Shocks: An Eigenfunction Method.
ApJ, 542(1):235–242, October 2000.

[146] C. S. Kochanek, B. J. Shappee, K. Z. Stanek, T. W. S. Holoien, Todd A. Thompson, J. L. Prieto, Subo Dong, J. V. Shields, D. Will, C. Britt, D. Perzanowski, and G. Pojmański.

The All-Sky Automated Survey for Supernovae (ASAS-SN) Light Curve Server v1.0.
, 129(980):104502, October 2017.

[147] S. Komossa, D. Grupe, M. L. Parker, J. L. Gómez, M. J. Valtonen, M. A. Nowak, S. G. Jorstad, D. Haggard, S. Chandra, S. Ciprini, L. Dey, A. Gopakumar, K. Hada, S. Markoff, and J. Neilsen.
X-ray spectral components of the blazar and binary black hole candidate OJ 287 (2005-2020).
MNRAS, 504(4):5575–5587, July 2021.

[148] Masaaki Kusunose and Fumio Takahara.
A Photohadronic Model of the Large-scale Jet of PKS 0637-752.
ApJ, 835:20, January 2017.

[149] V. M. Larionov, M. Villata, and C. M. Raiteri.
The nature of optical and near-infrared variability of ¡ASTROBJ¿BL Lacertae¡/ASTROBJ¿.
A&A, 510:A93, February 2010.

[150] Tiffany R. Lewis, Justin D. Finke, and Peter A. Becker.
Electron Acceleration in Blazars: Application to the 3C 279 Flare on 2013 December 20.
ApJ, 884(2):116, October 2019.

[151] Xiaofeng Li, P. Mohan, T. An, Xiaoyu Hong, Xiaopeng Cheng, Jun Yang, Yingkang Zhang, Zhongli Zhang, and Wei Zhao.
Imaging and Variability Studies of CTA 102 during the 2016 January γ-ray Flare.
ApJ, 854(1):17, February 2018.

[152] Ioannis Liodakis, Roger W. Romani, Alexei V. Filippenko, Daniel Kocevski, and WeiKang Zheng.
Probing Blazar Emission Processes with Optical/Gamma-Ray Flare Correlations.
ApJ, 880(1):32, July 2019.

[153] P. Lipari, M. Lusignoli, and D. Meloni.
Flavor composition and energy spectrum of astrophysical neutrinos.
Phys. Rev. D, 75(12):123005, June 2007.

[154] Ruo-Yu Liu, Kai Wang, Rui Xue, Andrew M. Taylor, Xiang-Yu Wang, Zhuo Li, and Huirong Yan.
Hadronuclear interpretation of a high-energy neutrino event coincident with a blazar flare.

Phys. Rev. D, 99(6):063008, March 2019.

[155] B. Lott, L. Escande, S. Larsson, and J. Ballet.
An adaptive-binning method for generating constant-uncertainty/constant-significance light curves with Fermi-LAT data.
A&A, 544:A6, August 2012.

[156] Greg M. Madejski, Marek Sikora, Tess Jaffe, MichaŁ BŁażejowski, Keith Jahoda, and RafaŁ Moderski.
X-Ray Observations of BL Lacertae during the 1997 Outburst and Association with Quasar-like Characteristics.
ApJ, 521(1):145–154, August 1999.

[157] MAGIC Collaboration, V. A. Acciari, S. Ansoldi, L. A. Antonelli, A. Arbet Engels, D. Baack, A. Babić, B. Banerjee, P. Bangale, U. Barres de Almeida, J. A. Barrio, J. Becerra González, W. Bednarek, E. Bernardini, A. Berti, J. Besenrieder, W. Bhattacharyya, C. Bigongiari, A. Biland, O. Blanch, G. Bonnoli, R. Carosi, G. Ceribella, S. Cikota, S. M. Colak, P. Colin, E. Colombo, J. L. Contreras, J. Cortina, S. Covino, V. D'Elia, P. da Vela, F. Dazzi, A. de Angelis, B. de Lotto, M. Delfino, J. Delgado, F. di Pierro, E. Do Souto Espiñera, A. Domínguez, D. Dominis Prester, D. Dorner, M. Doro, S. Einecke, D. Elsaesser, V. Fallah Ramazani, A. Fattorini, A. Fernández-Barral, G. Ferrara, D. Fidalgo, L. Foffano, M. V. Fonseca, L. Font, C. Fruck, D. Galindo, S. Gallozzi, R. J. García López, M. Garczarczyk, M. Gaug, P. Giammaria, N. Godinović, D. Guberman, D. Hadasch, A. Hahn, T. Hassan, J. Herrera, J. Hoang, D. Hrupec, S. Inoue, K. Ishio, Y. Iwamura, H. Kubo, J. Kushida, D. Kuveždić, A. Lamastra, D. Lelas, F. Leone, E. Lindfors, S. Lombardi, F. Longo, M. López, A. López-Oramas, C. Maggio, P. Majumdar, M. Makariev, G. Maneva, M. Manganaro, K. Mannheim, L. Maraschi, M. Mariotti, M. Martínez, S. Masuda, D. Mazin, M. Minev, J. M. Miranda, R. Mirzoyan, E. Molina, A. Moralejo, V. Moreno, E. Moretti, P. Munar-Adrover, V. Neustroev, A. Niedzwiecki, M. Nievas Rosillo, C. Nigro, K. Nilsson, D. Ninci, K. Nishijima, K. Noda, L. Nogués, M. Nöthe, S. Paiano, J. Palacio, D. Paneque, R. Paoletti, J. M. Paredes, G. Pedaletti, P. Peñil, M. Peresano, M. Persic, P. G. Prada Moroni, E. Prandini, I. Puljak, J. R. Garcia, W. Rhode, M. Ribó, J. Rico, C. Righi, A. Rugliancich, L. Saha, T. Saito, K. Satalecka, T. Schweizer, J. Sitarek, I. Šnidarić, D. Sobczynska, A. Somero, A. Stamerra, M. Strzys, T. Surić, F. Tavecchio, P. Temnikov, T. Terzić, M. Teshima, N. Torres-Albà, S. Tsujimoto, J. van Scherpenberg, G. Vanzo,

M. Vazquez Acosta, I. Vovk, M. Will, D. Zarić, F. D'Ammando, K. Hada, S. Jorstad, A. P. Marscher, M. Z. Mobeen, T. Hovatta, V. M. Larionov, G. A. Borman, T. S. Grishina, E. N. Kopatskaya, D. A. Morozova, A. A. Nikiforova, A. Lähteenmäki, M. Tornikoski, and I. Agudo.
A fast, very-high-energy γ-ray flare from BL Lacertae during a period of multi-wavelength activity in June 2015.
A&A, 623:A175, March 2019.

[158] R. Mahadevan, R. Narayan, and I. Yi.
Harmony in Electrons: Cyclotron and Synchrotron Emission by Thermal Electrons in a Magnetic Field.
ApJ, 465:327, July 1996.

[159] Anwesh Majumder, Kaustav Mitra, Ritaban Chatterjee, C. M. Urry, C. D. Bailyn, and Prantik Nandi.
Physical inference from the γ-ray, X-ray, and optical time variability of a large sample of Fermi blazars.
MNRAS, 490(1):124–134, November 2019.

[160] K. Mannheim.
The proton blazar.
A&A, 269:67–76, March 1993.

[161] K. Mannheim and P. L. Biermann.
Photomeson production in active galactic nuclei.
A&A, 221:211–220, September 1989.

[162] L. Maraschi, G. Ghisellini, and A. Celotti.
A Jet Model for the Gamma-Ray–emitting Blazar 3C 279.
ApJL, 397:L5, September 1992.

[163] L. Maraschi, G. Ghisellini, and A. Celotti.
A jet model for the gamma-ray emitting blazar 3C 279.
ApJL, 397:L5–L9, September 1992.

[164] Alessandro Marchini, Pietro Aceti, Massimo Banfi, Fabio Mortari, Riccardo Papini, Fabio Salvaggio, Giuseppe Marino, Claudio Arena, Antonio Frasca, Massimo Conti, Simone Leonini, Paolo Rosi, Luz Marina Tinjaca Ramirez, and Giacomo Bonnoli.
The flaring blazar BL Lacertae observed below R=11.5, a new record for its optical brightness.
The Astronomer's Telegram, 14328:1, January 2021.

[165] Alessandro Marchini, University of Siena Italy), Lorenzo Bellizzi, Andrea Lorini, Stefano Menchiari, Vincenzo Millucci, Riccardo Paoletti, Leonardo Stiaccini, Stefano Truzzi, Sofia Ventura, Carolin Wunderlich, Claudio Arena, Antonio Frasca, Giuseppe Marino, Fabio Mortari, Massimo Conti, Simone Leonini, Paolo Rosi, Luz Marina Tinjaca Ramirez, Pietro Aceti, Massimo Banfi, Riccardo Papini, Fabio Salvaggio, and Giacomo Bonnoli.
The optical state of the flaring blazar BL Lacertae approaches again the historical brightness of the 2020 outburst.
The Astronomer's Telegram, 14318:1, January 2021.

[166] A. Marcowith and J. Malzac.
Cyclotron-synchrotron: Harmonic fitting functions in the non-relativistic and trans-relativistic regimes.
A&A, 409:9–19, October 2003.

[167] Alan P. Marscher, Svetlana G. Jorstad, Francesca D. D'Arcangelo, Paul S. Smith, G. Grant Williams, Valeri M. Larionov, Haruki Oh, Alice R. Olmstead, Margo F. Aller, Hugh D. Aller, Ian M. McHardy, Anne Lähteenmäki, Merja Tornikoski, Esko Valtaoja, Vladimir A. Hagen-Thorn, Eugenia N. Kopatskaya, Walter K. Gear, Gino Tosti, Omar Kurtanidze, Maria Nikolashvili, Lorand Sigua, H. Richard Miller, and Wesley T. Ryle.
The inner jet of an active galactic nucleus as revealed by a radio-to-γ-ray outburst.
Nature, 452(7190):966–969, April 2008.

[168] E. Massaro, A. Tramacere, M. Perri, P. Giommi, and G. Tosti.
Log-parabolic spectra and particle acceleration in blazars. III. SSC emission in the TeV band from Mkn501.
A&A, 448(3):861–871, March 2006.

[169] A. Mastichiadis and J. G. Kirk.
Self-consistent particle acceleration in active galactic nuclei.
A&A, 295:613, March 1995.

[170] A. Mastichiadis, R. J. Protheroe, and J. G. Kirk.
Spectral and temporal signatures of ultrarelativistic protons in compact sources. I. Effects of Bethe-Heitler pair production.
A&A, 433:765–776, April 2005.

[171] Apostolos Mastichiadis and Maria Petropoulou.
Hadronic X-Ray Flares from Blazars.
ApJ, 906(2):131, January 2021.

[172] J. R. Mattox, D. L. Bertsch, J. Chiang, B. L. Dingus, S. W. Digel, J. A. Esposito, J. M. Fierro, R. C. Hartman, S. D. Hunter, G. Kanbach, D. A. Kniffen, Y. C. Lin, D. J. Macomb, H. A. Mayer-Hasselwander, P. F. Michelson, C. von Montigny, R. Mukherjee, P. L. Nolan, P. V. Ramanamurthy, E. Schneid, P. Sreekumar, D. J. Thompson, and T. D. Willis.
The Likelihood Analysis of EGRET Data.
ApJ, 461:396, April 1996.

[173] I. Mereu.
Fermi-LAT detection of record gamma-ray flare in BL Lacertae contemporaneous with record X-ray flare.
The Astronomer's Telegram, 14072:1, October 2020.

[174] Manuel Meyer, Jeffrey D. Scargle, and Roger D. Blandford.
Characterizing the Gamma-Ray Variability of the Brightest Flat Spectrum Radio Quasars Observed with the Fermi LAT.
ApJ, 877(1):39, May 2019.

[175] R. Middei, P. Giommi, M. Perri, S. Turriziani, N. Sahakyan, Y. L. Chang, C. Leto, and F. Verrecchia.
The first hard X-ray spectral catalogue of Blazars observed by NuSTAR.
MNRAS, 514(3):3179–3190, August 2022.

[176] G. Minervini, G. Piano, and et al.
AGILE detection of enhanced gamma-ray emission from the FSRQ CTA 102.
The Astronomer's Telegram, 9743, November 2016.

[177] JW Motz, Haakon A Olsen, and HW Koch.
Pair production by photons.
Reviews of Modern Physics, 41(4):581, 1969.

[178] A. Mücke, R. Engel, J. P. Rachen, R. J. Protheroe, and T. Stanev.
Monte Carlo simulations of photohadronic processes in astrophysics.
Computer Physics Communications, 124:290–314, February 2000.

[179] A. Mücke and R. J. Protheroe.
A proton synchrotron blazar model for flaring in Markarian 501.
Astroparticle Physics, 15(1):121–136, March 2001.

[180] A. Mücke, R. J. Protheroe, R. Engel, J. P. Rachen, and T. Stanev.
BL Lac objects in the synchrotron proton blazar model.
Astroparticle Physics, 18:593–613, March 2003.

[181] K. Murase, F. Oikonomou, and M. Petropoulou.
Blazar Flares as an Origin of High-energy Cosmic Neutrinos?
ApJ, 865:124, October 2018.

[182] Krzysztof Nalewajko, Mitchell C. Begelman, and Marek Sikora.
Constraining the Location of Gamma-Ray Flares in Luminous Blazars.
ApJ, 789(2):161, July 2014.

[183] Yu. I. Neshpor, N. N. Chalenko, A. A. Stepanian, O. R. Kalekin, N. A. Jogolev, V. P. Fomin, and V. G. Shitov.
BL Lac: A New Ultrahigh-Energy Gamma-Ray Source.
Astronomy Reports, 45(4):249–254, April 2001.

[184] K. Nilsson, E. Lindfors, L. O. Takalo, R. Reinthal, A. Berdyugin, A. Sillanpää, S. Ciprini, A. Halkola, P. Heinämäki, T. Hovatta, V. Kadenius, P. Nurmi, L. Ostorero, M. Pasanen, R. Rekola, J. Saarinen, J. Sainio, T. Tuominen, C. Villforth, T. Vornanen, and B. Zaprudin.
Long-term optical monitoring of TeV emitting blazars. I. Data analysis.
A&A, 620:A185, December 2018.

[185] K. Nilsson, T. Pursimo, C. Villforth, E. Lindfors, and L. O. Takalo.
The host galaxy of 3C 279.
A&A, 505(2):601–604, October 2009.

[186] P. L. Nolan, D. L. Bertsch, C. E. Fichtel, R. C. Hartman, S. D. Hunter, G. Kanbach, D. A. Kniffen, Y. C. Lin, J. R. Mattox, H. A. Mayer-Hasselwander, P. F. Michelson, C. von Montigny, E. Schneid, P. Sreekumar, and D. J. Thompson.
Observation of High-Energy Gamma Rays from the Quasi-stellar Object CTA 102.
ApJ, 414:82, September 1993.

[187] Roopesh Ojha and Janeth Valverd.
Fermi-LAT detection of record gamma-ray flare in BL Lacertae contemporaneous with record optical flaring.
The Astronomer's Telegram, 13964:1, August 2020.

[188] P. Padovani, D. M. Alexander, R. J. Assef, B. De Marco, P. Giommi, R. C. Hickox, G. T. Richards, V. Smolčić, E. Hatziminaoglou, V. Mainieri, and M. Salvato.
Active galactic nuclei: what's in a name?
A&AR, 25(1):2, August 2017.

[189] P. Padovani, P. Giommi, E. Resconi, T. Glauch, B. Arsioli, N. Sahakyan, and M. Huber.

Dissecting the region around IceCube-170922A: the blazar TXS 0506+056 as the first cosmic neutrino source.
MNRAS, 480(1):192–203, October 2018.

[190] P. Padovani, F. Oikonomou, M. Petropoulou, P. Giommi, and E. Resconi.
TXS 0506+056, the first cosmic neutrino source, is not a BL Lac.
MNRAS, 484(1):L104–L108, March 2019.

[191] P. Padovani, E. Resconi, P. Giommi, B. Arsioli, and Y. L. Chang.
Extreme blazars as counterparts of IceCube astrophysical neutrinos.
MNRAS, 457(4):3582–3592, April 2016.

[192] Paolo Padovani and Paolo Giommi.
The connection between x-ray- and radio-selected BL Lacertae objects.
ApJ, 444:567–581, 1995.

[193] Simona Paiano, Renato Falomo, Paolo Padovani, Paolo Giommi, Adriana Gargiulo, Michela Uslenghi, Andrea Rossi, and Aldo Treves.
The redshift and the host galaxy of the neutrino candidate 4FGL J0955.1+3551 (3HSP J095507.9+355101).
MNRAS, 495(1):L108–L111, June 2020.

[194] Vaidehi S. Paliya.
Fermi-Large Area Telescope Observations of the Exceptional Gamma-Ray Flare from 3C 279 in 2015 June.
ApJL, 808(2):L48, August 2015.

[195] Vaidehi S. Paliya, M. Böttcher, A. Olmo-García, A. Domínguez, A. Gil de Paz, A. Franckowiak, S. Garrappa, and R. Stein.
Multifrequency Observations of the Candidate Neutrino-emitting Blazar BZB J0955+3551.
ApJ, 902(1):29, October 2020.

[196] Vaidehi S. Paliya, M. L. Parker, A. C. Fabian, and C. S. Stalin.
Broadband Observations of High Redshift Blazars.
ApJ, 825(1):74, July 2016.

[197] J. Park, D. Caprioli, and A. Spitkovsky.
Simultaneous Acceleration of Protons and Electrons at Nonrelativistic Quasiparallel Collisionless Shocks.
Physical Review Letters, 114(8):085003, February 2015.

[198] A. Pe'er and E. Waxman.

Time-dependent Numerical Model for the Emission of Radiation from Relativistic Plasma.
ApJ, 628:857–866, August 2005.

[199] M. Petropoulou and A. Mastichiadis.
Bethe-Heitler emission in BL Lacs: filling the gap between X-rays and γ-rays.
MNRAS, 447(1):36–48, February 2015.

[200] M. Petropoulou and A. Mastichiadis.
Bethe-Heitler emission in BL Lacs: filling the gap between X-rays and γ-rays.
MNRAS, 447(1):36–48, February 2015.

[201] M. Petropoulou, K. Nalewajko, M. Hayashida, and A. Mastichiadis.
A hadronic minute-scale GeV flare from quasar 3C 279?
MNRAS, 467(1):L16–L20, May 2017.

[202] Maria Petropoulou, Kohta Murase, Marcos Santander, Sara Buson, Aaron Tohuvavohu, Taiki Kawamuro, Georgios Vasilopoulos, Hiroshi Negoro, Yoshihiro Ueda, Michael H. Siegel, Azadeh Keivani, Nobuyuki Kawai, Apostolos Mastichiadis, and Stavros Dimitrakoudis.
Multi-epoch Modeling of TXS 0506+056 and Implications for Long-term High-energy Neutrino Emission.
ApJ, 891(2):115, March 2020.

[203] Maria Petropoulou, Foteini Oikonomou, Apostolos Mastichiadis, Kohta Murase, Paolo Padovani, Georgios Vasilopoulos, and Paolo Giommi.
Comprehensive Multimessenger Modeling of the Extreme Blazar 3HSP J095507.9+355101 and Predictions for IceCube.
ApJ, 899(2):113, August 2020.

[204] E. Pian, R. Falomo, and A. Treves.
Hubble Space Telescope ultraviolet spectroscopy of blazars: emission-line properties and black hole masses.
MNRAS, 361(3):919–926, August 2005.

[205] Elena Pian, Giuseppe Vacanti, Gianpiero Tagliaferri, Gabriele Ghisellini, Laura Maraschi, Aldo Treves, C. Megan Urry, Fabrizio Fiore, Paolo Giommi, Eliana Palazzi, Lucio Chiappetti, and Rita M. Sambruna.

BeppoSAX Observations of Unprecedented Synchrotron Activity in the BL Lacertae Object Markarian 501.
ApJL, 492(1):L17–L20, January 1998.

[206] T. S. Poole, A. A. Breeveld, M. J. Page, W. Landsman, S. T. Holland, P. Roming, N. P. M. Kuin, P. J. Brown, C. Gronwall, S. Hunsberger, S. Koch, K. O. Mason, P. Schady, D. vanden Berk, A. J. Blustin, P. Boyd, P. Broos, M. Carter, M. M. Chester, A. Cucchiara, B. Hancock, H. Huckle, S. Immler, M. Ivanushkina, T. Kennedy, F. Marshall, A. Morgan, S. B. Pandey, M. de Pasquale, P. J. Smith, and M. Still.
Photometric calibration of the Swift ultraviolet/optical telescope.
MNRAS, 383(2):627–645, January 2008.

[207] V. Popov and R. Bachev.
Intra-night optical activity of the blazar CTA 102 during its maximum state.
The Astronomer's Telegram, 9776, November 2016.

[208] Raj Prince.
Broad-band study of BL Lac during flare of 2020: spectral evolution and emergence of HBL component.
MNRAS, 507(4):5602–5612, November 2021.

[209] Raj Prince, Gayathri Raman, Joachim Hahn, Nayantara Gupta, and Pratik Majumdar.
Fermi-Large Area Telescope Observations of the Brightest Gamma-Ray Flare Ever Detected from CTA 102.
ApJ, 866(1):16, October 2018.

[210] C. M. Raiteri, M. Villata, J. A. Acosta-Pulido, I. Agudo, A. A. Arkharov, R. Bachev, G. V. Baida, E. Benítez, G. A. Borman, W. Boschin, V. Bozhilov, M. S. Butuzova, P. Calcidese, M. I. Carnerero, D. Carosati, C. Casadio, N. Castro-Segura, W. P. Chen, G. Damljanovic, F. D'Ammando, A. di Paola, J. Echevarría, N. V. Efimova, Sh. A. Ehgamberdiev, C. Espinosa, A. Fuentes, A. Giunta, J. L. Gómez, T. S. Grishina, M. A. Gurwell, D. Hiriart, H. Jermak, B. Jordan, S. G. Jorstad, M. Joshi, E. N. Kopatskaya, K. Kuratov, O. M. Kurtanidze, S. O. Kurtanidze, A. Lähteenmäki, V. M. Larionov, E. G. Larionova, L. V. Larionova, C. Lázaro, C. S. Lin, M. P. Malmrose, A. P. Marscher, K. Matsumoto, B. McBreen, R. Michel, B. Mihov, M. Minev, D. O. Mirzaqulov, A. A. Mokrushina, S. N. Molina, J. W. Moody, D. A. Morozova, S. V. Nazarov, M. G. Nikolashvili, J. M. Ohlert, D. N. Okhmat, E. Ovcharov, F. Pinna, T. A.

Polakis, C. Protasio, T. Pursimo, F. J. Redondo-Lorenzo, N. Rizzi, G. Rodriguez-Coira, K. Sadakane, A. C. Sadun, M. R. Samal, S. S. Savchenko, E. Semkov, B. A. Skiff, L. Slavcheva-Mihova, P. S. Smith, I. A. Steele, A. Strigachev, J. Tammi, C. Thum, M. Tornikoski, Yu. V. Troitskaya, I. S. Troitsky, A. A. Vasilyev, and O. Vince.

Blazar spectral variability as explained by a twisted inhomogeneous jet.

Nature, 552(7685):374–377, December 2017.

[211] C. M. Raiteri, M. Villata, L. Bruschini, A. Capetti, O. M. Kurtanidze, V. M. Larionov, P. Romano, S. Vercellone, I. Agudo, H. D. Aller, M. F. Aller, A. A. Arkharov, U. Bach, A. Berdyugin, D. A. Blinov, M. Böttcher, C. S. Buemi, P. Calcidese, D. Carosati, R. Casas, W. P. Chen, J. Coloma, C. Diltz, A. di Paola, M. Dolci, N. V. Efimova, E. Forné, J. L. Gómez, M. A. Gurwell, A. Hakola, T. Hovatta, H. Y. Hsiao, B. Jordan, S. G. Jorstad, E. Koptelova, S. O. Kurtanidze, A. Lähteenmäki, E. G. Larionova, P. Leto, E. Lindfors, R. Ligustri, A. P. Marscher, D. A. Morozova, M. G. Nikolashvili, K. Nilsson, J. A. Ros, P. Roustazadeh, A. C. Sadun, A. Sillanpää, J. Sainio, L. O. Takalo, M. Tornikoski, C. Trigilio, I. S. Troitsky, and G. Umana.

Another look at the BL Lacertae flux and spectral variability. Observations by GASP-WEBT, XMM-Newton, and Swift in 2008-2009.

A&A, 524:A43, December 2010.

[212] C. M. Raiteri, M. Villata, A. Capetti, M. F. Aller, U. Bach, P. Calcidese, M. A. Gurwell, V. M. Larionov, J. Ohlert, K. Nilsson, A. Strigachev, I. Agudo, H. D. Aller, R. Bachev, E. Benítez, A. Berdyugin, M. Böttcher, C. S. Buemi, S. Buttiglione, D. Carosati, P. Charlot, W. P. Chen, D. Dultzin, E. Forné, L. Fuhrmann, J. L. Gómez, A. C. Gupta, J. Heidt, D. Hiriart, W. S. Hsiao, M. Jelínek, S. G. Jorstad, G. N. Kimeridze, T. S. Konstantinova, E. N. Kopatskaya, A. Kostov, O. M. Kurtanidze, A. Lähteenmäki, L. Lanteri, L. V. Larionova, P. Leto, G. Latev, J. F. Le Campion, C. U. Lee, R. Ligustri, E. Lindfors, A. P. Marscher, B. Mihov, M. G. Nikolashvili, Y. Nikolov, E. Ovcharov, D. Principe, T. Pursimo, B. Ragozzine, R. M. Robb, J. A. Ros, A. C. Sadun, R. Sagar, E. Semkov, L. A. Sigua, R. L. Smart, M. Sorcia, L. O. Takalo, M. Tornikoski, C. Trigilio, K. Uckert, G. Umana, A. Valcheva, and A. Volvach.

WEBT multiwavelength monitoring and XMM-Newton observations of ¡ASTROBJ¿BL Lacertae¡/ASTROBJ¿ in 2007-2008. Unveiling different emission components.

A&A, 507(2):769–779, November 2009.

[213] C. M. Raiteri, M. Villata, F. D'Ammando, V. M. Larionov, M. A. Gurwell, D. O. Mirzaqulov, P. S. Smith, J. A. Acosta-Pulido, I. Agudo, M. J. Arévalo, R. Bachev, E. Benítez, A. Berdyugin, D. A. Blinov, G. A. Borman, M. Böttcher, V. Bozhilov, M. I. Carnerero, D. Carosati, C. Casadio, W. P. Chen, V. T. Doroshenko, Yu. S. Efimov, N. V. Efimova, Sh. A. Ehgamberdiev, J. L. Gómez, P. A. González-Morales, D. Hiriart, S. Ibryamov, Y. Jadhav, S. G. Jorstad, M. Joshi, V. Kadenius, S. A. Klimanov, M. Kohli, T. S. Konstantinova, E. N. Kopatskaya, E. Koptelova, G. Kimeridze, O. M. Kurtanidze, E. G. Larionova, L. V. Larionova, R. Ligustri, E. Lindfors, A. P. Marscher, B. McBreen, I. M. McHardy, Y. Metodieva, S. N. Molina, D. A. Morozova, S. V. Nazarov, M. G. Nikolashvili, K. Nilsson, D. N. Okhmat, E. Ovcharov, N. Panwar, M. Pasanen, S. Peneva, J. Phipps, N. G. Pulatova, R. Reinthal, J. A. Ros, A. C. Sadun, R. D. Schwartz, E. Semkov, S. G. Sergeev, L. A. Sigua, A. Sillanpää, N. Smith, K. Stoyanov, A. Strigachev, L. O. Takalo, B. Taylor, C. Thum, I. S. Troitsky, A. Valcheva, A. E. Wehrle, and H. Wiesemeyer.
The awakening of BL Lacertae: observations by Fermi, Swift and the GASP-WEBT.
MNRAS, 436(2):1530–1545, December 2013.

[214] Bhoomika Rajput, C. S. Stalin, and S. Sahayanathan.
Correlation between optical and γ-ray flux variations in bright flat spectrum radio quasars.
MNRAS, 498(4):5128–5148, November 2020.

[215] B. Rani, B. Lott, T. P. Krichbaum, L. Fuhrmann, and J. A. Zensus.
Constraining the location of rapid gamma-ray flares in the flat spectrum radio quasar 3C 273.
A&A, 557:A71, September 2013.

[216] M. Ravasio, G. Tagliaferri, G. Ghisellini, P. Giommi, R. Nesci, E. Massaro, L. Chiappetti, A. Celotti, L. Costamante, L. Maraschi, F. Tavecchio, G. Tosti, A. Treves, A. Wolter, T. Balonek, M. Carini, T. Kato, O. Kurtanidze, F. Montagni, M. Nikolashvili, J. Noble, G. Nucciarelli, C. M. Raiteri, S. Sclavi, M. Uemura, and M. Villata.
BL Lacertae: Complex spectral variability and rapid synchrotron flare detected with BeppoSAX.
A&A, 383:763–772, March 2002.

[217] M. Ravasio, G. Tagliaferri, G. Ghisellini, F. Tavecchio, M. Böttcher, and M. Sikora.
BeppoSAX and multiwavelength observations of BL Lacertae in 2000.

A&A, 408:479–491, September 2003.

[218] Anita Reimer, Markus Böttcher, and Sara Buson.
Cascading Constraints from Neutrino-emitting Blazars: The Case of TXS 0506+056.
ApJ, 881(1):46, August 2019.

[219] Helena X. Ren, Matteo Cerruti, and Narek Sahakyan.
Quasi-periodic oscillations in the γ-ray light curves of bright active galactic nuclei.
arXiv e-prints, page arXiv:2204.13051, April 2022.

[220] M. M. Reynoso, M. C. Medina, and G. E. Romero.
A lepto-hadronic model for high-energy emission from FR I radiogalaxies.
A&A, 531:A30, July 2011.

[221] C. Righi, F. Tavecchio, and L. Pacciani.
A multiwavelength view of BL Lac neutrino candidates.
MNRAS, 484(2):2067–2077, April 2019.

[222] Xavier Rodrigues, Shan Gao, Anatoli Fedynitch, Andrea Palladino, and Walter Winter.
Leptohadronic Blazar Models Applied to the 2014-2015 Flare of TXS 0506+056.
ApJL, 874(2):L29, April 2019.

[223] Abhradeep Roy, S. R. Patel, A. Sarkar, A. Chatterjee, and V. R. Chitnis.
Multiwavelength study of the quiescent states of six brightest flat-spectrum radio quasars detected by Fermi-LAT.
MNRAS, 504(1):1103–1114, June 2021.

[224] G. B. Rybicki and A. P. Lightman.
Radiative processes in astrophysics.
1979.

[225] N. Sahakyan.
Lepto-hadronic γ-Ray and Neutrino Emission from the Jet of TXS 0506+056.
ApJ, 866:109, October 2018.

[226] N. Sahakyan.
Origin of the multiwavelength emission of PKS 0502+049.
A&A, 622:A144, February 2019.

[227] N. Sahakyan.
Broad-band study of high-synchrotron-peaked BL Lac object 1ES 1218+304.
MNRAS, 496(4):5518–5527, July 2020.

[228] N. Sahakyan.
Investigation of the γ-ray spectrum of CTA 102 during the exceptional flaring state in 2016-2017.
A&A, 635:A25, March 2020.

[229] N. Sahakyan.
Modelling the broad-band emission of 3C 454.3.
MNRAS, 504(4):5074–5086, July 2021.

[230] N. Sahakyan, V. Baghmanyan, and D. Zargaryan.
Fermi-LAT observation of nonblazar AGNs.
A&A, 614:A6, June 2018.

[231] N. Sahakyan and S. Gasparyan.
High energy gamma-ray emission from PKS 1441+25.
MNRAS, 470(3):2861–2869, September 2017.

[232] N. Sahakyan and P. Giommi.
The strange case of the transient HBL blazar 4FGL J1544.3-0649.
MNRAS, 502(1):836–844, March 2021.

[233] N. Sahakyan and P. Giommi.
A 13-yr-long broad-band view of BL Lac.
MNRAS, 513(3):4645–4656, July 2022.

[234] N. Sahakyan, P. Giommi, P. Padovani, M. Petropoulou, D. Bégué, B. Boccardi, and S. Gasparyan.
A multi-messenger study of the blazar PKS 0735+178: a new major neutrino source candidate.
arXiv e-prints, page arXiv:2204.05060, April 2022.

[235] N. Sahakyan, D. Israyelyan, G. Harutyunyan, M. Khachatryan, and S. Gasparyan.
Multiwavelength study of high-redshift blazars.
MNRAS, 498(2):2594–2613, August 2020.

[236] Rita M. Sambruna, Gabriele Ghisellini, Eric Hooper, R. I. Kollgaard, Joseph E. Pesce, and C. Megan Urry.
ASCA and Contemporaneous Ground-based Observations of the BL Lacertae Objects 1749+096 and 2200+420 (BL Lac).

ApJ, 515(1):140–152, April 1999.

[237] Jeffrey D. Scargle, Jay P. Norris, Brad Jackson, and James Chiang.
Studies in Astronomical Time Series Analysis. VI. Bayesian Block Representations.
ApJ, 764(2):167, February 2013.

[238] Maarten Schmidt.
Large Redshifts of Five Quasi-Stellar Sources.
ApJ, 141:1295, April 1965.

[239] A. Shukla, K. Mannheim, S. R. Patel, J. Roy, V. R. Chitnis, D. Dorner, A. R. Rao, G. C. Anupama, and C. Wendel.
Short-timescale γ-Ray Variability in CTA 102.
ApJL, 854(2):L26, February 2018.

[240] M. Sikora, M. C. Begelman, and M. J. Rees.
Comptonization of diffuse ambient radiation by a relativistic jet: The source of gamma rays from blazars?
ApJ, 421:153–162, January 1994.

[241] M. Sikora, H. Sol, M. C. Begelman, and G. M. Madejski.
Radiation drag in relativistic active galactic nucleus jets.
MNRAS, 280:781–796, June 1996.

[242] Marek Sikora, Mitchell C. Begelman, and Martin J. Rees.
Comptonization of Diffuse Ambient Radiation by a Relativistic Jet: The Source of Gamma Rays from Blazars?
ApJ, 421:153, January 1994.

[243] Marek Sikora, Łukasz Stawarz, Rafał Moderski, Krzysztof Nalewajko, and Greg M. Madejski.
Constraining Emission Models of Luminous Blazar Sources.
ApJ, 704(1):38–50, October 2009.

[244] Marek Sikora, Łukasz Stawarz, Rafał Moderski, Krzysztof Nalewajko, and Greg M. Madejski.
Constraining Emission Models of Luminous Blazar Sources.
ApJ, 704(1):38–50, October 2009.

[245] Lorenzo Sironi and Anatoly Spitkovsky.
Relativistic Reconnection: An Efficient Source of Non-thermal Particles.
ApJL, 783(1):L21, March 2014.

[246] P. S. Smith, E. Montiel, S. Rightley, J. Turner, G. D. Schmidt, and B. T. Jannuzi.
Coordinated Fermi/Optical Monitoring of Blazars and the Great 2009 September Gamma-ray Flare of 3C 454.3.
arXiv e-prints, page arXiv:0912.3621, December 2009.

[247] Anatoly Spitkovsky.
Particle Acceleration in Relativistic Collisionless Shocks: Fermi Process at Last?
ApJL, 682(1):L5, July 2008.

[248] Stamatios I. Stathopoulos, Maria Petropoulou, Paolo Giommi, Georgios Vasilopoulos, Paolo Padovani, and Apostolos Mastichiadis.
Probing Neutrino Emission from X-ray Blazar Flares observed with Swift-XRT.
arXiv e-prints, page arXiv:2107.14632, July 2021.

[249] Errol J. Summerlin and Matthew G. Baring.
Diffusive Acceleration of Particles at Oblique, Relativistic, Magnetohydrodynamic Shocks.
ApJ, 745(1):63, January 2012.

[250] F. Tavecchio, J. Becerra-Gonzalez, G. Ghisellini, A. Stamerra, G. Bonnoli, L. Foschini, and L. Maraschi.
On the origin of the γ-ray emission from the flaring blazar PKS 1222+216.
A&A, 534:A86, October 2011.

[251] F. Tavecchio and G. Ghisellini.
On the magnetization of BL Lac jets.
MNRAS, 456:2374–2382, March 2016.

[252] Fabrizio Tavecchio and Gabriele Ghisellini.
Spine-sheath layer radiative interplay in subparsec-scale jets and the TeV emission from M87.
MNRAS, 385(1):L98–L102, March 2008.

[253] Lev Titarchuk and Elena Seifina.
BL Lacertae: X-ray spectral evolution and a black-hole mass estimate.
A&A, 602:A113, June 2017.

[254] A. Tramacere, P. Giommi, M. Perri, F. Verrecchia, and G. Tosti.
Swift observations of the very intense flaring activity of Mrk 421 during 2006. I. Phenomenological picture of electron acceleration and predictions for MeV/GeV emission.

A&A, 501(3):879–898, July 2009.

[255] A. Tramacere, E. Massaro, and A. M. Taylor.
Stochastic Acceleration and the Evolution of Spectral Distributions in Synchro-Self-Compton Sources: A Self-consistent Modeling of Blazars' Flares.
ApJ, 739(2):66, October 2011.

[256] Andrea Tramacere.
JetSeT: Numerical modeling and SED fitting tool for relativistic jets, September 2020.

[257] C. Megan Urry and Paolo Padovani.
Unified Schemes for Radio-Loud Active Galactic Nuclei.
, 107:803, September 1995.

[258] M. Villata and C. M. Raiteri.
Helical jets in blazars. I. The case of MKN 501.
A&A, 347:30–36, July 1999.

[259] I. Vurm and J. Poutanen.
Time-Dependent Modeling of Radiative Processes in Hot Magnetized Plasmas.
ApJ, 698:293–316, June 2009.

[260] Z. R. Weaver, K. E. Williamson, S. G. Jorstad, A. P. Marscher, V. M. Larionov, C. M. Raiteri, M. Villata, J. A. Acosta-Pulido, R. Bachev, G. V. Baida, T. J. Balonek, E. Benítez, G. A. Borman, V. Bozhilov, M. I. Carnerero, D. Carosati, W. P. Chen, G. Damljanovic, V. Dhiman, D. J. Dougherty, S. A. Ehgamberdiev, T. S. Grishina, A. C. Gupta, M. Hart, D. Hiriart, H. Y. Hsiao, S. Ibryamov, M. Joner, G. N. Kimeridze, E. N. Kopatskaya, O. M. Kurtanidze, S. O. Kurtanidze, E. G. Larionova, K. Matsumoto, R. Matsumura, M. Minev, D. O. Mirzaqulov, D. A. Morozova, A. A. Nikiforova, M. G. Nikolashvili, E. Ovcharov, N. Rizzi, A. Sadun, S. S. Savchenko, E. Semkov, J. J. Slater, K. L. Smith, M. Stojanovic, A. Strigachev, Yu. V. Troitskaya, I. S. Troitsky, A. L. Tsai, O. Vince, A. Valcheva, A. A. Vasilyev, E. Zaharieva, and A. V. Zhovtan.
Multiwavelength Variability of BL Lacertae Measured with High Time Resolution.
ApJ, 900(2):137, September 2020.

[261] Ann E. Wehrle, Dirk Grupe, Svetlana G. Jorstad, Alan P. Marscher, Mark Gurwell, Mislav Baloković, Talvikki Hovatta, Grzegorz M. Madejski, Fiona H. Harrison, and Daniel Stern.

Erratic Flaring of BL Lac in 2012-2013: Multiwavelength Observations.
ApJ, 816(2):53, January 2016.

[262] Zhong-Zu Wu, Min-Feng Gu, and Dong-Rong Jiang.
The debeamed luminosity, sychrotron peak frequency and black hole mass of BL Lac objects.
Research in Astronomy and Astrophysics, 9(2):168–178, February 2009.

[263] Rui Xue, Ruo-Yu Liu, Maria Petropoulou, Foteini Oikonomou, Ze-Rui Wang, Kai Wang, and Xiang-Yu Wang.
A Two-zone Model for Blazar Emission: Implications for TXS 0506+056 and the Neutrino Event IceCube-170922A.
ApJ, 886(1):23, November 2019.

[264] Rui Xue, Ruo-Yu Liu, Xiang-Yu Wang, Huirong Yan, and Markus Böttcher.
On the Minimum Jet Power of TeV BL Lac Objects in the p-γ Model.
ApJ, 871(1):81, January 2019.

[265] Dahai Yan, Li Zhang, Qiang Yuan, Zhonghui Fan, and Houdun Zeng.
Emitting Electrons Spectra and Acceleration Processes in the Jet of Mrk 421: From the Low State to the Giant Flare State.
ApJ, 765(2):122, March 2013.

[266] M. Zacharias, M. Böttcher, F. Jankowsky, J. P. Lenain, S. J. Wagner, and A. Wierzcholska.
Cloud Ablation by a Relativistic Jet and the Extended Flare in CTA 102 in 2016 and 2017.
ApJ, 851(2):72, December 2017.

[267] M. Zacharias, M. Böttcher, F. Jankowsky, J. P. Lenain, S. J. Wagner, and A. Wierzcholska.
The Extended Flare in CTA 102 in 2016 and 2017 within a Hadronic Model through Cloud Ablation by the Relativistic Jet.
ApJ, 871(1):19, January 2019.

[268] M. Zamaninasab, E. Clausen-Brown, T. Savolainen, and A. Tchekhovskoy.
Dynamically important magnetic fields near accreting supermassive black holes.
Nature, 510(7503):126–128, June 2014.

[269] D. Zargaryan, S. Gasparyan, V. Baghmanyan, and N. Sahakyan.
Comparing 3C 120 jet emission at small and large scales.
A&A, 608:A37, December 2017.

[270] GT Zatsepin and VA Kuz'min.
Neutrino production in the atmosphere.
Soviet Physics JETP, 14(6), 1962.

[271] A. Zech, M. Cerruti, and D. Mazin.
Expected signatures from hadronic emission processes in the TeV spectra of BL Lacertae objects.
A&A, 602:A25, June 2017.

[272] S. Zenitani and M. Hoshino.
The Generation of Nonthermal Particles in the Relativistic Magnetic Reconnection of Pair Plasmas.
ApJL, 562(1):L63–L66, November 2001.

[273] Lixia Zhang, Sina Chen, Hubing Xiao, Jinting Cai, and Junhui Fan.
Doppler Factor Estimation for Fermi Blazars.
ApJ, 897(1):10, July 2020.

[274] Y. H. Zhang, A. Celotti, A. Treves, L. Chiappetti, G. Ghisellini, L. Maraschi, E. Pian, G. Tagliaferri, F. Tavecchio, and C. M. Urry.
Rapid X-Ray Variability of the BL Lacertae Object PKS 2155-304.
ApJ, 527(2):719–732, December 1999.

[275] Y. G. Zheng, G. B. Long, C. Y. Yang, and J. M. Bai.
Formation of the Electronic Spectrum in Relativistic Jets of Gamma-Ray Blazars.
, 130(990):083001, August 2018.

[276] P A Zyla, R M Barnett, J Beringer, O Dahl, D A Dwyer, D E Groom, C J Lin, K S Lugovsky, E Pianori, D J Robinson, C G Wohl, W M Yao, K Agashe, G Aielli, B C Allanach, C Amsler, M Antonelli, E C Aschenauer, D M Asner, H Baer, Sw Banerjee, L Baudis, C W Bauer, J J Beatty, V I Belousov, S Bethke, A Bettini, O Biebel, K M Black, E Blucher, O Buchmuller, V Burkert, M A Bychkov, R N Cahn, M Carena, A Ceccucci, A Cerri, D Chakraborty, R Sekhar Chivukula, G Cowan, G D'Ambrosio, T Damour, D de Florian, A de Gouvêa, T DeGrand, P de Jong, G Dissertori, B A Dobrescu, M D'Onofrio, M Doser, M Drees, H K Dreiner, P Eerola, U Egede, S Eidelman, J Ellis, J Erler, V V Ezhela, W Fetscher, B D Fields, B Foster, A Freitas, H Gallagher, L Garren, H J Gerber, G Gerbier, T Gershon, Y Gershtein, T Gherghetta, A A Godizov, M C Gonzalez-Garcia, M Goodman, C Grab, A V Gritsan, C Grojean, M Grünewald, A Gurtu, T Gutsche, H E Haber, C Hanhart, S Hashimoto, Y Hayato, A Hebecker, S Heinemeyer, B Heltsley, J J Hernández-Rey, K Hikasa,

J Hisano, A Höcker, J Holder, A Holtkamp, J Huston, T Hyodo, K F Johnson, M Kado, M Karliner, U F Katz, M Kenzie, V A Khoze, S R Klein, E Klempt, R V Kowalewski, F Krauss, M Kreps, B Krusche, Y Kwon, O Lahav, J Laiho, L P Lellouch, J Lesgourgues, A R Liddle, Z Ligeti, C Lippmann, T M Liss, L Littenberg, C Lourengo, S B Lugovsky, A Lusiani, Y Makida, F Maltoni, T Mannel, A V Manohar, W J Marciano, A Masoni, J Matthews, U G Meißner, M Mikhasenko, D J Miller, D Milstead, R E Mitchell, K Mönig, P Molaro, F Moortgat, M Moskovic, K Nakamura, M Narain, P Nason, S Navas, M Neubert, P Nevski, Y Nir, K A Olive, C Patrignani, J A Peacock, S T Petcov, V A Petrov, A Pich, A Piepke, A Pomarol, S Profumo, A Quadt, K Rabbertz, J Rademacker, G Raffelt, H Ramani, M Ramsey-Musolf, B N Ratcliff, P Richardson, A Ringwald, S Roesler, S Rolli, A Romaniouk, L J Rosenberg, J L Rosner, G Rybka, M Ryskin, R A Ryutin, Y Sakai, G P Salam, S Sarkar, F Sauli, O Schneider, K Scholberg, A J Schwartz, J Schwiening, D Scott, V Sharma, S R Sharpe, T Shutt, M Silari, T Sjöstrand, P Skands, T Skwarnicki, G F Smoot, A Soffer, M S Sozzi, S Spanier, C Spiering, A Stahl, S L Stone, Y Sumino, T Sumiyoshi, M J Syphers, F Takahashi, M Tanabashi, J Tanaka, M Taševský, K Terashi, J Terning, U Thoma, R S Thorne, L Tiator, M Titov, N P Tkachenko, D R Tovey, K Trabelsi, P Urquijo, G Valencia, R Van de Water, N Varelas, G Venanzoni, L Verde, M G Vincter, P Vogel, W Vogelsang, A Vogt, V Vorobyev, S P Wakely, W Walkowiak, C W Walter, D Wands, M O Wascko, D H Weinberg, E J Weinberg, M White, L R Wiencke, S Willocq, C L Woody, R L Workman, M Yokoyama, R Yoshida, G Zanderighi, G P Zeller, O V Zenin, R Y Zhu, S L Zhu, F Zimmermann, J Anderson, T Basaglia, V S Lugovsky, P Schaffner, and W Zheng.
Review of Particle Physics.
Progress of Theoretical and Experimental Physics, 2020(8), 08 2020.
083C01.